

***Ab initio* Calculations of Spin-Wave Excitation Spectra from Time-Dependent Density-Functional Theory**

Von der Fakultät für Mathematik, Informatik und
Naturwissenschaften der RWTH Aachen University zur
Erlangung des akademischen Grades eines Doktors der
Naturwissenschaften genehmigte Dissertation

vorgelegt von

Diplom-Physiker Manfred Niesert

aus Essen

Berichter: Univ.-Prof. Dr. rer. nat. Stefan Blügel
Univ.-Prof. Dr. rer. nat. Arno Schindlmayr
Tag der mündlichen Prüfung: 20.05.2011

Diese Dissertation ist auf den Internetseiten der
Hochschulbibliothek online verfügbar.

CONTENTS

1	Introduction	1
2	Density-Functional Theory	5
2.1	The Many-Body Problem	5
2.2	Density-Functional Fundamentals	9
2.3	The Kohn-Sham Formalism	10
2.4	Performance of DFT	16
2.5	Time-Dependent DFT	19
3	The Spin Response	23
3.1	Magnetism in Solids and Spin Waves	24
3.2	The Correlation Function	28
3.3	The Response in Time-Dependent DFT	37
3.4	The Bigger Context	40
4	The Spin-Polarized Homogeneous Electron Gas	47
4.1	Characteristic Quantities	48
4.2	The Kohn-Sham Response	53
4.3	The Exchange-Correlation Kernel in ALDA	57
4.4	Spin Waves from ALDA	60
4.5	The Correlation Contribution	66
4.6	Differences and Conclusions for Real Materials	69
5	Implementation	73
5.1	Reformulation for Lattice-Periodic Systems	74
5.2	DFT and the FLAPW method	75
5.3	ALDA and the Mixed Product Basis	86
6	Results for Real Materials	95
6.1	General remarks	95
6.2	Tests of the Method	99
6.3	Iron	103
6.4	Nickel	108
6.5	Cobalt	113
6.6	Comparison to Adiabatic Approximation	118
7	Conclusions	123

A Notation	125
B Derivations	131
Bibliography	139

CHAPTER 1

INTRODUCTION

Magnetism is an intriguing phenomenon. It has fascinated people already in ancient times, when performers demonstrated the invisible magnetostatic forces which enable amber to attract lint and dust in an – at that time – incomprehensible and miraculous way. Since then, the exploration of magnetic effects has long been extended beyond pure curiosity. Nowadays a lot of the fundamental magnetic mechanisms are well understood, leading to a manifold of applications that are part of our every-day life in one way or another, ranging from effects on a macroscopic scale, such as the compass or the generator, to omnipresent applications of modern micro- and nanoelectronics most notably in the area of computing and information technology. The delightful journey into the magnetic realm has just begun, and – sufficient fundamental knowledge provided – stimulating developments are ahead of us!

Applications of magnetism The most prominent utilization on a microscopic scale is probably magnetic data storage – including computer hard disk drives – which is present in all aspects of information technology, ranging from IT infrastructure to consumer devices. The astonishing growth in electronics capabilities (e.g., computing power or storage capacity), which is commonly dubbed synonymously with Moore’s Law, would not have been possible without continuous improvement in the underlying basic technology, and extension of the understanding and application of magnetism on a microscopic level.

A key achievement in this regard was the discovery of the effect of Giant Magnetoresistance (GMR), which is based on the orientation of magnetic moments in an assembly of different magnetic and non-magnetic slim layers of a thickness of only a few atoms. It is this effect which boosted the development and enabled the tremendous growth of hard disk capacity of the last decade. Further applications include new magnetic sensors. The outstanding relevance of this development is reflected by the joint awarding of the Nobel Prize of Physics in 2007 to the discoverers of this effect, Peter Grünberg and Albert Fert.

Magnetic data storage is now a key technology of the information age and will continue to be so for the foreseeable future. In order to fuel the development of ever miniaturized areas in magnetic storage and ever decreasing switching times of devices a deepened understanding of the magnetic properties of the materials in use, in particular its magnetic excitations and switching dynamics is indispensable.

Theoretical and experimental investigations While macroscopic properties have been understood quite early from a phenomenological point of view, its microscopic origin has been unclear for a long time. This has only been revealed after the development of

quantum mechanics and the discovery of the electron spin in the early 20th century and the emerging solid-state physics.

However, it is this nano-scale insight into magnetism which is indispensable in order to match the continuous demand for device engineering on an atomic level. One important kind of corroboration is provided by theoretical investigations, which nowadays prominently include computer simulations. These computations serve not only as a tool to better understand the results of conducted experiments; they should also feature a significant extend of predictive power. In this sense, the implementations of theoretical methods in computer codes can act as a virtual laboratory, enabling the investigation of new problems not yet realized in real-world setups, and providing answers as well as new input for novel experiments.

The goal is to bring together theoretical and practical experiments as two different branches of related investigations, with the aim to harmonize their findings, or to identify and systematically categorize remaining deviations and learn about their origins. Such a combined approach should enable for the utilization of the advantages of each discipline, leading to new ideas to be thought, and will finally result in new applications of magnetic effects, leading to new real-world products available to customers.

The spin-flip response function According to the very fundamental rules that make the world stick together, a system not being exposed to any perturbing interaction is striving towards its energetical ground state, which has an associated magnetic structure. This can include very diverse setups such as ferromagnetic, ferrimagnetic or antiferromagnetic orientation of the magnetic moments on an atomic scale.

Apart from the inherent magnetic ground-state structure of solids and molecules, the reaction of a system to external magnetic fields is the key property to study. This is condensed in the response function χ^{+-} which, from a mathematical point of view, is defined as a functional derivative of the magnetization with respect to the external perturbing magnetic field. From a physical point of view, this quantity describes how a charge-neutral elementary spin excitation (i.e., an increase or decrease of the total spin of the system due to an external probe) propagates in the system. In model calculations, two distinct kinds of such excitations can be distinguished:

- single-particle excitations that involve individual particles of the system (in the scope of the density functional theory: fictitious non-interacting particles), which are called spin-flip excitations; and
- collective excitations that involve the whole ensemble of particles of the system, which are called spin-wave excitations. In the Heisenberg model, these excitations can be conveniently visualized as wave-like spin oscillations which spread throughout the system.

In real materials, these two kinds of excitations cannot be clearly separated. Subsequently, the according response function χ^{+-} which describes both of these effects can be called spin-flip response function or spin-wave response function.

The representation of this spin-flip response function in the energy and momentum domain, which reads $\chi^{+-}(\mathbf{q}, \omega)$, provides information on the strength of the response to probes of the given characteristics. For example, spin waves of a given energy and momentum are excited in neutron scattering experiments by matching neutrons. Another example includes a

change of the magnetic structure (like the switching of magnetic orientation in a microscopic domain, representing a data bit in a storage device) which also involves elementary magnetic excitations. For the design of electromagnetic devices the necessary energies to be applied and the encountered switching times are key factors.

Method of investigation Different methods have been developed to compute the electronic structure of solids, which can be grouped into model approaches and first-principles (also called *ab initio*) approaches. Each approach has its specific advantages and disadvantages. First-principles methods (such as the Density Functional Theory) establish a calculation procedure essentially without any material-specific parameters, which enables such calculations for predictive statements. Model-based approaches, on the other hand, comprise such adjustable parameters. However, specifically tailored model approaches might yield significant advantages in terms of computation time or in terms of physical systems which are accessible. (For instance, models based on the Hubbard Hamiltonian are geared towards the investigation of strongly correlated systems which are barely accessible with Density Functional Theory.)

The investigations in this thesis are based on the Density Functional Theory (DFT), which is the prevalent *ab initio* approach. It is geared towards the determination of the ground state of a physical system. Any excited states, though, are beyond the scope of this theory. Subsequently, the task to determine the magnetic response function results in a two-step procedure: In the first part the ground state is determined using DFT, in the subsequent second part the response function is calculated on top of the DFT result. Two common methods exist for this task: The many-body perturbation theory (MBPT) and the time-dependent extension of the conventional DFT (TDDFT).

Calculations in this thesis In this thesis, the spin-flip response function χ^{+-} is determined by means of the TDDFT. This method is suited in particular for charge-neutral excitations, which include spin-wave excitations. The detailed incarnation involves the full-potential linearized augmented plane-wave method (FLAPW). Up to the author's knowledge, this combination has not been implemented so far.

Several characteristic features of the spin-flip response can be efficiently studied for the homogeneous electron gas. The according formalism is derived in this thesis. The results help both in the implementation of the method as well as in the understanding of the results.

Subsequently, the method is tested on real systems. The focus is put on a systematic analysis of the method. The influence of the computational parameters is evaluated for the simple transition metals Iron, Cobalt and Nickel. The resulting spin-wave dispersions are compared to other calculations and measurements.

Structure of this thesis According to the statements above, this text contributes to the exploration of magnetism a theoretical investigation based on first-principles methods. A new combination of methods is implemented. Therefore the main goal of this thesis is a consistent formulation and presentation of the theory, and a reliable assessment of the implementation. The structure is as follows.

- The basic theory that underlies all the calculations of this work – the conventional

density-functional theory (DFT) as well as its time-dependent extension (TDDFT) – is introduced in chapter 2.

- The crucial physical quantity that is to be investigated, the spin-flip correlation function $\chi^{+-}(\mathbf{q}, \omega)$, is worked out in chapter 3 and connected to the density-functional formalism.
- In order to deepen the understanding and put the relations from the preceding chapter into perspective, the formalism is executed in chapter 4 on the homogeneous electron gas.
- Practical implementation issues for real materials are worked out in chapter 5, in particular the FLAPW and the mixed-basis method.
- Results from this implementation are presented in chapter 6.

Each of these chapters starts with a brief overview. The work concludes with an outlook (chapter 7). Derivations and a notation index are found in the appendices.

CHAPTER 2

DENSITY-FUNCTIONAL THEORY

Contents

2.1	The Many-Body Problem	5
2.2	Density-Functional Fundamentals	9
2.3	The Kohn-Sham Formalism	10
2.4	Performance of DFT	16
2.5	Time-Dependent DFT	19

In this chapter I introduce the theory that underlies the current work, namely the methods used to obtain the electronic structure of the solids. The theory of the magnetic response is explored later in chapter 3.

The fundamental framework for any such system is the quantum-mechanical many-body formalism (section 2.1), which in all its beauty is equally universal and insoluble except for very simple cases. Subsequently, focus is put on density-functional theory (DFT, section 2.2), one of the most capable first-principles theories in solid-state physics, which – though providing a framework only – leads to a practical method to handle complex systems. The practicability stems from the ansatz of Kohn and Sham (section 2.3) that leads to the Kohn-Sham equations (2.25) of fictitious non-interacting particles in a replacement system with an additional exchange-correlation potential. Special emphasis is put on one specific approximation for this exchange-correlation potential – the local-density approximation (LDA) – and on the spin-specific aspects of the formalism, both of central importance in the further chapters.

Though enormously powerful, DFT also has some shortcomings briefly discussed in section 2.4. (This should clarify why the particular methods – adiabatic LDA on top of a FLAPW DFT calculation – have been chosen.) The time-dependent extension to the density-functional theory (section 2.5), which overcomes some of these problems, provides the theoretical link to the response function that is the subject of chapter 3.

2.1 The Many-Body Problem

A realistic quantum-mechanical many-body system is not a trivial composition of its constituents, likewise it is highly non-trivial to calculate seemingly elementary properties, such as the energies of the addition to or the removal of one particle from such a system. In fact, the single constituents of such an interacting many-body system can no longer be identified

separately, but the concept of quasi-particles needs to be established. This holds true even for the homogeneous electron gas that is probably the simplest periodic system, which is the class of systems we are interested in. In order to establish a deep understanding of the physical properties of solids, a quantum-mechanical treatment has to be applied that reflects the physical interactions between its constituents. This is best taken into account by employing the true physical interactions, namely the Coulomb attraction and repulsion between the charges of electrons and nuclei. Such an *ab initio* description yields, for instance, the complete energy spectrum, containing all excitations.

According to elementary quantum mechanics, the state $|\Psi(t)\rangle$ of a given system contains the complete information of the system at time t . If zero temperature and an isolated setup without interaction with any environment is assumed, the state vector is determined by the time-dependent Schrödinger equation¹

$$i\hbar \frac{\partial}{\partial t} |\Psi(t)\rangle = \hat{\mathcal{H}}_{\text{mb}} |\Psi(t)\rangle. \quad (2.1)$$

As a first-order differential equation in the time coordinate this equation poses an initial-value problem which demands the specification of an initial state $|\Psi(0)\rangle$. Commonly the ground state is chosen as the initial state.

Finally, we are interested in the response to arbitrary external fields which will, however, be treated as a perturbation in linear response. For the moment, we can therefore neglect them and remain with a many-body Hamilton operator which does not vary in time in any way, $\hat{\mathcal{H}}_{\text{mb}} \neq \hat{\mathcal{H}}_{\text{mb}}(t)$. Then, the time-dependent part of the state can be separated,

$$|\Psi(t)\rangle = |\Psi\rangle e^{-\frac{i}{\hbar}Et} \quad (2.2)$$

with the system's stationary state $|\Psi\rangle$ understood as a function of, e.g., spin and spatial variables of all particles. Together with the total energy E this stationary state is given (for the ground state as well as for excited states) by the time-independent Schrödinger equation

$$\hat{\mathcal{H}}_{\text{mb}} |\Psi\rangle = E |\Psi\rangle. \quad (2.3)$$

Due to the second derivative in the kinetic-energy operator \hat{T} , this equation is a boundary-value problem that requires adequate boundary conditions, e.g., the crystallographic spatial periodicity. These statements are also true for the Kohn-Sham equations (2.25) and (2.50) presented in the coming sections. Independent of the kind of the differential problem, both Schrödinger equations have the further boundary condition of yielding physical states which for fermionic systems need to be anti-symmetric with respect to particle interchange.

The setups considered here are solids consisting of N electrons moving in the potential of N_{nuc} positive nuclear point charges at positions \mathbf{R}_α . The Hamiltonian

$$\hat{\mathcal{H}}_{\text{mb}} = \hat{T} + \hat{V} + \hat{U} + \hat{U}_{\text{nuc}} \quad (2.4)$$

is made up of the operators of the kinetic energy \hat{T} , the electron-nuclei interaction \hat{V} and the electron-electron interaction \hat{U} as well as the nuclei-nuclei interaction \hat{U}_{nuc} . The operators in

¹The presentation in this work is restricted to the non-relativistic case.

first quantization and in SI units read

$$\begin{aligned}
 \hat{T} &= -\frac{\hbar^2}{2m_e} \sum_{i=1}^N \hat{\nabla}_i^2 \\
 \hat{V} &= \sum_{i=1}^N V_{\text{ext}}(\hat{\mathbf{r}}_i), \quad V_{\text{ext}}(\hat{\mathbf{r}}_i) = -\frac{1}{4\pi\epsilon_0} \sum_{\alpha=1}^{N_{\text{nuc}}} \frac{Z_\alpha e^2}{|\hat{\mathbf{r}}_i - \hat{\mathbf{R}}_\alpha|} \\
 \hat{U} &= \frac{1}{2} \frac{1}{4\pi\epsilon_0} \sum_{i \neq j}^N \frac{e^2}{|\hat{\mathbf{r}}_i - \hat{\mathbf{r}}_j|} \\
 \hat{U}_{\text{nuc}} &= \frac{1}{2} \frac{1}{4\pi\epsilon_0} \sum_{\alpha \neq \beta}^{N_{\text{nuc}}} \frac{Z_\alpha Z_\beta e^2}{|\hat{\mathbf{R}}_\alpha - \hat{\mathbf{R}}_\beta|}
 \end{aligned} \tag{2.5}$$

We apply the Born-Oppenheimer approximation, that is we assume fixed coordinates of the nuclei and thus exclude phononic degrees of freedom. The nuclear coordinates \mathbf{R}_α are then understood not as expectation values of operators, but as fixed parameters. Then, the operators read in second quantization:

$$\begin{aligned}
 \hat{T} &= -\frac{\hbar^2}{2m_e} \sum_i \int d^3r \hat{\psi}_i^\dagger(\mathbf{r}) \nabla^2 \hat{\psi}_i(\mathbf{r}) \\
 \hat{V} &= \sum_{i=1}^N \int d^3r \hat{\psi}_i^\dagger(\mathbf{r}) V_{\text{ext}}(\mathbf{r}_i) \hat{\psi}_i(\mathbf{r}), \quad V_{\text{ext}}(\mathbf{r}_i) = -\frac{1}{4\pi\epsilon_0} \sum_{\alpha=1}^{N_{\text{nuc}}} \frac{Z_\alpha e^2}{|\mathbf{r}_i - \mathbf{R}_\alpha|} \\
 \hat{U} &= \frac{1}{2} \frac{1}{4\pi\epsilon_0} \sum_{i \neq j}^N \int d^3r d^3r' \hat{\psi}_i^\dagger(\mathbf{r}) \hat{\psi}_j^\dagger(\mathbf{r}') \frac{e^2}{|\mathbf{r}_i - \mathbf{r}_j|} \hat{\psi}_j(\mathbf{r}') \hat{\psi}_i(\mathbf{r}) \\
 \hat{U}_{\text{nuc}} &= \frac{1}{2} \frac{1}{4\pi\epsilon_0} \sum_{\alpha \neq \beta}^{N_{\text{nuc}}} \frac{Z_\alpha Z_\beta e^2}{|\mathbf{R}_\alpha - \mathbf{R}_\beta|}.
 \end{aligned} \tag{2.6}$$

In this context the external potential² V_{ext} is understood as being external to the electronic part of the system, and takes up the sum of all nuclear potentials. It would also take up scalar potentials external to the system, however we neglected such potentials earlier. Such a ‘true’ external field will be used in the time-dependent formalism in section 2.5. The term U_{nuc} yields a constant energy value E_{nuc} ³ for a given setup of coordinates \mathbf{R}_α .

The Hilbert space encompassing the state vector is built out of subspaces of its constituents, and many-body operators are composed of single-particle operators (like $\hat{\mathbf{r}}_i$ or $\hat{\nabla}_i$

²It should be noted that the unit of the potentials used in this thesis are that of energy, since it acts on the particle density instead of the charge density, which does *not* contribute the factor e , according to (2.13). In atomic units, however, this distinction disappears.

³This should express that the value is constant for one given setup of nuclear coordinates. It is finite if calculated for one unit cell of a periodic system, but diverges for the whole system.

above) acting on the according subspaces. The particle and spin density read

$$n(\mathbf{r}) = \langle \Psi | \sum_{i=1}^N \delta(\mathbf{r} - \hat{\mathbf{r}}_i) | \Psi \rangle \quad (2.7)$$

$$\boldsymbol{\sigma}(\mathbf{r}) = \langle \Psi | \sum_{i=1}^N \hat{\boldsymbol{\sigma}}_i \delta(\mathbf{r} - \hat{\mathbf{r}}_i) | \Psi \rangle \quad (2.8)$$

where $\hat{\boldsymbol{\sigma}}_i = (\sigma_x, \sigma_y, \sigma_z)_i$ is the vector of Pauli Matrices

$$\sigma^x = \begin{pmatrix} 0 & 1 \\ 1 & 0 \end{pmatrix} \quad \sigma^y = \begin{pmatrix} 0 & -i \\ i & 0 \end{pmatrix} \quad \sigma^z = \begin{pmatrix} 1 & 0 \\ 0 & -1 \end{pmatrix} \quad (2.9)$$

acting on the 2×2 spin subspace of particle i .

In practice, it turns out that many mesoscopic and macroscopic solids (like the lattice-periodic crystals we consider) are either non-magnetic, i.e., $\boldsymbol{\sigma}(\mathbf{r}) = \mathbf{0}$ in the whole system, or collinear, i.e., the spin density $\boldsymbol{\sigma}$ is everywhere parallel to one fixed axis commonly chosen as the z direction. As a consequence, the four-component description $(n, \boldsymbol{\sigma})$ can be simplified to $(n_\uparrow, n_\downarrow)$ or (n, σ) or (n, ξ) , involving the spin polarization ξ .

$$n(\mathbf{r}) = n_\uparrow(\mathbf{r}) + n_\downarrow(\mathbf{r}) \quad (2.10)$$

$$\boldsymbol{\sigma}(\mathbf{r}) = n_\uparrow(\mathbf{r}) - n_\downarrow(\mathbf{r}), \quad \boldsymbol{\sigma}(\mathbf{r}) = \sigma(\mathbf{r}) \mathbf{e}_z \quad (2.11)$$

$$\xi(\mathbf{r}) = \frac{\sigma(\mathbf{r})}{n(\mathbf{r})}, \quad 0 \leq |\xi(\mathbf{r})| \leq 1. \quad (2.12)$$

The consequences of collinearity for the formulation of the theory will be pointed out throughout the text. The connection between charge and particle density and between magnetization and spin density read :

$$\rho(\mathbf{r}) = -en(\mathbf{r}) \quad (2.13)$$

$$\mathbf{m}(\mathbf{r}) = -g \frac{\mu_B}{\hbar} \mathbf{S}(\mathbf{r}) = -\frac{g}{2} \frac{\mu_B}{\hbar} \boldsymbol{\sigma}(\mathbf{r}) \quad (2.14)$$

with the Bohr magneton μ_B (whose value in SI units is $\frac{e\hbar}{2m_e}$, please confer appendix A.1) and positively defined elementary charge e . The spin operators are related by

$$\hat{\mathbf{S}} = \frac{\hbar}{2} \hat{\boldsymbol{\sigma}}. \quad (2.15)$$

The factor

$$g = 2 \left(1 + \frac{\alpha}{2\pi} + \mathcal{O}(\alpha^2) \right) \approx 2.0023 \quad (2.16)$$

is called Landé factor. $\alpha \approx 1/137$ is the universal fine-structure constant. The value $g = 2$ can be obtained from the Dirac equation, however, a proper treatment according to quantum electrodynamics leads to the small deviations noted above.

From now on, the atomic Hartree units (see appendix A.1) are used, which are the standard set of units for quantum-mechanical calculations, involving the setting $e = m_e = \hbar = 1$,

$\mu_B = 1/2$. However, I will continue to use the symbol μ_B since it usually appears together with the Landé factor and $\mu_B g \approx 1$.

The effort to solve (2.3) scales exponentially with the number of particles and is much too complex to be solved exactly [Koh99]. In spatial representation the system's eigenstate reads $\Psi(\mathbf{r}_1, \sigma_1, \dots, \mathbf{r}_N, \sigma_N)$, being a function of $3N$ spatial variables and N spin variables. Both the computation and storage of the eigenvector of all but the smallest systems (that are, depending on the exact method, systems of maybe a handful of particles) exceed any existing and foreseeable future resources. Furthermore, the full state vector is a bulk of data of which only few exclusive pieces of information – like some operator expectation values – are of interest, while the rest is undesired overhead.

Thus, more efficient formalisms have to be employed that are on the one hand practically applicable, while on the other hand still comprise the essential physics of the system in order to reliably compute the desired quantities.

2.2 Density-Functional Fundamentals

Draw the curtain for density-functional theory (DFT), the de facto standard framework for *ab initio* calculations of solids! It is a powerful tool with predictive power that has led to a deep insight into the inner workings of matter. It was developed in 1964 by Hohenberg and Kohn [HK64].

Its central theorem comes in two parts. The first statement establishes the fundamental importance of the particle density $n(\mathbf{r})$. Utilizing the Rayleigh-Ritz variational principle, it is proved by contradiction that there is an invertible mapping between the external potential $V_{\text{ext}}(\mathbf{r})$ (2.5) and the particle density (2.7) of the ground state, $n_0(\mathbf{r})$, with the sole ambiguity of an additional constant in the potential. For a solid described by equation (2.3) this means that the charge distribution determines the lattice structure, and vice versa. Therefore, if the external potential V_{ext} is a functional of the ground-state density, so is the Hamiltonian $\hat{\mathcal{H}}_{\text{mb}} = \hat{\mathcal{H}}_{\text{mb}}[n_0]$ as well as the many-body state $|\Psi\rangle = |\Psi[n_0]\rangle$, and the expectation value of any observable \hat{O} in the ground state, is determined as

$$O_0 = O[n_0] = \langle 0 | \hat{O} | 0 \rangle, \quad |0\rangle = |\Psi[n_0]\rangle \quad (2.17)$$

with the many-body ground state $|0\rangle$. In practice, however, no feasible way is known to calculate most of these physical quantities from the ground-state density directly, which still has to be determined in the first place.

The second part of the theorem states that for each possible physical potential $V_{\text{ext}}(\mathbf{r})$ there exists a unique functional $E[n]$ which under the boundary condition of particle conservation $\int n(\mathbf{r}) d^3r = N$ obtains its minimum for the ground-state density $n_0(\mathbf{r})$ and yields the ground-state energy E_0 :

$$E_0 = E[n_0] \stackrel{!}{=} \min_n E[n]. \quad (2.18)$$

While the initial proof was limited to a non-degenerate ground state, this restriction was removed later [DG90]. In a more elegant derivation of the above theorems, Levy [Lev79] furthermore showed that the unique energy functional $E[n]$ for any physical density $n(\mathbf{r})$ can

be defined as the minimum over all many-body states $|\Psi\rangle$ which yield the density $n(\mathbf{r})$,

$$E[n] = \min_{|\Psi\rangle \rightsquigarrow n} \langle \Psi | \hat{T} + \hat{U} + \hat{V}_{\text{ext}} | \Psi \rangle \quad (2.19)$$

and can be written as

$$E[n] = F[n] + \int n(\mathbf{r}) V_{\text{ext}}(\mathbf{r}) d^3r, \quad (2.20)$$

where the simple functional dependence of the energy on V_{ext} is explicitly displayed. The functional

$$F[n] = \min_{|\Psi\rangle \rightsquigarrow n} \langle \Psi | \hat{T} + \hat{U} | \Psi \rangle \quad (2.21)$$

is universal in the sense that it does not depend on V_{ext} and that it has the same form for all systems described by the Schrödinger equation (2.3).

It should be noted that this formalism also holds for systems containing particles with a spin degree of freedom. The magnetization is then given as a functional of the charge density, $m = m[n]$. However, this turns out to be impractical, consequently the *spin-density functional theory* has emerged, which describes all the functionals with respect to both charge density and magnetization, e.g., $E = E[n, \mathbf{m}]$. This description is used in the forthcoming sections. An equivalent formulation involves a four-component density matrix $\rho_{\alpha\beta}$.

If external fields are present, the central conclusion of the Hohenberg-Kohn theorem, the mapping between charge and external potential breaks down⁴; further development on this led to the *current-density functional theory* [VR87], which uses functionals $E = E[n, \mathbf{m}, \mathbf{j}]$ of charge and magnetization as well as the current density $\mathbf{j}(\mathbf{r})$. This will not be a subject in this thesis.

2.3 The Kohn-Sham Formalism

Density-functional theory has led us to a vast reduction of the problem, from handling the $4N$ -dimensional function Ψ to finding the minimum of $E[n]$ with respect to the three-dimensional trial function $n(\mathbf{r})$. However, since the explicit form (with respect to the density) of the functional $F[n]$ remains unknown, the theory seems to be rather academic and of little use. At this point, the work of Kohn and Sham [KS65] enters the stage, for the moment being presented for a non-spin-polarized system. (Thus, the number of electrons N is considered to be even. This limitation is lifted in the next paragraph on the spin-dependent Kohn-Sham formalism.)

The central idea is to construct a fictitious auxiliary system of N *independent* particles described by wave functions $\varphi_i(\mathbf{r})$ moving in an *effective* potential $V_{\text{eff}}(\mathbf{r})$. This potential is

⁴To be more precise, the Hohenberg-Kohn theorem still holds for physical external fields of finite size. However, the Hamiltonians in use frequently lead to infinite fields, let it be scalar fields of a form $V_z = -Ez$ or magnetic fields mediated by a vector potential. Such fields cannot be covered by the Hohenberg-Kohn theorem anymore because they possess no well-defined ground state.

chosen such that the density of this auxiliary system

$$n(\mathbf{r}) = \sum_i |\varphi_i(\mathbf{r})|^2 f(\epsilon_i) \quad (2.22)$$

equals the interacting system's density. The energy functional (2.20) then reads

$$E_s[n] = T_s[n] + \int n(\mathbf{r}) V_{\text{eff}}(\mathbf{r}) d^3r. \quad (2.23)$$

with the kinetic energy functional

$$T_s[n] = -\frac{1}{2} \sum_i^{\text{occ}} \int \varphi_i^*(\mathbf{r}) \nabla^2 \varphi_i(\mathbf{r}) d^3r. \quad (2.24)$$

Since we are within the scope of DFT, we only describe the ground state, and our many-body state is combined out of the N energetically lowest single-particle states. This is reflected by the Fermi occupation function f in (2.22). The variation of $E_s[n]$ with respect to the complex conjugate of these orbitals φ then leads to the Kohn-Sham equations

$$\left[-\frac{1}{2} \nabla^2 + V_{\text{eff}}(\mathbf{r}) \right] \varphi_i(\mathbf{r}) = \epsilon_i \varphi_i(\mathbf{r}) \quad (2.25)$$

which resemble one-particle Schrödinger equations. The Lagrange parameters ϵ_i enter due to the boundary condition of charge conservation, $\int n(\mathbf{r}) d^3r = N$, and further ensure normalization $\langle \varphi_i | \varphi_j \rangle = \delta_{ij}$. These parameters as well as the eigenfunctions are a purely mathematical construct without physical meaning.⁵ Nevertheless, it is common practice to interpret the ϵ_i not only as single-particle energies of the Kohn-Sham system but as quasi-particle energies of the interacting system. Experience shows both qualitative agreement with experimental results, e.g., obtained by angular-resolved photo-emission spectroscopy (ARPES), as well as systematic quantitative deviations.

Since we consider a non-spin-polarized (also casually called paramagnetic) system, each state $\varphi_i(\mathbf{r})$ is occupied twice. Subsequently one can understand the index i to cover electrons of one spin channel only, and account for the other spin channel by a factor of 2 where necessary. However, this notation is not picked up in this text.

In order to apply this scheme, a useful expression for the effective potential V_{eff} must be found. The important achievement of Kohn and Sham was to write the true system's total energy (2.20) as

$$E[n] = T_s[n] + E_H[n] + E_{\text{ext}}[n] + E_{\text{xc}}[n] + E_{\text{nuc}} \quad (2.26)$$

with the Hartree energy

$$E_H[n] = \frac{1}{2} \int \frac{n(\mathbf{r})n(\mathbf{r}')}{|\mathbf{r} - \mathbf{r}'|} d^3r d^3r' \quad (2.27)$$

⁵ Exempt from this is the highest occupied eigenvalue ϵ_N , which according to Janak's theorem [Jan78] equals the chemical potential of the real system.

and the “external energy” resulting from the influence of the external potential,

$$E_{\text{ext}}[n] = \int n(\mathbf{r})V_{\text{ext}}(\mathbf{r}) d^3r. \quad (2.28)$$

The term E_{nuc} accounts for the repulsion of the atomic nuclei, c.f., \hat{U}_{nuc} in (2.6). Finally, the newly introduced *exchange-correlation energy* E_{xc} is defined such that the sum in (2.26) results in the total energy E of the interacting system. The exact form of this exchange-correlation energy is unknown, and its exact determination amounts to the solution of the many-body problem.

The functional variation of the total energy (2.26) that yielded the Kohn-Sham equations (2.25) leads to the effective potential

$$V_{\text{eff}}(\mathbf{r}) = V_{\text{H}}(\mathbf{r}) + V_{\text{ext}}(\mathbf{r}) + V_{\text{xc}}(\mathbf{r}) \quad (2.29)$$

$$V_{\text{H}}(\mathbf{r}) = \int \frac{n(\mathbf{r}')}{|\mathbf{r} - \mathbf{r}'|} d^3r' \quad (2.30)$$

$$= \int v(\mathbf{r}, \mathbf{r}')n(\mathbf{r}') d^3r', \quad v(\mathbf{r}, \mathbf{r}') = \frac{1}{|\mathbf{r} - \mathbf{r}'|}. \quad (2.31)$$

Analogously, the exchange-correlation potential V_{xc} is the functional derivative of the exchange-correlation energy

$$V_{\text{xc}}(\mathbf{r}) = \frac{\delta E_{\text{xc}}}{\delta n(\mathbf{r})}, \quad (2.32)$$

which makes it a local function of the spatial coordinate \mathbf{r} . The Kohn-Sham equations (2.25) facilitate real-world calculations, provided that approximations to this functional of sufficient accuracy as well as analytic simplicity are available.

Since both the Hartree potential V_{H} and exchange-correlation potential V_{xc} are determined by the density $n(\mathbf{r})$, this establishes a self-consistency cycle pictured in figure 2.1. If an initial density $n(\mathbf{r})$ – for instance from a superposition of atomic densities – is provided, the effective potential and the Hamiltonian can subsequently be constructed. The eigenvalues and eigenvectors provide a new density $n^{\text{new}}(\mathbf{r})$ to be constructed according to (2.22) that the procedure can work on. In practice, a DFT cycle will most likely not converge if, for an iteration started with density $n^{(n)}(\mathbf{r})$, the next iteration’s density is set straightforward as $n^{(n+1)}(\mathbf{r}) = n^{\text{new}}(\mathbf{r})$. Instead some kind of mixing between the old and the new density is necessary in order to smooth the changes in density and to yield convergence. The simplest method is the linear mixing

$$n^{(n+1)}(\mathbf{r}) = (1 - \alpha)n^{(n)}(\mathbf{r}) + \alpha n^{\text{new}}(\mathbf{r}), \quad 0 < \alpha < 1. \quad (2.33)$$

If used in solid-state physics, α is typically of the size of just a few percent. Usually more sophisticated mixing algorithms are used, see, e.g., [Joh88] and references therein. The calculation is considered to be converged if the distance between the iteration’s initial density $n^{(n)}(\mathbf{r})$ and the newly constructed density $n^{\text{new}}(\mathbf{r})$ is sufficiently small. If successfully converged, the final density enables us to explore the system’s ground-state properties, such as total energies, band structures, density of states, magnetic moments and many more.

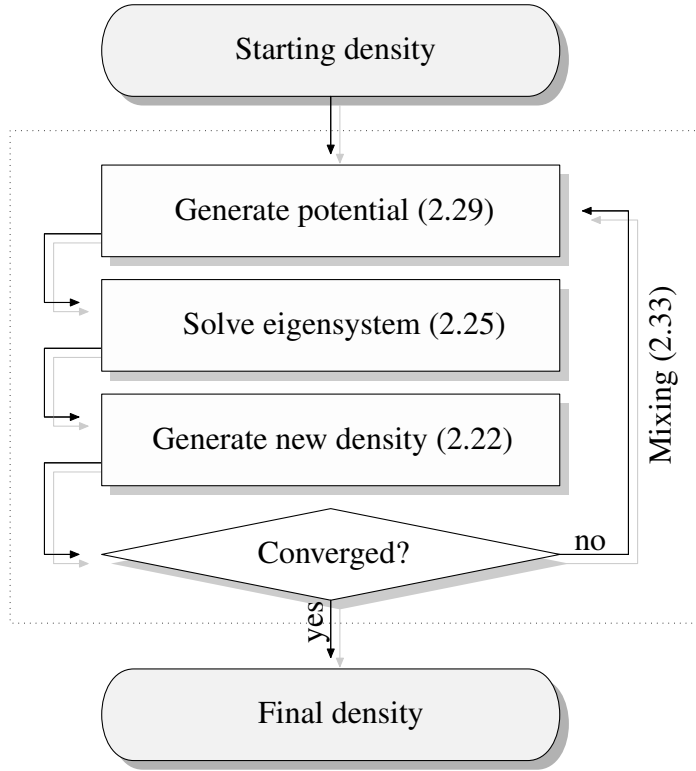


Figure 2.1: Sketch of the self-consistency that leads from an initial to the final charge density by use of the Kohn-Sham self-consistency cycle (which is boxed by dotted lines).

Spin-Polarized Kohn-Sham Method The Kohn-Sham formalism introduced in the preceding lines did not include any freedom in the spin coordinate. However, an extension to spin-polarized systems is possible [PR72, vH72] starting from (2.23), treating the electrons of the Kohn-Sham system as spinors⁶ of wave functions $\varphi_{i\sigma}$,

$$\varphi_i(\mathbf{r}) = \begin{pmatrix} \varphi_{i\uparrow}(\mathbf{r}) \\ \varphi_{i\downarrow}(\mathbf{r}) \end{pmatrix} \quad (2.34)$$

with $\sigma \in \{\uparrow, \downarrow\}$ denoting the spin coordinate.

As stated earlier the exchange-correlation potential $E_{xc}[n]$ is determined solely by the charge density also in the case of spin-polarized systems where the magnetization can also be understood as a functional of the density, $\mathbf{m}[n]$. However, it is most helpful to parametrize it with respect to both charge and magnetization density, $E_{xc} = E_{xc}[n, \mathbf{m}]$. The Kohn-Sham equations

$$\left[\left(-\frac{1}{2} \nabla^2 + V_{\text{eff}}(\mathbf{r}) \right) \mathbb{1} - \hat{\mathbf{m}} \cdot \mathbf{B}_{xc}(\mathbf{r}) \right] \varphi_i(\mathbf{r}) = \epsilon_i \varphi_i(\mathbf{r}) \quad (2.35)$$

⁶This notation treats a Kohn-Sham particle as a spinor based on the spin coordinate σ . This excludes a fully-relativistic treatment (in which the spin is not a good quantum number anymore), which would require the introduction of the combined moment $\hat{\mathbf{J}} = \hat{\mathbf{L}} + \hat{\mathbf{S}}$ of the angular and the spin moment. In the method presented in section 5.2.4 the core electrons are calculated separately in a fully relativistic way while the valence electrons are calculated scalar-relativistic.

are then a system of two equations, now also containing the magnetic moment vector operator $\hat{\mathbf{m}}$, c.f., (2.9), (2.14), and the exchange-correlation magnetic field

$$\mathbf{B}_{\text{xc}}(\mathbf{r}) = -\frac{\delta E_{\text{xc}}[n, \mathbf{m}]}{\delta \mathbf{m}(\mathbf{r})}. \quad (2.36)$$

Thus, the independent Kohn-Sham electrons are not only moving in the mean-field potential V_{eff} , but also couple to the effective magnetic field $\mathbf{B}_{\text{eff}} = \mathbf{B}_{\text{xc}} + \mathbf{B}_{\text{ext}}$ (where $B_{\text{ext}} = 0$ was assumed). In order to properly account for this, the momentum operator would be needed to be replaced by $\frac{1}{i}\nabla \rightsquigarrow \frac{1}{i}\nabla + \mathbf{A}$, introducing a vector potential \mathbf{A} and leading to the aforementioned current-spin-density-functional theory. However, this modification causes very small corrections in the situation discussed here, and is neglected in the following.

The coupling between the two equations is due to the magnetic moment operator $\hat{\mathbf{m}}$. However, in systems with collinear spin structure the states φ_i can be chosen to exclusively have either spin-up or spin-down contributions,

$$\varphi_i = \begin{pmatrix} \varphi_{i\uparrow} \\ 0 \end{pmatrix} \quad \text{or} \quad \varphi_i = \begin{pmatrix} 0 \\ \varphi_{i\downarrow} \end{pmatrix} \quad (2.37)$$

and the charge per spin channel can be written

$$n_\sigma(\mathbf{r}) = \sum_i |\varphi_{i\sigma}(\mathbf{r})|^2 f(\epsilon_{i\sigma}). \quad (2.38)$$

With relations (2.9), (2.14) the Kohn-Sham system of equations (2.35) separates into two single equations

$$\left[-\frac{1}{2}\nabla^2 + V_{\text{eff}}(\mathbf{r}) + \frac{1}{2}\mu_{\text{B}}g\sigma B_{\text{xc}}(\mathbf{r}) \right] \varphi_{i\sigma}(\mathbf{r}) = \epsilon_{i\sigma}\varphi_{i\sigma}(\mathbf{r}) \quad (2.39)$$

with the variable $\sigma = \pm 1$ for the spin index $\sigma = \uparrow, \downarrow$, respectively. The index i now separately runs over the states of each spin channel. The last term in the brackets can result in a splitting between the two spin directions, leading to a net magnetization of the system. However, magnetism, which is omnipresent in single atoms, becomes increasingly suppressed with higher dimensionality. Among the three-dimensional pure (i.e., systems consisting of one element only) bulk transition metals, only the five elements chromium and manganese (both anti-ferromagnets) and iron, cobalt and nickel (all ferromagnets) show a magnetic order in the ground state [Blu05]. More on the features of magnetic systems is presented in section 3.1.

The Exchange-Correlation Energy The exchange-correlation energy constitutes the link in order to perform practical calculations. All the effects that lie beyond the Hartree picture are put into this functional. The magnitude of this energy in comparison to the kinetic and Coulomb terms is illustrated in table 2.1. The big advantage of the Kohn-Sham approach compared to earlier approaches like the Thomas-Fermi model [Fer27, Tho27] is the accurate description of the kinetic term which is obviously of major significance. Furthermore, the exchange-correlation contribution to the total energy plays a significant role and needs to be represented accurately. Since it is not possible in general to obtain an analytical expression

	Nickel	Silicon
$T_s[n]$	+1545.25	+290.87
$E_{\text{Coul}}[n]$	-3002.49	-560.03
$E_{\text{xc}}[n]$	-63.59	-20.88
$E_{\text{tot}}[n]$	-1520.83	-290.04

Table 2.1: Contributions to the total energy (2.26) for two different crystals, given in Hartree per unit cell. All Coulomb interactions are summed up in the term $E_{\text{Coul}} = E_{\text{H}} + E_{\text{ext}} + E_{\text{nuc}}$. The Perdew-Burke-Ernzerhof GGA is used. The numbers also suggest a good agreement with the virial theorem that holds also for solids [Jan74].

some kind of approximation is needed, commonly involving some fitted parametrization. Fortunately functionals have been found that are both feasible and accurate. The goal in solid-state physics is to provide universally applicable methods. The involved approximations might include adjustable parameters, but they are fixed globally for any given calculation to physically sound values. In particular, they are *independent* of properties of the specific system setup (such as the elements involved). These parameters are not to be understood as a degree of freedom in order to fit, e.g., computational results to their experimental counterparts. This needs to be kept in mind when referring to these calculations as *parameter-free* or *ab initio*.

The simplest approximation to this functional is the *local-density approximation* (LDA) that has the form

$$E_{\text{xc}} = E_{\text{xc}}^{\text{LDA}}[n, |\mathbf{m}|] = \int n(\mathbf{r}) [\varepsilon_{\text{x}}(n, m) + \varepsilon_{\text{c}}(n, m)] \Big|_{\substack{n=n(\mathbf{r}) \\ m=|\mathbf{m}(\mathbf{r})|}} d^3r. \quad (2.40)$$

It is separated into an exchange and a correlation contribution, represented by the energies per particle ε_{x} and ε_{c} . Both terms are negative. The exchange part is usually larger than the correlation part, typically by a factor of 3 to 10 in crystallographic systems.

This approximation is inspired by the homogeneous electron gas: In this case the LDA exchange term is equal to the Fock term of the Hartree-Fock method. Thus, it accounts for exchange effects; further correlation effects are covered by the correlation energy per particle ε_{c} . Due to the nature of the homogeneous electron gas, this functional $E_{\text{xc}}^{\text{LDA}}$ depends only on the absolute value of the magnetization $m(\mathbf{r}) = |\mathbf{m}(\mathbf{r})|$. The energy densities ε_{x} and ε_{c} are commonly given as functions of n and ξ . The exchange energy density is known analytically as

$$\varepsilon_{\text{x}}(n, \xi) = \varepsilon_{\text{x}}(n, 0) + [\varepsilon_{\text{x}}(n, 1) - \varepsilon_{\text{x}}(n, 0)] f(\xi) \quad (2.41)$$

with the spin polarization ξ from (2.12). The constituents read

$$\varepsilon_{\text{x}}(n, 0) = -C_{\text{x}} n^{1/3}, \quad \varepsilon_{\text{x}}(n, 1) = -2^{1/3} C_{\text{x}} n^{1/3}, \quad C_{\text{x}} = \frac{3}{4} \left(\frac{3}{\pi} \right)^{1/3} \quad (2.42)$$

and

$$f(\xi) = \frac{(1 + \xi)^{4/3} + (1 - \xi)^{4/3} - 2}{2^{4/3} - 2}. \quad (2.43)$$

The correlation part, however, is not known in an analytical form, but numerically from quantum Monte-Carlo calculations [CA80]. Different parametrizations exist in order to provide an analytical approximation. In this work the parametrization of Perdew and Wang [PW92] is used. The LDA exchange-correlation functions are detailed out in chapter 4 in the evaluation of the homogeneous electron gas.

While this LDA approach is surprisingly successful, some shortcomings are attributed to it, which led to the subsequent level of approximation to the exchange-correlation energy beyond the LDA, namely the class of *generalized gradient approximations* (GGA) [PK98]. It approximates the missing functional by

$$E_{xc}^{\text{GGA}}[n] = \int g(n, g)|_{\substack{n=n(\mathbf{r}) \\ g=\nabla n(\mathbf{r})}} d^3r \quad (2.44)$$

where the scalar function g depends not only on the density at one coordinate like in the LDA but also on its gradient, which makes this method infinitesimally non-local. Different than in the case of the LDA, the function g is not unique and many different forms have been suggested (e.g., prominent functionals from Perdew and coworkers [PCV⁺92, PBE96] and subsequent improvements [ZY98, HHN99]) incorporating a number of known properties of the exact functional, for instance limits and scaling behaviors. Recent developments [KPB99, TPSS03], termed *meta-GGAs*, include further variables into the functional such as

$$E_{xc}^{\text{meta-GGA}}[n] = \int g(n, g, \tau)|_{\substack{n=n(\mathbf{r}) \\ g=\nabla n(\mathbf{r}) \\ \tau=\tau(\mathbf{r})}} d^3r \quad (2.45)$$

with the kinetic energy density

$$\tau(\mathbf{r}) = -\frac{1}{2} \sum_i^{\text{occ}} \varphi_i^*(\mathbf{r}) \nabla^2 \varphi_i(\mathbf{r}). \quad (2.46)$$

In practice, however, these meta-GGA functionals are typically used as an add-on calculation step after the self-consistency cycle applying one of the aforementioned functionals. Other work focuses on orbital functionals, that are more general functional approximations to the exchange-correlation energy which depend on the Kohn-Sham orbitals. One prominent representative is the *exact exchange* method [Har84] calculating the Hartree-Fock exchange of the Kohn-Sham orbitals, which in particular avoids self-interaction. So-called *hybrid functionals* [Bec93] combine such exact-exchange functionals with conventional GGA functionals. While the notation above on GGAs and meta-GGAs has neglected the spin degree, it can be easily generalized to the magnetic case where the function g depends on twice the number of arguments, the density, density gradient and kinetic energy density of both spin directions.

The magnetic response calculations later in this thesis, however, are restricted to the LDA and do not involve gradient corrections.

2.4 Performance of DFT

The history of density-functional theory is characterized by a continuous and ever-growing diversity of methods that have been developed and implemented within this framework with

different problems and applications in mind. There are for instance real-space and basis-representation methods; methods taking into account the interactions between all the system's constituents (commonly scaling to the third power of the system size N) and order- N methods considering only the near neighborhood; basis-representation methods based on Bloch functions or on localized functions; full-potential and pseudo-potential methods; and many more. Subsequent research led to detailed insight into the physics of materials in general and their actual properties in particular.

However, due to the complicated nature of electronic interactions on the one hand and their intransparent mapping onto the Kohn-Sham system on the other it is difficult to pose statements of general validity regarding their capabilities, yet more difficult to provide an overview of properly detailed scope. For such reviews, please refer to, e.g., [JG89] or [AG98]. In particular, it is often difficult to clearly attribute a deficiency either to the DFT in general, to a particular parametrization of the exchange-correlation energy (such as LDA) or to the method actually used. Below I will outline some capabilities of DFT in view of my spin-response calculations presented later.

Successes and Problems DFT has become the undisputed number-one ab initio theory for the computation of the electronic structure of condensed matter, being widely used in solid-state physics and quantum chemistry as well as in bio-chemistry. Many calculated properties are in very good agreement with corresponding experiments, unveiling predictive power for properties that still have to be measured or even materials that have yet to be synthesized.

In the focus of the majority of solid-state DFT calculations are often semi-conductors, simple metals and, partially, transition metals, applying LDA or GGA. For these materials, features that are well described by DFT include:

- Total energy differences can be well determined, leading to reliable structure information such as lattice type or molecular coordination.
- Lattice constants are commonly matched within a few percent. (LDA tends to underestimate lattice constants while GGA overestimates them a little bit.)
- Many ground-state properties, such as bulk moduli and other mechanical properties, are well described, including phonon frequencies.
- Magnetic structures can be accurately determined, including magnetic moments of atoms and non-collinear configurations.

However, no light without shade. Problems met in practice include:

- There are no conceptual limitations as far as DFT itself is concerned. However, the actual method of choice might imply additional constraints, such as pseudo-potential methods ruling out certain classes of elements.
- All kinds of excitations are by definition beyond the scope of DFT.
- The interpretation of Kohn-Sham eigenstates and eigenenergies (both occupied and unoccupied) as one-particle states (more precisely quasi-particle states in the many-body

framework that is also used in chapter 3) is invalid – doing so nevertheless, however, yields reasonable results in many cases.

- Simple approximations to the exchange-correlation energy such as LDA and GGA fail to reproduce certain features, which are correctly described by the true exchange-correlation functional, partly also by exact exchange. This includes the large and systematic underestimation of semi conductor and isolator band gaps, as well as the wrongly predicted exponential decay instead of the true *van der Waals* attraction $\sim 1/r$ [DN92]. In a few cases the spatial or magnetic structure or conductance character (metallic instead of semi-conducting) is predicted wrong.
- LDA and GGA in particular are not suited to treat strongly correlated systems [KSH⁺06], such as, e.g., *4f* systems or Mott-Hubbard insulators.
- Accuracy for most of the properties that can be well described is often limited to very few percent. This might be insufficient, e.g., for certain tasks of quantum chemistry.

Methods beyond Several ways have been explored beyond the formalism presented up to now in order to address certain problems, including the following:

- If a particular restriction originates only from the applied method itself, it might possibly be extended. For instance, the incompleteness of the LAPW basis set presented in chapter 5 can lead to problems for localized states. In this case the basis can be augmented with local orbitals.
- Some deficiencies of the local-density approximation (LDA) might get cured by a better exchange-correlation functional, such as the mentioned more involved GGA or meta-GGA functionals.
- Several corrections can be combined with DFT, such as the self-energy correction (SIC) [PZ81], which is important for localized electron states, or the LDA+U method that incorporates localization effects in a Hubbard-model manner. The latter one addresses systems with dominant correlation effects [AAL⁺88] and insulators in which the exchange treatment is corrected for proper band gaps.
- Finally there are methods that truly go beyond DFT, e.g., in order to determine energies and lifetimes of different kinds of excitations.

The last item is the proper choice when tackling excited states. Two very different ab initio frameworks exist for this purpose. The first one is the many-body perturbation theory briefly referred to in section 3.4, which utilizes the tool of Feynman diagrams. Applications include the by now well-established *GW* approximation [Hed65] for Kohn-Sham energy corrections and the Bethe-Salpeter equation for calculating the proper correlation function. These approaches typically involve a significant increase of computational effort compared to LDA.

The second option in order to access excited states is the time-dependent extension of the density-functional theory. Its central quantity remains the charge density, which keeps the computational effort significantly smaller compared to many-body approaches. It is introduced in the next section and consequently applied in the coming chapters. Both methods can be applied in linear response on-top of a self-consistent DFT calculation.

Position of the Methods used in this Work The DFT method used in this work – the FLAPW method introduced in section 5.2.3 – is among the most costly DFT methods with respect to both implementation and computing effort while being one of the most flexible and accurate DFT methods. It has no limitation to certain classes of systems and is therefore a genuine and proven tool for the investigation of the ground state of magnetic solids such as transition metals. The time-dependent density-functional theory promises to be a suitable and efficient approach to access the charge-neutral spin excitations presented in section 3.

2.5 Time-Dependent DFT

The time-dependent formulation of density-functional theory (TDDFT) [MG06] extends the applicability of the framework to time-dependent phenomena, i.e., a time-dependent Hamiltonian operator. In particular, it can treat external electro-magnetic fields, and with it excitation and de-excitation of the system. It is an alternative formulation to the time-dependent wave-function mechanics (2.1), as is conventional DFT to the time-independent wave-function mechanics contained in (2.3). Apart from the access to particle-conserving excitations, both the time-dependent density-functional framework and its Kohn-Sham formulation inherit most of the restrictions from their time-independent counterparts.

The derivation of TDDFT is similar to that of conventional DFT, yet it is more involved, and there are significant differences in the details. The first difference stems from the fact that for a time-dependent Hamiltonian $\hat{\mathcal{H}}_{\text{mb}}(t)$ its expectation value – the total energy E – is not a conserved quantity anymore. However, there exists a different quantity that does not change in time, the quantum-mechanical action

$$\mathcal{A}[\Psi(t)] = \int_{t_0}^{t_1} dt \langle \Psi(t) | i \frac{\partial}{\partial t} - \hat{\mathcal{H}}(t) | \Psi(t) \rangle, \quad (2.47)$$

from which the time-dependent Schrödinger equation emerges by equating its functional derivative to zero. Therefore, solving for the time-dependent state $|\Psi(t)\rangle$, is equivalent to calculating the stationary point of the action \mathcal{A} . Since \mathcal{A} is zero for the true physical solution $|\Psi(t)\rangle$, it does not yield any further useful information.

The time-dependent Schrödinger equation as a first-order differential equation in the time coordinate poses an initial-value problem, while the time-independent equation – being a second-order differential equation in the space coordinates – poses a boundary-value problem. This also holds true for the derived time-dependent and time-independent Kohn-Sham equations (2.25) and (2.50).

The analogous statement to that of Hohenberg and Kohn is the Runge-Gross theorem [RG84, GK85, GK86]. Its proof is more elaborate, since no minimization principle can be applied on the quantum-mechanical action, but only a condition of extremalization. The theorem states a one-to-one correspondence – up to a time-dependent function $c(t)$ – between the external potential $V(\mathbf{r}, t)$ and the density $n(\mathbf{r}, t)$ now both being time-dependent:

$$n(\mathbf{r}, t) \quad \leftrightarrow \quad V_{\text{ext}}(\mathbf{r}, t) + c(t). \quad (2.48)$$

Analogously to (2.17) this means that also in the time-dependent setting the external potential $V_{\text{ext}}(t)$ as well as the Hamiltonian $\hat{\mathcal{H}}_{\text{mb}}(t)$, the many-body states $|\Psi(t)\rangle$ or any observable

$O(t)$ can be considered as a functional of the density n . It is important to realize that in this time-dependent framework this means that these quantities are functionals of the density in the whole space and the current time *as well as all past times*. This is important since one can construct two systems which have identical densities $n(\mathbf{r}, t)$ and external potentials $V_{\text{ext}}(\mathbf{r}, t)$ in the whole space and for a given time t , but propagate differently for future times. Therefore identical densities and external potentials for one given time are not sufficient; instead identical densities and potentials have to be ensured for all past times as well.

Consequently, one-particle orbitals φ can be constructed in the spirit of Kohn and Sham, which in the collinear case are related to the density by

$$n(\mathbf{r}, t) = \sum_{i,\sigma} |\varphi_{i\sigma}(\mathbf{r}, t)|^2 f(\epsilon_{i\sigma}) \quad (2.49)$$

and are determined by the time-dependent Kohn-Sham equations:

$$i \frac{\partial}{\partial t} \varphi_{i\sigma}(\mathbf{r}, t) = \left[-\frac{1}{2} \nabla^2 + V_{\text{eff}}(\mathbf{r}, t) + \frac{1}{2} \mu_B g \sigma B_{\text{eff}}(\mathbf{r}, t) \right] \varphi_{i\sigma}(\mathbf{r}, t). \quad (2.50)$$

The external contribution to the now time-dependent effective potential

$$V_{\text{eff}}(\mathbf{r}, t) = V_{\text{ext}}(\mathbf{r}, t) + V_{\text{H}}(\mathbf{r}, t) + V_{\text{xc}}(\mathbf{r}, t) \quad (2.51)$$

takes up the external field newly added in TDDFT, as does the external contribution to the effective magnetic field

$$\mathbf{B}_{\text{eff}}(\mathbf{r}, t) = \mathbf{B}_{\text{ext}}(\mathbf{r}, t) + \mathbf{B}_{\text{xc}}(\mathbf{r}, t). \quad (2.52)$$

The exchange-correlation functional now depends on the density and magnetization in the whole space at all past times. The potential and magnetic field could naively be defined in analogy to conventional DFT as functional derivatives of the quantum-mechanical action with respect to the density and magnetization. However, the exchange-correlation potential now memorizes the development of the system in time, provoking a problem related to causality [GDP96, GUG95]. This theoretical issue was resolved by van Leeuwen [van98] using the Keldysh formalism, leading to an alternative action functional $\tilde{\mathcal{A}}[n, \mathbf{m}]$ that the derivatives are applied on.

While this general statement about E_{xc} completes the theoretical framework of TDDFT, the exchange-correlation potentials are still unknown but nevertheless as crucial for practical applications as they are in conventional DFT. The easiest and most apparent approximation is the use of *adiabatic* functionals, i.e., the functionals from common DFT are evaluated with the time-dependent density:

$$V_{\text{xc}}^{\text{TDDFT}}[n, \mathbf{m}] = V_{\text{xc}}^{\text{DFT}}[n, \mathbf{m}] \Big|_{\substack{n(\mathbf{r})=n(\mathbf{r}, t) \\ \mathbf{m}(\mathbf{r})=\mathbf{m}(\mathbf{r}, t)}}. \quad (2.53)$$

This makes the functional local in time, which is a quite drastic approximation, but also avoids the causality problem mentioned above. Since $V_{\text{xc}}^{\text{DFT}}$ is derived as a ground-state property, we can expect this to work only in cases where the temporal dependence is small and the time-dependent system is locally close to equilibrium. The particular use of the LDA functional in the TDDFT framework is commonly denoted as TDLDA or adiabatic LDA (ALDA).

Other approximations for the action are the exact-exchange (EXX) and optimized effective potential methods (OEP) or to functionals with memory. For more details, please refer to a review on TDDFT, e.g., [BSDR07, MG06]. The time-dependent DFT excels in particular in the computation of finite systems, however, also applications to solids are very promising. Due to its efficiency compared to the formalism of many-body perturbation theory, it is one of the premier tools to employ.

Linear Response and Applicability In practice, the full TDDFT method needs to be applied only if the time-dependent potential is significant compared to the initial system, such as, e.g., for strong laser pulses. In the regime of weak perturbation – such as those that excite our desired low-energy spin-wave excitations – it is sufficient to resort to the linear-response theory, which is performed in chapters 3 and 4 in the particular form of the adiabatic LDA. It enables us to calculate the response from the ground state only, which is determined by common DFT. In fact, the vast majority of TDDFT calculations have been performed in linear response, and most of such ab initio TDDFT calculations are based on pseudo-potentials (which are briefly mentioned in chapter 5).

CHAPTER 3

THE SPIN RESPONSE

Contents

3.1	Magnetism in Solids and Spin Waves	24
3.2	The Correlation Function	28
3.2.1	Definition and Shape	28
3.2.2	The Lehmann Representation	30
3.2.3	Properties	32
3.2.4	The Susceptibility of Non-Interacting Particles	36
3.3	The Response in Time-Dependent DFT	37
3.4	The Bigger Context	40

The focus of this chapter is the response of an electronic system’s charge and magnetization to external scalar and vector potentials, i.e., to electric potentials V and magnetic fields \mathbf{B} . While the essential quantities are quoted for the dielectric response as well, focus is put on the magnetic response and magnetic *excitations* whose context is presented in section 3.1, identifying (3.3) as the central operator to describe the coupling to magnetic fields. Among the magnetic excitations two kinds can be distinguished which can both be understood as quasi-particles: the single-particle spin-flip (or Stoner) excitations and the collective spin-wave (or magnon) excitations.

The central quantity of interest as presented in section 3.2 is the correlation function χ^{-+} defined in (3.17) which, provided collinearity, is shown to contain single $S \pm 1$ spin excitations. In its projected (macroscopic) representation $\chi^{+-}(\mathbf{q}, \omega)$ (3.40) it exhibits the quasi-particle excitations of momentum \mathbf{q} and energy dispersion $\omega(\mathbf{q})$. While single magnetic excitations are described to the full extent by this quantity, effects like magnon-magnon scattering are beyond this formalism.

Actual means to calculate this correlation function is provided by time-dependent density-functional theory (section 3.3), based on an equivalent definition of the correlation function as a functional derivative (3.49). For systems with collinear ground state we obtain a universal formalism for the computation of χ^{+-} through the Dyson equation (3.64). This relation is general within the range of TDDFT if regarding linear coupling to the perturbing magnetic field. The required ingredients are the Kohn-Sham response χ_{KS}^{+-} (3.46) and the exchange-correlation kernel f_{xc}^{+-} . This kernel is investigated in more detail in chapter 4 in the regime of the adiabatic LDA.

In the closing section 3.4 of this chapter the formalism is connected to the well known language of Feynman diagrams. Both the magnetic and the dielectric response are covered, highlighting crucial differences. More extensive derivations are moved to appendix B. This combined machinery of applying ALDA on a ground state obtained by a DFT calculation is carried out analytically for the homogeneous electron gas in the following chapter 4.

Notation In chapter 2 the quantities describing the magnetic degree of freedom were chosen according to common literature, i.e., the magnetization density \mathbf{m} (see (2.36)) and the spin polarization ξ (see (2.40)). While the latter parametrization is also used in section 2.3 in the evaluation of the exchange-correlation kernel within the LDA, it turns out that for the framework of the spin response the spin density \mathbf{S} is suited best.

The magnetic and dielectric components of the fields and densities are denoted x, y, z and 0. The correlation and response functions are in general 4×4 tensors, which suggests the definition of a combined four-component charge consisting of scalar and magnetic charge density, and a four-component potential containing scalar potential and magnetic field. However, since we are mainly interested in the transversal magnetic response (its components denoted by $+$ and $-$), we avoid the overhead of such a notation and stay with the 3×3 magnetic quantities in most places, explaining in words when referring to the tensor components involving dielectric contributions.

3.1 Magnetism in Solids and Spin Waves

Magnetism is an inherently complex phenomenon that originates from the combination of the orbital and spin moments of the ensemble of all electrons, which need to fulfill the Pauli exclusion principle as a boundary condition. The moments of the nuclei are several orders of magnitude smaller than the electrons' moments since they scale proportionally to the inverse of the particle mass, leading to very small so-called *hyper fine-field effects* which are neglected here.

While the combination of two angular momenta is already non-trivial, the coupling of many of them is extremely complicated. In order to identify the operators which describe the essential interactions, the effect of spin and magnetic momenta is recapitulated, starting from single atoms leading to solids.

Atomic Magnetism The proper fully-relativistic description of an atom would be the Dirac formalism which yields the existence of the electron spin as a necessary quantity and couples both spin and angular momentum of the electrons. In the non-relativistic Schrödinger formulation the spin is postulated as a angular momentum of type one-half. Such a Hamilton operator for an atom of one electron then reads [Nol86a]

$$\hat{\mathcal{H}}^{\text{atom}} = \hat{T} + \hat{V}_{\text{coul}} + \hat{\mathcal{H}}_{\text{SO}} \quad (3.1)$$

with the kinetic term \hat{T} and the Coulomb term \hat{V}_{coul} expressing attraction between nucleus and electrons as well as repulsion between electrons. The spin-orbit coupling $\hat{\mathcal{H}}_{\text{SO}} \sim \hat{\mathbf{L}} \cdot \hat{\mathbf{S}}$ is composed of the total angular-momentum operator $\hat{\mathbf{L}}$ and the total spin operator $\hat{\mathbf{S}}$. It is the largest of three lowest-order terms which are obtained from a relativistic expansion: the other

two are a kinetic-energy correction that can be put into \hat{T} and the smaller so-called Darwin term that was neglected in (3.1). Since the orbital moment is mostly suppressed in solids, the spin-orbit term becomes small and can subsequently be treated as a perturbation or even be omitted.

In the presence of a magnetic field \mathbf{B} additional terms appear due to the coupling of the orbital moment \mathbf{m}_L and spin moment \mathbf{m} to that field. The total Hamiltonian then reads

$$\hat{\mathcal{H}}_B^{\text{atom}} = \hat{\mathcal{H}}^{\text{atom}} - (\hat{\mathbf{m}}_L + \hat{\mathbf{m}}) \cdot \mathbf{B} + \hat{\mathcal{H}}_{\text{dia}}. \quad (3.2)$$

The diamagnetic term $\hat{\mathcal{H}}_{\text{dia}}$ is very small (thus neglected in the following) and relevant only if the other terms vanish. In this case, however, it leads to the macroscopic effect of diamagnetism.

The density-functional theory which is the basis for the studies of this work operates at the one-electron level, thus using the one-electron operators $\hat{\mathbf{m}}$ in the formula above.

Magnetism in Solids Magnetism is prevalent for single atoms whose atomic shells are occupied according to Hund's rule. It turns out that with higher dimensionality (i.e., going from single atoms or clusters of atoms to wires, slabs and bulk materials) magnetism is more and more suppressed, and many magnetic structures take a collinear magnetic order. While nearly all single atoms carry a net magnetic moment, only few elements possess a magnetization in the bulk state. On the other hand it is not obvious from the spin-polarized Kohn-Sham equations (2.35) how magnetism at all comes into existence. It turns out that the exchange interaction is the driving mechanism leading to magnetism in solids (and not for instance a direct interaction between magnetic moments). Different models have been built on this insight, like the mean-field Stoner model [Sto39] or the Heisenberg model of localized spins [Nol86b].

A more detailed investigation reveals that in particular the orbital moments get suppressed in solids and one can subsequently put the focus on the spin-moments. According to (3.2) a single localized spin then couples to a magnetic field \mathbf{B} (be it an external field or an effective field created by the surrounding particles) yielding a magnetic contribution to the Hamilton operator

$$\hat{\mathcal{H}}^{\text{magn}} = -\hat{\mathbf{m}} \cdot \mathbf{B} = \mu_B g \hat{\mathbf{S}} \cdot \mathbf{B} = \frac{\mu_B g}{2} \hat{\boldsymbol{\sigma}} \cdot \mathbf{B} \quad (3.3)$$

which is also called *Zeeman term*. This kind of operator $\hat{\mathcal{H}}^{\text{magn}}$ has already been used to account for the magnetic contribution to the Kohn-Sham equations (2.35), and is an essential operator in the derivations of the following sections. (In appendix B.2 it is used in its many-body notation.)

Magnetic Excitations The magnetic (or spin) excitations of a system are particle-conserving excitations which increase or decrease the total spin of the system by one. More precisely, a collinear setup is assumed, and such an excitation corresponds to the change of the z -component of the total spin (along the preferential magnetic direction) by plus or minus one: $S_z \rightarrow S_z \pm 1$. These excitations are thus of bosonic character, obeying the Bose-Einstein energy distribution with respect to temperature. However, this detail is of no concern in this text since the zero-temperature formalism is used. Being elementary

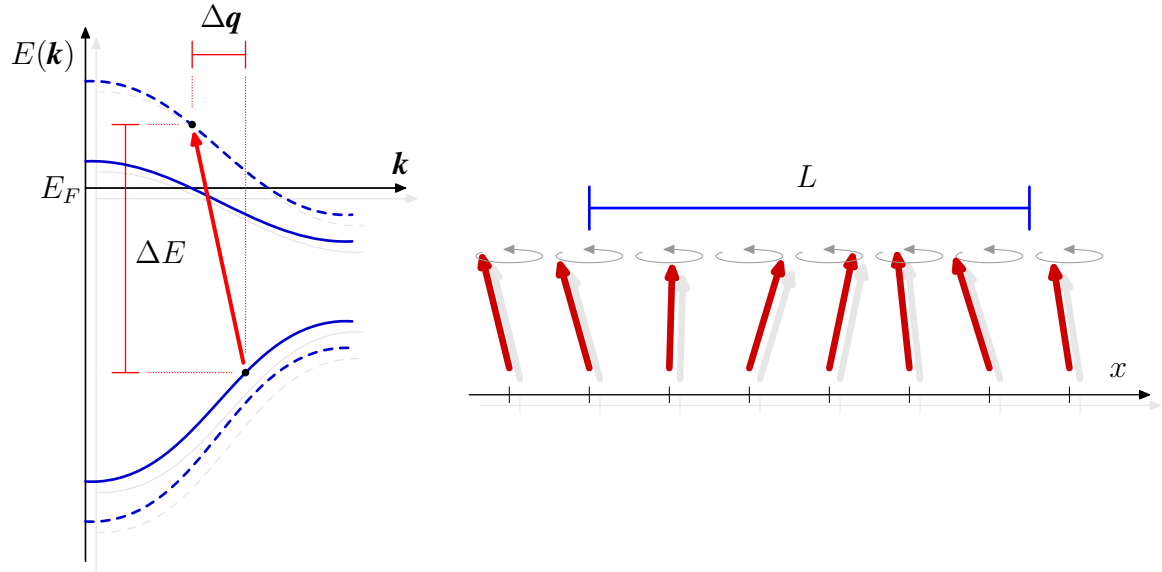


Figure 3.1: A sketch of the two kinds of magnetic excitations. On the left, a spin-flip excitation of band electrons is pictured, flipping an occupied state from the majority band (solid blue line) to an unoccupied state of the minority band (dashed blue line). The transition involves a transfer of momentum $\Delta\mathbf{q}$ and energy ΔE . On the right, an excited state of the Heisenberg model is shown. The periodicity L relates to the momentum $|\mathbf{q}| = 2\pi/L$. For evolving time all the spins precess on a cone which due to the constant phase shift between sites appear as a wave-like pattern.

excitations of the many-particle system, they can be classified as quasi-particles [FW71] carrying a momentum \mathbf{q} and energy ω .

On a micromagnetic scale, many calculations have successfully mapped experimental results to calculations of the prominent Landau-Lifshitz-Gilbert theory. It models the magnetic structure by magnetic moments obeying the rules of electro-dynamics. This method relies on empirical parameters. For a parameter-free theory one needs to turn to the quantum-mechanical nanoscale which comprises the origin of magnetism. Nevertheless, it is an essential topic of future research to bridge the gap in system size by obtaining the parameters of the models on the micromagnetic scale from nano-scale calculations.

On a nano-scale one needs to handle transitions between quantum-mechanical spin eigenstates. In this framework it is advantageous to introduce the ladder operators and fields

$$\hat{S}^{\pm} = \hat{S}_x \pm i\hat{S}_y \quad (3.4)$$

$$B^{\pm} = B^x \pm iB^y. \quad (3.5)$$

which allow for the alternative expression of the magnetic term (3.3) in the Hamiltonian as

$$\mu_B g \hat{\mathbf{S}} \cdot \mathbf{B} = \frac{\mu_B g}{2} (\hat{S}^- B^+ + \hat{S}^+ B^-) + \mu_B g \hat{S}^z B^z. \quad (3.6)$$

Two different kinds of excitations can be identified, depending on the method in use. The first one is the change of one single spin, like the spin of one Kohn-Sham electron in DFT or the

spin on one site in the Heisenberg model. Such excitations are called spin-flip or Stoner excitations. A spin-flip between band electrons is sketched on the left side of figure 3.1. While a spin-flip between Bloch electrons is not strictly local but bound to two single (but extended) Bloch states, nevertheless the whole class of one-particle excitations is occasionally denoted as *local* excitations, stemming from the picture of localized spins.

However, there can be further excitations of the many-body system not described by this concept, namely collective excitations which is the topic of the current chapter and this whole thesis.

Collective Excitations Excitations which are beyond the scope of flips of independent spins are called collective spin excitations. They are delocalized and can extend throughout the whole system. The respective quasi-particles are called spin waves or magnons. In the Heisenberg model the ground state and isolated single excited states of this kind can be analytically calculated, involving the time evolution of the system. While all the spins perform a uniform precession movement along the z axis in the ground state, there exist excitation states which are characterized by a constant phase shift of this precession from one site to the next. These excitations are pictured on the right side of figure 3.1.

Several properties of the excitations can be extracted from the Heisenberg model [Nol86b] which also hold true for general itinerant systems. These include thermodynamical properties as well as characteristics of the dispersion. In the Heisenberg model there exists only one single acoustic mode which for small momenta \mathbf{q} has quadratic dispersion $\omega_{\text{sw}}(\mathbf{q}) \sim \mathbf{q}^2$ for ferromagnets and linear dispersion $\omega_{\text{sw}}(\mathbf{q}) \sim |\mathbf{q}|$ for antiferromagnets. For larger \mathbf{q} the excitation strength becomes weaker, and fades out if it enters the range of the Stoner excitations.

Spin-flip excited states are collinear, since they only change the magnetization along the preferential direction. Spin-wave excitations instead excite the magnetic moments off this preferential axis, leading to a non-collinear state. However, also the latter can be calculated within a collinear framework provided the linear-response formalism is used. Both spin-flip and spin-wave excitations originate from the ladder operators (3.4) or, in other words, from the components $\chi^{[x,y]}$ of the response function (3.15). This means they involve the x - and y -components of the spin operators, perpendicular to the preferential z axis. Therefore both kinds of excitations together form the *transversal* response of the system, while the *longitudinal* component of the response does not contain spin excitations.

Experimental Techniques There is a large amount of experimental methods that allow for the investigation of the magnetic structure of matter. In the analysis of magnetic excitations, however, two methods are dominant, namely inelastic neutron scattering which deeply penetrates the sample due to the weakly interacting neutrons, and the spin-polarized electron-energy loss spectroscopy (SPEELS) which mainly investigates the surface. Spin waves have been observed in different kind of materials such as ferromagnets, ferrimagnets, and antiferromagnets.

3.2 The Correlation Function

3.2.1 Definition and Shape

The charge- and spin-correlation function χ is the central quantity that describes the response of a system to external fields. It is defined as a 4×4 tensor

$$i\chi^{ij}(\mathbf{r}, t, \mathbf{r}', t') = \langle 0 | [\hat{S}^i(\mathbf{r}, t), \hat{S}^j(\mathbf{r}', t')] | 0 \rangle \Theta(t - t') \quad (3.7)$$

$$= \frac{1}{(\mu_B g)^2} \langle 0 | [\hat{m}^i(\mathbf{r}, t), \hat{m}^j(\mathbf{r}', t')] | 0 \rangle \Theta(t - t') \quad (3.8)$$

where the indices $i, j \in \{x, y, z, 0\}$ indicate the charge or spin component, and the many-body ground state $|0\rangle$ is the same as in (2.17). The Heisenberg picture is used, with the time dependence moved from the states $|\Psi(t)\rangle \rightarrow |\Psi(t_0)\rangle$ into the operators $\hat{A} \rightarrow \hat{A}(t)$,

$$\hat{A} \rightarrow \hat{A}(t) = e^{+\frac{i}{\hbar}\hat{\mathcal{H}}(t-t_0)} \hat{A} e^{-\frac{i}{\hbar}\hat{\mathcal{H}}(t-t_0)} \quad (3.9)$$

for a time-independent Hamiltonian $\hat{\mathcal{H}} \neq \hat{\mathcal{H}}(t)$ and some constant time $t_0 < t$ usually set $t_0 = 0$. The spin-density operators can further be written as

$$\hat{S}^i(\mathbf{r}, t) = \sum_{\alpha, \beta} \hat{\psi}_\alpha^\dagger(\mathbf{r}, t) S_{\alpha\beta}^i \hat{\psi}_\beta(\mathbf{r}, t), \quad (3.10)$$

involving the creation and annihilation operators $\hat{\psi}_\alpha^\dagger, \hat{\psi}_\alpha$ which create or annihilate a particle in spin channel α .¹ The operator S^i is a 2×2 operator in spin-space that is connected to the Pauli matrices by (2.15). The density operator $\hat{n}(\mathbf{r}, t) = \hat{S}^0(\mathbf{r}, t)$ is contained in (3.10) by the definition of the diagonal matrix

$$S^0 = \begin{pmatrix} 1 & 0 \\ 0 & 1 \end{pmatrix}. \quad (3.11)$$

The field operators for electrons (which are fermions) obey the anticommutation relations

$$\left\{ \hat{\psi}_\alpha(\mathbf{r}, t), \hat{\psi}_\beta^\dagger(\mathbf{r}', t') \right\} = \delta(\mathbf{r} - \mathbf{r}') \delta(t - t') \delta_{\alpha\beta} \quad (3.12)$$

$$\left\{ \hat{\psi}_\alpha^\dagger(\mathbf{r}, t), \hat{\psi}_\beta^\dagger(\mathbf{r}', t') \right\} = \left\{ \hat{\psi}_\alpha(\mathbf{r}, t), \hat{\psi}_\beta(\mathbf{r}', t') \right\} = 0. \quad (3.13)$$

The definition of (3.7) is causal (i.e., retarded), indicated by the step function in time and by the commutator brackets. The expanded bracket

$$[\hat{S}^i(\mathbf{r}, t), \hat{S}^j(\mathbf{r}', t')] = \hat{S}^i(\mathbf{r}, t) \hat{S}^j(\mathbf{r}', t') + \hat{S}^j(\mathbf{r}', t') \hat{S}^i(\mathbf{r}, t) \quad (3.14)$$

includes a plus sign since the spin-density operators \hat{S} involve one creation and one annihilation operator each, according to (3.10).

¹Such an operator applied to a Slater determinant of collinear single-particle states will create or annihilate a spin-up or spin-down electron. In the non-collinear case, however, only the spin-up or spin-down component (that means only a fraction) of a non-collinear single electron is created or annihilated.

In general all coefficients of this tensor can be independent. The spin operators act on the many-body state $|0\rangle$ which is composed of a linear combination of Slater determinants of single-particle states. In collinear systems, due to the particular shape of the Pauli matrices (2.9) the correlation function takes the simpler block-diagonal form

$$\chi^{[x,y,z,0]} = \begin{pmatrix} \chi^{xx} & \chi^{xy} & 0 & 0 \\ \chi^{yx} & \chi^{yy} & 0 & 0 \\ 0 & 0 & \chi^{zz} & \chi^{z0} \\ 0 & 0 & \chi^{0z} & \chi^{00} \end{pmatrix}. \quad (3.15)$$

This means that the transversal part (the x and y magnetization components that we will further investigate) and the longitudinal part (the z magnetization and charge component) each form independent 2×2 tensors. In the longitudinal part, it is common to separate the longitudinal magnetic (zz) and the dielectric (00) contribution. The latter one is also called polarization function $P = \chi^{00}$. Further evaluation using the particular shape of the Pauli matrices (2.9) reveals the antisymmetric form of the transversal part:

$$\chi^{[x,y,z,0]} = \begin{pmatrix} \chi^{xx} & \chi^{xy} & 0 & 0 \\ -\chi^{xy} & \chi^{xx} & 0 & 0 \\ 0 & 0 & \chi^{zz} & 0 \\ 0 & 0 & 0 & P \end{pmatrix}. \quad (3.16)$$

For magnetic excitations we will focus on the transversal part. Instead of the $[x, y]$ representation above it is advantageous to access the $[+, -]$ representation using the ladder operators (3.4), resulting in the definition of the spin-flip response

$$i\chi^{-+}(\mathbf{r}, t, \mathbf{r}', t') = \langle 0 | [\hat{S}^{-}(\mathbf{r}, t), \hat{S}^{+}(\mathbf{r}', t')] | 0 \rangle \Theta(t - t') \quad (3.17)$$

and analogous for χ^{+-} . The transforms to cartesian components read

$$\begin{aligned} \chi^{-+} &= 2\chi^{xx} + 2i\chi^{xy} \\ \chi^{+-} &= 2\chi^{xx} - 2i\chi^{xy}. \end{aligned} \quad (3.18)$$

In the spin subspace the spin-flip operators read

$$S^{-} = \begin{pmatrix} 0 & 0 \\ 1 & 0 \end{pmatrix} \quad S^{+} = \begin{pmatrix} 0 & 1 \\ 0 & 0 \end{pmatrix} \quad (3.19)$$

$$S^{-+} = S^{-}S^{+} = \begin{pmatrix} 0 & 0 \\ 0 & 1 \end{pmatrix} \quad S^{+-} = S^{+}S^{-} = \begin{pmatrix} 1 & 0 \\ 0 & 0 \end{pmatrix} \quad (3.20)$$

and further $S^{++} = S^{--} = 0$. The susceptibility tensor – now transformed to the $[+, -, z, 0]$ basis – then simplifies to

$$\chi^{[+, -, z, 0]} = \begin{pmatrix} 0 & \chi^{+-} & 0 & 0 \\ \chi^{-+} & 0 & 0 & 0 \\ 0 & 0 & \chi^{zz} & 0 \\ 0 & 0 & 0 & P \end{pmatrix}. \quad (3.21)$$

3.2.2 The Lehmann Representation

For a time-independent Hamiltonian, the correlation function becomes translationally invariant in time,

$$\chi(\mathbf{r}, t, \mathbf{r}', t') \rightsquigarrow \chi(\mathbf{r}, \mathbf{r}'; t - t'), \quad (3.22)$$

and a Fourier transform on the time coordinate can be performed. Further on, a Lehmann representation can be derived (please confer section B). For this we characterize the many-body states as $|n, S_z\rangle$, where S_z is the expectation value of the z -component of the total spin of the system defined by

$$\hat{S}_z |n, S_z\rangle = S_z |n, S_z\rangle \quad (3.23)$$

The index n incorporates all other degrees of freedom, most notably the total particle number N and the total spin S . In this notation the ground state keeps its common abbreviation $|0, S_z^{(0)}\rangle = |0\rangle$. The Lehmann representation for the spin-flip correlation function then reads

$$\chi^{-+}(\mathbf{r}, \mathbf{r}'; \omega) = \lim_{\eta \rightarrow 0^+} \left[\sum_n \frac{\langle 0 | \hat{S}^-(\mathbf{r}) |n, S_z^{(0)} + 1\rangle \langle n, S_z^{(0)} + 1 | \hat{S}^+(\mathbf{r}') |0\rangle}{\omega - (E_{n, S_z^{(0)}+1} - E_0) + i\eta} - \sum_n \frac{\langle 0 | \hat{S}^+(\mathbf{r}') |n, S_z^{(0)} - 1\rangle \langle n, S_z^{(0)} - 1 | \hat{S}^-(\mathbf{r}) |0\rangle}{\omega + (E_{n, S_z^{(0)}-1} - E_0) + i\eta} \right] \quad (3.24)$$

with the ground state assumed to be non-degenerate in order to keep the energy difference in the denominator to be non-zero. Due to the form of the spin-flip operators only states $S_z^{(0)} \pm 1$ contribute, which is indicated by the square brackets at the sums, and could alternatively be understood as a constraint to the summation. The index n runs over all total spin quantum numbers S (which therefore do not have any particular meaning in this formalism) and all further electronic excitations, with the restriction that the total number of particles is kept constant. Single terms in the sums and thus the whole correlation function can diverge when a denominator becomes zero. We will follow the common diction and refer to these poles as $S \pm 1$ excitations instead of $S_z^{(0)} \pm 1$ excitations, neglecting the z index.

For the dielectric correlation function P we obtain, according to notation (3.11), the Lehmann representation

$$P(\mathbf{r}, \mathbf{r}'; \omega) = \lim_{\eta \rightarrow 0^+} \left[\sum_{n \neq 0} \frac{\langle 0 | \hat{\rho}(\mathbf{r}) |n\rangle \langle n | \hat{\rho}(\mathbf{r}') |0\rangle}{\omega - (E_n - E_0) + i\eta} - \sum_{n \neq 0} \frac{\langle 0 | \hat{\rho}(\mathbf{r}') |n\rangle \langle n | \hat{\rho}(\mathbf{r}) |0\rangle}{\omega + (E_n - E_0) + i\eta} \right]. \quad (3.25)$$

The sum runs over all excited states. No explicit restriction was performed as in the Lehmann representation of χ^{-+} above; however, only charge-conserving excited states with unchanged spin quantity $S_z^{(0)}$ will contribute non-zero matrix elements in the numerator. As above, a non-degenerate ground state is assumed. Furthermore, the ground state itself is excluded from the sum, indicated by the index $n \neq 0$. The ground state did not need to be excluded in (3.24) since it does not lead to any contribution.

Since the sum over all excited states $|n\rangle$ also contains each complex conjugate, the numerators in the Lehmann representation can be considered real and can be factored out.

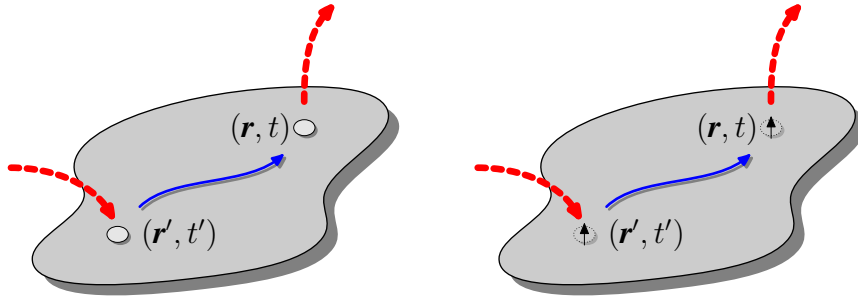


Figure 3.2: The physical meaning of the one-particle Green function G and the spin correlation function χ^{-+} . On the left, the propagation (blue arrow) of an additional particle (light-filled circle) is sketched which is injected at space-time coordinate (\mathbf{r}', t') and removed at coordinate (\mathbf{r}, t) (red arrows). On the right, a particle-conserving spin-up excitation (dotted non-colored circle) is injected instead. The functions G and χ^{-+} are the probability amplitude of these processes.

Interpretation Apart from the causal definition (3.7), also a time-ordered (t.o.) definition is possible,

$$i\chi_{\text{t.o.}}^{-+}(\mathbf{r}, t, \mathbf{r}', t') = \langle 0 | \mathcal{T}[\hat{S}^{-}(\mathbf{r}, t)\hat{S}^{+}(\mathbf{r}', t')] | 0 \rangle \quad (3.26)$$

with the time-ordering operator

$$\mathcal{T}[\hat{S}^{-}(\mathbf{r}, t)\hat{S}^{+}(\mathbf{r}', t')] = \begin{cases} \hat{S}^{-}(\mathbf{r}, t)\hat{S}^{+}(\mathbf{r}', t') & \text{for } t > t' \\ \hat{S}^{+}(\mathbf{r}', t')\hat{S}^{-}(\mathbf{r}, t) & \text{for } t < t' \end{cases} \quad (3.27)$$

which does not contain a minus sign for the same reasons as in (3.14). This formulation pronounces the similarity to the one-particle Green function G which describes the propagation of one additional particle (or hole) through a system, as sketched in figure 3.2. Completely analogous, $\chi_{\text{t.o.}}^{-+}$ is the probability amplitude that a charge- and particle-neutral additional spin injected at space-time coordinate (\mathbf{r}', t') propagates to coordinate (\mathbf{r}, t) for $t > t'$; for $t < t'$ a “spin hole” propagation is described. $\chi_{\text{t.o.}}^{+-}$ describes the same propagation of spins and spin holes for $t < t'$ and $t > t'$, respectively.

The Green function, whose Lehmann representation of course has the same structure as (3.24), exhibits poles at the excitation energies of particle addition to and particle removal from the system. Analogously, the poles of the spin-flip correlation function determine the energies of spin addition to and spin removal from the system, that are spin flips $S \rightarrow S \pm 1$. Indeed, the Lehmann representation (3.24) of χ^{-+} reveals² that the poles corresponding to the $S + 1$ excitations lie on the positive ω axis, while those of the $S - 1$ excitations lie on the negative axis, c.f., figure 3.3. For magnetic materials the two excitation spectra should be strictly different. The Lehmann representation of χ^{+-} reveals poles for the excitations $S - 1$ on the positive and $S + 1$ on the negative axis. In order to catch all the $S \pm 1$ excitations one either has to evaluate one of χ^{-+} and χ^{+-} on the whole frequency axis, or evaluate the sum of it on the positive or negative axis.

²This form of the spectral function demands the form (A.12) of the Fourier transform of the time coordinate. The inverse choice of signs in the exponent would lead to a substitution $\omega \rightarrow -\omega$ with a flip of the $S + 1$ excitations to the negative axis and $S - 1$ excitations to the positive axis.

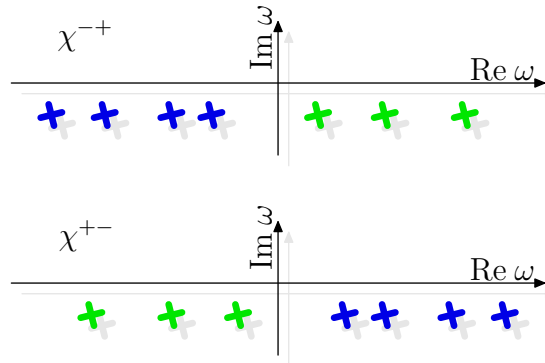


Figure 3.3: A sketch of the position of the poles of the spin-flip response functions χ^{-+} and χ^{+-} in the complex frequency plane, according to the Lehmann representation (3.24). Excitations $S + 1$ are marked by green crosses, while $S - 1$ excitations are marked in blue. All positions lie below the real axis by an infinitesimal constant shift η .

The positive sign of the imaginary contribution $+i\eta$ of the two denominators in the Lehmann representation (3.24) reflect the retarded nature of these functions, causing all the poles to lie in fact not on the real ω axis, but slightly below by an infinitesimally small value η (which will, however, not be explicitly stated anymore). For the time-ordered functions, the poles on the positive ω axis lie infinitesimally below the axis, while lying infinitesimally above on the negative ω axis.

The interpretation of both the definition of χ^{-+} and its Lehmann representation shows that only single spin excitations are described by (3.17). Neither simultaneous magnon excitations nor processes of higher order, like for instance magnon-magnon or magnon-phonon scattering, are contained in this quantity. However, for a low density of excitations they can be treated independently, and mentioned linearization is valid. Further on, these single-spin excitations can be both of single-particle or of collective nature, i.e., being Stoner excitations or spin waves.

The understanding of the polarization function P is mostly equivalent. It describes the propagation of a charge fluctuation from (\mathbf{r}', t') to (\mathbf{r}, t) for $t > t'$, or the propagation of a charge-hole fluctuation for $t < t'$. The excitations on the negative axis are possible only for non-zero temperature, please compare to the explicitly evaluated Kohn-Sham correlation function on page 36. However, the temperature-dependent formalism is not treated in this work.

3.2.3 Properties

Symmetries For the correlation function defined in a time-ordered manner $\chi_{\text{t.o.}}^{ij}$ (and in particular for its dielectric component P) the following symmetries in space and time stand,

$$\chi_{\text{t.o.}}^{ij}(\mathbf{r}, \mathbf{r}'; \omega) = \chi_{\text{t.o.}}^{ji}(\mathbf{r}', \mathbf{r}; \omega) \quad (3.28)$$

$$\chi_{\text{t.o.}}^{ij}(\mathbf{r}, \mathbf{r}'; \omega) = \chi_{\text{t.o.}}^{ij}(\mathbf{r}, \mathbf{r}'; -\omega) \quad (3.29)$$

which follow from the Lehmann representation for $\chi_{t.o.}^{ij}$. The tensor indices are flipped from ij to ji for the spatial symmetry relation. The proof uses $(\hat{S}^i)^\dagger = \hat{S}^i$ for $i \in \{x, y, z, 0\}$ and the fact that for each eigenstate also its complex conjugate solves the Schrödinger equation. The sum in the Lehmann representation runs over all states, including their conjugates. As a consequence, the complexity of the response function only stems from the denominators, and the principal relation (B.1) can be applied. The aforementioned time symmetry only holds for the time-ordered correlation function $\chi_{t.o.}^{ij}$; for the retarded function χ^{ij} defined by (3.7) a distinction has to be made for the real and imaginary contributions:

$$\chi^{ij}(\mathbf{r}, \mathbf{r}'; \omega) = \chi^{ji}(\mathbf{r}', \mathbf{r}; \omega) \quad (3.30)$$

$$\text{Re } \chi^{ij}(\mathbf{r}, \mathbf{r}'; \omega) = \text{Re } \chi^{ij}(\mathbf{r}, \mathbf{r}'; -\omega) \quad (3.31)$$

$$\text{Im } \chi^{ij}(\mathbf{r}, \mathbf{r}'; \omega) = -\text{Im } \chi^{ij}(\mathbf{r}, \mathbf{r}'; -\omega).$$

For the spin-flip correlation function, obeying $(\hat{S}^\pm)^\dagger = \hat{S}^\mp$ the relations read a bit different:

$$\chi^{-+}(\mathbf{r}, \mathbf{r}'; \omega) = \chi^{-+}(\mathbf{r}', \mathbf{r}; \omega) \quad (3.32)$$

$$\text{Re } \chi^{-+}(\mathbf{r}, \mathbf{r}'; \omega) = \text{Re } \chi^{+-}(\mathbf{r}, \mathbf{r}'; -\omega) \quad (3.33)$$

$$\text{Im } \chi^{-+}(\mathbf{r}, \mathbf{r}'; \omega) = -\text{Im } \chi^{+-}(\mathbf{r}, \mathbf{r}'; -\omega).$$

The flip in tensor components – from χ^{-+} to χ^{+-} – now occurs in the symmetry relation for time inversion instead. This needs to be considered, e.g., in an implementation of the Kramers-Kronig transform mentioned in the next paragraph.

Spectral Function A retarded correlation function χ can be expressed component-wise through its corresponding spectral function S by

$$\chi^{ij}(\mathbf{r}, \mathbf{r}'; \omega) = \lim_{\eta \rightarrow 0^+} \int_{-\infty}^{+\infty} d\varpi \frac{S^{ij}(\mathbf{r}, \mathbf{r}'; \varpi)}{\omega - \varpi + i\eta}, \quad (3.34)$$

and equally for the spin-flip function χ^{-+} . Its spectral function is of the form

$$S^{-+}(\mathbf{r}, \mathbf{r}'; \omega) = \sum_m^{[S_z+1]} \langle 0 | \hat{S}^-(\mathbf{r}) | m, S_z + 1 \rangle \langle m, S_z + 1 | \hat{S}^+(\mathbf{r}') | 0 \rangle \delta(\omega - [E_{m, S_z+1} - E_0]) - \sum_m^{[S_z-1]} \langle 0 | \hat{S}^+(\mathbf{r}') | m, S_z - 1 \rangle \langle m, S_z - 1 | \hat{S}^-(\mathbf{r}) | 0 \rangle \delta(\omega + [E_{m, S_z-1} - E_0]). \quad (3.35)$$

It is a real function since the spin-flip operators are real, acting on eigenstates. As can be seen from (B.1), the imaginary part of the correlation function further obeys

$$-\frac{1}{\pi} \text{Im } \chi^{-+}(\mathbf{r}, \mathbf{r}'; \omega) = S^{-+}(\mathbf{r}, \mathbf{r}'; \omega). \quad (3.36)$$

Thus, in order to obtain information about the excitation spectra, the imaginary part of the correlation function is a convenient quantity to study. A direct connection between the real

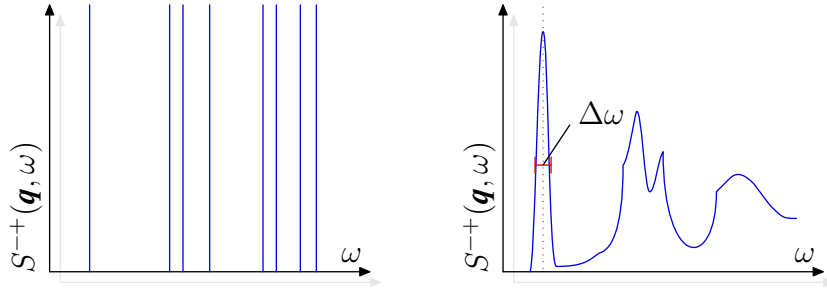


Figure 3.4: The structure of the spectral function $S^{--}(\mathbf{q}, \omega)$ as function of ω for one fixed vector \mathbf{q} , sketched for a finite (left) and an infinite system (right). The poles on the left are broadened to peaks of finite height on the right. The lifetime attributed to the excitation scales with the width of the peak according to $\Delta\tau \sim \Delta\omega^{-1}$.

and the imaginary part is provided by the Hilbert transform

$$\begin{aligned} \operatorname{Re} \chi^{ij}(\omega) &= +\frac{1}{\pi} \mathcal{P} \int_{-\infty}^{+\infty} d\varpi \frac{\operatorname{Im} \chi^{ij}(\varpi)}{\varpi - \omega} \\ \operatorname{Im} \chi^{ij}(\omega) &= -\frac{1}{\pi} \mathcal{P} \int_{-\infty}^{+\infty} d\varpi \frac{\operatorname{Re} \chi^{ij}(\varpi)}{\varpi - \omega} \end{aligned} \quad (3.37)$$

where spatial variables to χ have been omitted. Utilizing the time symmetry (3.31) the Kramers-Kronig relations [Kra26, dLK26] emerge which restrict the integration to positive frequencies only:

$$\begin{aligned} \operatorname{Re} \chi^{ij}(\omega) &= +\frac{2}{\pi} \mathcal{P} \int_0^{+\infty} d\varpi \frac{\varpi \operatorname{Im} \chi^{ij}(\varpi)}{\varpi^2 - \omega^2} \\ \operatorname{Im} \chi^{ij}(\omega) &= -\frac{2\omega}{\pi} \mathcal{P} \int_0^{+\infty} d\varpi \frac{\operatorname{Re} \chi^{ij}(\varpi)}{\varpi^2 - \omega^2}. \end{aligned} \quad (3.38)$$

These relations only hold for $i, j \in \{x, y, z, 0\}$. For the components χ^{--} or χ^{+-} , these convenient simplifications (3.38) do not hold because of their different time-symmetry relations (3.33).

Sum Rule From the spin response the magnetization $m(\mathbf{r})$ can be obtained by the following integration:

$$\int d^3r' \lim_{\delta \rightarrow 0} \frac{i}{2\pi} \int_{-\infty}^{+\infty} d\omega \chi^{+-}(\mathbf{r}, \mathbf{r}'; \omega) e^{-i\omega\delta} = m(\mathbf{r}) \quad (3.39)$$

Macroscopic Quantities For macroscopic properties, matter is usually probed with some quantum (for instance photons, electrons, neutrons) carrying a momentum \mathbf{q} . For describing the interaction (or transfer) of this momentum there is usually no need for information of atomic spatial resolution. Instead, a projection of the functions onto a plane wave of according momentum is considered:

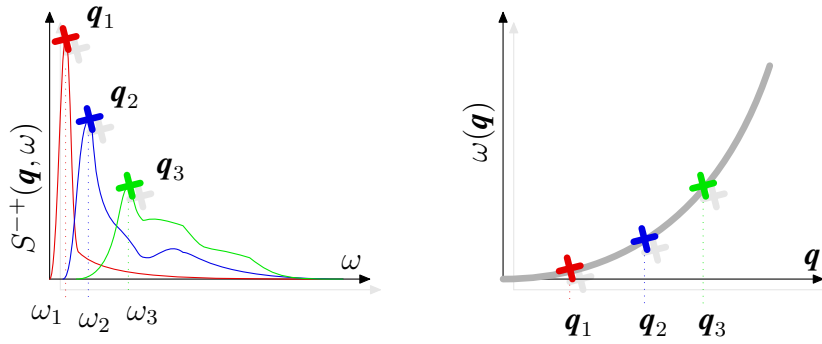


Figure 3.5: The positions of the peaks on the energy scale on the left yield the dispersion relation $\omega_{\text{sw}}(q)$ on the right, omitting the detailed structure of the spectral function.

$$\chi^{+-}(\mathbf{q}, \omega) = \int e^{-i\mathbf{q}\mathbf{r}} \chi^{+-}(\mathbf{r}, \mathbf{r}'; \omega) e^{+i\mathbf{q}\mathbf{r}'} d^3r d^3r'. \quad (3.40)$$

The above formula can also be understood as the $\mathbf{G} = \mathbf{G}' = 0$ element (also called the *head element*) of a Fourier representation $\chi_{\mathbf{G}\mathbf{G}'}^{+-}(\mathbf{q}, \omega)$ of χ^{+-} with full spatial resolution. The head element contains the contribution constant on atom scale, while higher elements contain the variations on atomic scale.

The spectral function of infinite systems as well as all the related functions have a different analytical structure than for finite systems. Instead of a finite number of δ -peaks like in (3.35), the spectrum changes to a continuous function of finite height. It can be separated into a peak contribution (if present) that consists of clearly defined peaks, which are attributed to the spin waves, and a continuum contribution that is a smooth function over a broad range of frequencies without pronounced maxima, which is attributed to the Stoner excitations. The spin-wave peaks have a certain width $\Delta\omega$ in the spectrum and a corresponding finite lifetime $\Delta\tau$, see figure 3.4. The peak positions on the energy scale can then be plotted against the corresponding \mathbf{q} -vector to yield the dispersion relation of these quasi-particles, see figure 3.5.

In the limit $\mathbf{q} \rightarrow 0$ the function χ^{+-} (or similar quantities like the polarization function P or the dielectric function ε) do still depend on the direction of the small vector \mathbf{q} . As a consequence the scalar function $P(\mathbf{q}, \omega)$ becomes a 3×3 tensor $P(\mathbf{q} = 0, \omega)$ of the spatial directions x, y, z . Its number of independent coefficients can be reduced due to symmetry reasons [Nye57] to, e.g., one coefficient for cubic structures, two coefficients for hexagonal structures etc. However, it should be stressed that this kind of tensor is inherently different to the tensors (3.7) introduced in this chapter. This limit $\mathbf{q} \rightarrow 0$ is important for instance for excitations with photons of optical energies, which have a negligible momentum compared to the size of the Brillouin zone. Magnons, however, are usually excited with finite momenta, and the limit of small \mathbf{q} -vectors is not pursued further in this context. (However, in the discussion of the homogeneous electron gas in chapter 4.4 this limit needs to be investigated.)

3.2.4 The Susceptibility of Non-Interacting Particles

For systems of independent particles – like the Kohn-Sham electrons – the Lehmann representation (3.24) can be explicitly evaluated. The many-body eigenstates such as $|0\rangle$ and $|n, S_z^{(0)} \pm 1\rangle$ take the form of a single Slater determinant composed of single-particle spinors (2.34). The spin operators \hat{S}^\pm read

$$\hat{S}^\pm(\mathbf{r}) = \hat{\psi}^\dagger(\mathbf{r})S^\pm\hat{\psi}(\mathbf{r}) \quad (3.41)$$

where the field operator spinors $\hat{\psi}$, $\hat{\psi}^\dagger$ create or annihilate one single-particle spinors on which the S^\pm (3.19) operate. The introduction of the creation and annihilation operators of single particle states \hat{a}_n , \hat{a}_n^\dagger ,

$$\hat{\psi}^\dagger(\mathbf{r}) = \sum_n \varphi_n^*(\mathbf{r})\hat{a}_n^\dagger \quad (3.42)$$

$$\hat{\psi}(\mathbf{r}) = \sum_n \varphi_n(\mathbf{r})\hat{a}_n \quad (3.43)$$

allows for the expression of the spin-flip response function of a collinear system as

$$\chi_0^{-+}(\mathbf{r}, \mathbf{r}'; \omega) = \lim_{\eta \rightarrow 0^+} \left[\sum_{n, n'} \frac{f(\epsilon_{n\downarrow})[1 - f(\epsilon_{n'\uparrow})]}{\omega - (\epsilon_{n'\uparrow} - \epsilon_{n\downarrow}) + i\eta} \varphi_{n\downarrow}^*(\mathbf{r})\varphi_{n'\uparrow}(\mathbf{r})\varphi_{n'\uparrow}^*(\mathbf{r}')\varphi_{n\downarrow}(\mathbf{r}') - \sum_{n, n'} \frac{f(\epsilon_{n\uparrow})[1 - f(\epsilon_{n'\downarrow})]}{\omega + (\epsilon_{n'\downarrow} - \epsilon_{n\uparrow}) + i\eta} \varphi_{n\uparrow}^*(\mathbf{r}')\varphi_{n'\downarrow}(\mathbf{r}')\varphi_{n'\downarrow}^*(\mathbf{r})\varphi_{n\uparrow}(\mathbf{r}) \right], \quad (3.44)$$

with the Fermi occupation function f . The one-particle energies and wave functions are obtained for instance from the Kohn-Sham equation (2.39). As the sums partially cancel each other, this result can also be written in the more compact form

$$\chi_0^{-+}(\mathbf{r}, \mathbf{r}'; \omega) = \lim_{\eta \rightarrow 0^+} \sum_{n, n'} \frac{f(\epsilon_{n\downarrow}) - f(\epsilon_{n'\uparrow})}{\omega - (\epsilon_{n'\uparrow} - \epsilon_{n\downarrow}) + i\eta} \varphi_{n\downarrow}^*(\mathbf{r})\varphi_{n'\uparrow}(\mathbf{r})\varphi_{n'\uparrow}^*(\mathbf{r}')\varphi_{n\downarrow}(\mathbf{r}') \quad (3.45)$$

and

$$\chi_0^{+-}(\mathbf{r}, \mathbf{r}'; \omega) = \lim_{\eta \rightarrow 0^+} \sum_{n, n'} \frac{f(\epsilon_{n\uparrow}) - f(\epsilon_{n'\downarrow})}{\omega - (\epsilon_{n'\downarrow} - \epsilon_{n\uparrow}) + i\eta} \varphi_{n\uparrow}^*(\mathbf{r})\varphi_{n'\downarrow}(\mathbf{r})\varphi_{n'\downarrow}^*(\mathbf{r}')\varphi_{n\uparrow}(\mathbf{r}'). \quad (3.46)$$

The polarization function for non-interacting particles read

$$P_0(\mathbf{r}, \mathbf{r}'; \omega) = \lim_{\eta \rightarrow 0^+} \sum_{\sigma} \sum_{n, n'} \frac{f(\epsilon_{n\sigma}) - f(\epsilon_{n'\sigma})}{\omega - (\epsilon_{n'\sigma} - \epsilon_{n\sigma}) + i\eta} \varphi_{n\sigma}^*(\mathbf{r})\varphi_{n'\sigma}(\mathbf{r})\varphi_{n'\sigma}^*(\mathbf{r}')\varphi_{n\sigma}(\mathbf{r}'). \quad (3.47)$$

For a non-magnetic system it is $P_0 = 2\chi^{+-} = 2\chi^{-+}$. The symmetry relations regarding $\omega \leftrightarrow -\omega$ introduced in section 3.2.3 become apparent.

This correlation functions are evaluated analytically for the homogeneous electron gas in chapter 4, and calculated numerically for the Kohn-Sham systems investigated in the further course of chapter 6.

These correlation functions solely contain the single-particle spin-flip excitations, which term a flip of an particle from an occupied state in the spin-down channel to an unoccupied spin-up state, or vice versa from spin-up to spin-down channel. The collective spin-wave excitations naturally lie beyond the scope of the one-particle view of this system. To acquire these excitations other means are needed like the Dyson equation introduced in the coming sections.

3.3 The Response in Time-Dependent DFT

The response function of a system describes in general the reaction of the charge to an external field it couples to, in linear order with respect to that field. We are interested in the response of the spin density \mathbf{S} to an external magnetic field \mathbf{B}_{ext} . The expansion with respect to the external field reads

$$\mathbf{m}(\mathbf{r}, t) = \mathbf{m}^{(0)}(\mathbf{r}, t) + \int R(\mathbf{r}, t, \mathbf{r}', t') \mathbf{B}_{\text{ext}}(\mathbf{r}', t') d^3r' dt' + \dots \quad (3.48)$$

where $\mathbf{m}^{(0)}$ is the magnetization density of the ground state, with no external field applied. The factor in the integral – the *response function* R – is defined as

$$R(\mathbf{r}, t, \mathbf{r}', t') = \left. \frac{\delta \mathbf{m}(\mathbf{r}, t)}{\delta \mathbf{B}_{\text{ext}}(\mathbf{r}', t')} \right|_{\mathbf{B}_{\text{ext}}(\mathbf{r}', t')=0} \quad (3.49)$$

and is causal by definition. If the coupling equation (3.48) is formulated in a more general manner in order to couple both the charge and spin density to scalar and magnetic fields, the susceptibility becomes a 4×4 tensor. However, since we are mainly interested in the magnetic response we restrict ourselves to the notation above (see page 24). The evaluation of the response function in time-dependent perturbation theory in first order to the perturbing field (please confer to appendix B) results in an expression nearly identical to the retarded correlation function (3.7):

$$R^{ij}(\mathbf{r}, t, \mathbf{r}', t') = -(\mu_B g)^2 \chi^{ij}(\mathbf{r}, t, \mathbf{r}', t'). \quad (3.50)$$

Assuming the Hamiltonian to contain a magnetic term (3.3) the susceptibility can also be written as a functional derivative of the total energy:

$$R(\mathbf{r}, t, \mathbf{r}', t') = - \left. \frac{\delta^2 E}{\delta \mathbf{B}_{\text{ext}}(\mathbf{r}, t) \delta \mathbf{B}_{\text{ext}}(\mathbf{r}', t')} \right|_{\mathbf{B}_{\text{ext}}(\mathbf{r}', t')=0}, \quad (3.51)$$

compare also to (3.7). Since we are interested in the spin-flip processes, it is reasonable to consider not only the cartesian components χ^{ij} of the correlation function but also the spin-flip components χ^{-+} and χ^{+-} . Up to now they have not been defined in terms of functional derivatives. In order to keep the equality between the variational and the many-body approach (3.50) (please see appendix B), one has to use the following *definition*³ when

³This definition is opposite in sign to the intuitive definition $\delta/\delta B^\pm = \delta/\delta(B_x \pm iB_y) = \delta/\delta B_x \mp i\delta/\delta B_y$. Also does it not correspond to a unitary transformation from the cartesian components to the spin-flip components based on (3.4), (3.5).

performing functional derivatives with respect to the spin-flip magnetic field B^\pm :

$$\frac{\delta}{\delta B^\pm} = \frac{\delta}{\delta B^x} \pm i \frac{\delta}{\delta B^y}. \quad (3.52)$$

Since we assume the external field to be a small perturbation, we do not need to employ the full TDDFT formalism, but stay with the concept of linear response. The response function can then be derived from ground-state properties only which are obtained from DFT. Starting from the definition (3.49) the decomposition of the external magnetic field \mathbf{B}_{ext} into an effective and an exchange-correlation contribution according to (2.52) allows for the derivation of a Dyson equation

$$\frac{\delta m^i(\mathbf{r}, t)}{\delta B_{\text{ext}}^j(\mathbf{r}', t')} = \frac{\delta m^i(\mathbf{r}, t)}{\delta B_{\text{eff}}^j(\mathbf{r}', t')} + \int d^3r_1 d^3r_2 dt_1 dt_2 \sum_{k,l} \frac{\delta m^i(\mathbf{r}, t)}{\delta B_{\text{eff}}^k(\mathbf{r}', t')} \frac{\delta B_{\text{xc}}^k(\mathbf{r}, t)}{\delta m^l(\mathbf{r}', t')} \frac{\delta m^l(\mathbf{r}, t)}{\delta B_{\text{ext}}^j(\mathbf{r}', t')}. \quad (3.53)$$

Using (3.50) this can also be written as

$$\chi^{ij}(\mathbf{r}, t, \mathbf{r}', t') = \chi_{\text{KS}}^{ij}(\mathbf{r}, t, \mathbf{r}', t') + (\mu_{\text{B}}g)^2 \int d^3r_1 d^3r_2 dt_1 dt_2 \sum_{l,m} \chi_{\text{KS}}^{il}(\mathbf{r}, t, \mathbf{r}_1, t_1) f_{\text{xc}}^{lm}(\mathbf{r}_1, t_1, \mathbf{r}_2, t_2) \chi^{mj}(\mathbf{r}_2, t_2, \mathbf{r}', t') \quad (3.54)$$

with the Kohn-Sham response function

$$-(\mu_{\text{B}}g)^2 \chi_{\text{KS}}^{ij}(\mathbf{r}, t, \mathbf{r}', t') = \frac{\delta m^i(\mathbf{r}, t)}{\delta B_{\text{eff}}^j(\mathbf{r}', t')}. \quad (3.55)$$

and the exchange-correlation kernel

$$f_{\text{xc}}^{ij}(\mathbf{r}, t, \mathbf{r}', t') = -\frac{\delta B_{\text{xc}}^i(\mathbf{r}, t)}{\delta m^j(\mathbf{r}', t')} = \frac{\delta^2 E_{\text{xc}}}{\delta m^i(\mathbf{r}, t) \delta m^j(\mathbf{r}', t')} \quad (3.56)$$

which will be examined in more detail in the next section. For systems with a time-independent Hamiltonian a Fourier transformation can be pursued, where the convolution in time resolves to a plain product in frequency space

$$\chi^{ij}(\mathbf{r}, \mathbf{r}'; \omega) = \chi_{\text{KS}}^{ij}(\mathbf{r}, \mathbf{r}'; \omega) + (\mu_{\text{B}}g)^2 \int d^3r_1 d^3r_2 \sum_{l,m} \chi_{\text{KS}}^{il}(\mathbf{r}, \mathbf{r}_1; \omega) f_{\text{xc}}^{lm}(\mathbf{r}_1, \mathbf{r}_2; \omega) \chi^{mj}(\mathbf{r}_2, \mathbf{r}'; \omega). \quad (3.57)$$

In a symbolic notation (please see appendix A) this reads

$$\chi = \chi_{\text{KS}} + (\mu_{\text{B}}g)^2 \chi_{\text{KS}} f_{\text{xc}} \chi \quad (3.58)$$

$$= \chi_{\text{KS}} + (\mu_{\text{B}}g)^2 \chi_{\text{KS}} f_{\text{xc}} \chi_{\text{KS}} + (\mu_{\text{B}}g)^4 \chi_{\text{KS}} f_{\text{xc}} \chi_{\text{KS}} f_{\text{xc}} \chi_{\text{KS}} + \dots \quad (3.59)$$

with f_{xc} the magnetic exchange-correlation kernel tensor. If this series converges, it can be solved by inversion

$$\chi = [\mathbb{1} - (\mu_B g)^2 \chi_{KS} f_{xc}]^{-1} \chi_{KS}. \quad (3.60)$$

One commonly says that χ_{KS} is *renormalized* by f_{xc} in order to yield χ .

In the collinear case the response χ has the shape (3.15), and the Dyson equation (3.58) separates into two Dyson equations for the transversal components $\chi^{[x,y]}$ and the longitudinal components $\chi^{[z,0]}$. We focus on the transversal part and understand (3.58) and (3.60) as equations of 2×2 tensors in $[x, y]$ representation. The kernel is defined as a double derivative which can be applied in both orders. Furthermore, the x and y directions (and thus derivatives with respect to the according component of the spin magnetization) are equivalent. Therefore the kernel would have the symmetrical shape

$$f_{xc}^{[x,y]} = \begin{pmatrix} f_{xc}^{xx} & f_{xc}^{xy} \\ f_{xc}^{xy} & f_{xc}^{xx} \end{pmatrix}, \quad (3.61)$$

opposed to the shape of the response function (3.16). Indeed, this is not yet consistent with the Dyson equation (3.57) but furthermore demands the off-diagonal terms f_{xc}^{xy} to be zero. This is also equivalent to the straight-forward application of the ladder field components (3.52) which results in

$$f_{xc}^{-+} = f_{xc}^{+-} = 2K_{xc}^{xx} \quad (3.62)$$

(please compare to (3.18)). Altogether this leads us from the equation (3.58) of 2×2 tensors to the Dyson equations

$$\chi^{-+} = \chi_{KS}^{-+} + \left(\frac{\mu_B g}{2}\right)^2 \chi_{KS}^{-+} f_{xc}^{-+} \chi^{-+} \quad (3.63)$$

$$\chi^{+-} = \chi_{KS}^{+-} + \left(\frac{\mu_B g}{2}\right)^2 \chi_{KS}^{+-} f_{xc}^{+-} \chi^{+-} \quad (3.64)$$

of scalar functions. Though we are finally interested only in the imaginary part of χ^{-+} , we need both the real and the imaginary part of χ_{KS}^{-+} in order to solve this equation.

Dyson equation (3.64) is a universal scheme to calculate spin-wave excitations, restricted only by the general applicability of time-dependent density-functional theory (falling short for instance of the description of strongly correlated systems). While means to calculate χ_{KS}^{-+} are already provided by (3.45), further evaluation of the exchange-correlation kernel takes place in chapter 4.

The Dielectric Incarnation In order to show the differences to the better known dielectric case the corresponding formulas should be presented briefly. The response of the charge density n to a weak external potential V reads

$$n(\mathbf{r}, t) = n^{(0)}(\mathbf{r}, t) + \int P(\mathbf{r}, t, \mathbf{r}', t') V_{\text{ext}}(\mathbf{r}', t') d^3 r' dt' + \dots \quad (3.65)$$

with the polarization function now written as

$$P(\mathbf{r}, t, \mathbf{r}', t') = \left. \frac{\delta n(\mathbf{r}, t)}{\delta V_{\text{ext}}(\mathbf{r}', t')} \right|_{V_{\text{ext}}(\mathbf{r}', t')=0}. \quad (3.66)$$

The initial substitution is performed according to the separation of the time-dependent effective potential V_{eff} (2.51). Due to definition (2.30) of the Hartree potential the Coulomb interaction v enters the integration kernel of the Dyson equation:

$$P(\mathbf{r}, \mathbf{r}', \omega) = P_{\text{KS}}(\mathbf{r}, \mathbf{r}', \omega) + \int d^3r_1 d^3r_2 P_{\text{KS}}(\mathbf{r}, \mathbf{r}_1, \omega) [v(\mathbf{r}_1, \mathbf{r}_2) + f_{\text{xc}}(\mathbf{r}_1, \mathbf{r}_2, \omega)] P(\mathbf{r}_2, \mathbf{r}', \omega). \quad (3.67)$$

The Kohn-Sham polarization function

$$P_{\text{KS}}(\mathbf{r}, t, \mathbf{r}', t') = \frac{\delta n(\mathbf{r}, t)}{\delta V_{\text{eff}}(\mathbf{r}', t')} \quad (3.68)$$

coincides with (3.47), and the scalar dielectric exchange-correlation kernel reads

$$f_{\text{xc}}(\mathbf{r}, t, \mathbf{r}', t') = \frac{\delta^2 E_{\text{xc}}}{\delta n(\mathbf{r}, t) \delta n(\mathbf{r}', t')} = \frac{\delta V_{\text{xc}}(\mathbf{r}, t)}{\delta n(\mathbf{r}', t')}. \quad (3.69)$$

which is also contained in definition (3.56) as $f_{\text{xc}} = f_{\text{xc}}^{00}$ if understood in a four-component notation.

3.4 The Bigger Context

In order to better understand the context of the theory of spin response it is contrasted to the dielectric response, which in this section is expressed both in formulas and in terms of Feynman diagrams. Starting from the dielectric case, the proper inclusion of the spin coordinate should be worked out, as well as the misleading similar shape but different meaning of the RPA dielectric response and the TDDFT spin response.

The dielectric response function P and all other response functions which are referred to in this chapter are used in their time-ordered shape, whose connection to the causal shape was pointed out earlier on page 31ff. This will not be explicitly stated anymore, and subsequently indices such as in $P_{t.o.}$ as used earlier will be omitted. Furthermore, the shorthand notation $1 = (\mathbf{r}_1, t_1)$, $2 = (\mathbf{r}_2, t_2)$ etc. will be used. The influence of the spin coordinate is discussed in paragraph on the magnetic TDDFT on page 43.

Since the polarization function P contains each two creation and annihilation operators according to (3.7) the response function P is a special case of the two-particle Green function G_2 , a function of four space-time coordinates defined as

$$i^2 G_2(1, 2, 3, 4) = \langle 0 | \mathcal{T} [\hat{\psi}(1) \hat{\psi}(2) \hat{\psi}^\dagger(3) \hat{\psi}^\dagger(4)] | 0 \rangle. \quad (3.70)$$

In analogy to the one-particle Green function G this quantity G_2 is the probability amplitude of a propagation of two quasi-particles through the system. Depending on the order of the time coordinates, this quantity describes either particle-particle propagation (if $t_3, t_4 < t_1, t_2$), particle-hole propagation (if $t_2, t_4 < t_1, t_3$) or hole-hole propagation (if $t_1, t_2 < t_3, t_4$). These three cases are represented by the following three Feynman diagram symbols

$$\quad (3.71)$$

where electrons propagate from left to right and holes from right to left and the labels are set accordingly. We are interested in the charge-neutral processes sketched by the middle graph, denoted \bar{G}_2 and, in order to simplify matters, omit the labels and the arrows on its four legs. Hence \bar{G}_2 quantity can be expanded in an infinite series of Feynman diagrams [GR86] like:

$$\begin{array}{c} \text{shaded rectangle} \end{array} = \begin{array}{c} \text{two parallel lines} \end{array} + \begin{array}{c} \text{crossed lines} \end{array} + \begin{array}{c} \text{wavy line between lines} \end{array} + \begin{array}{c} \text{wavy line between lines} \end{array} + \begin{array}{c} \text{circle between lines} \end{array} + \dots \quad (3.72)$$

Solid lines with an arrow are free electron or hole propagators $G^{(0)}$ while wiggly lines correspond to the Coulomb interaction v as formulated in (2.31). Small opaque circles represent the external parameter variables 1, 2, 3, 4, while empty circles represent integration variables internal to the diagram.

The polarization function P as defined earlier is related to the two-particle Green function \bar{G}_2 by essentially contracting the legs on the left and on the right (i.e., the coordinates are set $2 = 3$ and $4 = 1$)

$$iP_{t.o.}(1, 2) = \bar{G}_2(1, 2, 2, 1) - G(1, 1^+)G(2, 2^+) \quad (3.73)$$

where G is the one-particle Green function. Here the coordinate 1^+ implies a limit $G(1, 1^+) = \lim_{\eta \rightarrow 0} G(\mathbf{r}_1, t_1, \mathbf{r}_2, t_1 + \eta)$ in order to properly resolve the implicit time-ordering operator. Visualized in diagrams it reads

$$\begin{array}{c} \text{shaded eye} \end{array} = \begin{array}{c} \text{shaded rectangle} \end{array} - \begin{array}{c} \text{two circles} \end{array} \quad (3.74)$$

The symbol newly introduced on the left is the dielectric response function P , while the shaded symbol on the right-hand side is the two-particle Green function \bar{G}_2 from (3.72) with its legs contracted on the left and on the right. The subtracted term on the right just corresponds to the exclusion $n \neq 0$ from the summation in the Lehmann representation (3.25). The response function P can thus be equally expressed through a series of Feynman diagrams. These diagrams can be grouped into those diagrams which can be cut into two separate diagrams by just removing one Coulomb interaction wiggly (such as the third diagrams on the right-hand side of (3.72)) and those diagrams which cannot be split in such a way. The latter ones are collected into a newly defined quantity named *irreducible polarization propagator* Q , and the series can be rewritten in terms of diagrams as

$$\begin{array}{c} \text{shaded eye} \end{array} = \begin{array}{c} \text{hatched eye} \end{array} + \begin{array}{c} \text{hatched eye} \end{array} \begin{array}{c} \text{wavy line} \end{array} \begin{array}{c} \text{shaded eye} \end{array} \quad (3.75)$$

where Q has been depicted by the hatched bubble on the right-hand side. The full (or so-called reducible) polarization function P is the sum of all possible queueings of the irreducible polarization propagator Q connected by Coulomb interactions. Expressed in formulas it reads

$$P(1, 2) = Q(1, 2) + \int d3 d4 Q(1, 3)v(3, 4)P(4, 1). \quad (3.76)$$

This equation is the general Dyson equation for the polarization function P . It is completely general, with the complexity of the problem being moved into the quantity Q . Crucial quantities commonly derived from this include the dielectric function ϵ which describes, e.g.,

absorption spectra, and its inverse ε^{-1} crucial for electron energy loss spectra (EELS) or inelastic X-ray scattering:

$$\varepsilon(1, 2) = 1 - \int d3 v(1, 3)Q(3, 2) \quad (3.77)$$

$$\varepsilon^{-1}(1, 2) = 1 + \int d3 v(1, 3)P(3, 2). \quad (3.78)$$

The latter one connects the Coulomb potential to the screened interaction

$$W(1, 2) = \int d3 \varepsilon^{-1}(1, 3)v(3, 2). \quad (3.79)$$

used for instance in the so-called *GW*-approximation which is nowadays the premium ab initio method to improve density-functional results by means of many-body perturbation theory [AG98].

RPA The simplest and most commonly used method in this context is the random-phase approximation (RPA, also called ring-graph approximation or time-dependent Hartree theory). It considers for the irreducible polarization Q only the lowest-order term of $P^{(0)}$ (the empty polarization bubble)

$$Q_{\text{RPA}}(1, 2) \equiv P^{(0)}(1, 2) = iG(1, 2)G(2, 1^+) \quad (3.80)$$

which is the polarization propagator of non-interacting particles. The variable 1^+ implies a limit in the time coordinate as mentioned before. This polarization bubble is a very descriptive visualization of the physical process: at some space-time coordinate 2 a particle-hole pair comes into existence and propagates to coordinate 1. The Dyson equation (3.76) now in RPA then reads

$$P_{\text{RPA}}(1, 2) = P^{(0)}(1, 2) + \int d3 d4 P^{(0)}(1, 3)v(3, 4)P_{\text{RPA}}(4, 2). \quad (3.81)$$

Expressed in diagrams this reads

$$\begin{aligned} \text{Diagram} &= \text{Diagram} + \text{Diagram} \\ &= \text{Diagram} + \text{Diagram} + \text{Diagram} + \dots \end{aligned} \quad (3.82)$$

This result for the response function can also be obtained by solving the time-dependent Hartree equations. The RPA results are exact in the limit of an infinitely dense homogeneous system, therefore it has been applied to real metallic materials quite successfully. However, processes that are naturally distinct from these boundary conditions – such as excitonic effects in semi-conductors – are not at all reproduced by RPA.

In practical DFT calculations the free Green function (or polarization function, respectively) are substituted by the Kohn-Sham quantities, $P^{(0)} = P_{\text{KS}}$, and the Dyson equation then reads

$$P_{\text{RPA}}(1, 2) = P_{\text{KS}}(1, 2) + \int d3 d4 P_{\text{KS}}(1, 3)v(3, 4)P_{\text{RPA}}(4, 2). \quad (3.83)$$

Dielectric TDDFT For the dielectric framework a Dyson equation was derived within TDDFT (3.67), now written in the new notation as

$$P(1, 2) = P_{\text{KS}}(1, 2) + \int d3 d4 P_{\text{KS}}(1, 3)[v(3, 4) + f_{\text{xc}}(3, 4)]P(4, 2). \quad (3.84)$$

This can also be *sketched* in terms of diagrams

$$\text{Diagram} = \text{Diagram} + \text{Diagram} + \text{Diagram} \quad (3.85)$$

The zig-zag wiggly in the last term represents the dielectric exchange-correlation kernel f_{xc} . It should be stressed that this is merely a visualization and not a valid expansion in Feynman diagrams anymore, because the zig-zag can *not* be expressed in terms of free Green functions $G^{(0)}$ and Coulomb interactions v ; time-dependent DFT, which is itself completely general, is definitely a non-diagrammatic method. It can be seen from the derivation before that it is not possible to express the kernel zig-zag in terms of diagrams: Any diagram resulting from (3.85) has at least one empty polarization bubble attached on the left, thus not all diagrams can be constructed if the kernel would be a combination of other diagrams. However, since this is not the case, the kernel can compensate for that since it has a difficult functional structure, and can lead to exact and general results by itself.

This allows the following classification of the presented Dyson equations: The RPA Dyson equation (3.81) simplifies the general Dyson equation (3.76) by considering the ring diagrams only. The TDDFT Dyson equation (3.84) extends the RPA equation and recovers generality while keeping the mathematical form of the RPA equation, by moving the complex many-body interactions from the irreducible polarization propagator Q into the exchange-correlation kernel f_{xc} . In this context the RPA naturally appears as a theory that neglects exchange and correlation effects (the kernel f_{xc}), thus being the time-dependent Hartree theory.

It is valuable to realize that the two renormalizations of v and f_{xc} can be performed subsequently. Equation (3.84) can also be written in the form

$$P(1, 2) = P_{\text{RPA}}(1, 2) + \int d3 d4 P_{\text{RPA}}(1, 3)f_{\text{xc}}(3, 4)P(4, 2). \quad (3.86)$$

with P_{RPA} given by (3.83). It would be equally possible to renormalize first with f_{xc} and with v afterwards. The effect of the kernel is expected to be small compared to that of the Coulomb potential which is the dominant effect in solids. This can also be seen from the different magnitude of the Coulomb energy E_{coul} and the exchange-correlation energy E_{xc} in table 2.1.

Spin Coordinates and Magnetic TDDFT Up to now the spin index has been neglected in the formulation of this section. A natural extension would be to use the shorthand $1 = (\mathbf{r}_1, t_1, \sigma_1)$ in all the formulas of this section 3.4, which means for the creation and annihilation operators – the operators at the very bottom of the whole theory discussed in this chapter – a formulation $\hat{\psi}(1) = \hat{\psi}(\mathbf{r}_1, t_1, \sigma_1)$. However, it turns out that this is impractical. Instead it is much more reasonable to keep the interpretation of the quantities as it is up to now – e.g., $P(1,2)$ is the propagation of charge fluctuations between space-time coordinates

2 and 1, *irrespective* of spin coordinates – and replace in the according definitions the scalar field operators with spinors

$$\hat{\psi}(1) = \hat{\psi}(\mathbf{r}_1, t_1) = \begin{pmatrix} \hat{\psi}(\mathbf{r}_1, t_1, \uparrow) \\ \hat{\psi}(\mathbf{r}_1, t_1, \downarrow) \end{pmatrix} \quad (3.87)$$

$$\hat{\psi}^\dagger(1) = \hat{\psi}^\dagger(\mathbf{r}_1, t_1) = \begin{pmatrix} \hat{\psi}^\dagger(\mathbf{r}_1, t_1, \uparrow) \\ \hat{\psi}^\dagger(\mathbf{r}_1, t_1, \downarrow) \end{pmatrix}. \quad (3.88)$$

Many-body states consist of a single or a linear combination of Slater determinants, which themselves consist of scalar functions in the non-magnetic case and spinors in the magnetic formulation. The field operator spinors shown above can thus conveniently operate on these states.

The basic building blocks of Feynman diagrams are the spin-independent and spin-conserving Coulomb interaction and free propagators, which should now be understood as free spinor propagators. A change in spin can happen with neither of these two ingredients. Instead, additional spin-flip operators (3.41) have to be included that were not present in the dielectric-only theory. Since they are local they can act only at crossing points in Feynman diagrams, denoted by small diamonds. E.g., the expansion (3.72) now additionally contains all the diagrams decorated with any combination of spin-flip operators. Also the polarization propagator $P(1, 2)$ contains all kinds of spin flips; physically this means that any kinds of spin flips are allowed on the way $2 \rightarrow 1$, as long as the initial and the final spin are equal. In the general Dyson equation (3.75) for P the spin-flip operators are contained in the irreducible propagator Q , the hatched bubble. In the RPA equation (3.81), however, these processes have been excluded.

The magnetic response $\chi^{-+}(1, 2)$ is equivalently interpreted as a particle propagation $2 \rightarrow 1$ yet with a spin-flip occurring from down to up. (Only the final spin orientation matters, of course multiple spin flips might occur during the scattering through the system.) Its relation to the two-particle Green function is sketched analogously as

$$\text{Diagram with hatched bubble and diamond} = \text{Diagram with hatched bubble} \quad (3.89)$$

Here the small diamond symbols represent spin-flip operators $\hat{S}^\pm(1)$. The whole graph on the left can be understood as the spin-flip response χ^{-+} (or χ^{+-} , respectively). The term on the right side is the two-particle Green function from formula (3.72) with its legs both on the left and on the right-hand side contracted and a spin-flip operator attached. As an important difference to the dielectric case, no local term needs to be subtracted like the local polarization term in (3.74), since it does not contribute due to the spin-flip operators. Furthermore, no distinction has been made between spin-up and spin-down flips, thus it is not clear initially whether the equation above refers to χ^{-+} or χ^{+-} ; however, this should be either insignificant or obvious from context. With this notation the magnetic Dyson equation (3.64), written again as

$$\chi^{-+}(1, 2) = \chi_{\text{KS}}^{-+}(1, 2) + \frac{1}{4} \chi_{\text{KS}}^{-+}(1, 3) K_{\text{xc}}^{-+}(3, 4) \chi^{-+}(4, 2), \quad (3.90)$$

can be *sketched* as

$$\text{Diagram with hatched bubble and diamond} = \text{Diagram with hatched bubble} + \text{Diagram with hatched bubble and diamond} \quad (3.91)$$

which is the magnetic analogon to (3.85). As in the dielectric diagrams the empty diamonds denote spin flips at internal integration coordinates. Most importantly, these are no valid Feynman diagrams as reasoned before since the exchange correlation kernel is not a diagrammatic quantity. The kernel wiggle is decorated with two spin-flip operators: this indicates that the magnetic kernel K_{xc} needs to be used instead of the dielectric kernel f_{xc} .

In the dielectric TDDFT equation the interaction can be separated into the dominant Coulomb term and the exchange-correlation term. In the magnetic case there is no Coulomb interaction, thus no RPA-like approximation is possible, instead the exchange-correlation term has to be treated accurately. In particular, though the shape of (3.91) is very similar to (3.82) there is no theoretical link between dielectric RPA and magnetic TDDFT.

Effect on Non-Magnetic Systems It should be remarked that the magnetic formalism can of course also be employed on non-magnetic systems. The Kohn-Sham susceptibilities turn out to be identical,

$$\chi_{KS}^{-+}(1, 2) = \chi_{KS}^{+-}(1, 2) = \frac{1}{2}P_{KS}(1, 2). \quad (3.92)$$

Also the dielectric and magnetic kernels are very similar, as shown in section 4.3. The full response functions, however, are definitely unequal, since they obey different Dyson equations. While the magnetic Kohn-Sham response is renormalized by the magnetic kernel only, the dielectric counterpart is renormalized by the sum of dielectric kernel and Coulomb interaction. It is made plausible for the case of the homogeneous electron gas in the next chapter that there cannot appear spin waves in non-magnetic materials.

Another Approach A theoretical framework to evaluate the spin-flip response diagrammatically has been established by Aryasetiawan and Karlsson [AK99]. Starting from the two-particle Green function (3.72) a higher class of vertex diagrams is included, which involves the GW -approximation for the self-energy, $\Sigma = iGW$. This leads to a series of ladder diagrams involving the screened interaction W (3.79). Approximations such as on-site only interactions are applied. The result is a Bethe-Salpeter equation, resembling in structure the Dyson equation of TDDFT. On the one hand this approach is more systematic compared to TDDFT in the sense that you can select certain classes of diagrams which might be connected to specific physical processes. On the other hand it is expected to be computationally more demanding if the screened interaction is properly accounted for.

CHAPTER 4

THE SPIN-POLARIZED HOMOGENEOUS ELECTRON GAS

Contents

4.1	Characteristic Quantities	48
4.2	The Kohn-Sham Response	53
4.3	The Exchange-Correlation Kernel in ALDA	57
4.4	Spin Waves from ALDA	60
4.5	The Correlation Contribution	66
4.6	Differences and Conclusions for Real Materials	69

The formalism of spin-wave excitations introduced in the previous chapter is now applied to the homogeneous electron gas. Apart from allowing a lot of calculations to be done analytically, it is very instructive to see the formalism work on simple formulas, giving rise to spin waves.

In the beginning section 4.1, the characteristic quantities such as density, spin polarization and total energy are discussed. At this stage only the exchange is taken into account while the correlation contribution is neglected for the moment. While this restriction allows for an exact analytical treatment, the resulting densities for which the homogeneous electron gas is spin-polarized corresponds closer to the values of real physical systems which are polarized (such as for instance the bulk transition metals). The one-particle viewpoint is treated within the Kohn-Sham DFT picture. In section 4.2 the spin-flip response of this Kohn-Sham system is investigated. The following section details out the formulas of the exchange-correlation kernel in adiabatic LDA. These ingredients are combined into the ALDA spin-wave treatment in section 4.4, employing the Dyson equation that was introduced in the previous chapter. Two important insights are that this method is very sensitive to inaccuracies, and that exchange and correlation need to be treated consistently in the single-particle Kohn-Sham equation and the ALDA linear-response part.

The correlation energy is finally treated in section 4.5. While it is an additional contribution which is parametrized with more complicated formulas, it does not change the principle findings of the previous sections. The chapter closes with an outlook on real materials, pointing out some differences and conclusions that can be drawn from the homogeneous system.

4.1 Characteristic Quantities

The electron gas is infinitely extended in space, and is characterized by the two constant spin densities n_\uparrow and n_\downarrow . The total density n , spin density σ , magnetization m and spin polarization ξ are defined as

$$n = n_\uparrow + n_\downarrow, \quad \sigma = n_\uparrow - n_\downarrow, \quad \xi = \frac{n_\uparrow - n_\downarrow}{n_\uparrow + n_\downarrow} = \frac{\sigma}{n}, \quad (4.1)$$

$$m = -\mu_B g S = -\frac{1}{2} \mu_B g \sigma = -\frac{1}{2} \mu_B g n \xi, \quad (4.2)$$

where \uparrow and \downarrow are the majority and the minority components, respectively, and S is the total-spin quantum number. The electron gas is thus either non-magnetic or collinear magnetic along an arbitrary axis, which we choose as the z axis. The Fermi wave vectors result in

$$k_{F\uparrow}^3 = 6\pi^2 n_\uparrow, \quad k_{F\downarrow}^3 = 6\pi^2 n_\downarrow. \quad (4.3)$$

This can also be expressed as

$$k_{F\uparrow} = k_F (1 + \xi)^{\frac{1}{3}}, \quad k_{F\downarrow} = k_F (1 - \xi)^{\frac{1}{3}}, \quad k_F^3 = 3\pi^2 n \quad (4.4)$$

k_F is the Fermi vector of the non-magnetic case. The total energy reads

$$E(n, \xi) = - \sum_i \frac{k_i^2}{2} + E_{xc}(n, \xi) + E_{ext}(n, \xi) \quad (4.5)$$

In the case of the homogeneous electron gas the local-density approximation (LDA) yields the correct value for the exchange-correlation energy. It can be separated into two contributions $E_{xc} = E_x + E_c$, see (2.40). The latter one, the correlation contribution E_c , is neglected until section 4.5. The exchange contribution reads

$$E_x(n, \xi) = V n \epsilon_x(n, \xi) = -C_x V n^{\frac{4}{3}} \left[1 - (2^{\frac{1}{3}} - 1) f(\xi) \right]. \quad (4.6)$$

The quantities in this equation have been introduced in chapter 2:

$$C_x = \frac{3}{4} \left(\frac{3}{\pi} \right)^{\frac{1}{3}}, \quad f(\xi) = \frac{(1 + \xi)^{\frac{4}{3}} + (1 - \xi)^{\frac{4}{3}} - 2}{2^{\frac{4}{3}} - 2}. \quad (4.7)$$

The exchange energy's derivatives are

$$V_x = \frac{1}{V} \frac{\partial E_x}{\partial n}, \quad (4.8)$$

$$\mathbf{B}_x = -\frac{1}{V} \frac{\partial E_x}{\partial \mathbf{m}} = \frac{2}{\mu_B g V n} \frac{\partial E_x}{\partial \xi} \mathbf{e}_z. \quad (4.9)$$

The contribution due to a constant external magnetic field \mathbf{B}_{ext} (which can be chosen to point into the z direction without loss of generality) is

$$E_{ext}(n, \xi) = - \int \mathbf{m}(\mathbf{r}) \cdot \mathbf{B}_{ext}(\mathbf{r}) d^3r = \frac{1}{2} n V \mu_B g \xi B_{ext}. \quad (4.10)$$

Altogether the energy reads¹

$$E(n, \xi) = \frac{3}{20}(3\pi^2)^{\frac{2}{3}} \left[(1 + \xi)^{\frac{5}{3}} + (1 - \xi)^{\frac{5}{3}} \right] Vn^{\frac{5}{3}} - \frac{3}{4} \left(\frac{3}{\pi} \right)^{\frac{1}{3}} \left[1 + (2^{\frac{1}{3}} - 1)f(\xi) \right] Vn^{\frac{4}{3}} + \frac{1}{2}\xi\mu_B g B_{\text{ext}} Vn. \quad (4.11)$$

The positive kinetic term counters the negative exchange energy. They have different functional dependencies on n and ξ . For a given density n the physical spin polarization ξ is determined by minimizing the total energy (4.11). If another spin polarization is desired, an external magnetic field B_{ext} can be used to pin any desired value. Without any external field applied, $B_{\text{ext}} = 0$, the polarization that yields the minimal energy is

$$\xi(n) = \begin{cases} 0 & n > n_1 \\ 1 & n < n_1 \end{cases} \quad (\text{no external field}) \quad (4.12)$$

with the threshold density

$$n_1 = \frac{125}{24\pi^5(2^{\frac{1}{3}} + 1)^3} = 1.47 \cdot 10^{-3} \frac{1}{a_B^3}, \quad r_{s1} = \frac{2}{5}(2^{\frac{1}{3}} + 1) \left(\frac{9\pi^4}{4} \right)^{\frac{1}{3}} = 5.45a_B. \quad (4.13)$$

When numerical values for charge radii and densities are given in this section, the units – if not explicitly provided – are understood as the standard atomic units for these quantities: Bohr radii or the inverse third power of Bohr radii, respectively. The corresponding density radius r_{s1} is also provided, which relates to the density like

$$\frac{4}{3}\pi r_s^3 = \frac{1}{n}. \quad (4.14)$$

The total energy without external field has interesting features. Two further threshold values are defined:

$$n_0 = \frac{1}{3\pi^5} = 1.09 \cdot 10^{-3} \frac{1}{a_B^3}, \quad r_{s0} = \left(\frac{9\pi^4}{4} \right)^{\frac{1}{3}} = 6.03a_B, \quad (4.15)$$

$$n_2 = \frac{4}{3\pi^5} = 4.36 \cdot 10^{-3} \frac{1}{a_B^3}, \quad r_{s2} = \left(\frac{9\pi^4}{16} \right)^{\frac{1}{3}} = 3.80a_B. \quad (4.16)$$

For different fixed densities n the total energy is plotted in the right tableau of figure 4.1 as a function of the spin polarization ξ . It has the following characteristics:

- For $n < n_0$: Maximum at $\xi = 0$, absolute minimum at $\xi = 1$ (black and red curves on the right-hand side of figure 4.1).
- For $n_0 < n < n_1$: Local minimum at $\xi = 0$, maximum in the range $0 < \xi_{\text{max}}(n) < \xi_{\text{max}}(n_1)$ with $\xi_{\text{max}}(n_1) \approx 0.788$, absolute minimum at $\xi = 1$. (In the plot there is no curve for a corresponding density from this range, it would lie between the red and the blue curve.)

¹This ground-state total energy in DFT without correlation is identical to the value obtained from the Hartree-Fock method; however, the one-particle energy dispersion and thus the susceptibility is different for Hartree-Fock and is not treated in this work.

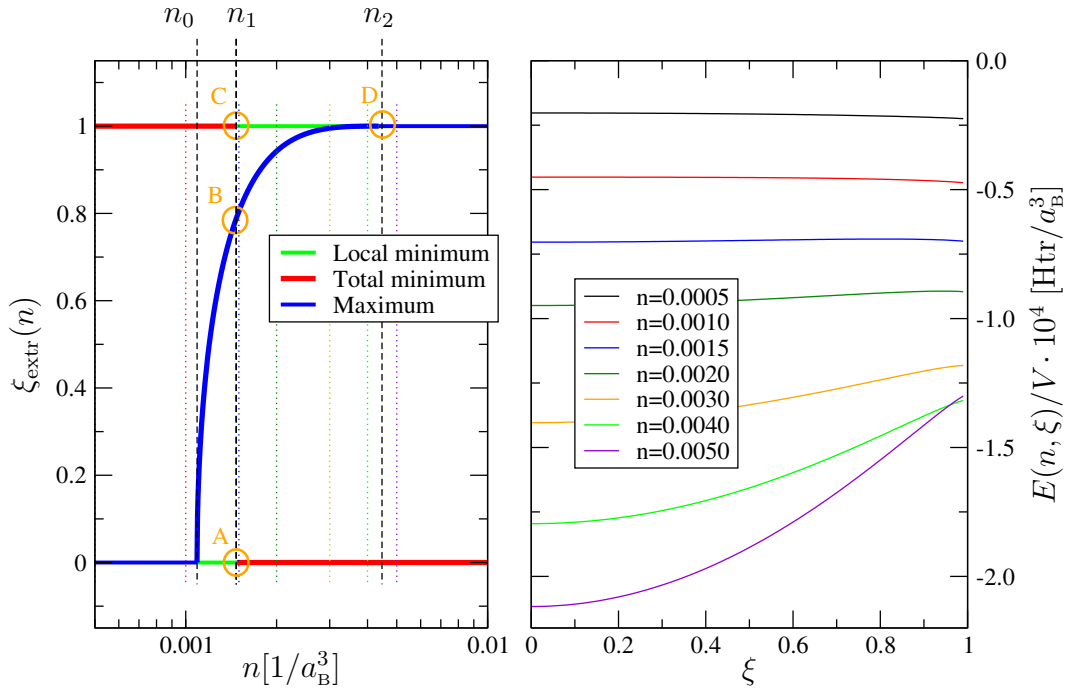


Figure 4.1: On the right-hand side the total energy $E(n, \xi)$, c.f. (4.11), is plotted as a function of ξ for different densities n . Since the extrema are difficult to identify with the bare eye, their positions are pictured separately on the left-hand side by thick lines in the (n, ξ) -plot. The thin dotted vertical lines correspond to the values of the densities for which $E(n, \xi)$ was plotted on the right-hand side. The vertical dashed black lines indicate the threshold values n_0, n_1, n_2 . The four orange circles indicate the (n, ξ) values named (A)-(D) for which a spectrum is shown in figure 4.4.

- For $n_1 < n < n_2$: absolute minimum at $\xi = 0$, maximum in the range $\xi_{\text{max}}(n_1) < \xi_{\text{max}}(n) < 1$. (Blue, dark green, orange and light green curves. For the last two, the local minimum cannot be identified in this magnification.)
- For $n > n_2$: Absolute minimum at $\xi = 0$, maximum at $\xi = 1$.

Between these extrema the function is strictly monotonous. The location of the maximum $\xi_{\text{max}}(n)$ cannot be obtained analytically, but only numerically, e.g., by interval nesting. Summarizing, for a given density n the following spin polarizations $\xi(n)$ yield an extremum of the total energy $E(n, \xi(n))$:

$$\begin{aligned}
 \text{Absolute minimum} & & \xi(n) &= \begin{cases} 1 & n < n_1 \\ 0 & n > n_1 \end{cases} \\
 \text{(thick red lines)} & & & \\
 \text{Local minimum} & & \xi(n) &= \begin{cases} 0 & n_0 < n < n_1 \\ 1 & n_1 < n < n_2 \end{cases} \\
 \text{(thick green lines)} & & & \\
 \text{Maximum} & & \xi(n) &= \begin{cases} 0 & n < n_0 \\ \xi_{\text{max}}(n) & n_0 \leq n \leq n_2 \\ 1 & n > n_2 \end{cases} \\
 \text{(thick blue lines)} & & &
 \end{aligned} \tag{4.17}$$

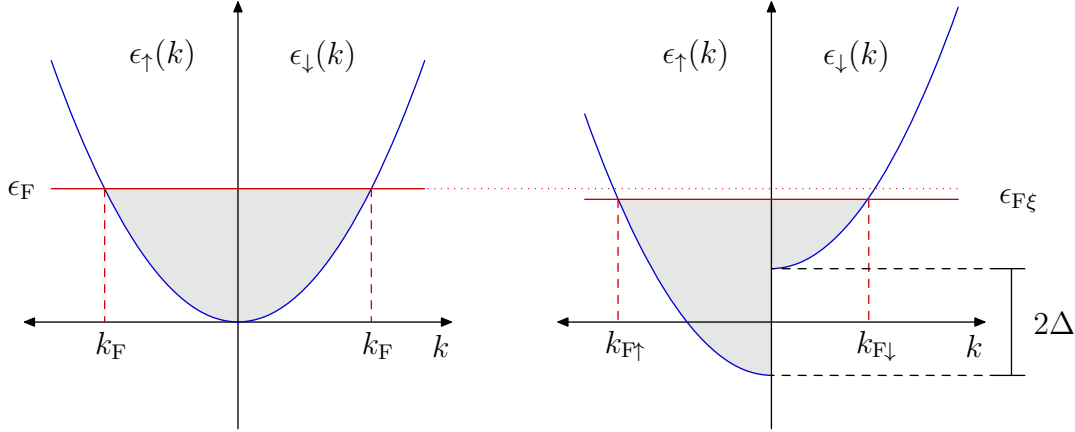


Figure 4.2: The energy dispersion $\epsilon(k)$ of both spin channels in the paramagnetic case (left) and the spin-polarized case (right). The origin of the energy axis is the crossing point of the two coordinate axes. The gray area represents the occupied states. In particular, it is $\epsilon_F \neq \epsilon_{F\xi}$.

The color of the lines refers to the left plot in figure 4.1. Real materials commonly have a density radius of the valence electrons from roughly the region $2a_B < r_s < 5a_B$. As discussed above, the density radii for which the homogeneous electron gas – calculated with exchange only – becomes magnetic are below these values: $r > r_{s1} = 5.45a_B$. This corresponds to densities slightly lower than the average density of typical real materials. This might be kept in mind when comparing results with those obtained here for the homogeneous electron gas.

One-Particle Point of View Along the lines of the density-functional formalism introduced in chapter 2, the electron gas can now be studied with the help of an auxiliary system of independent non-interacting particles. According to (2.39) the collinear Kohn-Sham equations read

$$\left[-\frac{1}{2}\nabla^2 + V_{\text{eff}} + \frac{1}{2}\mu_B g \sigma B_{\text{eff}} \right] \varphi_{k\sigma}(\mathbf{r}) = \epsilon_{\sigma}(\mathbf{k}) \varphi_{k\sigma}(\mathbf{r}) \quad (4.18)$$

with the scalar constant effective fields

$$V_{\text{eff}} = V_{\text{xc}}, \quad B_{\text{eff}} = B_{\text{xc}} + B_{\text{ext}}. \quad (4.19)$$

The spin index $\sigma \in \{\uparrow, \downarrow\}$ has also been used on the left-hand side of the equation in the Hamiltonian with the values $\sigma = \pm 1$. (This should not be confused with the spin density $\sigma = n\xi$. However, the correct meaning should be apparent from the context.) The magnetic term in the Kohn-Sham equation above corresponds to a magnetic term $-\mathbf{m} \cdot \mathbf{B}_{\text{eff}}$, c.f. (2.35). The value B_{eff} is negative, or pointing in the $-z$ direction, respectively. Therefore the ground-state magnetization also points in the $-z$ direction in order to yield a lower energy contribution, and the spin polarization points in the $+z$ direction. Thus, the spin-up component is indeed the majority channel. The energies and wave functions evaluate to

$$\epsilon_{\sigma}(\mathbf{k}) = \frac{1}{2}k^2 + V_{\text{eff}} + \frac{1}{2}\mu_B g \sigma B_{\text{eff}}, \quad \varphi_{k\sigma}(\mathbf{r}) = \frac{1}{\sqrt{V}} e^{i\mathbf{k} \cdot \mathbf{r}}. \quad (4.20)$$

The volume V of the system goes to infinity. The effective potential V_{eff} is identical for both spin channels, thus corresponding to a global energy shift which can consequently be neglected. For the moment we set the external magnetic field $B_{\text{ext}} = 0$. For a fixed density n this equation has to be iterated: Starting from an initial spin polarization $\xi^{(0)}$ one obtains the effective magnetic field and scalar potential and can solve the Kohn-Sham equations, leading to parabolas

$$\epsilon_{\sigma}(\mathbf{k}) = \frac{1}{2}k^2 - \sigma\Delta, \quad \Delta = -\frac{1}{2}\mu_B g B_{\text{xc}}, \quad (4.21)$$

with the spin-dependent energy splitting 2Δ . This is sketched in figure 4.2. If the system is not completely spin polarized, $0 \leq \xi < 1$, there exists a bijective mapping from the density n and spin polarization ξ to the splitting Δ :

$$\Delta(n, \xi) = \frac{1}{4}(k_{\text{F}\uparrow}^2 - k_{\text{F}\downarrow}^2) = \frac{1}{4}k_{\text{F}}^2 \left[(1 + \xi)^{\frac{2}{3}} - (1 - \xi)^{\frac{2}{3}} \right] \quad \text{if} \quad 0 \leq \xi < 1. \quad (4.22)$$

The condition $0 \leq \xi < 1$ is equivalent to the condition $|\Delta| < \Delta_{\text{lim}}$ where the limiting value

$$\Delta_{\text{lim}} = 2^{-\frac{4}{3}}k_{\text{F}}^2 \quad (4.23)$$

is the minimal spin splitting which yields full spin polarization $\xi = 1$. If Δ increases beyond this value the spin polarization remains the same, there is no invertible mapping between ξ and Δ anymore and one cannot construct a functional relation $\Delta(n, \xi)$ for $\xi = 1$. This argumentation is the same for the Fermi energy:

$$\epsilon_{\text{F}\xi} = \begin{cases} \frac{1}{4}(k_{\text{F}\uparrow}^2 + k_{\text{F}\downarrow}^2) = \frac{1}{4}k_{\text{F}}^2 \left[(1 + \xi)^{\frac{2}{3}} + (1 - \xi)^{\frac{2}{3}} \right] & \text{if } 0 \leq \xi < 1 \\ -|\Delta| + 2^{-\frac{1}{3}}k_{\text{F}}^2 & \text{if } \xi = 1. \end{cases} \quad (4.24)$$

Thus, the new spin polarization (a mixing procedure as mentioned in chapter 2 is not necessary for this simple setup) can be obtained as the inverse function of (4.22) as

$$\xi = \begin{cases} \xi(\Delta) & |\Delta| \leq \Delta_{\text{lim}} \\ \pm 1 & |\Delta| > \Delta_{\text{lim}}. \end{cases} \quad (4.25)$$

The convergence can be understood best by imaging the two quantities $\Delta(\xi)$ and $-\frac{1}{2}\mu_B g B_{\text{xc}}(\xi)$ being plotted in one graph as functions of ξ . The self-consistency cycle corresponds to an iteration of $\xi^{(0)} \rightarrow B_{\text{xc}}(\xi) \rightarrow \Delta(B_{\text{xc}}) = -\frac{1}{2}\mu_B g B_{\text{xc}} \rightarrow \xi(\Delta)$, provided the mentioned condition is fulfilled. The obtained ξ is the starting value for another loop. The result is as follows:

- For $n < n_0$, polarization converges to $\xi = 1$.
- For $n_0 < n < n_2$ and $\xi^{(0)} > \xi_{\text{max}}(n)$, polarization converges to $\xi = 1$.
- For $n_0 < n < n_2$ and $\xi^{(0)} = \xi_{\text{max}}(n)$, polarization does not change and is already converged to $\xi = \xi_{\text{max}}(n)$.
- For $n_0 < n < n_2$ and $\xi^{(0)} < \xi_{\text{max}}(n)$, polarization converges to $\xi = 0$.

- For $n > n_2$, polarization converges to $\xi = 0$.

In the region $n_0 < n < n_2$ the starting spin polarization $\xi^{(0)}$ is essential for the result. If chosen not close enough to the final result the convergence might lead to a local minimum instead of the total minimum. In the special case where the initial spin polarization is set equal the polarization of the energy maximum $\xi_{\max}(n)$ that was obtained earlier, the calculation does not at all converge to a minimum.

In summary it turns out that for a given density n , the DFT method determines the extremal points of the total energy, just as it is expected for a variational method operating on this energy. The solutions $\xi_{\max}(n)$ are usually discarded because the resulting state has an energy maximum. This leaves only DFT solutions $\xi = 0$ (for large densities) and $\xi = 1$ (for small densities). However, one might be interested to make an electron-gas calculation for a spin polarization other than these values. Thus, for testing purposes one can, instead of discarding the energy-maximum solutions as being unphysical, determine $n \in [n_0, n_2]$ for a desired ξ for which $\xi_{\max}(n) = \xi$, and use this setup (namely the (n, ξ) value pair) in the further ALDA formalism. Consequently setup (B) from figure 4.1 is used in the following chapters.²

These statements do refer to the case of absent external magnetic field, $B_{\text{ext}} = 0$ as we have implied starting from equation (4.20). If we lift this restriction, we can choose a proper B_{ext} for any (n, ξ) such that this is the ground state (i.e., the state of minimum energy) of the electron gas. Formulated in another way: When doing the variation of the total energy (4.5) in order to obtain the Kohn-Sham equations (please refer to chapter 2) one introduces Lagrange Parameters ϵ which ensure the boundary condition of particle conservation. Analogously one can introduce another Lagrange Parameter which provides for a given total magnetization. This parameter is just the external magnetic field B_{ext} .

4.2 The Kohn-Sham Response

The spin-flip susceptibility for the homogeneous electron gas χ_{KS}^{+-} can be easily obtained from equation (3.46). Using the known shape of the eigenstates (4.20) and eigenvalues (4.21) and performing a Fourier transform leads to

$$\chi_{\text{KS}}^{+-}(\mathbf{q}, \omega) = \frac{1}{V} \lim_{\eta \rightarrow 0^+} \sum_{\mathbf{k}} \frac{f(\epsilon_{\uparrow}(\mathbf{k})) - f(\epsilon_{\downarrow}(\mathbf{k} + \mathbf{q}))}{\omega - [\epsilon_{\downarrow}(\mathbf{k} + \mathbf{q}) - \epsilon_{\uparrow}(\mathbf{k})] + i\eta}. \quad (4.26)$$

The susceptibility is spherically symmetric with respect to \mathbf{q} . According to the derivations in appendix B.3 the real and imaginary part can be evaluated to

$$\text{Re } \chi_{\text{KS}}^{+-}(q, \omega) = -\frac{1}{4\pi^2 q} \sum_{\sigma} \sigma \left[\frac{1}{2} (k_{\text{F}\sigma}^2 - u_{\sigma}^2) \ln \left| \frac{u_{\sigma} + k_{\text{F}\sigma}}{u_{\sigma} - k_{\text{F}\sigma}} \right| + u_{\sigma} k_{\text{F}\sigma} \right] \quad (4.27)$$

$$\text{Im } \chi_{\text{KS}}^{+-}(q, \omega) = -\frac{1}{8\pi q} \sum_{\sigma} \sigma (k_{\text{F}\sigma}^2 - u_{\sigma}^2) \Theta(k_{\text{F}\sigma} - |u_{\sigma}|) \quad (4.28)$$

²It should be noted that the spin-wave excitations calculated from such a non-ground state should in principle have negative energies. Nevertheless, the ALDA method is applied onto this state for positive energies. It turns out that the formalism yields positive spin-wave energies, see figure 4.7.

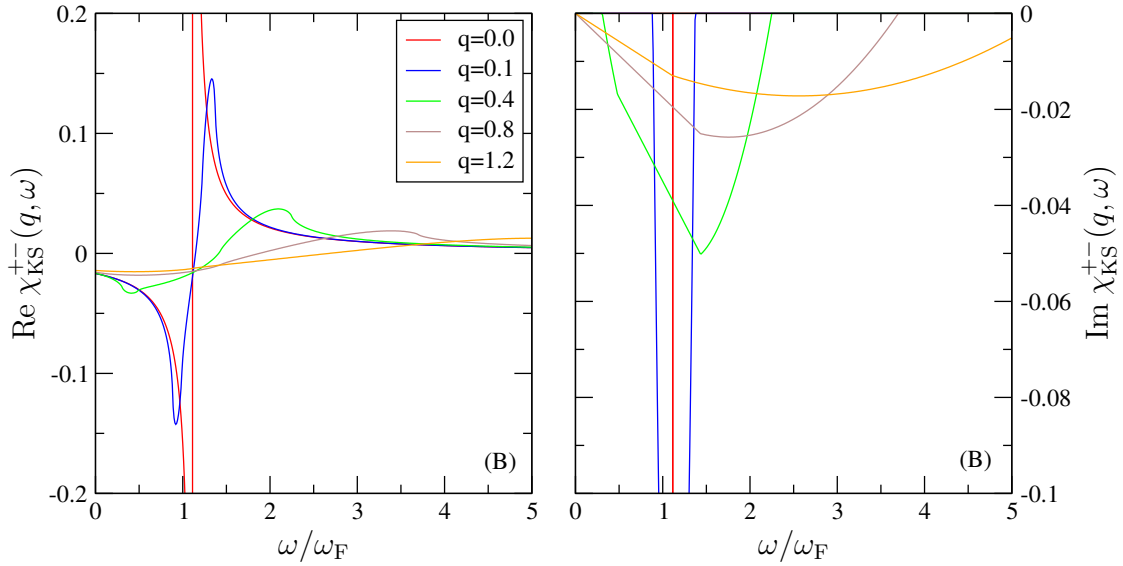


Figure 4.3: The real and imaginary part of the Kohn-Sham susceptibility χ_{KS}^{+-} displayed as a function of energy ω for different q vectors and $n = n_1 = 1.47 \cdot 10^{-3}$, $\xi = 0.788$. (This setup is labeled (B) in the following.) q vectors are given in Fermi wave vectors $k_{\text{F}} = 0.3518 \frac{1}{a_{\text{B}}}$, ω in Fermi energies $\omega_{\text{F}} = 0.06188 \text{Htr}$.

with the abbreviation

$$u_{\sigma} = \frac{2\Delta - \omega + \frac{1}{2}\sigma q^2}{q}. \quad (4.29)$$

Samples of these functions are plotted in figure 4.3. For small q vectors the imaginary part has a narrow high peak which lowers and broadens for increasing q . The peak is a superposition of two parabolas with different axis offsets and opposite sign, as is obvious from (4.28). The θ functions limit the contributions to the negative sections. The real part has a characteristic peak structure due to very small or very large arguments of the logarithm. The peak quickly decreases and changes its shape for increasing q vector.

Since we are mainly interested in the imaginary part it is plotted in a color-contour plot in figure 4.4. In order to better understand this function it is shown for four different (n, ξ) setups labeled (A) to (D), which are also denoted by orange circles in figure 4.1. Plot (A) on the top left shows the paramagnetic case while plot (B) has intermediate polarization and plots (C) and (D) show a fully polarized system. According to the previous discussion, cases (A) and (C) correspond to states of minimal total energy with respect to the spin polarization ξ , i.e., physical spin polarizations. In plot (C) it is $\Delta > \Delta_{\text{lim}}$, c.f. (4.23), leading to a spectrum contour of the imaginary part that is shifted that much to larger energies that it does not cross the q axis. For reasons of better illustration, the following plots will use the (n, ξ) settings (B) and (D). In the white areas of the plots the imaginary part of the susceptibility is zero, while it has non-zero values in the colored region and in particular large values in the yellow regions. It has diverging values for $(q \rightarrow 0, \omega = 2\Delta)$.

The contour of the spectrum (i.e., the area of the Stoner excitations) has a typical form that is sketched in figure 4.5. Three characteristic cases are highlighted with their transition in k -space (right-hand side) and their place of contribution to the spectrum (left-hand side). The

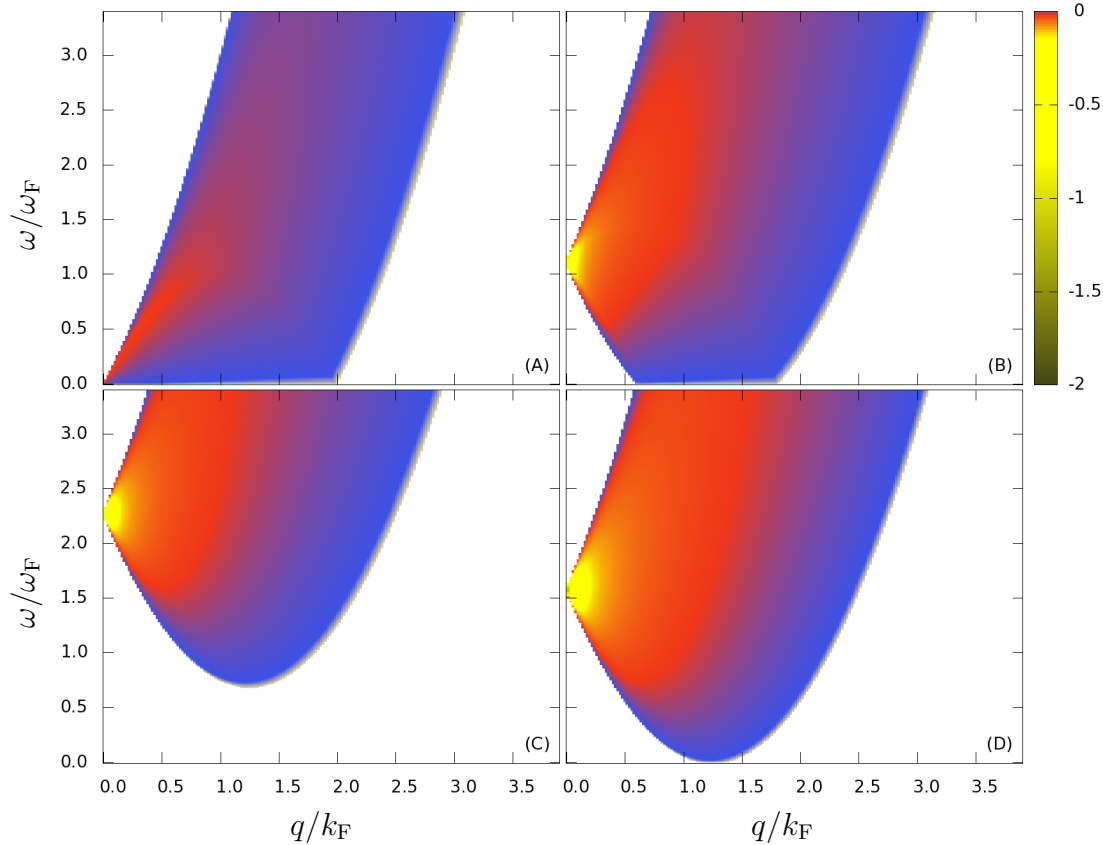


Figure 4.4: The spectrum $\text{Im } \chi_{\text{KS}}^{+-}(q, \omega)$ for four different value pairs (n, ξ) labeled (A) to (D): $(n_1, 0.0)$, $(n_1, 0.788)$, $(n_1, 1.0)$ and $(n_2, 1.0)$. These values correspond to the four orange circles in figure 4.1. The parameters q and ω are rescaled with the corresponding Fermi values.

red and the blue markers, respectively, correspond to transitions from majority to minority states without energy transfer ($\omega = 0$), thus transitions from one Fermi surface to the other, which by definition have the same energy. These transitions require a momentum $k_{\text{F}\uparrow} - k_{\text{F}\downarrow} \leq q \leq k_{\text{F}\uparrow} + k_{\text{F}\downarrow}$. The green markers represent transitions without momentum transfer ($q = 0$), which can occur anywhere in k -space where majority is occupied and minority is unoccupied. In all these places there is the same energy difference $\epsilon_{\uparrow}(\mathbf{q}) - \epsilon_{\downarrow}(\mathbf{q}) = 2\Delta$. This is stressed by the set of green markers in the right sketch in figure 4.5. Since the valid region in k -space is not only a surface but a volume this leads to the aforementioned pole at $(q \rightarrow 0, \omega = 2\Delta)$.

As can be easily shown by performing the integration on formulas (4.27), (4.28), the susceptibility obeys the sum rule

$$\int_{-\infty}^{\infty} \chi_{\text{KS}}^{+-}(q, \omega) d\omega = -2\pi i n \xi. \quad (4.30)$$

for any fixed value q , c.f. (3.39). Also the right-hand side is understood as a complex quantity, thus the integral over the real part equals zero.

Limits For the investigation of spin waves in section 4.4 it is necessary to evaluate the limit of small q vectors. In particular, the logarithm from the real part of the susceptibility

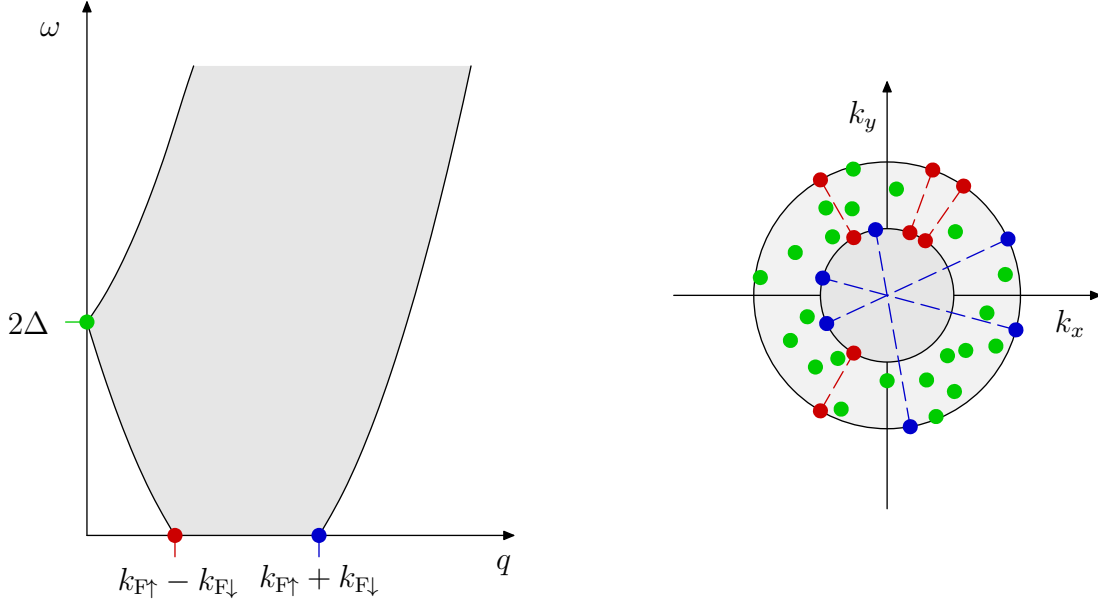


Figure 4.5: On the left-hand side a spectrum $\text{Im } \chi_{\text{KS}}^{+-}(q, \omega)$ is sketched, with the gray area indicating values unequal zero. Three limiting cases are highlighted by colored markers, the corresponding transitions are pictured in the two-dimensional reciprocal space on the right.

evaluates to

$$\ln \left| \frac{u_\sigma + k_{F\sigma}}{u_\sigma - k_{F\sigma}} \right| = \frac{2k_{F\sigma}}{2\Delta - \omega} q + \left[\frac{\frac{8}{3}k_{F\sigma}^3}{(2\Delta - \omega)^3} - \frac{2\sigma k_{F\sigma}}{(2\Delta - \omega)^2} \right] q^3 + \mathcal{O}(q^4). \quad (4.31)$$

It is important to also take the order $\mathcal{O}(q^3)$ into account. The real part simplifies to

$$\text{Re } \chi_{\text{KS}}^{+-}(q, \omega) = -\frac{1}{4\pi^2} \left\{ \frac{\frac{2}{3}(k_{F\uparrow}^3 - k_{F\downarrow}^3)}{2\Delta - \omega} + \left(\frac{\frac{1}{4}(k_{F\uparrow} - k_{F\downarrow})}{2\Delta - \omega} - \frac{\frac{5}{3}(k_{F\uparrow}^3 + k_{F\downarrow}^3)}{(2\Delta - \omega)^2} + \frac{\frac{4}{3}(k_{F\uparrow}^5 - k_{F\downarrow}^5)}{(2\Delta - \omega)^3} \right) q^2 \right\}. \quad (4.32)$$

At the (q, ω) origin the real part takes the value

$$\text{Re } \chi_{\text{KS}}^{+-}(0, 0) = -\frac{1}{4\pi^2} \frac{k_{F\uparrow}^3 - k_{F\downarrow}^3}{3\Delta}. \quad (4.33)$$

In the limit $q \rightarrow 0$ the non-zero values of the imaginary part narrow to the frequency $\omega = 2\Delta$:

$$\lim_{q \rightarrow 0} \text{Im } \chi_{\text{KS}}^{+-}(q, \omega) = \begin{cases} 0 & \omega \neq 2\Delta \\ \infty & \omega = 2\Delta \end{cases} \quad (4.34)$$

with the asymptotic proportionality

$$\text{Im } \chi_{\text{KS}}^{+-}(q, 2\Delta) \approx -\frac{k_{F\uparrow}^2 - k_{F\downarrow}^2}{8\pi q} \quad \text{for small } q, \quad (4.35)$$

compare figure 4.4.

4.3 The Exchange-Correlation Kernel in ALDA

In order to employ the ALDA formalism the exchange-correlation kernel which has been defined in section 3.3 needs to be evaluated for the homogeneous electron gas.

Exchange-Correlation Quantities in General In order to make a general point of the exchange-correlation kernel we reconsider the shape of the exchange-correlation energy in LDA for general densities. For a homogeneous system the value of the exact functional is identical to the value of the LDA functional:

$$E_{xc}^{\text{hom}} = E_{xc}^{\text{LDA}}. \quad (4.36)$$

However, the general functional dependence on the density n or even on infinitesimal deviations from homogeneity is unknown. The exchange-correlation potential and magnetic field read

$$V_{xc}(\mathbf{r}) = \frac{\delta E_{xc}}{\delta n(\mathbf{r})}, \quad \mathbf{B}_{xc}(\mathbf{r}) = -\frac{\delta E_{xc}}{\delta \mathbf{m}(\mathbf{r})}. \quad (4.37)$$

For a homogeneous system both derivatives become constants value due to the homogeneity:

$$V_{xc}^{\text{hom}}(\mathbf{r}) = V_{xc}^{\text{LDA}}, \quad \mathbf{B}_{xc}^{\text{hom}}(\mathbf{r}) = B_{xc}^{\text{LDA}} \mathbf{e}_z. \quad (4.38)$$

The exact values (i.e., the derivatives of the exact functional E_{xc} for the case of homogeneous density) on the left-hand side of the equations are identical to the LDA values on the right-hand side.

However, this identity of the LDA quantities to the quantities of the homogeneous electron gas holds only for the exchange-correlation energy, potential and magnetic field, but not for the kernel. The dielectric and magnetic exchange-correlation kernels in general read

$$f_{xc}(\mathbf{r}, t, \mathbf{r}', t') = \frac{\delta E_{xc}}{\delta n(\mathbf{r}, t) \delta n(\mathbf{r}', t')}, \quad f_{xc}^{ij}(\mathbf{r}, t, \mathbf{r}', t') = \frac{\delta E_{xc}}{\delta m^i(\mathbf{r}, t) \delta m^j(\mathbf{r}', t')}. \quad (4.39)$$

For a homogeneous system these quantities become homogeneous in time and space,

$$f_{xc}^{\text{hom}}(\mathbf{r}, t, \mathbf{r}', t') = f_{xc}^{\text{hom}}(\mathbf{r} - \mathbf{r}', t - t'), \quad (4.40)$$

$$f_{xc}^{ij, \text{hom}}(\mathbf{r}, t, \mathbf{r}', t') = f_{xc}^{ij, \text{hom}}(\mathbf{r} - \mathbf{r}', t - t'), \quad (4.41)$$

which is further approximated in the ALDA to be local in time and space:

$$f_{xc}^{\text{ALDA}}(\mathbf{r}, t, \mathbf{r}', t') = f_{xc}^{\text{ALDA}} \delta(\mathbf{r} - \mathbf{r}') \delta(t - t'), \quad (4.42)$$

$$f_{xc}^{ij, \text{ALDA}}(\mathbf{r}, t, \mathbf{r}', t') = f_{xc}^{ij, \text{ALDA}} \delta(\mathbf{r} - \mathbf{r}') \delta(t - t'). \quad (4.43)$$

The Fourier transforms read $f_{xc}^{\text{hom}}(\mathbf{q}, \omega)$, $f_{xc}^{+-, \text{hom}}(\mathbf{q}, \omega)$, which are constant in ALDA. This summary was to elucidate the fact that the general kernel of a homogeneous system indeed has a (\mathbf{q}, ω) -dependence, which might not be obvious from the beginning. On the other hand this is same for the kernel $f_{xc} \sim \delta^2 E_{xc} / (\delta m \delta m)$ as it is for the susceptibility $\chi \sim -\delta^2 E / (\delta B \delta B)$ for which the (q, ω) -dependence is intuitive.

As shown in the next paragraph, the kernel becomes constant (i.e., depending only on n and ξ , not on \mathbf{q} and ω) if evaluated within ALDA. For the dielectric kernel there exists a relation (called *compressibility sum rule* [DPT02]) identifying the ALDA kernel as the proper limit of the exact kernel for the homogeneous electron gas f_{xc}^{hom} for vanishing q vector and energy ω :

$$\lim_{q \rightarrow 0} f_{xc}^{\text{hom}}(q, 0) = f_{xc}^{\text{ALDA}}. \quad (4.44)$$

According to (3.62) the spin-flip kernel is constructed as $f_{xc}^{+-} = 2f_{xc}^{xx}$. Based on our derivations on page 63 for the check of the Goldstone theorem we can assume an equivalent statement as for the magnetic kernel:

$$\lim_{q \rightarrow 0} f_{xc}^{+-, \text{hom}}(q, \omega_{\text{sw}}(q)) = f_{xc}^{+-, \text{ALDA}} \quad (4.45)$$

with the spin-wave energy $\omega_{\text{sw}}(q)$.

Exchange-Correlation Quantities in ALDA The exchange-correlation energy for a homogeneous electron gas of density n and magnetization m (i.e., spin polarization ξ) in LDA reads

$$E_{xc}[n, m] = \int n(\mathbf{r}) \epsilon_{xc}(n, \xi) d^3r = V n \epsilon_{xc}(n, \xi) \quad (4.46)$$

with $\epsilon_{xc} = \epsilon_x + \epsilon_c$, and its derivatives

$$V_{xc}(n, m) = \frac{1}{V} \frac{\partial E_x}{\partial n} = \epsilon_{xc}(n, \xi) + n \frac{\partial \epsilon_{xc}}{\partial n}, \quad (4.47)$$

$$B_{xc}(n, m) = -\frac{1}{V} \frac{\partial E_x}{\partial m} = -n \frac{\partial \epsilon_{xc}}{\partial m} = \frac{2}{\mu_B g} \frac{\partial \epsilon_{xc}}{\partial \xi} \quad (4.48)$$

with $m = -\frac{1}{2} \mu_B g n \xi$, c.f. (4.8), (4.9). The scalar dielectric exchange kernel and the magnetic exchange kernel tensor evaluate as

$$f_{xc}(n, m) = \frac{1}{V^2} \frac{\partial^2 E_x}{\partial n^2} = \frac{2}{V} \frac{\partial \epsilon_{xc}}{\partial n} + \frac{n}{V} \frac{\partial^2 \epsilon_{xc}}{\partial n^2}, \quad (4.49)$$

$$f_{xc}^{ij}(n, m) = \frac{1}{V^2} \frac{\partial^2 E_x}{\partial m_i \partial m_j} = \frac{n}{V} \frac{\partial^2 \epsilon_{xc}}{\partial m^i \partial m^j}. \quad (4.50)$$

In this whole chapter m is considered negative, thus it relates to the absolute value like

$$m = -|\mathbf{m}| = -\sqrt{m_x^2 + m_y^2 + m_z^2}, \quad \frac{dm}{dm_i} = \frac{m_i}{m}. \quad (4.51)$$

Calculating for general magnetizations \mathbf{m} and applying an appropriate chain rule leads to

$$f_{xc}^{ij}(n, m) = \frac{n}{V} \left(\frac{\partial^2 \epsilon_{xc}}{\partial m^2} \frac{m_i m_j}{m^2} + \frac{\partial \epsilon_{xc}}{\partial m} \frac{\delta_{ij}}{m} - \frac{\partial \epsilon_{xc}}{\partial m} \frac{m_i m_j}{m^3} \right). \quad (4.52)$$

Evaluating for $\mathbf{m} = (0, 0, m)$ leads to

$$f_{xc}^{+-}(n, m) = \frac{2n}{mV} \frac{\partial \epsilon_{xc}}{\partial m} = -\frac{2}{V} \frac{B_{xc}}{m}, \quad f_{xc}^{+-}(n, \xi) = \frac{8}{(\mu_B g)^2 n \xi} \frac{\partial \epsilon_{xc}}{\partial \xi}. \quad (4.53)$$

Illustration of the Kernel In order to get an idea of the role of the magnetic exchange-correlation kernel one might imagine a homogeneous electron gas whose magnetization $\mathbf{m} \neq \mathbf{0}$ is modified by an infinitesimally small arbitrary vector $\delta\mathbf{m}$. Then, the exchange-correlation energy of the modified magnetization $\mathbf{m} + \delta\mathbf{m}$ is

$$E_{\text{xc}}(n, \mathbf{m} + \delta\mathbf{m}) = E_{\text{xc}}(n, \mathbf{m}) - \sum_i B_{\text{xc}}^i(n, \mathbf{m})\delta m_i + \frac{1}{2} \sum_{i,j} \delta m_i f_{\text{xc}}^{ij}(n, \mathbf{m})\delta m_j + \mathcal{O}((\delta\mathbf{m})^3). \quad (4.54)$$

If we assume the magnetization density along the z axis, $\mathbf{m} = (0, 0, m_0)$, the derivatives simplify to

$$\mathbf{B}_{\text{xc}} = \begin{pmatrix} 0 \\ 0 \\ B_{\text{xc}}^z(n, m) \end{pmatrix}, \quad (4.55)$$

$$f_{\text{xc}} = \begin{pmatrix} \frac{1}{2}f_{\text{xc}}^{+-} & 0 & 0 \\ 0 & \frac{1}{2}f_{\text{xc}}^{+-} & 0 \\ 0 & 0 & f_{\text{xc}}^{zz} \end{pmatrix}. \quad (4.56)$$

Neglecting terms of third and higher order, the energy reads

$$E_{\text{xc}}(n, \mathbf{m} + \delta\mathbf{m}) = E_{\text{xc}}(n, m) - B_{\text{xc}}(n, m)\delta m_z + f_{\text{xc}}^{zz}(n, m)\delta m_z^2 + \frac{1}{2}f_{\text{xc}}^{+-}(n, m)(\delta m_x^2 + \delta m_y^2). \quad (4.57)$$

The variations of E_{xc} can be separated into longitudinal components \parallel along the magnetization axis and transversal components \perp perpendicular to the given magnetization:

$$E_{\text{xc}}(n, \mathbf{m} + \delta\mathbf{m}) - E_{\text{xc}}(n, m) = -B_{\text{xc}}(n, m)\delta m_{\parallel} + \frac{1}{2}f_{\text{xc}}^{+-}(n, m)\delta m_{\perp}^2. \quad (4.58)$$

The term $\sim \delta m_z^2 (= \delta m_{\parallel}^2)$ has been neglected since there is already a lower-order term $\sim \delta m_{\parallel}$ in the equation. The longitudinal contribution, a first-order term in δm , describes the change of energy if the magnetization is increased or decreased along the given magnetization direction, while the transversal contribution, which is of second order, describes the energy change for a tilt of the magnetization.

If the magnetization goes to zero ($m \rightarrow 0$), the longitudinal term vanishes due to $B_{\text{xc}} \rightarrow 0$. Although $f_{\text{xc}}^{+-} \sim m^{-1}$, c.f. (4.53), the total transversal contribution to E_{xc} remains infinitesimally small due to the factor $(\delta m_{\perp})^2$, in total it is $\sim \delta m$. For zero magnetization there is no distinguished axis and the exchange-correlation energy changes isotropic with respect to an infinitesimal magnetization $\delta\mathbf{m}$. Consequently there is no distinction of its derivatives into longitudinal and transversal contributions.

Evaluation of the Exchange Contribution The exchange-energy density ϵ_x (or exchange energy per particle) is known analytically and already given in (2.41):

$$\epsilon_x(n, \xi) = \epsilon_x(n, 0) + [\epsilon_x(n, 1) - \epsilon_x(n, 0)] f(\xi) \quad (4.59)$$

$$\epsilon_x(n, 0) = -C_x n^{\frac{1}{3}}, \quad \epsilon_x(n, 1) = -2^{\frac{1}{3}} C_x n^{\frac{1}{3}}, \quad C_x = \frac{3}{4} \left(\frac{3}{\pi} \right)^{\frac{1}{3}}. \quad (4.60)$$

The spin polarization factor $f(\xi)$ and limit for small ξ read

$$f(\xi) = \frac{(1+\xi)^{\frac{4}{3}} + (1-\xi)^{\frac{4}{3}} - 2}{2^{\frac{4}{3}} - 2} = \frac{2}{9} \frac{\xi^2}{2^{\frac{1}{3}} - 1} + \frac{5}{243} \frac{\xi^4}{2^{\frac{1}{3}} - 1} + \mathcal{O}(\xi^6) \quad (4.61)$$

$$\frac{\partial f}{\partial \xi} = \frac{4}{3} \frac{(1+\xi)^{\frac{1}{3}} - (1-\xi)^{\frac{1}{3}}}{2^{\frac{4}{3}} - 2} = \frac{4}{9} \frac{\xi}{2^{\frac{1}{3}} - 1} + \frac{20}{243} \frac{\xi^3}{2^{\frac{1}{3}} - 1} + \mathcal{O}(\xi^5). \quad (4.62)$$

For small spin polarization the factor $f(\xi)$ is well approximated already by the lowest-order term $f(\xi) \approx 0.855\xi^2$. The exchange potential and magnetic field read

$$V_x = -\frac{4}{3} C_x n^{\frac{1}{3}} \left[1 + \left(2^{\frac{1}{3}} - 1 \right) f(\xi) \right] \quad (4.63)$$

$$B_x = -\frac{2C_x}{\mu_B g} n^{\frac{1}{3}} \left(2^{\frac{1}{3}} - 1 \right) \frac{df}{d\xi}. \quad (4.64)$$

The magnetic and the dielectric exchange kernel read

$$f_x^{+-}(n, \xi) = \frac{8}{\xi} C_x n^{-\frac{2}{3}} \left(2^{\frac{1}{3}} - 1 \right) \frac{\partial f}{\partial \xi} \quad (4.65)$$

$$f_x(n, \xi) = -\frac{4}{9} C_x n^{-\frac{2}{3}} \left(1 + \left(2^{\frac{1}{3}} - 1 \right) f(\xi) \right). \quad (4.66)$$

Both kernels are very similar in a small- ξ expansion:

$$f_x^{+-}(n, \xi) = -\frac{32}{9} C_x n^{-\frac{2}{3}} \left(1 + \frac{5}{27} \xi^2 + \mathcal{O}(\xi^4) \right) \quad (4.67)$$

$$f_x(n, \xi) = -\frac{4}{9} C_x n^{-\frac{2}{3}} \left(1 + \frac{2}{9} \xi^2 + \mathcal{O}(\xi^4) \right). \quad (4.68)$$

4.4 Spin Waves from ALDA

Now we would like to apply the adiabatic LDA as introduced in section 3.3 in order to obtain the full spin-flip response χ^{+-} starting from the Kohn-Sham susceptibility χ_{KS}^{+-} .

The Dyson Equation The starting point is the Dyson equation (3.64) which in the case of the homogeneous electron gas can be evaluated as

$$\chi^{+-}(q, \omega) = \chi_{\text{KS}}^{+-}(q, \omega) + \left(\frac{\mu_B g}{2} \right)^2 \chi_{\text{KS}}^{+-}(q, \omega) f_{\text{xc}}^{+-}(q, \omega) \chi^{+-}(q, \omega) \quad (4.69)$$

$$= \frac{\chi_{\text{KS}}^{+-}(q, \omega)}{1 - \left(\frac{\mu_B g}{2} \right)^2 f_{\text{xc}}^{+-}(q, \omega) \chi_{\text{KS}}^{+-}(q, \omega)} \quad (4.70)$$

with all quantities in this equation being scalar functions. In ALDA the kernel becomes a constant, $f_{\text{xc}}^{+-}(q, \omega) = f_{\text{xc}}^{+-}$. The imaginary part of the full (or *renormalized*) susceptibility then reads

$$\text{Im } \chi^{+-}(q, \omega) = \frac{\text{Im } \chi_{\text{KS}}^{+-}(q, \omega)}{\left[1 - \left(\frac{\mu_B g}{2} \right)^2 f_{\text{xc}}^{+-} \text{Re } \chi_{\text{KS}}^{+-}(q, \omega) \right]^2 + \left[\left(\frac{\mu_B g}{2} \right)^2 f_{\text{xc}}^{+-} \text{Im } \chi_{\text{KS}}^{+-}(q, \omega) \right]^2}. \quad (4.71)$$

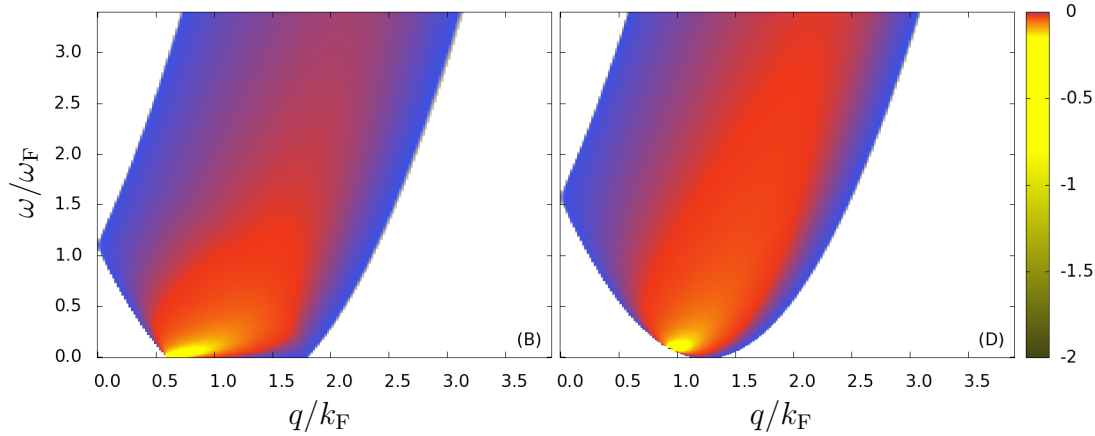


Figure 4.6: The spectrum $\text{Im } \chi^{+-}(q, \omega)$ of the full (renormalized) susceptibility for the (n, ξ) values of cases (B) and (D) from figure 4.4. The spin waves are not included yet.

Due to its denominator it appears to have the same pole structure as $\text{Im } \chi_{\text{KS}}^{+-}(q, \omega)$, i.e., the two quantities are zero at exactly the same (q, ω) values. The distribution of small and large values, however, are different as can be seen from the example plot in figure 4.6. While the Kohn-Sham response χ_{KS}^{+-} has its large values close to the (q, ω) value $(0, 2\Delta)$, c.f. figure 4.4, the renormalized susceptibility has large values close to the q axis (see yellow region in figure 4.6).

A more detailed inspection of (4.71), however, reveals that the imaginary part can take non-zero values also for the particular case (*spin-wave condition*)

$$1 - \left(\frac{\mu_B g}{2}\right)^2 f_{\text{xc}}^{+-} \text{Re } \chi_{\text{KS}}^{+-}(q, \omega_{\text{sw}}(q)) = 0 \quad \text{if} \quad \text{Im } \chi_{\text{KS}}^{+-}(q, \omega_{\text{sw}}(q)) = 0. \quad (4.72)$$

Solving this equation yields the spin-wave dispersion $\omega_{\text{sw}}(q)$.

The Goldstone Theorem In non-magnetic materials the non-existent magnetization is isotropic in all directions. In magnetic materials, on the other hand, this rotational symmetry with respect to the magnetization is broken. In the common collinear case, for instance, the magnetization commonly points into one designated direction.

The Goldstone theorem (in its non-relativistic incarnation) states that when a global symmetry of the system under consideration is broken spontaneously, there corresponds a quasi-particle in the excitation spectrum with no energy gap.

Applied to our setting this means that in the case of a magnetic material (in which the rotational symmetry of magnetization is broken) possible magnetic excitations are quantized in quasi-particles (namely magnons) which have zero energy for vanishing wave vector: $\omega_{\text{sw}}(0) = 0$. In other words, the spin-wave branch starts in the origin.

Obtaining the Spin-Wave Dispersion According to the discussion above the spin-wave dispersion $\omega_{\text{sw}}(q)$ is an additional branch to the spectrum not present in the Kohn-Sham response. It starts at the origin and, as it turns out, has infinitely small line width (in the case of the homogeneous electron gas) until it enters the region of Stoner excitations. Combining

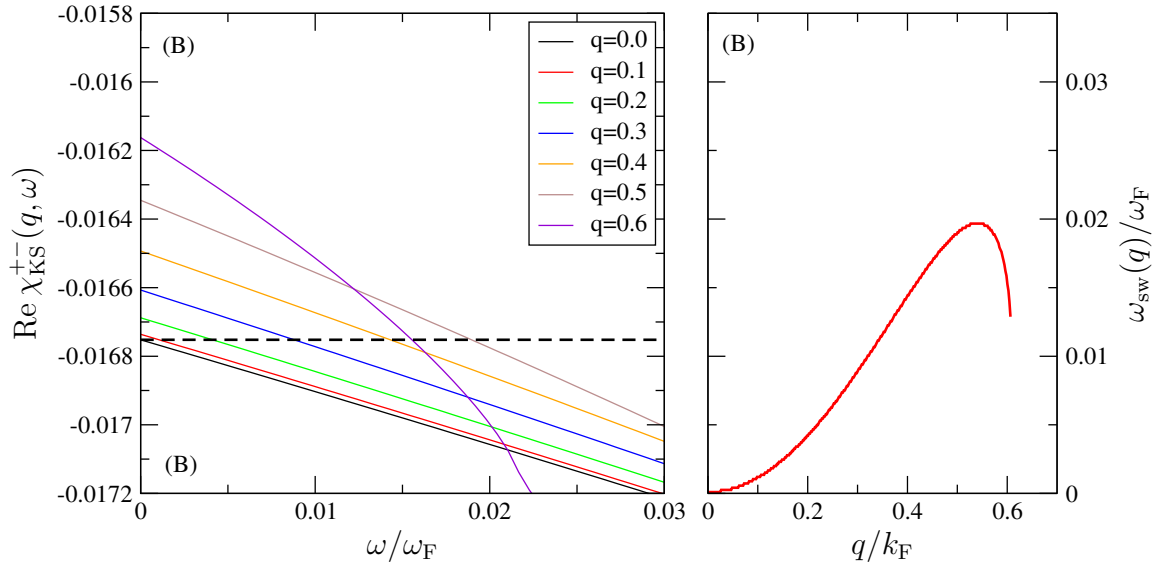


Figure 4.7: Left-hand side: the real part of the susceptibility χ_{KS}^{+-} for different q vectors for setting (B) of figure 4.4, i.e., $n = 0.00147$, $\xi = 0.788$. This is a small clipping of the left plot in figure 4.3. The thick dashed black line indicates the value $\chi_{\text{KS}}^{+-}(0, 0)$. Crossings of curves for different q with this line determine the spin-wave dispersion $\omega_{\text{sw}}(q)$ which is shown on the right-hand side as a red curve.

the Goldstone theorem with (4.72), the spin-wave condition can be written as

$$\chi_{\text{KS}}^{+-}(q, \omega_{\text{sw}}(q)) = \chi_{\text{KS}}^{+-}(0, 0). \quad (4.73)$$

This equation is solved for a given q by interval nesting. It is equivalent to solving the Dyson equation for spin waves with the boundary condition of a gap-less dispersion. Therefore the kernel is in fact not needed in this step due to this boundary condition; however, it is used below in the check of the Goldstone theorem. The choice of exchange and correlation is already embedded in the Kohn-Sham response through the energy splitting of the two spin channels which is determined by B_{xc} . The plots that are shown here are calculated with exchange only.

In order to understand how this condition is fulfilled the real part of the non-interacting susceptibility is plotted in figure 4.7. The first part of the spin-wave condition (4.72) corresponds to the cut of the curve of the corresponding q vector with the thick dash-dotted line which has the value $\chi_{\text{KS}}^{+-}(0, 0)$. Solving for this leads to the spin-wave dispersion curve which is plotted in red on the right-hand side. The curves stop where the spin-wave dispersion enters the region of Stoner excitations.

The blue curve in the right plot in figure 4.7 shows the spin-wave dispersion for setup (D) with full spin-polarization $\xi = 1.0$. Apparently the spin waves have smaller gradients (or *spin stiffness*) for lower spin polarizations, and enter the Stoner region for smaller q values. Furthermore, the energy scale of the spin excitations is so small that it would be barely visible in figure 4.6. The spin-wave region of these plots is shown on an enlarged scale for the same two (n, ξ) value pairs in figure 4.8. The spin waves enter the Stoner regime at the $(q, \omega_{\text{sw}}(q))$ point where this has its largest (diverging) value.

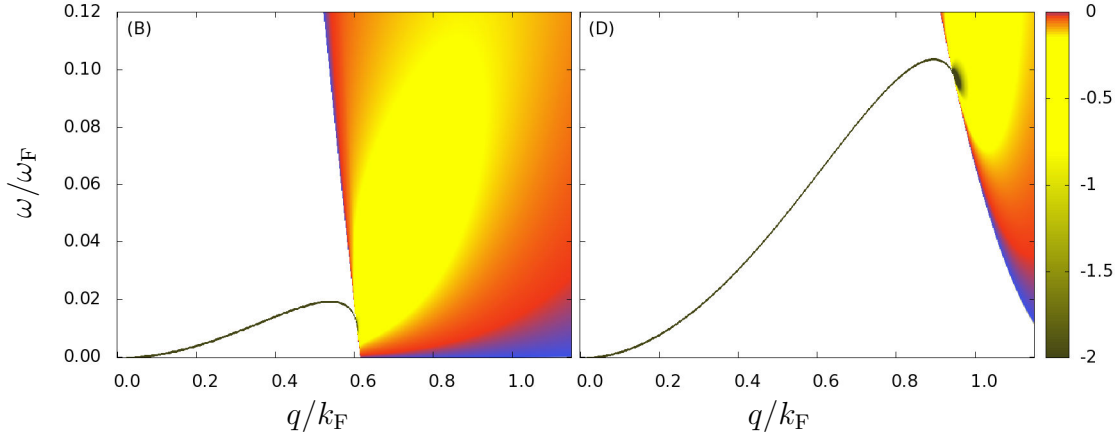


Figure 4.8: The spectrum $\text{Im } \chi^{+-}(q, \omega)$ of the ALDA-renormalized susceptibility including the spin-wave excitations. This is a magnification of figure 4.6.

Sensitivity of the Procedure Another important feature of the spin-wave dispersion becomes apparent when the spin-wave energy is determined by searching for the cut of graphs on the left-hand side in figure 4.7. This procedure is very sensitive to the proper values of the exchange-correlation kernel f_{xc}^{+-} (and hence the susceptibility χ_{KS}^{+-}). While this is not a problem in the case of the homogeneous electron gas, for which we know the analytical formulas, it might result in problems in the case of real materials. In order to simulate the effect one might solve the Dyson equation (4.69) with the kernel multiplied by a scalar factor x close to one which should account for inaccuracies:

$$\chi^{+-}(q, \omega) = \chi_{\text{KS}}^{+-}(q, \omega) + \left(\frac{\mu_{\text{B}}g}{2}\right)^2 \chi_{\text{KS}}^{+-}(q, \omega) x f_{\text{xc}}^{+-}(q, \omega) \chi^{+-}(q, \omega).$$

In figure 4.9 two spin-wave dispersions are shown: setup (B) on the left-hand side which was already presented in figure 4.7, and setup (D) on the right-hand side. In both cases different scalar factors $x \in [0.98, \dots, 1.02]$ have been used in the solution of the Dyson equation, and the corresponding curves are presented. Already for deviations as small as one percent the dispersion changes considerably, either by having a spin-wave dispersion that starts at positive energies ($x < 1$), or by starting not for $q = 0$ but at finite values of q ($x > 1$).

Check of the Goldstone Theorem for this Special Case As explained above, the Goldstone theorem demands the spin-wave dispersion to start at the origin, $\omega_{\text{sw}}(0) = 0$. In the case of the homogeneous electron gas this can be demonstrated by evaluating the kernel and the susceptibility, which is a convenient check for the spin-wave condition and our derivations so far. Evaluating the ALDA spin-wave condition (4.72) for $(q, \omega) = (0, \omega_{\text{sw}}(0))$ reads

$$1 - \left(\frac{\mu_{\text{B}}g}{2}\right)^2 f_{\text{xc}}^{+-} \text{Re } \chi_{\text{KS}}^{+-}(0, \omega_{\text{sw}}(0)) = 0, \quad (4.74)$$

where general exchange and correlation is taken into account. Due to (4.32) it is

$$\text{Re } \chi_{\text{KS}}^{+-}(0, \omega_{\text{sw}}(0)) = -\frac{1}{4\pi^2} \frac{\frac{2}{3}(k_{\text{F}\uparrow}^3 - k_{\text{F}\downarrow}^3)}{2\Delta - \omega_{\text{sw}}(0)} \quad (4.75)$$

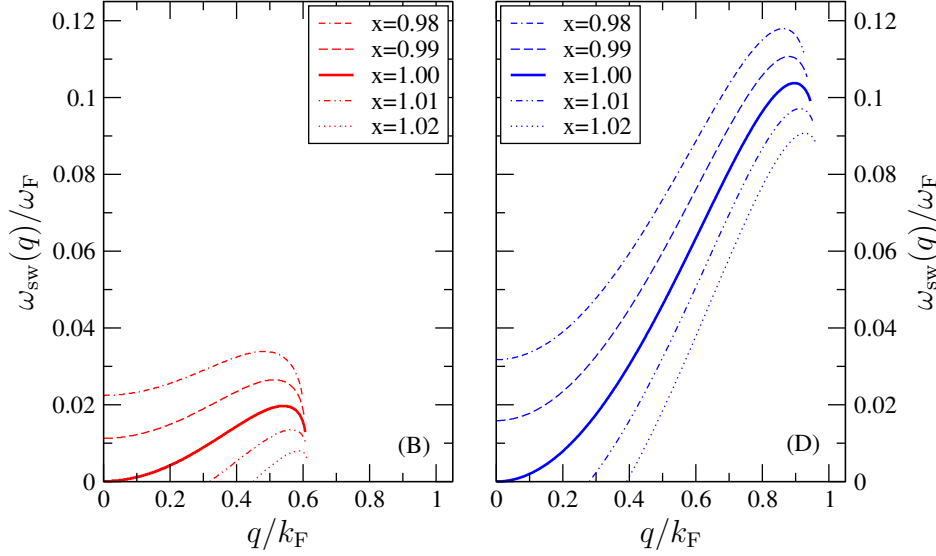


Figure 4.9: The spin-wave dispersion for setups (B) in red and (D) in blue (c.f. right-hand side of figure 4.7) with an arbitrarily introduced factor x close to one multiplied to the exchange-correlation kernel. This shows the sensitivity of the procedure (please confer to the corresponding paragraph in the text).

Furthermore, according to (4.53),

$$f_{\text{xc}}^{+-} = \frac{2B_{\text{xc}}}{m} \quad (4.76)$$

$$k_{\text{F}\uparrow}^3 - k_{\text{F}\downarrow}^3 = 6\pi^2(n_{\uparrow} - n_{\downarrow}) = 6\pi^2 \frac{m}{-\frac{1}{2}\mu_{\text{B}}g} \quad (4.77)$$

$$\Delta = -\frac{1}{2}\mu_{\text{B}}gB_{\text{eff}}, \quad (4.78)$$

altogether leading to

$$B_{\text{ext}} + \frac{1}{\mu_{\text{B}}g}\omega_{\text{sw}}(0) = 0. \quad (4.79)$$

This equation is solved by $\omega_{\text{sw}}(0) = -\mu_{\text{B}}gB_{\text{ext}}$. If no external field is applied, the spin-wave dispersion starts at the origin.

If there is an external field present, the result can be understood in the following way: The additional field B_{ext} is supposed to be negative, the energy of an electron of spin $+\frac{1}{2}$ in this field is supposed to be $-\mathbf{m} \cdot \mathbf{B}_{\text{ext}} = \frac{\mu_{\text{B}}g}{2}B_{\text{ext}}$. If such a spin-up electron is removed and a spin-down electron (spin $-\frac{1}{2}$) is added to the system, the total energy difference matches $-\mu_{\text{B}}gB_{\text{ext}} = \omega_{\text{sw}}(0)$. This means that the $S-1$ spin excitation (with S the total-spin quantum number of the system) described by χ^{+-} couples to the applied field B_{ext} and contributes an energy shift.

It should be stressed that the derivation in this paragraph is not restricted to exchange-only formulas. Equation (4.74) is solved by any f_{xc}^{+-} and χ_{KS}^{+-} which are consistently obtained from DFT, i.e., for any proper correlation contribution. This is not fulfilled if the (n, ξ) value pair is not a proper solution of DFT according to section 4.1.

From the derivations above, we conclude that the ALDA in fact yields the proper limit of the true exchange-correlation kernel for the homogeneous electron gas for $q \rightarrow 0$, c.f. (4.45).

Another common Treatment in Literature: RPA The way the spin waves in the homogeneous electron gas are treated in this chapter should briefly be contrasted to another method which is common in literature. It is labeled *RPA* and is presented for instance in a book by Moriya [Mor85]. In this method (which is also based on the one-particle picture, but is not related to density-functional theory) the homogeneous electron gas of density n is *set* to have a specific spin splitting Δ and consequently spin polarization ξ . From the corresponding one-electron states the spin-flip susceptibility of independent particles $\chi_{\text{KS}}^{+-}(q, \omega)$ is obtained.

In a second step a renormalization is applied to obtain from this quantity the full spin-flip susceptibility $\chi^{+-}(q, \omega)$. This specific renormalization step gives the RPA method its name. However, this does not refer to time-dependent Hartree theory such as in section 3.4, but refers to time-dependent Hartree-Fock theory. With some approximations this results in a Dyson equation

$$\chi^{+-}(q, \omega) = \frac{\chi_{\text{KS}}^{+-}(q, \omega)}{1 - I \cdot \chi_{\text{KS}}^{+-}(q, \omega)}$$

featuring the *exchange integral* I . The equation has the same shape as the Dyson equation (4.70) but with the exchange integral taking the place of the exchange-correlation kernel, $I = (\frac{\mu_B g}{2})^2 f_{\text{xc}}^{+-}$. This term I is considered as an adjustable parameter: It is chosen such that the resulting spin-wave dispersion starts in the origin, $\omega_{\text{sw}}(0) = 0$ so that the Goldstone theorem is fulfilled.

While the RPA method appears to be very similar to the ALDA, there are some crucial differences that should be highlighted.

- The exchange integral I is considered as an arbitrary parameter, while the corresponding term f_{xc}^{+-} from ALDA has no freedom of choice, but is fixed through the values of n and ξ .
- The spin polarization within the RPA method is fixed by *parameter* ξ which can be freely chosen. In contrast to this, in ALDA the spin polarization ξ results from the self-consistency cycle for the ground state. For the homogeneous electron gas, this yields the values $\xi = 1$ for $n < n_1$ and $\xi = 0$ for $n > n_1$, c.f. figure 4.1.
- In ALDA, a magnetic field needs to be applied in order to tune the spin polarization to a specific value (unequal to those spin polarizations of the ground state). In RPA, no magnetic field is necessary since any spin polarization can be set through parameter Δ .
- As a consequence, the Goldstone theorem is fulfilled in the RPA as soon as the suitable exchange integral I is *chosen*, independent of the spin polarization. In the ALDA framework, however, the Goldstone theorem *cannot* be fulfilled for spin polarizations that require an external magnetic field.

As a side note it should be mentioned that the formulas in the book of Moriya [Mor85] differ in a few ways from the notation in this chapter. Relation (B.53) has been utilized in that book to rescale momentum and frequency with their Fermi values, $q \rightarrow q/q_F$ and $\omega \rightarrow \omega/\omega_F$. The resulting formulas for the Kohn-Sham susceptibility show some subtle differences to (4.27) and (4.28).

4.5 The Correlation Contribution

In the calculations up to now only the analytically known exchange contribution has been taken into account. (However, some statements such as the shape of the spin-flip kernel or the check of the Goldstone theorem have been stated for the general exchange-correlation term.) In this section the missing treatment should be completed by introducing formulas for the correlation part.

The correlation contribution to the exchange-correlation energy in LDA is, in contrast to the exchange part, not known analytically. However, it has been determined numerically through quantum Monte-Carlo calculations by Ceperley and Alder [CA80]. For practical calculations one usually uses some parametrization of the exchange-correlation energy, which is essentially a fit function $\varepsilon_c(n, \xi)$ to obtain reasonably good values, augmented with analytically known asymptotic behavior [PW92].

ε_c in Perdew-Wang-92 One of the more recent of these parametrizations is the Perdew-Wang LDA energy per particle [PW92]

$$\varepsilon_c(n, \xi) = \varepsilon_c(n, 0) + \alpha_c(n) \frac{f(\xi)}{f''(0)} (1 - \xi^4) + [\varepsilon_c(n, 1) - \varepsilon_c(n, 0)] f(\xi) \xi^4, \quad (4.80)$$

where energy densities $\varepsilon_c(n, 1)$, $\varepsilon_c(n, 0)$ and the spin stiffness $\alpha_c(n)$ are themselves fit functions. The spin interpolation function f is already given in (4.61), the second derivative at the origin has the value $f''(0) = \frac{4}{9}(2^{\frac{1}{3}} - 1)^{-1} \approx 1.71$. An expansion for small ξ leads to the simpler expression

$$\varepsilon_c(n, \xi) = \varepsilon_c(n, 0) + \frac{1}{2} \alpha_c(n) \xi^2 + \mathcal{O}(\xi^4). \quad (4.81)$$

The functions $\alpha_c(n)$, $\varepsilon_c(n, 0)$, $\varepsilon_c(n, 1)$ are fit functions set equal to a parametrization function G

$$\left. \begin{array}{l} -\alpha_c(n) \\ \varepsilon_c(n, 0) \\ \varepsilon_c(n, 1) \end{array} \right\} = G(r_s, A, \alpha_1, \beta_1, \beta_2, \beta_3, \beta_4, p), \quad (4.82)$$

each for a different set of parameters:

	A	α_1	β_1	β_2	β_3	β_4
$-\alpha_c(n)$	0.016887	0.11125	10.357	3.6231	0.88026	0.49671
$\varepsilon_c(n, 0)$	0.031091	0.21370	7.5957	3.5876	1.6382	0.49294
$\varepsilon_c(n, 1)$	0.015545	0.20548	14.1189	6.1977	3.3662	0.62517

The last constant is chosen $p = 1$ for all three functions. The function G reads

$$G(r_s) = -2A(1 + \alpha_1 r_s) \ln \left[1 + \frac{1}{X(r_s)} \right] \quad (4.83)$$

$$X(r_s) = 2A(\beta_1 r_s^{\frac{1}{2}} + \beta_2 r_s + \beta_3 r_s^{\frac{3}{2}} + \beta_4 r_s^{p+1}). \quad (4.84)$$

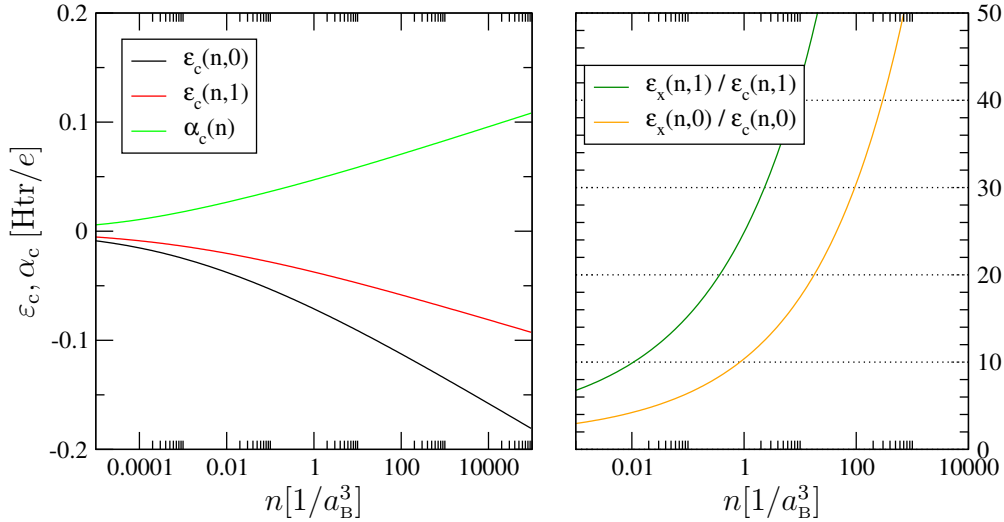


Figure 4.10: Left-hand side: The three crucial functions from the PW92 parametrization, shown on a logarithmic scale of densities. Right-hand side: The ratio of the exchange and the PW92 correlation contributions to the exchange-correlation energy.

Apart from the constants $A, \alpha_1, \beta_1, \beta_2, \beta_3, \beta_4, p$ it depends on the density radius r_s , which relates to the density n according to (4.14). The function G is constructed such that certain analytically known limiting cases of $\varepsilon_c(n, \xi)$ are reproduced. While this establishes a relation between some of these parameters, the remaining numerical values are determined by a fit to the quantum Monte-Carlo results of Ceperley and Alder, which leads to the constants in the table above.

Correlation Kernel For the correlation contribution of the magnetic kernel these functions do not need to be investigated in detail. According to (4.53) the kernel and its small- ξ limit read

$$f_c^{+-}(n, \xi) = \frac{8}{n\xi} \left[\frac{\alpha_c(n)}{f''(0)} \left(\frac{\partial f}{\partial \xi} (1 - \xi^4) - 4f(\xi)\xi^3 \right) + \left[\varepsilon_c(n, 1) - \varepsilon_c(n, 0) \right] \left(\frac{\partial f}{\partial \xi} \xi^4 + 4f(\xi)\xi^3 \right) \right] \quad (4.85)$$

$$= \frac{8}{n} \alpha_c(n) \left(1 + \frac{5}{27} \xi^2 + \mathcal{O}(\xi^4) \right). \quad (4.86)$$

Thus, for reasonably small ξ only the spin-stiffness $\alpha_c(n)$ has an influence, while the functions $\varepsilon_c(n, 0)$ and $\varepsilon_c(n, 1)$ do not contribute. The evaluation of the dielectric correlation kernel is more complicated because it involves derivatives of G . According to (4.49) we need the derivatives

$$\frac{\partial \varepsilon_c}{\partial n} = \frac{\partial \varepsilon_c(n, 0)}{\partial n} + \frac{\partial \alpha_c(n)}{\partial n} \frac{f(\xi)}{f''(0)} (1 - \xi^4) + \left[\frac{\partial \varepsilon_c(n, 1)}{\partial n} - \frac{\partial \varepsilon_c(n, 0)}{\partial n} \right] f(\xi) \xi^4 \quad (4.87)$$

$$\frac{\partial^2 \varepsilon_c}{\partial n^2} = \frac{\partial^2 \varepsilon_c(n, 0)}{\partial n^2} + \frac{\partial^2 \alpha_c(n)}{\partial n^2} \frac{f(\xi)}{f''(0)} (1 - \xi^4) + \left[\frac{\partial^2 \varepsilon_c(n, 1)}{\partial n^2} - \frac{\partial^2 \varepsilon_c(n, 0)}{\partial n^2} \right] f(\xi) \xi^4. \quad (4.88)$$

Due to (4.82) the single and double derivatives of $\varepsilon_c(n, 0)$, $\varepsilon_c(n, 1)$, $\alpha_c(n)$ with respect to the density involve the corresponding density derivatives of the function G ,

$$\frac{\partial G}{\partial n} = \frac{\partial G}{\partial r_s} \frac{\partial r_s}{\partial n}, \quad \frac{\partial^2 G}{\partial n^2} = \frac{\partial^2 G}{\partial r_s^2} \left(\frac{\partial r_s}{\partial n} \right)^2 + \frac{\partial G}{\partial r_s} \frac{\partial^2 r_s}{\partial n^2} \quad (4.89)$$

with the density radius derivatives

$$\frac{\partial r_s}{\partial n} = -\frac{1}{3} \left(\frac{3}{4\pi} \right)^{\frac{1}{3}} n^{-\frac{4}{3}}, \quad \frac{\partial^2 r_s}{\partial n^2} = \frac{4}{9} \left(\frac{3}{4\pi} \right)^{\frac{1}{3}} n^{-\frac{7}{3}}. \quad (4.90)$$

The derivatives of the function G with respect to the density radius

$$\frac{\partial G}{\partial r_s} = -2A\alpha_1 \ln \left[1 + \frac{1}{X} \right] + 2A(1 + \alpha_1 r_s) \frac{1}{X^2 + X} \frac{\partial X}{\partial r_s} \quad (4.91)$$

$$\frac{\partial^2 G}{\partial r_s^2} = \frac{4A\alpha_1}{X^2 + X} \frac{\partial X}{\partial r_s} + 2A(1 + \alpha_1 r_s) \left[\frac{1}{X^2 + X} \frac{\partial^2 X}{\partial r_s^2} - \frac{2X + 1}{(X^2 + X)^2} \left(\frac{\partial X}{\partial r_s} \right)^2 \right] \quad (4.92)$$

incorporate derivatives of X as well:

$$\frac{\partial X}{\partial r_s} = 2A \left(\frac{1}{2} \beta_1 r_s^{-\frac{1}{2}} + \beta_2 + \frac{3}{2} \beta_3 r_s^{\frac{1}{2}} + (p+1) \beta_4 r_s^p \right) \quad (4.93)$$

$$\frac{\partial^2 X}{\partial r_s^2} = 2A \left(-\frac{1}{4} \beta_1 r_s^{-\frac{3}{2}} + \frac{3}{4} \beta_3 r_s^{-\frac{1}{2}} + p(p+1) \beta_4 r_s^{p-1} \right). \quad (4.94)$$

Altogether, this makes up the correlation part of the dielectric kernel.

Comparison to the Exchange Contribution In order to get an impression of the influence of the correlation contribution and how it relates to the exchange part, the correlation energy per particle in PW92 parametrization $\epsilon_c(n, \xi)$ is plotted in figure 4.10. As expected, it is always negative, as is the exchange contribution. Comparing the black and the red curve on the left-hand side, it is apparent that the magnitude of ϵ_c for a given n becomes smaller for increasing spin polarization. This is opposite to the exchange contribution, which has a larger absolute value for increasing spin polarization. Therefore the ratio of the two contributions is plotted on the right-hand side of the same figure as a function of the density n , both for zero spin polarization as well as for full spin polarization. The exchange contribution dominates with increasing density.

In figure 4.11 the spin-flip exchange-correlation kernel f_{xc}^{+-} is shown in a similar fashion. On the left-hand side, both the exchange and the correlation contribution are plotted, while their ratio is shown on the right-hand side for zero and for full spin polarization. Different than for the exchange-correlation energy, now both contributions have a larger absolute value for larger spin polarization. However, the two contributions have opposite sign now. The ratio of the two contributions to the kernel is smaller than but similar in shape to the ratio of the energies in the previous figure.

While the correlation contribution to the exchange-correlation energy is significantly smaller than the exchange contribution, it is nevertheless important for a proper description of the system under consideration. The examination in section 4.1 shows that the

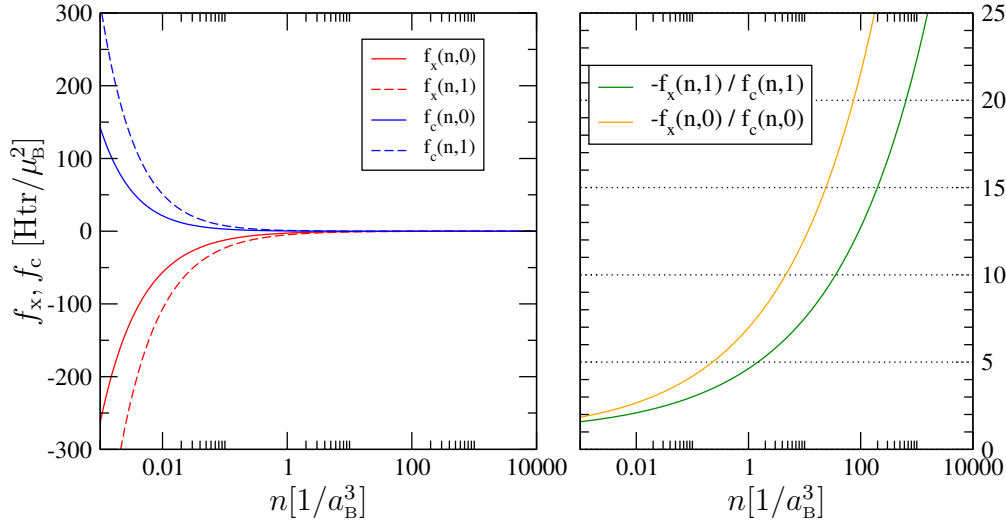


Figure 4.11: Left-hand side: The exchange and correlation contribution to the exchange-correlation spin-flip kernel are shown for zero and for full spin polarization. Right-hand side: The ratio of the exchange and the PW92 correlation contributions.

homogeneous electron gas becomes spin polarized only for low densities $r_s > 5.45a_B$ if only exchange is taken into account. If the correlation contribution is included as well this threshold value for r_s is shifted to much higher values, that is to lower densities. This is a substantial change of the system behavior. However, values such as $2a_B < r_s < 5a_B$ correspond closer to the electron densities of real systems, which is the reason (apart from analytical simplicity) that only the exchange part has been treated in most parts of this chapter. As has been pointed out in figure 4.9 also the ALDA spin-response calculation is very sensitive to small changes in the value of the exchange-correlation kernel.

These points indicate the importance of a full treatment of the exchange-correlation kernel. While the qualitative results from the previous sections obtained with exchange only (such as the check of the Goldstone theorem) remain true, the correlation part needs to be included for quantitative investigations. Hence in the calculations of chapter 6 the exchange-correlation kernel will be treated to the full extend within ALDA.

4.6 Differences and Conclusions for Real Materials

For non-homogeneous materials the Dyson equation does not simplify to an equation of scalars like (4.69). In the following chapter 5 the susceptibility is expanded in a Bloch basis, and the Dyson equation transforms to the same shape as (4.69) but with its constituents being matrices instead of scalars.

The dispersion of free electrons is strictly monotonous and isotropic, leading to a spherical Fermi surface. As a consequence the possible transitions between energy levels are limited and $\text{Im } \chi_{KS}^{+-}$ is non-zero only in a specific (q, ω) -range. Real materials, on the other hand, usually have multiple bands, much less symmetry and energy band dispersions of much

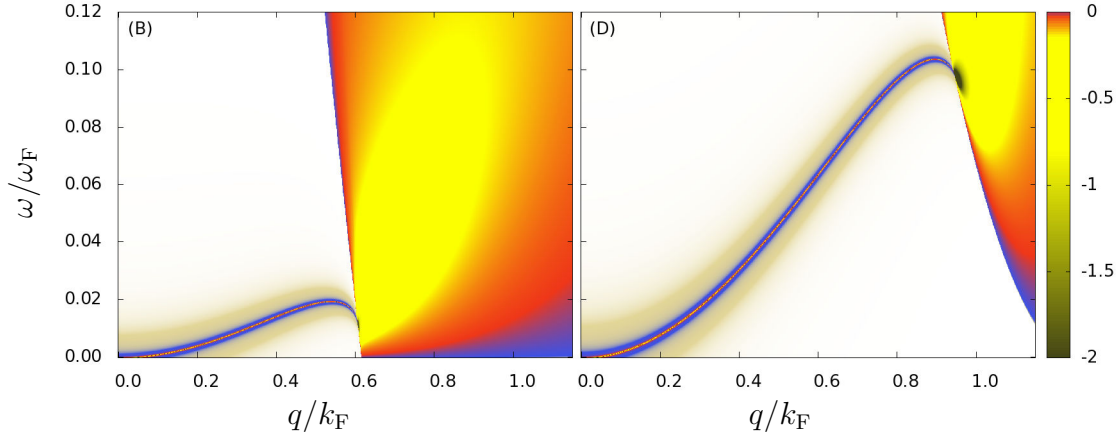


Figure 4.12: The spectrum $\text{Im } \chi^{+-}(q, \omega)$ of the ALDA-renormalized susceptibility including the spin-wave excitations. This is identical to figure 4.8, but solved straightforwardly by adding a small value to the imaginary part, resulting in a broadening of the otherwise infinitely small spin-wave peaks.

higher complexity, resulting in a very structured Fermi surface. Consequently for practically any (q, ω) -pair one can construct some band transition, and the imaginary part of the susceptibility $\text{Im } \chi_{\text{KS}}^{+-}$ usually has non-zero values for all ω , unlike for the homogeneous electron gas. Then, the spin-wave condition (4.72), namely the vanishing of the real part of the denominator of (4.71) does not lead to a pole since the imaginary part is still unequal zero. Nevertheless we expect this to lead to a peak in the full susceptibility $\text{Im } \chi^{+-}$. This implies a simplified procedure: while in the case of the homogeneous electron gas the infinitesimally extended poles almost certainly lie in-between the mesh points of any (q, ω) -mesh (demanding a separate interval nesting to determine the poles), they are not that strongly localized for real materials. Thus, one can directly solve the Dyson equation for the full susceptibility on a sufficiently dense (q, ω) -mesh and scan for peaks. This is pictured in figure 4.12: A small value (in this case -10^{-8}) is added to the imaginary part of the Kohn-Sham susceptibility, then the Dyson equation is solved. The resulting spectrum contains broadened spin-wave peaks. With larger numbers added to the imaginary part the peaks get lower and broader, illustrating the transition to real materials.

In the general formalism the dielectric and spin-flip kernel have been defined in (3.69) and (3.62). These quantities can easily be connected to the quantities derived in this chapter through

$$f_{\text{xc}}^{+-}(\mathbf{r}, t, \mathbf{r}', t') = \delta(\mathbf{r} - \mathbf{r}') \delta(t - t') f_{\text{xc}}^{+-}(n, \xi) \Big|_{\substack{n=n(\mathbf{r}) \\ \xi=\xi(\mathbf{r})}} \quad (4.95)$$

$$f_{\text{xc}}^{+-}(\mathbf{r}, \mathbf{r}'; \omega) = \delta(\mathbf{r} - \mathbf{r}') f_{\text{xc}}^{+-}(n, \xi) \Big|_{\substack{n=n(\mathbf{r}) \\ \xi=\xi(\mathbf{r})}} \quad (4.96)$$

for the magnetic kernel and

$$f_{\text{xc}}(\mathbf{r}, t, \mathbf{r}', t') = \delta(\mathbf{r} - \mathbf{r}') \delta(t - t') f_{\text{xc}}(n, \xi) \Big|_{\substack{n=n(\mathbf{r}) \\ \xi=\xi(\mathbf{r})}} \quad (4.97)$$

$$f_{\text{xc}}(\mathbf{r}, \mathbf{r}', \omega) = \delta(\mathbf{r} - \mathbf{r}') f_{\text{xc}}(n, \xi) \Big|_{\substack{n=n(\mathbf{r}) \\ \xi=\xi(\mathbf{r})}} \quad (4.98)$$

for the dielectric kernel, with the ALDA kernels $f_{\text{xc}}(n, \xi)$ and $f_{\text{xc}}^{+-}(n, \xi)$ given in (4.49) and (4.53), respectively.

Since this procedure to determine spin waves is very sensitive (c.f. figure 4.9) we will probably need to push the convergence parameters of our calculations for real materials in order to obtain thoroughly converged results.

Furthermore, the derivations in this chapter stress the need to consistently use the same exchange-correlation functional in the DFT self-consistency cycle as well as in the ALDA spin-wave calculation. If additional non-generic ingredients (such as the LDA+U method) are used in the DFT part, this has to be treated consistently in the ALDA part.

In this chapter we have shown the consistence with the Goldstone theorem (namely the start of the spin-wave dispersion in the origin) explicitly for the homogeneous electron gas. This can be also be derived in the general case (see appendix B.4). Therefore we would expect for highly converged ALDA calculation of a real magnetic material (which is spin polarized without an applied external field) to find a spin-wave dispersion which does indeed start at the origin such as it does for the homogeneous electron gas.

CHAPTER 5

IMPLEMENTATION

Contents

5.1	Reformulation for Lattice-Periodic Systems	74
5.2	DFT and the FLAPW method	75
5.2.1	The Kohn-Sham Formalism in Basis Representation	75
5.2.2	The APW Method	77
5.2.3	The LAPW Method	79
5.2.4	Further Implementation Details	83
5.3	ALDA and the Mixed Product Basis	86
5.3.1	The Dyson equation in basis notation	86
5.3.2	The Mixed Product Basis	87
5.3.3	TDDFT Implementation Details	92

The general theoretical framework of this thesis, time-dependent DFT, has been investigated in chapters 2 and 3. However, as has been pointed out already in section 2.4, there exist a large diversity of DFT methods to carry out calculations for different kinds of materials. We are interested in the particular case of magnetic crystalline materials.

Crystalline materials are characterized by their translational symmetry. In order to account for that, the central equations of the theory – namely the Kohn-Sham equations and susceptibility as well as the ALDA Dyson equation – are reformulated in section 5.1 by taking the lattice periodicity into account.

The representation of the DFT equations in terms of a set of basis functions is introduced in section 5.2, and specific basis sets are presented. While the plane-wave set is convenient for illustrations, the linearized augmented plane wave (LAPW, section 5.2.3) set is advantageous for materials with localized electronic states (such as the magnetic transition metals), and is used in this work for DFT calculations. A few details of the method are highlighted in section 5.2.4.

Also the spin-response part is treated in basis representation, see section 5.3. The Dyson equation becomes a matrix equation (section 5.3.1). The LAPW basis set is not well suited for the representation of the Kohn-Sham response function; instead the mixed product basis is used (section 5.3.2). Some details of the implementation are discussed in section 5.3.3.

The DFT part of the calculations for real materials in chapter 6 is performed with the FLEUR computer code [cca] that employs the FLAPW method. For the TDDFT part of the calculation the SPEX computer code [ccb], which can do response calculations as well as

exact-exchange and GW calculations, has been extended in order to treat magnetic excitations. Both codes have been developed in the group of Prof. Blügel in the research center Jülich [fFIFJ].

5.1 Reformulation for Lattice-Periodic Systems

Crystalline systems possess translational symmetry. Incorporating this lattice periodicity yields a reformulation of the central equations which is presented below.

Density-Functional Framework As described in appendix A.2, due to the Bloch theorem (A.18) the energies and wave functions of the system are now characterized by a reciprocal vector \mathbf{k} from the first unit cell in reciprocal space, i.e., the Brillouin zone (BZ): $(\epsilon_{i\sigma}, \varphi_{i\sigma}(\mathbf{r})) \rightsquigarrow (\epsilon_{ik\sigma}, \varphi_{ik\sigma}(\mathbf{r}))$. For practical calculations this volume must be sampled by a discrete set of \mathbf{k} points. At the same time many operations on the spatial coordinate \mathbf{r} can be reduced to one unit cell in the real space. The density is constructed from the one-particle Kohn-Sham states by

$$n(\mathbf{r}) = \frac{V}{(2\pi)^3} \int_{\text{BZ}} d^3k \sum_{i,\sigma} |\varphi_{ik\sigma}(\mathbf{r})|^2 f(\epsilon_{ik\sigma}). \quad (5.1)$$

V is the volume of the real-space unit cell. The Fermi factor f accounts for the occupation of the bands and can incorporate a temperature broadening. In the DFT calculations of this work this is used for convergence purposes only. The phononic degrees of freedom have been excluded right from the beginning by pinning the atomic nuclei at fixed positions in (2.5).

The collinear Kohn-Sham equation (2.39) now has to be solved independently for each \mathbf{k} point:

$$\underbrace{\left[-\frac{1}{2} \nabla_{\mathbf{r}}^2 + V_{\text{eff}}(\mathbf{r}) \pm \frac{\mu_{\text{B}} g}{2} B_{\text{xc}}(\mathbf{r}) \right]}_{\hat{\mathcal{H}}^{\text{KS}}(\mathbf{r})} \varphi_{ik\sigma}(\mathbf{r}) = \epsilon_{ik\sigma} \varphi_{ik\sigma}(\mathbf{r}). \quad (5.2)$$

The nabla operator acts on the spatial coordinate \mathbf{r} . The Kohn-Sham Hamiltonian $\hat{\mathcal{H}}^{\text{KS}}$ on the left is \mathbf{k} dependent in the sense that the kinetic-energy operator acts on the Bloch state $\varphi_{ik\sigma}(\mathbf{r}) = e^{i\mathbf{k}\mathbf{r}} z_{ik\sigma}(\mathbf{r})$, i.e., acting on the exponential factor. However, instead of using this decomposition and expanding $z(\mathbf{r})$ directly we choose Bloch basis functions in order to expand the wave function φ .

Spin-Response Function According to (A.21) in appendix A.2, the response function χ as well as its spectral function S can be equally characterized by a Brillouin-zone vector \mathbf{q} , $\chi^{+-}(\mathbf{r}, \mathbf{r}'; \omega) \rightsquigarrow \chi^{+-}(\mathbf{r}, \mathbf{r}'; \mathbf{q}, \omega)$, where both spatial coordinates \mathbf{r}, \mathbf{r}' are confined to one unit cell (u.c.). Then, the macroscopic spin-response function in analogy to (3.40) is determined by

$$\chi^{+-}(\mathbf{q}, \omega) = \int_{\text{u.c.}} e^{-i\mathbf{q}\mathbf{r}} \chi^{+-}(\mathbf{r}, \mathbf{r}'; \mathbf{q}, \omega) e^{+i\mathbf{q}\mathbf{r}'} d^3r d^3r' \quad (5.3)$$

with the two integrations being restricted to the real-space unit cell. This projection can also be understood as the $\mathbf{G} = \mathbf{G}' = 0$ component of a plane-wave representation $\chi^{+-}(\mathbf{r}, \mathbf{r}'; \mathbf{q}, \omega) \rightsquigarrow \chi_{\mathbf{G}\mathbf{G}'}^{+-}(\mathbf{q}, \omega)$, where \mathbf{r}, \mathbf{r}' are coordinates from within the real-space unit cell and \mathbf{G}, \mathbf{G}' are reciprocal lattice vectors. The spin-flip Dyson equation (3.64) for a local exchange-correlation kernel $f_{\text{xc}}^{+-}(\mathbf{r}) = f_{\text{xc}}^{+-}(\mathbf{r}, \mathbf{r}')\delta(\mathbf{r} - \mathbf{r}')$ such as in ALDA evaluates to

$$\chi^{+-}(\mathbf{r}, \mathbf{r}'; \mathbf{q}, \omega) = \chi_{\text{KS}}^{+-}(\mathbf{r}, \mathbf{r}'; \mathbf{q}, \omega) + \left(\frac{\mu_{\text{B}}g}{2}\right)^2 \int_{\text{u.c.}} d^3r_1 \chi_{\text{KS}}^{+-}(\mathbf{r}, \mathbf{r}_1; \mathbf{q}, \omega) f_{\text{xc}}^{+-}(\mathbf{r}_1) \chi^{+-}(\mathbf{r}_1, \mathbf{r}'; \mathbf{q}, \omega). \quad (5.4)$$

In here, the explicit form (4.95) of the spin-flip kernel f_{xc}^{+-} in the ALDA is used, being frequency- and \mathbf{k} independent. It should be remarked that while the mentioned quantities in the DFT part are integrated over (i.e., the \mathbf{k} dependent wave functions integrated yield the \mathbf{k} independent density, which in turn provides means to determine the wave functions again), the response function χ is studied for each wave vector independently. Therefore it is denoted as \mathbf{q} instead of \mathbf{k} . As explained in section 3.1, this vector corresponds to the momentum transfer $\Delta\mathbf{q}$ from an external perturbation to a quasi-particle excitation. The Kohn-Sham response (3.46) in crystal notation reads

$$\chi_{\text{KS}}^{+-}(\mathbf{r}, \mathbf{r}'; \mathbf{q}, \omega) = \lim_{\eta \rightarrow 0^+} \int_{\text{BZ}} d^3k \sum_{n, n'} \frac{f(\epsilon_{n\mathbf{k}\uparrow}) - f(\epsilon_{n'\mathbf{k}+\mathbf{q}\downarrow})}{\omega - (\epsilon_{n'\mathbf{k}+\mathbf{q}\downarrow} - \epsilon_{n\mathbf{k}\uparrow}) + i\eta} \varphi_{n\mathbf{k}\uparrow}^*(\mathbf{r}) \varphi_{n'\mathbf{k}+\mathbf{q}\downarrow}(\mathbf{r}) \varphi_{n'\mathbf{k}+\mathbf{q}\downarrow}^*(\mathbf{r}') \varphi_{n\mathbf{k}\uparrow}(\mathbf{r}'), \quad (5.5)$$

involving a Brillouin zone integration over \mathbf{k} . Together with the basis expansion presented in the following section, this leads to the work flow sketched in figure 5.1.

5.2 DFT and the FLAPW method

5.2.1 The Kohn-Sham Formalism in Basis Representation

The Kohn-Sham equation for periodic systems (5.2) needs to be solved. This can be done by sampling the wave functions on a real-space mesh, or by expanding the wave functions in basis functions ϕ (labeled by indices ν and \mathbf{k}) which are now assumed spin-dependent and of Bloch character $\phi \sim e^{i\mathbf{k}\mathbf{r}}$. Thus, the set of basis functions is denoted $\{\phi_{\nu\mathbf{k}\sigma}(\mathbf{r})\}$, and its corresponding biorthonormal set $\{\tilde{\phi}_{\nu\mathbf{k}\sigma}(\mathbf{r})\}$. They obey the orthonormality and closure relations

$$\frac{V}{(2\pi)^3} \int_{\text{BZ}} d^3k \sum_{\nu} |\tilde{\phi}_{\nu\mathbf{k}\sigma}\rangle \langle \phi_{\nu\mathbf{k}\sigma}| = \mathbb{1} \quad (5.6)$$

$$\langle \tilde{\phi}_{\nu\mathbf{k}\sigma} | \phi_{\nu'\mathbf{k}'\sigma} \rangle = \delta_{\mathbf{k}\mathbf{k}'} \delta_{\nu\nu'}. \quad (5.7)$$

The Dirac bra-ket notation indicates integrations over the spatial coordinate \mathbf{r} . The spin denotes that there are two independent sets of basis functions, each used for the representation of wave functions of the according spin alignment. When representing other Bloch functions

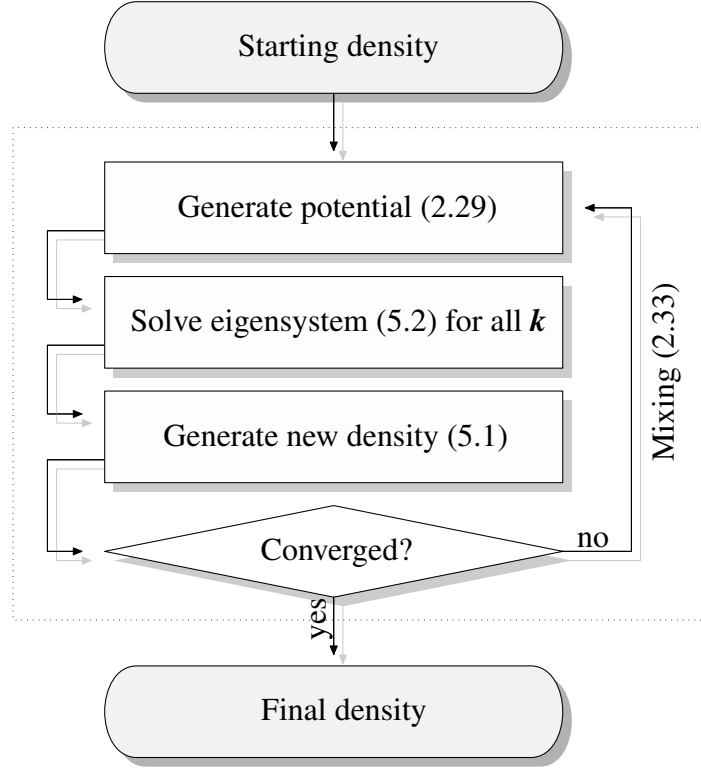


Figure 5.1: A sketch of the work flow of the density-functional self-consistency cycle, like figure 2.1 but applied on a periodic system.

such as the wave functions the \mathbf{k} integration disappears:

$$|\varphi_{i\mathbf{k}\sigma}\rangle = \int_{\text{BZ}} d^3k' \sum_{\nu} |\tilde{\phi}_{\nu\mathbf{k}'\sigma}\rangle \langle\phi_{\nu\mathbf{k}'\sigma}|\varphi_{i\mathbf{k}\sigma}\rangle \quad (5.8)$$

$$\Rightarrow \varphi_{i\mathbf{k}\sigma}(\mathbf{r}) = \sum_{\nu} c_{i\nu\mathbf{k}\sigma} \tilde{\phi}_{\nu\mathbf{k}\sigma}(\mathbf{r}), \quad c_{i\nu\mathbf{k}\sigma} = \langle\phi_{\nu\mathbf{k}\sigma}|\varphi_{i\mathbf{k}\sigma}\rangle. \quad (5.9)$$

The matrix elements of the Hamiltonian $\hat{\mathcal{H}}^{\text{KS}}(\mathbf{r})$ given in (5.2) and of the overlap matrix read

$$\mathcal{H}_{\mathbf{k}\sigma}^{[m,n]} = \langle\phi_{m\mathbf{k}\sigma}|\hat{\mathcal{H}}^{\text{KS}}(\mathbf{r})|\phi_{n\mathbf{k}\sigma}\rangle = \int_{\text{u.c.}} d^3r \phi_{m\mathbf{k}\sigma}^*(\mathbf{r}) \hat{\mathcal{H}}^{\text{KS}}(\mathbf{r}) \phi_{n\mathbf{k}\sigma}(\mathbf{r}) \quad (5.10)$$

$$\mathcal{S}_{\mathbf{k}\sigma}^{[m,n]} = \langle\phi_{m\mathbf{k}\sigma}|\phi_{n\mathbf{k}\sigma}\rangle = \int_{\text{u.c.}} d^3r \phi_{m\mathbf{k}\sigma}^*(\mathbf{r}) \phi_{n\mathbf{k}\sigma}(\mathbf{r}). \quad (5.11)$$

They are spin- and \mathbf{k} dependent as well as hermitian and in general complex. Consequently the Kohn-Sham equation (5.2) can be represented in these basis functions ϕ , resulting in a so-called *generalized eigenvalue problem* (alternatively termed *secular equation*)

$$\{\mathcal{H}_{\mathbf{k}\sigma} - \varepsilon_{i\mathbf{k}\sigma} \mathcal{S}_{\mathbf{k}\sigma}\} \mathbf{c}_{i\mathbf{k}\sigma} = 0 \quad (5.12)$$

with the vector \mathbf{c} being the eigenvector (i.e., the coefficients in the biorthogonal set) for a given (\mathbf{k}, σ) -pair while the index i counts the eigenstates. This equation can be solved independently for each \mathbf{k} vector and spin direction.

Using a Cholesky decomposition (see, for instance, Stoer [Sto94]) any hermitian and positive definite matrix can be decomposed into a matrix product of a lower triangular matrix with only positive diagonal elements and its transposed. This way a generalized eigenvalue problem can be reduced to an ordinary eigenvalue equation (which corresponds to (5.12) with S being a unity matrix) which standard linear-algebra methods can be applied on to solve it.

Plane-Wave Basis Set The simplest Bloch-wave expansion is the plane-wave expansion

$$\varphi_{i\mathbf{k}\sigma}(\mathbf{r}) = \sum_{\mathbf{G}} c_{i\mathbf{k}\mathbf{G}\sigma} \phi_{\mathbf{k}\mathbf{G}}(\mathbf{r}) \quad (5.13)$$

$$\phi_{\mathbf{k}\mathbf{G}}(\mathbf{r}) = \frac{1}{\sqrt{V}} e^{i(\mathbf{k}+\mathbf{G})\mathbf{r}}. \quad (5.14)$$

where the sum runs over all reciprocal lattice vectors \mathbf{G} . Since this is not possible in actual calculations, \mathbf{G} vectors are chosen from a sphere such that $|\mathbf{k}+\mathbf{G}| < G_{\max}$. This has the effect that for different \mathbf{k} points some $(\mathbf{k}+\mathbf{G})$ vectors can slip into or out of this sphere, leading to a slightly varying number of basis functions for different \mathbf{k} points. Also the LAPW basis set as well as the mixed product basis set which are presented in this chapter share this property. The plane waves form an orthogonal basis set. The Coulomb potential $v(r)$ represented in plane waves reads

$$v(\mathbf{r}, \mathbf{r}') = \frac{1}{|\mathbf{r} - \mathbf{r}'|} \rightsquigarrow v_{\mathbf{k}\mathbf{G}} = \frac{4\pi}{|\mathbf{k} + \mathbf{G}|^2} \quad (5.15)$$

revealing a most inconvenient singularity for $\mathbf{k} \rightarrow 0$. This needs to be properly taken care of for instance when applying RPA or dielectric TDDFT, however, not in magnetic TDDFT where the Coulomb interaction does not appear.

In practical calculations it turns out that the variations of the potential and thus the wave functions close to the nuclei are too large, which requires an excessive number of plane waves in order to properly expand these wave functions. On the other hand the chemical bonding and the electronic band structure is mostly determined by the shape of the wave functions in the overlapping region where only the valence electrons contribute. Based on this assumption the concept of pseudo-potentials was developed [KB82, BHS82]. The effective potential is replaced by a pseudo-potential which coincides with the original potential but has a smoother shape close to the nucleus. Pseudo-potential methods have proved very useful. However, it turns out that they are not capable of describing more localized systems (i.e., no proper pseudo-potentials can be generated) such as transition and rare-earth metals containing incomplete d - and f -shells, which happen to be those elements crucial in magnetism. Therefore other paths have to be explored.

5.2.2 The APW Method

A procedure to handle the strongly varying potential other than modifying this potential is a modification of the basis set in a way that it shows a stronger resemblance to the wave functions it should represent. A first such method was proposed by Slater [Slat37]. This so-called *augmented plane wave* (APW) method divides the space into spheres which are centered at the nuclei's position – the so-called *muffin-tin spheres* (MTs) – and the remaining

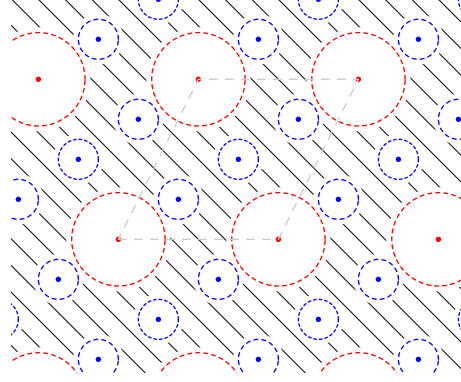


Figure 5.2: The space separation in the APW-type methods for a fictitious two-dimensional hexagonal periodic solid. The positions of the nuclei of the constituting atoms (which in this example are of different kind) are depicted by small red and blue opaque circles. The circular white region around them is their corresponding muffin-tin sphere. The remaining shaded space forms the interstitial region. A selected unit cell is marked by a dashed gray parallelogram.

interstitial region (IS), as depicted in figure 5.2. Assuming that the potential in the interstitial region is smooth, the expansion in plane waves is reasonable and thus retained in this region. Inside the muffin tin spheres the potential is assumed to be spherically symmetric, $\bar{V}(\mathbf{r}) = \bar{V}(r)$. A good set of basis functions consists of products of spherical harmonics Y_{lm} and radial basis functions u_l with the quantum number l :

$$\phi_{G\sigma}(\mathbf{r}) = \begin{cases} \frac{1}{V} e^{i(\mathbf{k}+\mathbf{G})\mathbf{r}} & \mathbf{r} \in \text{IS} \\ \sum_{l,m} a_{lm\mu G\sigma} u_{l\mu}(r; E_{l\mu\sigma}) Y_{lm}(\hat{\mathbf{r}}) & \mathbf{r} \in \text{MT}^\mu. \end{cases} \quad (5.16)$$

The different (kinds of) muffin-tin spheres in the unit cell are label μ .

While there are degrees of freedom in formula (5.16) as given above due to the a -coefficients, the APW basis functions ϕ are furthermore demanded to be continuous also on the muffin-tin sphere boundaries. The Rayleigh expansion provides a decomposition of a plane wave into an infinite sum of spherical harmonics,

$$e^{i\mathbf{K}\mathbf{r}} = 4\pi \sum_{l,m} i^l j_l(rK) Y_{lm}^*(\hat{\mathbf{K}}) Y_{lm}(\hat{\mathbf{r}}) \quad (5.17)$$

with $\mathbf{K} = \mathbf{k} + \mathbf{G}$, $K = |\mathbf{K}|$. Applying this for each radial muffin-tin sphere radius R_{MT^μ} allows for a proper determination of the a -coefficients in order to yield continuity. In practice a finite cut-off l_{max} for the spherical expansion is chosen and small mismatches persist.

The radial muffin-tin function u_l is determined as solution of a radial Schrödinger equation

$$\left\{ -\frac{1}{2} \frac{\partial^2 r}{\partial r^2} + \frac{1}{2} \frac{l(l+1)}{r^2} + \bar{V}_\mu(r) - E_{l\mu\sigma} \right\} r u_{l\mu\sigma}(r; E_{l\mu\sigma}) = 0 \quad (5.18)$$

for a given spin-dependent energy parameter $E_{l\mu\sigma}$ and a spherically symmetric potential

$\bar{V}(r)$. These radial basis functions are commonly normalized within the muffin-tin sphere,

$$\langle u_{l\mu} | u_{l'\mu} \rangle = \int_0^{R_{\text{MT}\mu}} r^2 |u_{l\mu}(r)|^2 dr = 1. \quad (5.19)$$

If the energy parameter E is chosen fixed throughout the whole calculation it turns out that the basis functions do not offer enough variational freedom, i.e., they are too stiff to properly represent the actual Kohn-Sham orbitals. The proper solution is to set E equal to the actual Kohn-Sham one-particle energy $\epsilon_{ik\sigma}$, for which the radial functions will evidently be a good choice of basis set. However, this poses the problem that an additional iteration has to be performed (at each \mathbf{k} point) for each Kohn-Sham orbital, starting from an initial value for E_l and converging to the actual Kohn-Sham energy. This non-linearity makes APW, while being very powerful, a very costly method. Further details of this method can be found in [Lou67].

5.2.3 The LAPW Method

A subsequent development is the *linearized* augmented plane wave (LAPW) method [And75] proposed by Anderssen. The central idea is to extend the variational freedom of the basis set by applying an expansion of the radial function u_l around a given fixed energy E_l :

$$u_l(r; \varepsilon) = u_l(r; E_l) + \dot{u}(r; E_l)(\varepsilon - E_l) + \mathcal{O}([\varepsilon - E_l]^2) \quad (5.20)$$

with the energy derivative $\dot{u} = \partial u / \partial \varepsilon$. Thus, the energy ε is not determined iteratively as in the APW method; instead it is approximated by the energy E_l which can, however, be adjusted from one iteration step of the DFT self-consistency to the next. Due to the variational principle, an error of second order of the term $(\varepsilon - E_l)$ in the wave functions results in errors of higher order in the energy eigenvalues. This higher order leads to very good results of this linearization in broad energy regions. Applying this expansion to (5.16) yields the LAPW basis functions

$$\phi_{\mathbf{G}\sigma}(\mathbf{r}) = \begin{cases} e^{i(\mathbf{k}+\mathbf{G})\mathbf{r}} & \mathbf{r} \in \text{IS} \\ \sum_{l,m} [a_{lm\mu\mathbf{G}\sigma} u_{l\mu}(r; E_{l\mu\sigma}) + b_{lm\mu\mathbf{G}\sigma} \dot{u}_{l\mu}(r; E_{l\mu\sigma})] Y_{lm}(\hat{\mathbf{r}}) & \mathbf{r} \in \text{MT}_{\mu}. \end{cases} \quad (5.21)$$

The energy derivative \dot{u} can be determined by taking the energy derivative of (5.18):

$$\left\{ -\frac{1}{2} \frac{\partial^2 r}{\partial r^2} + \frac{1}{2} \frac{l(l+1)}{r^2} + \bar{V}_{\mu}(r) - E_{l\mu\sigma} \right\} r \dot{u}_{l\mu}(r; E_{l\mu\sigma}) = r u_{l\mu}(r; E_{l\mu\sigma}). \quad (5.22)$$

The basis functions have to be continuous on the muffin-tin sphere boundaries in the same way as for the APW method, fixing a , now also their radial derivative is demanded to be continuous at the sphere boundaries, which fixes the b -coefficients. Orthogonality of u and \dot{u} inside the muffin-tin sphere has to be explicitly assured.

In many cases it is convenient to combine this actual form of the LAPW basis functions with the expansion (5.8) of the wave functions; the LAPW wave functions then have the form

$$\varphi_{ik\sigma}(\mathbf{r}) = \begin{cases} \sum_{\mathbf{G}} c_{\mathbf{k}\mathbf{G}} e^{i(\mathbf{k}+\mathbf{G})\mathbf{r}} & \mathbf{r} \in \text{IS} \\ \sum_{l,m} [A_{lm\mu\mathbf{k}\sigma} u_{l\mu}(r; E_{l\mu\sigma}) + B_{lm\mu\mathbf{k}\sigma} \dot{u}_{l\mu}(r; E_{l\mu\sigma})] Y_{lm}(\hat{\mathbf{r}}) & \mathbf{r} \in \text{MT}_{\mu}. \end{cases} \quad (5.23)$$

with the combined factors

$$A_{lm\mu\sigma}(\mathbf{k}) = \sum_{\mathbf{G}} c_{\mathbf{k},\mathbf{G}} a_{lm\mu\sigma}^{\mathbf{G}} \quad (5.24)$$

$$B_{lm\mu\sigma}(\mathbf{k}) = \sum_{\mathbf{G}} c_{\mathbf{k},\mathbf{G}} b_{lm\mu\sigma}^{\mathbf{G}}. \quad (5.25)$$

Also here it is obvious that the A and B coefficients are not independent components of the eigenvectors, but are determined by the plane-wave expansion coefficients c .

Shape Approximations and the FLAPW Method The potentials in the APW have a restricted shape: they are assumed constant in the interstitial region and spherically symmetric in the muffin-tin region,

$$V(\mathbf{r}) = \begin{cases} V_0^{\text{IS}} & \mathbf{r} \in \text{IS} \\ V_0^{\text{MT}}(r) & \mathbf{r} \in \text{MT}. \end{cases} \quad (5.26)$$

Here the potential V is one of the potentials V_{eff} , V_{H} , V_{xc} , V_{ext} as it appears in the eigenvalue problem (5.12). Such approximations may be reasonably justified for close-packed metallic systems, but not for open systems. Also early and more simple LAPW implementations are based on this shape approximation. A first step to lift these restrictions are warped interstitial potentials [Koe70] which employ a plane-wave expansion in the interstitial region. Further development led to the full-potential linearized augmented plane wave (or FLAPW) method [WKWF81, Ham79] which does a full expansion of the density and the potential including their non-spherical contributions. In a straightforward manner these two quantities could be expanded analogous to the wave functions: into plane waves in the interstitial region, and radial functions times spherical harmonics in the muffin-tin spheres. However, a lot of the expansion coefficients would turn out to be zero due to symmetry reasons.

Therefore it is advantageous to build the symmetry into the expansion. For this the symmetrized plane waves are defined in the interstitial region as

$$\phi_{\text{sym}}(\mathbf{r}) = \frac{1}{N_{\text{sym}}} \sum_j e^{i(\mathcal{R}_j \mathbf{G}) \mathbf{r}}. \quad (5.27)$$

The number of symmetry operations is denoted N_{sym} , and \mathcal{R}_j is the rotation matrix corresponding to symmetry operation j . There might be groups of \mathbf{G} vectors which have identical symmetrized plane waves. Each of these groups is combined to form one star $S_s(\mathbf{r})$ which can be written as

$$S_s(\mathbf{r}) = \sum_k d_{sk}^{\text{star}} e^{i\mathbf{G}_{sk} \mathbf{r}}. \quad (5.28)$$

The index s labels the star, and k runs over all members of this star. Thus, the star with index s is a linear combination of plane waves of vectors \mathbf{G}_{sk} with coefficients d_{sk}^{star} which are determined by symmetry and ensure normalization.

The same is done in the muffin tins: There exist groups of (lm) components for which the spherical harmonics are identical when applying symmetry operations. As a result the *lattice*

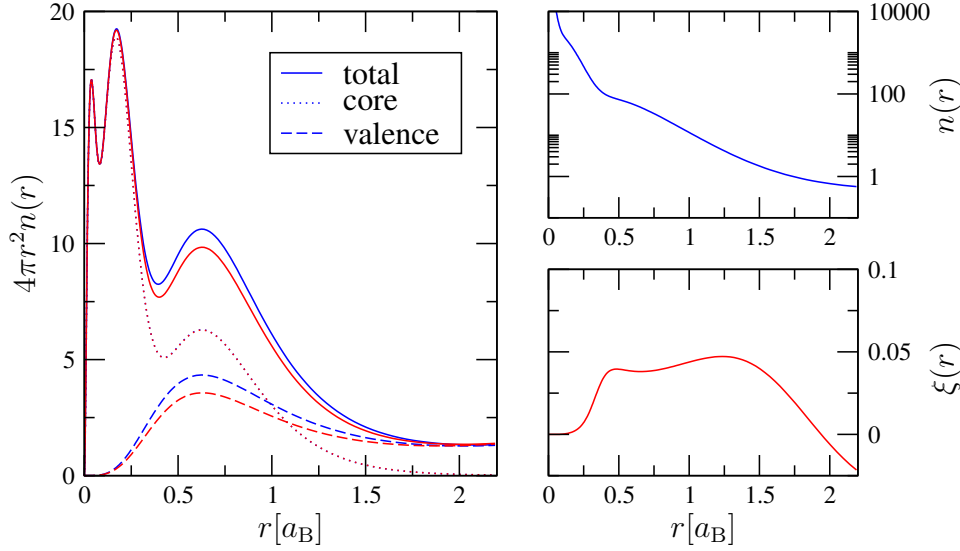


Figure 5.3: The spherical ($l = 0$) radial charge density for Nickel. In the left tableau the radial charge density $n(r)$ (multiplied by the shell surface $4\pi r^2$) is plotted. There are three curves for the spin-up (blue) and the spin-down (red) channel: The contribution of the core electrons and the valence contribution as well as the sum of the two (denoted *total*). According to (5.31) the radial integration yields the charge confined inside the muffin-tin sphere, in this case 26.8 out of 28 electrons. On the top right the total charge $n(r)$ (without the prefactor $4\pi r^2$) is shown, on the bottom right the relative spin polarization $\xi(r)$.

harmonics L_ν are defined which linearly combine one or more spherical harmonics of the same orbital quantum number l_ν but different magnetic quantum number $m_{\nu,i}$:

$$L_\nu(\hat{\mathbf{r}}) = \sum_{i=1}^{N_\nu^{\text{lh}}} d_{\nu i}^{\text{lh}} Y_{l_\nu m_{\nu,i}}(\hat{\mathbf{r}}). \quad (5.29)$$

N_ν^{lh} are the number of members (i.e., m -quantum numbers) that belong to the lattice harmonic labeled ν . In an actual calculation only the first n_{lh} lattice harmonics are taken into account when representing a function, see (5.33). The coefficients $d_{\nu i}^{\text{lh}}$ are in general complex and determined by the symmetry of the system and include the normalization as well. An example of the reduction is given in table 5.1 for the fcc structure.

These functions are then used to expand the charge density and the potentials. The spin-dependent density for instance reads

$$n_\sigma(\mathbf{r}) = \begin{cases} \sum_{s=1}^{N^{\text{st}}} n_{s\sigma}^{\text{star}} S_s(\mathbf{r}) & \mathbf{r} \in \text{IS} \\ \sum_{\nu=1}^{N^{\text{lh}}} n_{\nu\mu\sigma}^{\text{lh}}(r) L_\nu(\hat{\mathbf{r}}) & \mathbf{r} \in \text{MT}^\mu. \end{cases} \quad (5.30)$$

Inside the muffin-tin spheres the radial coordinates are shifted by the muffin-tin center, $\mathbf{r} \rightarrow \mathbf{r} - \mathbf{R}_{\text{MT}^\mu}$. The density is thus expressed in terms of expansion coefficients $n_{s\sigma}^{\text{star}}$ in the

ν	l_ν	N_ν^{lh}	$m_{\nu,i}, i = 1, \dots, N_\nu^{\text{lh}}$				
1	0	1	0				
2	4	3	-4	0	+4		
3	6	3	-4	0	+4		
4	8	5	-8	-4	0	+4	+8

ν	l_ν	N_ν^{lh}	$m_{\nu,i}, i = 1, \dots, N_\nu^{\text{lh}}$				
1	0	1	0				
2	3	2	-2	+2			
3	4	3	-4	0	+4		
4	6	3	-4	0	+4		
5	7	4	-6	-2	+2	+6	
6	8	5	-8	-4	0	+4	+8

Table 5.1: Non-zero contributions to the lattice harmonics up to $l = 8$ for two different cubic crystal structures with 48 symmetry operations each. On the left Nickel (fcc structure, one atom per unit cell) is shown, compared with Silicon on the right (diamond structure, two atoms per unit cell).

interstitial and radial functions $n_{\nu\mu\sigma}^{\text{lh}}(r)$ inside the muffin-tin spheres. The total charge n_σ^μ inside one muffin-tin sphere μ is given by the $l = 0$ component only,

$$n_{\mu\sigma} = 4\pi \int_0^{R_{\text{MT}}^\mu} r^2 n_{0\mu\sigma}(r) dr \quad (5.31)$$

while the higher components indicate charge-neutral deviations from the spherical charge distribution. Their total value integrates to zero due to $\int Y_{lm}(\hat{\mathbf{r}}) d^2r = \sqrt{4\pi} \delta_{l0}$. Their expansion $n(r)$ can be negative for $l_\nu > 0$.

Calculation of the Exchange-Correlation Potential in FLAPW The potential $V_{\text{xc}}(\mathbf{r})$, depending on the charge and magnetization density, is given as a function in real space, $V_{\text{xc}}(\mathbf{r}) = V_{\text{xc}}^{\text{LDA}}(n(\mathbf{r}), m(\mathbf{r}))$. The densities, however, are given in terms of stars and lattice harmonics. Therefore the following transforms have to be performed in order to calculate the exchange-correlation potential:

- First step: In the interstitial, starting from the coefficients $n_{s\sigma}^{\text{star}}$ the density is calculated on an equidistant real-space mesh by employing a Fast Fourier Transform (FFT), $n(\mathbf{r})$.
- In order to treat the muffin-tin spheres a set of coordinates on a unit sphere is constructed. Then, starting from the radial lattice-harmonics coefficients for the density $n_{\mu\nu\sigma}(r)$, the density $n(\mathbf{r})$ is calculated at the proper spherical coordinates on the shell of every radial coordinate.
- The density is now calculated on points in the real space both in the muffin-tin spheres and the interstitial region. In a second step the LDA exchange-correlation function $V_{\text{xc}}(\mathbf{r})$ can be calculated at these points.
- In a third step this function is projected back onto stars in the interstitial region, and onto lattice harmonics in the muffin-tin spheres.

This work flow can be sketched in the following way:

$$\left. \begin{array}{l} n_{s\sigma}^{\text{star}} \\ n_{\mu\nu\sigma}^{\text{lh}}(r) \end{array} \right\} \rightarrow n_\sigma(\mathbf{r}) \rightsquigarrow V_{\text{xc}}(\mathbf{r}) \rightarrow \begin{cases} V_s^{\text{star}} & \mathbf{r} \in \text{IS} \\ V_{\mu\nu}^{\text{lh}}(r) & \mathbf{r} \in \text{MT}^\mu. \end{cases} \quad (5.32)$$

The result is the potential provided in the stars/lattice harmonic expansion

$$V_{\text{xc}}(\mathbf{r}) = \begin{cases} \sum_s V_s^{\text{star}} S_s(\mathbf{r}) & \mathbf{r} \in \text{IS} \\ \sum_{\nu} V_{\nu\mu}^{\text{lh}}(r) L_{\nu}(\hat{\mathbf{r}}) & \mathbf{r} \in \text{MT}^{\mu}. \end{cases} \quad (5.33)$$

5.2.4 Further Implementation Details

An extensive review of the LAPW method is provided by Singh [Sin94]. Extensive derivations of the formulas of the FLAPW method are provided in [Kur00]. In this section some aspects of the method should be highlighted without giving an in-depth presentation.

Spatial Geometry In practical calculations the basis set must be chosen according to the physical system. The way the FLAPW Bloch basis, which has been defined in (5.21), is suitable for infinite periodic materials. Other choices are possible as well. For instance, modified LAPW basis sets have been developed for film [Kur00] and wire geometries [MBB05] and successfully applied to the investigation of magnetic nano-structures. In the same way the mixed product basis approach could be extended to these systems.

Relativistic Generalization The formalism presented so far is restricted to non-relativistic spin-collinear systems. As has been explained in chapter 2 in the general non-collinear case the Kohn-Sham equations have to be solved for a spinor wave function. In basis representation this means that one has a spinor of vectors that (in spin space) a 2×2 Hamilton matrix operates on. In the collinear case this Hamiltonian matrix becomes block-diagonal and can be solved independently for each spin. The FLAPW formalism [KFN⁺04] has also been implemented as a non-collinear treatment. Furthermore, a generalized Bloch theorem [San86] can be established which in addition to the spatial lattice periodicity implies a steady uniform tilt of magnetization from one unit cell to the next, which enables calculation of frozen magnons and spin spirals.

A fully relativistic treatment of the electrons would lead to a four-component spinor consisting of a large and a small component per spin orientation, the latter of which vanishes in the non-relativistic limit. Commonly the core electrons are in fact treated in a fully-relativistic fashion. The valence electrons, however, cannot be treated this way since separate spin and angular momentum quantum numbers σ and l are used independently in the LAPW method up from the beginning, while they are coupled in the relativistic framework. One can apply the so-called scalar-relativistic approximation (SRA) which takes the highest spin-diagonal relativistic correction terms into account, but neglects the non-diagonal spin-orbit term. This spin-orbit coupling can be treated afterwards in a variational manner. Typically the small component from the SRA is neglected in the interstitial and subsequently in the matching procedure at the muffin-tin sphere boundaries. This procedure is reasonable since relativistic effects have significant contributions only close to the nucleus.

It should be noted that the restriction to collinearity is not a principal limitation of our approach.

Enhancement of Basis Flexibility As already remarked at the definition of the APW basis set only the valence electrons are treated by the method so far. The core states are not determined by the solution of the eigenvalue problem (5.12) but in a separate \mathbf{k} independent step. They can mostly be considered to be confined to the muffin-tin sphere, thus not to overlap with the electrons in other muffin-tin spheres or in the interstitial region. This is physically justified. They do not take part in the chemical bonding.

However, some problems might occur. Some high-lying so-called semi-core states might not be reasonably confined into the muffin-tin sphere which has to be compensated. This can lead to wrong results, for instance during the calculation of lattice constants, phonon frequencies or forces. Furthermore, semi-core states can lead to so-called ghost bands, i.e., badly described core states which appear in the valence or conduction regions. One possible solution is the local-orbitals extension to the LAPW basis set [Sin91]. It adds additional basis functions to the set. This expands the variational freedom and makes the treatment of semi-core and valence states possible. An alternative approach to extend the variational freedom of the LAPW basis was developed in the APW+lo approach [SNS00].

Brillouin-Zone Integration In the present algorithm integrations over the Brillouin zone must be performed, e.g., in the construction of the density (5.1), the computation of the Kohn-Sham response (5.5) and the setup of the potentials involved in the Hamiltonian (5.12). In practice the first Brillouin zone is sampled by a finite number of \mathbf{k} points.

Two kinds of methods are common, the special points method [CC73, Cun74] and the tetrahedron method [JA71, LT72, BJA94], which both reduce to a weighted summation

$$\frac{V}{(2\pi)^3} \int_{\text{BZ}} d^3k F(\mathbf{k}) \rightsquigarrow \sum_i w(\mathbf{k}_i) F(\mathbf{k}_i). \quad (5.34)$$

The difference lies in the way the weights are obtained. The special-points method defines a \mathbf{k} point mesh given due to the spatial symmetry and calculates the integrand at the given points, which is straightforward to implement. The tetrahedron method on the other hand divides the Brillouin zone into tetrahedra and applies linear interpolations of band energies and the integrand $F(\mathbf{k})$ inside them, which corresponds to a linear combination of the corner values. The weights in the tetrahedron method are not necessarily symmetry-consistent as in the special-points method; on the other hand it can be reformulated to handle integrations over δ -peaks and is therefore preferable for spectral properties such as our Kohn-Sham response. The special-points method can only cope with such peaks by applying a broadening.

One step in the setup of the new density is the determination of the Fermi energy since only occupied states contribute to the new density. It is done simply by adding up states of energy below a test energy. This test energy is refined by nested intervals until the summed-up number of states coincides with the number of valence electrons.

Use of Symmetry The spatial and time-reversal symmetries can be exploited to significantly reduce the computational effort. Symmetry operations are real-space operations represented by a rotation matrix and a translational vector, $\{\mathcal{R}, \tau\} : \mathbf{r} \mapsto \mathcal{R}\mathbf{r} + \tau$ which leave the system invariant. Several simplifications are provided by symmetry:

- *Time-inversion symmetry*: If the system has time-inversion symmetry (such as for our time-independent Hamiltonian) there is a symmetry $\mathbf{k} \leftrightarrow -\mathbf{k}$ in the reciprocal space, $\epsilon_{i\mathbf{k}\sigma} = \epsilon_{i-\mathbf{k}\sigma}$. This means we only have to calculate half of the Brillouin zone.
- *Spatial symmetry*: The real-space and the reciprocal-space lattice have the same symmetries, thus all real-space symmetry operations can be applied in the reciprocal space. This reduces the Brillouin zone to a small irreducible part for which the Kohn-Sham equations need to be solved. This leads to huge savings in the eigenvalue part. The rest of the Brillouin zone the solutions can be reconstructed from the irreducible part.
- *Inversion symmetry*: Furthermore, in systems that possess inversion symmetry both the Hamiltonian and the overlap matrix are real symmetric rather than complex hermitian, provided that the basis functions obey $\phi(-\mathbf{r}) = \phi^*(\mathbf{r})$. This leads to lower memory demands for storage and faster computation.
- *Density/potential representation*: Physical observables such as the density and the potential have the symmetry of the lattice. Consequently many expansion coefficients are identical, or even zero. As shown on page 80, the definition of stars and lattice harmonics leads to an efficient storage and computation of these quantities.
- *Symmetry-equivalent atoms*: If two or more atoms can be mapped onto each other by virtue of one symmetry operation, they are said to form one *atom type*. All equivalent atoms share the same radial functions $u_l(r)$ and have the same muffin-tin contribution (apart from a symmetry operation applied) to the Hamiltonian. Thus, this contribution needs only be calculated once, which reduces the computational effort.

Parameters to the DFT Calculation The following are the most important parameters of a FLAPW DFT calculation:

- First of all the system has to be specified: atomic positions and element numbers, lattice structure and constants.
- The cut-offs l_{\max}^{LAPW} , G_{\max}^{LAPW} determine the size of the LAPW basis set, cut-offs for the density and potentials are commonly provided as well.
- The radius of the muffin-tin spheres are usually chosen as large as possible, with an exponential radial grid inside the spheres.
- Extensions to the basis set such as local orbitals can be included into the basis set to increase its flexibility.
- The \mathbf{k} point sampling is crucial for the integrated densities, in particular for the description of the Fermi surface in case of metals.
- Finally the choice of the exchange-correlation functional. In FLEUR different LDA and GGA functionals are implemented. In the calculations in chapter 6 the PW92 LDA functional is used.

5.3 ALDA and the Mixed Product Basis

5.3.1 The Dyson equation in basis notation

Also two-point functions such as the Kohn-Sham response can be conveniently represented in a basis. We use the spin-independent mixed product basis introduced below which is denoted by M_{Iq} with the capital basis index I . It obeys the closure and orthonormality relations (5.6) and (5.7) (with M instead of ϕ). The susceptibility expressed in this basis reads

$$\chi(\mathbf{r}, \mathbf{r}'; \mathbf{q}, \omega) = \sum_{I,J} M_{Iq}(\mathbf{r}) \chi_{IJ}(\mathbf{q}, \omega) M_{Jq}^*(\mathbf{r}') \quad (5.35)$$

$$\chi_{IJ}(\mathbf{q}, \omega) = \langle \tilde{M}_{Iq} | \chi(\mathbf{q}, \omega) | \tilde{M}_{Jq} \rangle = \int \tilde{M}_{Iq}^*(\mathbf{r}) \chi(\mathbf{r}, \mathbf{r}'; \mathbf{q}, \omega) \tilde{M}_{Jq}(\mathbf{r}') d^3r d^3r'. \quad (5.36)$$

The Kohn-Sham response (5.5) in particular takes the form

$$\chi_{\text{KS},IJ}^{+-}(\mathbf{q}, \omega) = \lim_{\eta \rightarrow 0^+} \int d^3k \sum_{n,n'} \frac{f(\epsilon_{nq\uparrow}) - f(\epsilon_{n'q+k\downarrow})}{\omega - (\epsilon_{n'q+k\downarrow} - \epsilon_{nq\uparrow}) + i\eta} \langle \tilde{M}_{Ik} \varphi_{nk\uparrow} | \varphi_{n'k+q\downarrow} \rangle \langle \varphi_{n'k+q\downarrow} | \varphi_{nk\uparrow} \tilde{M}_{Jk} \rangle. \quad (5.37)$$

The basis representation of the exchange-correlation kernel f_{xc} is conveniently chosen in the original basis M instead of \tilde{M} ,

$$f_{\text{xc},IJ}^{+-} = \langle M_{Iq} | f_{\text{xc}}^{+-} | M_{Jq} \rangle. \quad (5.38)$$

It should be noted that local functions are not necessarily diagonal in a basis representation; also real functions might have complex matrix elements depending on the chosen basis. The Dyson equation for the spin-flip susceptibility χ^{+-} in basis $\{M\}$ reads

$$\chi_{IJ}^{+-}(\mathbf{q}, \omega) = \chi_{\text{KS},IJ}^{+-}(\mathbf{q}, \omega) + \left(\frac{\mu_{\text{B}} g}{2} \right)^2 \sum_{K,L} \chi_{\text{KS},IK}^{+-}(\mathbf{q}, \omega) f_{\text{xc},KL}^{+-}(\mathbf{q}) \chi_{LJ}^{+-}(\mathbf{q}, \omega) \quad (5.39)$$

which is equivalent to (3.64) if the latter is understood as a matrix equation in the mixed product basis set. The projection (3.40) onto plane waves becomes a vector-matrix-vector product

$$\chi^{+-}(\mathbf{q}, \omega) = \sum_{I,J} e_{qI}^* \chi_{IJ}^{+-}(\mathbf{q}, \omega) e_{qJ} \quad (5.40)$$

with the plane-wave vectors

$$e_{qI} = \langle M_{qI} | e^{i\mathbf{q}\mathbf{r}} \rangle = \int d^3r M_{qI}^*(\mathbf{r}) e^{+i\mathbf{q}\mathbf{r}}. \quad (5.41)$$

The formulas for the dielectric case are analogous. The work flow resulting from these formulas is plotted in figure 5.4. If the vector \mathbf{q} is from the \mathbf{k} -point mesh the one-shot DFT calculation needs to be performed only once.

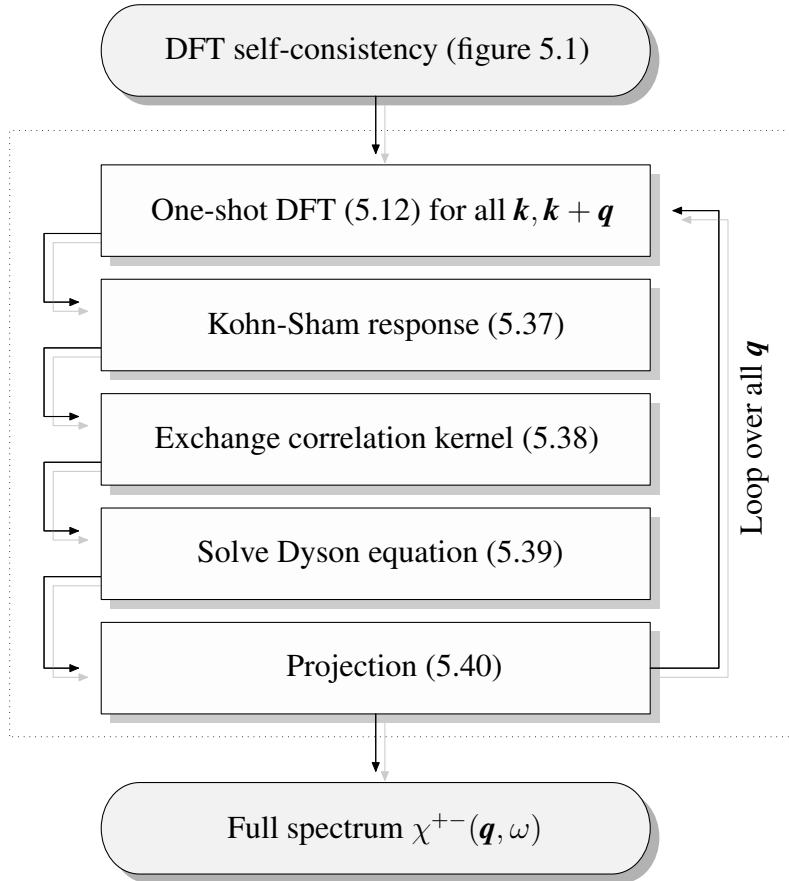


Figure 5.4: A sketch of the work flow of a TDDFT calculation of a spin response spectrum. Starting from a converged DFT calculation, a full response spectrum for a set of \mathbf{q} vectors is obtained by solving the Dyson equation for each \mathbf{q} vector independently (the steps in the dotted box). In the presented implementation, the DFT part is performed within the FLAPW method, while the other steps in the box utilize the mixed product basis set.

5.3.2 The Mixed Product Basis

The LAPW basis was chosen such that it properly represents the Kohn-Sham wave functions. Therefore the LAPW basis is well suited for the treatment of the Kohn-Sham equations. The solution of the Dyson equation, on the other hand, involves as a key ingredient the Kohn-Sham response χ_{KS}^{+-} (5.5) which contains products of wave functions. The so-called *mixed product basis* set of functions is designed in order to properly represent wave-function products. The current implementation [FSBK06] is inspired by an earlier work of Aryasetiawan [AG94]. First of all the set M of mixed product basis functions is a union set of muffin-tin and interstitial functions

$$M = \{M^{\text{MT}}, M^{\text{IS}}\} \quad (5.42)$$

which are non-zero only in their corresponding region. Unlike in the LAPW basis set, muffin-tin and interstitial functions are independent and not matched at the muffin-tin sphere boundary. Thus, the basis functions are not continuous at these boundary. However, if the basis set

is fully converged (by increasing the parameters G_{\max} and l_{\max} which are introduced shortly) products of wave functions – which are continuous – are exactly represented.

In the interstitial region, a product of two wave functions which are expanded in plane waves is conveniently represented in plane waves again. Therefore the interstitial basis functions read

$$M_{\mathbf{k},I}^{\text{IS}}(\mathbf{r}) = \frac{1}{\sqrt{V}} e^{i(\mathbf{k}+\mathbf{G}_I)\mathbf{r}} \Theta^{\text{IS}}(\mathbf{r}). \quad (5.43)$$

with the interstitial step function

$$\Theta^{\text{IS}}(\mathbf{r}) = \begin{cases} 1 & \text{if } \mathbf{r} \in \text{IS} \\ 0 & \text{else.} \end{cases} \quad (5.44)$$

The set of \mathbf{G} vectors is chosen such that $|\mathbf{k} + \mathbf{G}| < G_{\max}^{\text{MB}}$. In order to exactly represent the product of two LAPW wave functions, a value of the convergence parameter $G_{\max}^{\text{MB}} \geq 2G_{\max}^{\text{LAPW}}$ is necessary. In practice, however, a lower cut-off value such as $G_{\max}^{\text{MB}} \approx G_{\max}^{\text{LAPW}}$ is sufficient.

Products of spherical harmonics yield a linear combination of spherical harmonics, due to the relation

$$Y_{l'm'}^*(\hat{\mathbf{r}}) Y_{l''m''}(\hat{\mathbf{r}}) = \sum_{l,m} G_{l'm',l''m'',lm} Y_{lm}(\hat{\mathbf{r}}) \quad (5.45)$$

where

$$G_{l'm',l''m'',lm} = \int Y_{l'm'}^*(\hat{\mathbf{r}}) Y_{l''m''}(\hat{\mathbf{r}}) Y_{lm}(\hat{\mathbf{r}}) d^2\hat{\mathbf{r}} \quad (5.46)$$

are the Gaunt coefficients. Consequently, the muffin-tin basis functions are defined

$$M_I^{\text{MT}}(\mathbf{r}) = \Phi_I(|\mathbf{r} - \mathbf{R}_{\mu_I}|) Y_{lm}(\widehat{\mathbf{r} - \mathbf{R}_{\mu_I}}) \Theta^{\text{MT}\mu}(\mathbf{r}). \quad (5.47)$$

Here the muffin-tin step function of sphere μ is defined

$$\Theta^{\text{MT}\mu}(\mathbf{r}) = \begin{cases} 1 & \text{if } \mathbf{r} \in \text{MT}\mu \\ 0 & \text{else.} \end{cases} \quad (5.48)$$

Φ_I is the radial function of muffin-tin basis function of index I which is a composite index $I = (l_I n_I m_I \mu_I)$. The construction of these radial functions is described in the next paragraph. A crucial difference between the LAPW muffin-tin function set and the mixed product basis muffin-tin function set is the fact that the latter one can contain more than one radial function Φ_{nl} per l character denoted by the index n , in contrast to the LAPW radial functions u_l (neglecting the muffin-tin index μ for the moment).

In the construction of the mixed product basis functions all $l \leq l_{\max}^{\text{MB}}$ are taken into account. This l_{\max}^{MB} is a crucial convergence parameter of the method. Two angular momenta l' and l'' can be combined to new quantum numbers l in the range $|\mathbf{l}' - \mathbf{l}''| \leq l \leq \mathbf{l}' + \mathbf{l}''$. The wave functions are represented by LAPW basis functions with $l \leq l_{\max}^{\text{LAPW}}$. A product of two such wave functions contain contributions of angular momentum quantum number $l \leq 2l_{\max}^{\text{LAPW}}$.

l	\bar{n}_l	n_l	N_l
0	54	13	13
1	112	12	49
2	160	11	104
3	194	10	174
4	218	9	255
5	228	8	343
6	228	8	447
7	214	7	552
8	190	7	671

SELECT=(8,8;8,8)

l	\bar{n}_l	n_l	N_l
0	18	9	9
1	36	9	36
2	44	8	76
3	38	8	132
4	22	6	186

SELECT=(2,2;3,3)

l	\bar{n}_l	n_l	N_l
0	6	4	4
1	10	6	22
2	12	6	52
3	10	5	87
4	6	3	114

SELECT=(2,-;3,-)

Table 5.2: The number of basis functions for three different parameter settings for fcc Nickel.

For each l there are \bar{n}_l product functions which reduce to n_l functions due to linear dependency. $N_l = \sum_{l'=0}^l n_{l'}(2l'+1)$ is the resulting number of muffin-tin basis functions for $l_{\max}^{\text{MB}} = l$. The cut-offs for the construction of the product functions are given below each table in the form $\text{SELECT}=(l_{\max}^{\text{occ}}, j_{\max}^{\text{occ}}, l_{\max}^{\text{unocc}}, j_{\max}^{\text{unocc}})$. The tolerance to drop eigenvalues is 10^{-4} .

For a complete representation of these products one would thus need $l_{\max}^{\text{MB}} = 2l_{\max}^{\text{LAPW}}$. Experience shows, however, that a significantly lower cut-off works as well which is a significant saving, see table 5.2.

The above definition (5.47) is sufficient if matrix elements of a local function – such as the exchange-correlation kernel – need to be evaluated. For a general two-point function (for instance the Coulomb potential) a more general definition has to be constructed.

Construction of the Radial Functions In a first step intermediate radial product functions $\bar{\Phi}$ are constructed by all combinations of radial functions u_l and \dot{u}_l ,

$$\bar{\Phi}_{l\bar{n}}(\mathbf{r}) = \begin{cases} u_{l'}(\mathbf{r})u_{l''}(\mathbf{r}) \\ u_{l'}(\mathbf{r})\dot{u}_{l''}(\mathbf{r}) \\ \dot{u}_{l'}(\mathbf{r})u_{l''}(\mathbf{r}) \\ \dot{u}_{l'}(\mathbf{r})\dot{u}_{l''}(\mathbf{r}), \end{cases} \quad (5.49)$$

with valid angular momentum $|l' - l''| \leq l \leq l' + l''$. The number of such combinations is denoted \bar{n}_l , so $1 \leq \bar{n} \leq \bar{n}_l$. Independently for each muffin-tin sphere and l quantum number the overlap matrix of these functions is calculated and diagonalized. Very small eigenvalues (i.e., below a certain tolerance) indicate that eigenvectors are nearly linear dependent. This can cause numerical instabilities, thus these eigenvectors are dropped. The remaining eigenvectors are linear combinations of $\bar{\Phi}_{l\bar{n}}$; these are the radial functions Φ_{ln} . This procedure can reduce the number of radial functions \bar{n}_l to a lower value n_l , leading to significant computational resource savings. The resulting functions Φ are by construction normalized and orthogonal to each other.

Further it is possible to restrict the number of radial functions $u_{l'}$, $u_{l''}$ used in the construction of products in (5.49). For this one should remember that the mixed product basis

functions are used to build matrix products $\langle \tilde{M}_{Ik} \varphi_{nk\uparrow} | \varphi_{n'k+q\downarrow} \rangle$ in (5.37), including occupied states $\varphi_{nk\uparrow}$ and unoccupied states $\varphi_{n'k+q\downarrow}$. Therefore two separate cut-off values are chosen for the radial functions which contribute to (5.49): $l' \leq l_{\max}^{\text{occ}}$ for the occupied and $l'' \leq l_{\max}^{\text{unocc}}$ for the unoccupied states.

This should be illustrated by an example: For a Nickel calculation a cut-off $l_{\max}^{\text{LAPW}} = 10$ is chosen in the DFT part. We expect the main contribution to the susceptibility to come from the s , p and d electrons, thus we choose $l_{\max}^{\text{MB}} = 4$ in order to be capable of representing $d-d$ products. However, many other angular momenta (such as, e.g., $l' = 4$ and $l'' = 7$) can combine as well to $l = 4$, which we consider as an insignificant but computationally demanding contribution. Thus, the cut-offs $l_{\max}^{\text{occ}} = 2$ and $l_{\max}^{\text{unocc}} = 3$ have been chosen.

In order to properly represent products of LAPW wave functions, it is actually not sufficient to use the radial functions u_l in (5.49), but the energy derivatives \dot{u}_l have to be used as well. Consequently they are treated on the same footing, and additional limits l_{\max}^{occ} and l_{\max}^{unocc} are used. In practice it turns out that in many cases the energy derivatives can be omitted, i.e., one obtains accurate results with a mixed product basis comprising only the original radial LAPW functions u_l . Furthermore, it should be noted that the number of nodes of the radial function (i.e., the number of r values for which $\Phi(r) = 0$) is not directly related to the l quantum number. While an LAPW radial function $u_l(r)$ of quantum numbers n and l has $n - l - 1$ nodes, a product function $\Phi_{ln}(r)$ does not have a fixed number of nodes since it is constructed from many products $u_{l'}(r)u_{l''}(r)$ (or products involving $\dot{u}_{l'}(r)$, $\dot{u}_{l''}(r)$ with $|l' - l''| \leq l \leq l' + l''$).

An example of the construction of the set of radial product basis functions is shown in table 5.2 for a Nickel calculation for three different parameter sets, denoted by the SELECT statements. On the left large cut-offs are chosen leading to a very large basis set of 671 muffin-tin basis functions. Restricting oneself to that part of the basis that can properly represent $d-d$ wave function products leads to a set of 186 functions. Omitting the energy derivatives further reduces the set to 114 functions. Since the setup of the Kohn-Sham susceptibility is the main part of the calculation, its computation time scales roughly to the square of the basis size. Thus, a small basis set is essential for reasonably fast calculations, as well as for a sufficiently low memory demand.

A few generalizations to the procedure to build the radial product functions as discussed above should be pointed out which are possible and partly implemented.

- Other extensions to the set of LAPW basis function should be included into the mixed product basis functions. SPEX allows for the inclusion of FLEUR local orbitals (c.f., paragraph on page 84). Also the wave functions of the core electrons can be used.
- The present implementation actually offers the inclusion of arbitrary radial functions, if the need arises to represent functions very different from the usual product functions.
- The LAPW radial functions u_l are actually spin-dependent: For each spin a different energy $E_{l\mu\sigma}$ is used in (5.21). This has not been denoted in (5.49). In the code both spin up-up and spin down-down products are used in the construction of functions $\bar{\Phi}_{l\bar{n}}$ in (5.49).
- Inside the muffin-tin spheres the LAPW code generates basis functions from the scalar-relativistic approximation, consisting of a large and a small component (see page 83).

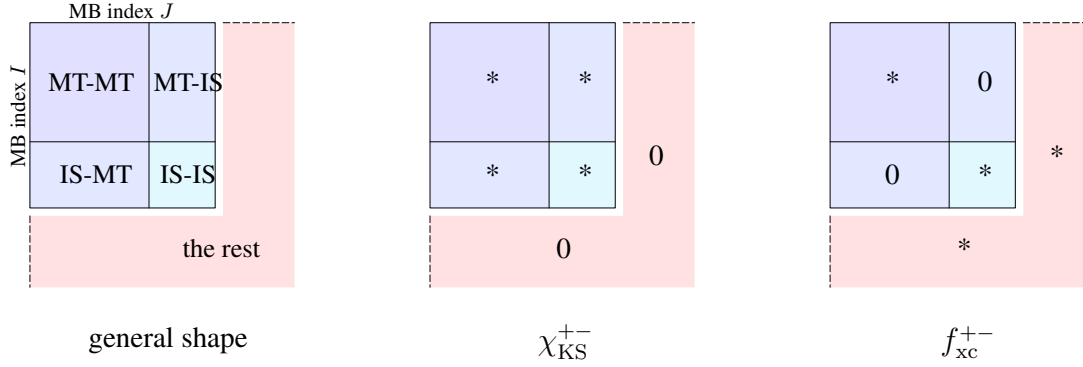


Figure 5.5: Left: Illustration of a general two-point function represented in the mixed product basis (blue region), abbreviated MB. It consists of representations of muffin-tin (MT-MT) and interstitial (IS-IS) parts (i.e., both coordinates from this spatial region), and cross parts (MT-IS and IS-MT). The red region indicates additions to the MB that would be needed in order to make it a complete basis. Center and right: The particular shape of the Kohn-Sham susceptibility and the kernel in MB representation. Stars indicate values that can in general be unequal zero.

In the construction of the product functions both components are taken into account by means of a spinor multiplication (regarding the two functions as spinors of large and small component).

Incompleteness of the Basis It should be noted that the mixed product basis is not complete, i.e., it is not suitable to represent a general two-point function. This is sketched in figure 5.5: The square on the left side is a matrix representation of a two-point function. The representation in the mixed product basis corresponds to the bluish region. If the basis set is augmented by (a possibly infinite number of) additional basis functions to make it complete, the matrix extends over the red region. However, the (fully converged) mixed product basis is well suited to fully represent the Kohn-Sham response χ_{KS}^{+-} , thus it only has zero values in the red regions (middle sketch). The mixed product basis representation can further be divided into pure muffin-tin sphere and pure interstitial regions (denoted MT-MT and IS-IS) and cross contributions (denoted MT-IS and IS-MT). The exchange-correlation kernel in ALDA has only zero values in the cross contributions (see right sketch), since it is a local function. But it could have significant contributions in the red region.

However, even if the exchange-correlation kernel is not well represented in the mixed product basis, it is sufficient nevertheless because its essential parts are represented. This is due to the Dyson equation which is sketched in figure 5.6 in the mixed product basis representation. Provided that the contributions of the exchange-correlation kernel in the red regions are finite, they are multiplied with zeros from the red region of the susceptibility χ_{KS}^{+-} . Subsequently the red region of the full susceptibility is zero and χ^{+-} has the same shape as the Kohn-Sham susceptibility, i.e., the complete red region is zero, and the Dyson equation can be solved in the mixed product basis, i.e., the bluish regions of the matrices.

$$\begin{array}{c}
 \begin{array}{|c|c|} \hline * & * \\ \hline * & * \\ \hline \end{array} \begin{array}{c} \\ 0 \end{array} \\
 \hline \\
 \begin{array}{|c|} \hline 0 \\ \hline \end{array} \\
 \chi^{+-}
 \end{array}
 =
 \begin{array}{c}
 \begin{array}{|c|c|} \hline * & * \\ \hline * & * \\ \hline \end{array} \begin{array}{c} \\ 0 \end{array} \\
 \hline \\
 \begin{array}{|c|} \hline 0 \\ \hline \end{array} \\
 \chi_{\text{KS}}^{+-}
 \end{array}
 +
 \begin{array}{c}
 \begin{array}{|c|c|} \hline * & * \\ \hline * & * \\ \hline \end{array} \begin{array}{c} \\ 0 \end{array} \\
 \hline \\
 \begin{array}{|c|} \hline 0 \\ \hline \end{array} \\
 \chi_{\text{KS}}^{+-}
 \end{array}
 \begin{array}{c}
 \begin{array}{|c|c|} \hline * & 0 \\ \hline 0 & * \\ \hline \end{array} \begin{array}{c} \\ * \end{array} \\
 \hline \\
 \begin{array}{|c|} \hline * \\ \hline \end{array} \\
 \left(\frac{\mu_{\text{B}}g}{2}\right)^2 f_{\text{xc}}^{+-}
 \end{array}
 \begin{array}{c}
 \begin{array}{|c|c|} \hline * & * \\ \hline * & * \\ \hline \end{array} \begin{array}{c} \\ 0 \end{array} \\
 \hline \\
 \begin{array}{|c|} \hline 0 \\ \hline \end{array} \\
 \chi^{+-}
 \end{array}$$

Figure 5.6: The Dyson equation (5.39) illustrated in the mixed product basis. Due to the particular shape of χ_{KS}^{+-} (see figure 5.5) the mixed-basis is sufficient to completely represent the Dyson equation. Extensions to the basis (red regions) are not necessary.

5.3.3 TDDFT Implementation Details

The Kohn-Sham Susceptibility The formula for the Kohn-Sham susceptibility χ_{KS}^{+-} in the mixed product basis is already provided in (5.37). Actually, the SPEX code initially calculates the spectral function – which is closely related (see (3.34)) and has a very similar shape in the mixed product basis – on a special exponential mesh of frequencies. From this the real and imaginary parts can be obtained by means of a Hilbert transformation.

As is apparent from (5.37), inside the integral and summations the frequency-dependent denominator can be separated from the frequency-independent matrix elements. The \mathbf{k} -space integration is performed by means of the tetrahedron method which is well suited to handle the δ -functions of the frequency term.

The ALDA Exchange-Correlation Kernel The ALDA kernel $f_{\text{xc}}^{+-}(n, \xi)$ has been derived in chapter 4.3 for the homogeneous electron gas, c.f., formulas (4.65) and (4.85). According to the connection to non-homogeneous systems given in (4.96) the exchange-correlation kernel in the mixed product basis reads

$$f_{\text{xc},IJ}^{+-} = \langle M_I | f_{\text{xc}}^{+-} | M_J \rangle \quad (5.50)$$

$$= \int_{u.c.} f_{\text{xc}}^{+-}(\mathbf{r}) M_I^*(\mathbf{r}) M_J(\mathbf{r}) d^3r. \quad (5.51)$$

This evaluation can be performed analogously to the evaluation of functions in the LAPW basis on page 82. The charge density for both spin channels is provided in stars and lattice harmonics, respectively. First it is transformed back to real space $n_{\sigma}(\mathbf{r})$ where the kernel function $f_{\text{xc}}^{+-}(n, \xi)$ is applied. In a third step it is transformed to its mixed product basis representation according to (5.51):

$$\left. \begin{array}{l} n_{s\sigma}^{\text{star}} \\ n_{\mu\nu\sigma}^{\text{lh}} \end{array} \right\} \rightarrow n_{\sigma}(\mathbf{r}) \rightsquigarrow f_{\text{xc}}^{+-}(\mathbf{r}) \rightarrow f_{\text{xc},IJ}^{+-}. \quad (5.52)$$

Dyson Equation After $\chi_{\text{KS},IJ}^{+-}(\mathbf{q}, \omega)$ and $f_{\text{xc},IJ}^{+-}$ are calculated the Dyson equation (5.39) can be solved for the renormalized susceptibility $\chi^{+-}(\mathbf{q}, \omega)$ by matrix inversion. The projection according to (5.40), (5.41) yields the macroscopic quantity.

Symmetries The central point where symmetries can be taken advantage of in the ALDA work flow is the Brillouin-zone integration in the Kohn-Sham susceptibility (5.37). An equidistant \mathbf{k} -point mesh is chosen. If the \mathbf{q} vector is from this mesh the integration is performed on, any vector $\mathbf{k} + \mathbf{q}$ lies on this mesh as well. Any vector \mathbf{k} or $\mathbf{k} + \mathbf{q}$ can be mapped to one vector inside the irreducible Brillouin zone (which also lies on the chosen \mathbf{k} point mesh), and the eigenenergies at this vector are identical to energies at the corresponding IBZ \mathbf{k} vector. The eigenvectors can be obtained from the eigenvectors at the IBZ \mathbf{k} vector by means of a transformation.

As a consequence, if the \mathbf{q} vector is from the \mathbf{k} point mesh one can restrict the \mathbf{k} point integration for χ_{KS}^{+-} to the irreducible zone. (This means that \mathbf{k} is from the IBZ, while $\mathbf{k} + \mathbf{q}$ cannot be restricted to the IBZ.) However, there is the additional effort of the mentioned transformation on the eigenvectors. If, on the other hand, the \mathbf{q} vector lies off the \mathbf{k} point set, symmetry cannot be exploited and on the whole Brillouin zone the integration has to be applied on.

Another symmetry that can actively be exploited is the inversion symmetry. For this the mixed product basis needs to be modified such that $M_I(\mathbf{r}) = M_I^*(-\mathbf{r})$. In this case the plane-wave coefficients provided by the DFT program are real. Furthermore, several quantities represented in the mixed product basis are real instead of complex, e.g., the matrix elements in (5.37) and the overlap and transformation matrices (c.f., previous paragraph on the slimmed basis) as well as the Coulomb, the exchange-correlation kernel and the susceptibility matrices.

Special Treatment at the Γ Point For \mathbf{q} vectors approaching $\mathbf{q} = \mathbf{0}$ numerical problems can arise in the computation of (5.37) since both numerator and denominator can take very small values. In the case $\mathbf{q} = \mathbf{0}$ one can separate the band transitions into inter-band and intra-band transitions, the latter one of which occurs only for metals and contributes a δ -peak at $\omega = 0$ to the imaginary part of the Kohn-Sham susceptibility. For this limit explicit formulas are derived and implemented.

Furthermore, the Coulomb potential reveals a divergence in the case $\mathbf{q} \rightarrow \mathbf{0}$ according to (5.15). This has to be taken care of properly, however, only for the Dyson equations of RPA and dielectric TDDFT involving the Coulomb potential, and not for the magnetic case where the Coulomb interaction does not appear.

Data needed from DFT The following data are passed from the FLEUR DFT program to the SPEX code:

- First of all the system setup is needed, such as the unit cell geometry, atomic positions and symmetry operations.
- LAPW basis information such as muffin-tin sphere radii, radial meshes and radial functions as well as $I_{\text{max}}^{\text{LAPW}}$ and $G_{\text{max}}^{\text{LAPW}}$ cut-offs, parameters for local orbitals.
- The \mathbf{k} points used in the DFT calculation. In the current calculations the \mathbf{k} point set is generated in advance by the SPEX code. This single \mathbf{k} point set is used for both DFT and TDDFT calculations.

- The eigenvalues and eigenvectors for a sufficient number of bands on the given k point set.
- For the exchange-correlation kernel: The symmetrized stars and lattice harmonics and the charge density stored in this data structure.

Parameters for the Calculation of the Response The following parameters can be adjusted in order to reach convergence:

- Most prominently the mesh of k points. It is created in advance and used for both the DFT and TDDFT step of the calculation.
- The size of the mixed product basis is modified with the l_{\max}^{MB} and G_{\max}^{MB} cut-offs. Furthermore, one can select the amount of functions that are used in the basis construction by the switches $(l_{\max}^{\text{occ}}, l_{\max}^{\text{occ}}, l_{\max}^{\text{unocc}}, l_{\max}^{\text{unocc}})$, see page 90.
- The frequency mesh on which the spectral function is calculated.
- The number of unoccupied states that are taken into account in the calculation of the Kohn-Sham response χ_{KS}^{+-} .
- Obviously the (\mathbf{q}, ω) points for which the renormalized response $\chi^{+-}(\mathbf{q}, \omega)$ should be calculated.

CHAPTER 6

RESULTS FOR REAL MATERIALS

Contents

6.1	General remarks	95
6.2	Tests of the Method	99
6.3	Iron	103
6.4	Nickel	108
6.5	Cobalt	113
6.6	Comparison to Adiabatic Approximation	118

In this chapter calculations of the spin response within ALDA using the mixed product basis method are presented. First general remarks are made in section 6.1 about the elements that are investigated, the paths in the Brillouin zone, and how the results are presented.

In section 6.2 the convergence and the influence of different parameters are investigated. The resulting parameters which yield both reasonably accurate and efficient calculations are determined.

In sections 6.3 to 6.5 the spin-wave dispersion is determined for the three different elements Iron, Cobalt and Nickel along the three principal directions (001), (011) and (111). Some of the results are compared to other ab initio calculations, either from TDDFT or many-body perturbation theory.

Section 6.6 is devoted to a brief presentation of the frozen-magnon approximation, and a comparison of results of this method and ALDA.

6.1 General remarks

Some general remarks should be made which apply to all the systems which are presented in this chapter. The elements involved in these calculations are the following transition metals:

element	symbol	structure	element number	valence electrons
Iron	Fe	bcc	26	$(3d)^6(4s)^2$
Cobalt	Co	hcp	27	$(3d)^7(4s)^2$
Nickel	Ni	fcc	28	$(3d)^8(4s)^2$

The separation of the electrons into two categories was already discussed in the presentation of the FLAPW code: Those electrons crucial for the chemical interaction between atoms are

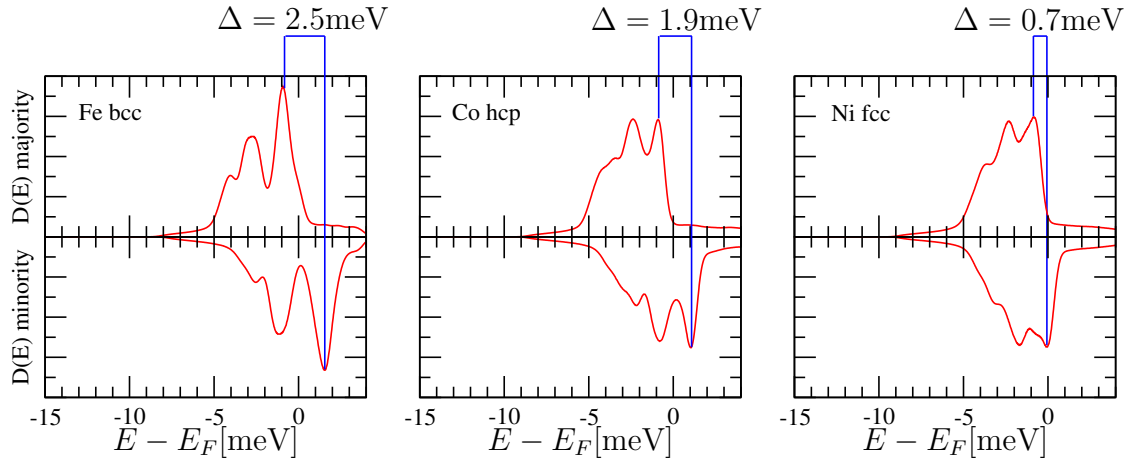


Figure 6.1: The density of states $D(E)$ for the three transition metals Fe, Co and Ni. The experimental lattice constant has been used. The spin splitting is marked with blue lines.

termed valence electrons. The inner electrons which do not interact with the other atoms' electrons are termed core states and treated separately. For the three elements shown above these core states are the 18 electrons $(1s)^2(2s)^2(2p)^6(3s)^2(3p)^6$.

Lattice constants As will be shown later the lattice constant has a significant influence on the resulting spin-wave dispersion. Therefore the following table presents the experimental as well as the theoretical lattice constants, the latter ones which are obtained as the minimum with respect to the lattice parameter of the total energy from a corresponding DFT calculation. All DFT calculations are performed with the aforementioned Perdew-Wang LDA parametrization (PW92) of the exchange-correlation energy. All calculations are performed with one atom per unit cell, with the exception of hcp Cobalt which has two atoms in the unit cell.

system	$a_{\text{exp}}[\text{pm}]$	$a_{\text{exp}}[a_{\text{B}}]$	$m^{\text{LDA}}[\mu_{\text{B}}]$	$a_{\text{th}}[\text{pm}]$	$a_{\text{th}}[a_{\text{B}}]$	$m^{\text{LDA}}[\mu_{\text{B}}]$	d
Iron bcc	286.7	5.418	2.21	275.2	5.201	0.00	-4.0%
Iron fcc	361.2	6.826	2.09	337.5	6.378	2.01	-6.5%
Cobalt bcc	280.9	5.308	1.69	273.4	5.167	1.65	-2.7%
Cobalt fcc	353.9	6.688	1.62	342.7	6.476	1.55	-3.1%
Cobalt hcp	(a) 250.7 (c) 407.0	4.738 7.691	1.62	— —	— —	—	—
Nickel bcc	279.7	5.286	0.72	272.2	5.143	0.38	-2.7%
Nickel fcc	352.4	6.659	0.64	342.4	6.471	0.57	-2.8%

The experimental lattice constants for the physical systems written in bold face (i.e., body-centered cubic for Iron, face-centered cubic for Nickel and hexagonal close-packed for Cobalt) are taken from literature [tptotn]. The “experimental” lattice constants of the non-physical structures are calculated from the true experimental ones by conserving the volume per atom. The hexagonal Cobalt structure is characterized by two two lattice constants, parameter a in hexagonal plane and parameter c perpendicular to it. The volume

of the unit cell is $V = 3a^2c \sin(60^\circ)$. For this structure the theoretical lattice constants have not been determined. The percental difference d of theoretical to experimental lattice constant is determined as

$$d = \frac{a_{\text{th}} - a_{\text{exp}}}{a_{\text{exp}}}. \quad (6.1)$$

The values of d are negative, indicating the well-known fact that LDA underestimates the true lattice constant. For the given lattice constants the magnetic moments m^{LDA} from an LDA calculation are shown as well. This value is the magnetic moment of the whole unit cell, not only that one from the muffin-tin spheres. For these calculations a $24 \times 24 \times 24$ \mathbf{k} -points set has been used.

Shape of and Special Points in the Brillouin Zone The real-space and reciprocal-space basis vectors of the three structures fcc, bcc and hcp are given by the matrices

$$A^{\text{fcc}} = \frac{a}{2} \begin{pmatrix} 0 & 1 & 1 \\ 1 & 0 & 1 \\ 1 & 1 & 0 \end{pmatrix}, \quad B^{\text{fcc}} = \frac{2\pi}{a} \begin{pmatrix} -1 & 1 & 1 \\ 1 & -1 & 1 \\ 1 & 1 & -1 \end{pmatrix}, \quad (6.2)$$

$$A^{\text{bcc}} = \frac{a}{2} \begin{pmatrix} -1 & 1 & 1 \\ 1 & -1 & 1 \\ 1 & 1 & -1 \end{pmatrix}, \quad B^{\text{bcc}} = \frac{2\pi}{a} \begin{pmatrix} 0 & 1 & 1 \\ 1 & 0 & 1 \\ 1 & 1 & 0 \end{pmatrix}, \quad (6.3)$$

$$A^{\text{hcp}} = \begin{pmatrix} \frac{a}{2} & \frac{a}{2} & 0 \\ \frac{a\sqrt{3}}{2} & -\frac{a\sqrt{3}}{2} & 0 \\ 0 & 0 & c \end{pmatrix}, \quad B^{\text{hcp}} = \begin{pmatrix} \frac{2\pi}{a} & \frac{2\pi}{a\sqrt{3}} & 0 \\ \frac{2\pi}{a} & -\frac{2\pi}{a\sqrt{3}} & 0 \\ 0 & 0 & \frac{2\pi}{c} \end{pmatrix}. \quad (6.4)$$

Some high-symmetry points in the reciprocal cells of these three structures (all written as row vectors) which lie on the surface of the Brillouin zone read

$$\text{fcc :} \quad X = \frac{2\pi}{a}(0, 0, 1) \quad K = \frac{\pi}{a}\left(0, \frac{3}{2}, \frac{3}{2}\right) \quad L = \frac{\pi}{a}(1, 1, 1) \quad (6.5)$$

$$\text{bcc :} \quad H = \frac{2\pi}{a}(0, 0, 1) \quad N = \frac{\pi}{a}(0, 1, 1) \quad P = \frac{\pi}{a}(1, 1, 1) \quad (6.6)$$

$$\text{hcp :} \quad K = \frac{2\pi}{a}\left(\frac{2}{3}, 0, 0\right) \quad M = \frac{2\pi}{a}\left(\frac{1}{2}, \frac{1}{3}, 0\right) \quad A = \frac{\pi}{c}(0, 0, 1). \quad (6.7)$$

The point $\Gamma = (0, 0, 0)$ is common to all lattices. These vectors \mathbf{q} are given in cartesian coordinates. If expressed in terms of the lattice vectors \mathbf{q}' , i.e.,

$$\mathbf{q} = B\mathbf{q}' \quad (6.8)$$

with the Bravais matrix of the reciprocal space B for the given structure, the mentioned coordinates read

$$\text{fcc :} \quad X' = \frac{1}{2}(1, 1, 0) \quad K' = \frac{3}{8}(2, 1, 1) \quad L' = \frac{1}{2}(1, 1, 1) \quad (6.9)$$

$$\text{bcc :} \quad H' = \frac{1}{2}(1, 1, -1) \quad N' = \frac{1}{2}(1, 0, 0) \quad P' = \frac{1}{4}(1, 1, 1) \quad (6.10)$$

$$\text{hcp :} \quad K' = \frac{1}{3}(1, 1, 0) \quad M' = \frac{1}{2}(1, 0, 0) \quad A' = \frac{1}{2}(0, 0, 1). \quad (6.11)$$

Paths in the Brillouin Zone The paths along the lines of highest symmetry, involving the coordinates above, are labeled:

Path name	direction	path in fcc	path in bcc	Path name	path in hcp
Δ	(001)	$\Gamma \rightarrow X$	$\Gamma \rightarrow H$	T	$\Gamma \rightarrow K$
Σ	(011)	$\Gamma \rightarrow K$	$\Gamma \rightarrow N$	Σ	$\Gamma \rightarrow M$
Λ	(111)	$\Gamma \rightarrow L$	$\Gamma \rightarrow P$	Δ	$\Gamma \rightarrow A$

The paths along the basis vectors are symmetric: Let \mathbf{B}_1 be one basis vector of the reciprocal lattice (i.e., one row of the Bravais matrix B), and M be the middle point of this vector. Then, the paths $\Gamma \rightarrow M$ and $\mathbf{B}_1 \rightarrow M$ are symmetry equivalent and the spin-response function is identical for corresponding \mathbf{q} vectors from these two paths. However, not all of the paths above are complete symmetric paths in this sense.

This should be exemplified for the fcc structure: The point X lies half the way from the Γ -point to a neighboring reciprocal lattice point in (001) direction, it is just the middle point M . Continuing the path $\Gamma \rightarrow X$ beyond X is equivalent to moving towards the Γ point again. The situation is different along the (011) direction. The special point K in this direction does not lie halfway to the next lattice vector in this direction but only three eighth of the way. As a consequence the section from K to the middle point M of the path to the next lattice vector contains spectral information which is not part of the path $\Gamma \rightarrow K$, but additional information. (However, these points can of course be mapped to other points in the irreducible part of the Brillouin zone.)

Therefore the spin-wave spectra which are presented in the following are calculated for the full distance from Γ to the middle point M of the path to the next lattice vector. As pointed out above this point does not necessarily coincide with the common high-symmetry point in this direction. In these cases, M is identical to another high-symmetry points. The resulting paths for the fcc and bcc structures in the three elemental directions then read

direction	fcc path	fcc path length	bcc path	bcc path length
(001)	$\Gamma \rightarrow X$	$\frac{2\pi}{a}$	$\Gamma \rightarrow H$	$\frac{2\pi}{a}$
(011)	$\Gamma \rightarrow K \rightarrow X$	$\frac{2\pi}{a}\sqrt{2}$	$\Gamma \rightarrow N$	$\frac{\pi}{a}\sqrt{2}$
(111)	$\Gamma \rightarrow L$	$\frac{\pi}{a}\sqrt{3}$	$\Gamma \rightarrow P \rightarrow H$	$\frac{2\pi}{a}\sqrt{3}$

Presentation of Spectra In the results sections starting from 6.3 the spin response is presented for all three elements Fe, Co and Ni. Both fcc and bcc structures are calculated, and spectra are shown for all six paths shown above. The dispersion along these paths is shown in one figure each. The dispersion is shifted such that the dispersion starts in the origin. The shift is specified in the according text paragraph.

The basis of the calculation is a $24 \times 24 \times 24$ \mathbf{k} -point mesh. For reasons of performance (see paragraph *Symmetries* on page 93 for more details) the vector \mathbf{q} should be chosen from this set of \mathbf{k} -points. Along each elemental directions this leaves 12 \mathbf{q} -points if the Γ -point is included and the finishing point is omitted.

Since the spin-wave dispersion alone does not show all the useful information, the imaginary part of the spin-response function $\chi^{+-}(\mathbf{q}, \omega)$ is presented as a function of ω . These 12 graphs are distributed into four plot for reasons of clarity. On the right-hand side the resulting spin-wave dispersion $\omega_{\text{sw}}(\mathbf{q})$ is shown. The curves on the left can easily mapped to the according values on the \mathbf{q} axis in the dispersion plot by counting the axis ticks. If the

curve for one given q is identified as a spin-wave peak, the area under the curve is colored on the left, and it is marked in the dispersion plot as a small filled red square with error bars attached. This bar indicate the width of the peak, i.e., the energies ω for which the amplitude of the response function has reduced to half of its maximum value. This does not indicate errors of the method, or an error energy range in which the maximum can be adjusted.

If no clear peak structure can be identified, the area under the curve is not filled. Clear maxima of the curves are noted in the dispersion plot by unfilled red squares without error bars. Occasionally it happens that the response nearly vanishes. This means that it takes very small values – less than $0.1 \frac{1}{\text{Htr}}$ or even much below that – and has no peak structure. This is indicated in the graphs by red circles on the q axis. This should not be interpreted as a spin-wave excitation of zero energy.

It is expected that the dispersion curve has a quadratical form for small q values. In order to illustrate this a green parabola $\omega = Dq^2$ is included in the plot which is scaled such that it matches the spin-wave dispersion $\omega_{\text{sw}}(q)$. The proportionality factor D is the spin-wave stiffness. However, it should be stressed that values obtained in this way are not very accurate, and inaccuracies of 5 to 10 percent are expected. The spin-wave stiffnesses are provided in two different units which are common in literature, mRy a_{B}^2 and [meV \AA^2].

6.2 Tests of the Method

This section describes the testing that has been performed on the code and the influence of the different convergence parameters. There are many parameters which, if changed, induce small changes in the spin response function. Since it is very costly (if possible) in terms of CPU and memory demand to converge all these parameters, one has to make reasonable choices on these parameters which are both in a regime which is nearly converged and which are still sufficiently low to perform the demanded number of calculations. As a result, a certain set of convergence parameters is chosen which is then used for the further calculations of the subsequent sections. calculations of the further

Consistency checks Some checks have been performed to check the correct working of the code.

- A setup for the ALDA code has been constructed which does not have any muffin-tin contributions. In the interstitial region (which then corresponds to the whole unit cell) the eigenvectors have been set to single plane waves. For this setup of the homogeneous electron gas the Kohn-Sham response $\chi_{\text{KS}}^{+-}(\mathbf{q}, \omega)$ has been calculated and successfully compared to the analytical solution (see chapter 4). The convergence is quick, yielding already good results for a 16x16x16 k point mesh. This step checks large parts of the code: the tetrahedron k space integration and the calculation of interstitial matrix elements are covered and the projection to plane waves is partly covered, while the calculation of muffin-tin matrix elements in the susceptibility is not covered by this procedure.
- In the ALDA Dyson equation the exchange-correlation kernel has been replaced with the Coulomb interaction. This RPA renormalization has been calculated and compared to other such results.

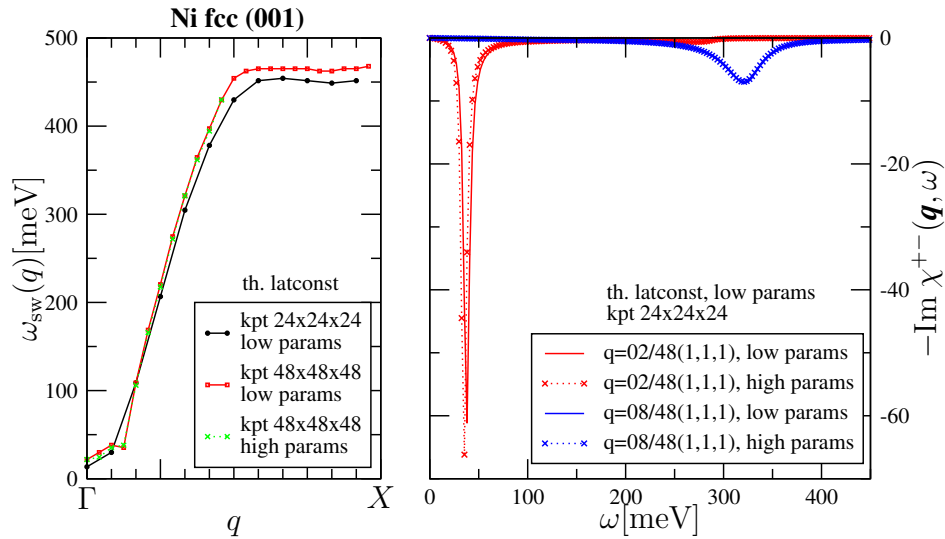


Figure 6.2: Convergence analysis exemplified for Nickel fcc along (001) direction with theoretical lattice constant. Left: The spin-wave dispersion $\omega_{sw}(q)$ for different sets of k -point mesh and mixed-product basis parameters. On the right the full response function is shown for two different q vectors. (This corresponds to two points from each the green and the red curve on the left side.)

- A modification of the muffin-tin sphere radius makes significant changes to the values that are processed, but do not significantly change the end result, just as it needs to be.

Convergence parameters There are a number of convergence parameters involved in the ALDA part of the calculation. The most important ones are the interstitial and muffin-tin cut-off parameters of the mixed-product basis – G_{\max}^{MB} , l_{\max}^{MB} and the SELECT statement, c.f. page 90 – the number of unoccupied bands and the number of frequency points for the calculation of the susceptibility, and finally the number of k points for the Brillouin zone sampling.

These parameters have been extensively checked separately. In order to properly present the results, however, two set of these parameters are chosen, excluding the number of k points: One parameter set of values that are considered sufficient (labeled *low params*), and a set of larger chosen parameters (labeled *high params*) which do not lead to significant changes.

label	low	high
G_{\max}^{MB}	2.0	3.0
l_{\max}^{MB}	4	6
SELECT	2,-;3,-	3,-;4,-
# of bands	15	20
# of frequencies	91	193

In figure 6.2 on the left-hand side the spin-wave dispersion is presented for the theoretical lattice constant. It is calculated for two different k point set, a $24 \times 24 \times 24$ set with 413 points in the irreducible zone, and a $48 \times 48 \times 48$ mesh with 2769 points in the IBZ. (For

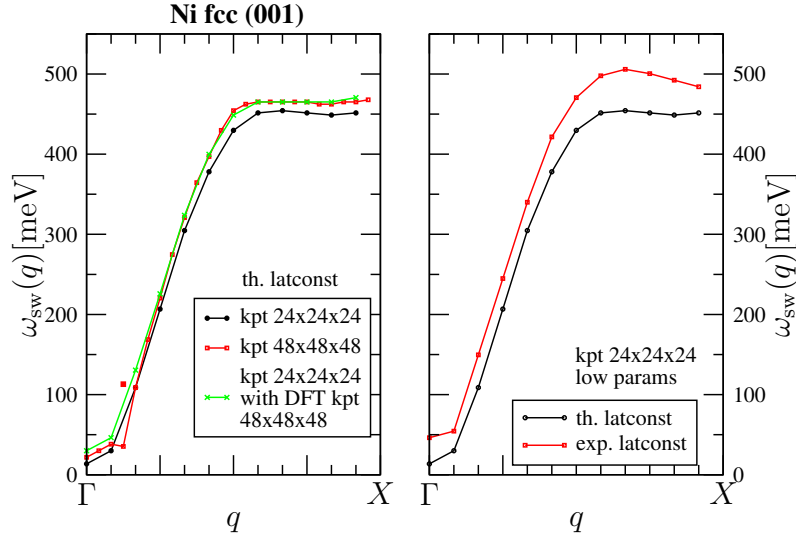


Figure 6.3: Effects on the spin-wave dispersion of Nickel fcc along (001) direction. Left-hand side: Influence of the k -point set in the DFT cycle. Right-hand side: Effect of different lattice constants.

the low params set this are the black and the red curves.) In terms of calculation time there is a factor of around 12 between points on the black and the red curve, and a further factor of around 3.5 between the red and the green curve. There are a few things to be noted:

- Most obvious, the curves do not start at the origin, as it needs to be according to the theory. According to extensive tests, this cannot be cured by higher values for the convergence parameters. The reason for this is still undetermined.
- The differences between the two k point sets are visible but (after shifting to a common origin) fairly small. Since also other points (such as lattice constant, for instance) have a small effect, I consider the smaller k point set sufficient for the desired accuracy.
- The *high params* set does not yield significant changes, see the green curve in the plot. Therefore the *low params* set is considered sufficient for the current calculations.

The effect of the different mixed-product basis parameters is exemplified on the right-hand side of figure 6.2 where the imaginary part of the spin-flip susceptibility is shown for both parameter sets for two different q points. The differences are barely visible for the larger q vector. For the lower q vector the differences are similarly small, but they are more significant due to the smaller peak width. It remains to be determined whether these parameters needs to be increased for very small q vectors, such as for instance $|q| < \frac{1}{100}$, which is way smaller than the q vectors in the calculations of this work.

The lattice constant also has a significant impact on the spin response. This is comprehensible since it modifies the Fermi surface to which the Kohn-Sham response is very sensitive. On the right-hand side of figure 6.3 the spin-wave dispersion is shown for the theoretical and the experimental lattice constant, which demonstrates that the lattice constant (among with other parameters) should be provided with any calculation. A few things are obvious:

- The offset for $q = 0$ changes significantly from $\omega \approx 20\text{meV}$ to $\omega \approx 50\text{meV}$.

- According to the first point on the \mathbf{q} axis, a spin-wave stiffness determined for these curves would yield different values.
- The shape for large \mathbf{q} vectors is different: While the dispersion has a plateau for large \mathbf{q} in case of the theoretical lattice constant, the dispersion decreases in this region for the experimental lattice constant.

Another aspect of convergence was observed in the studies: The \mathbf{k} -point mesh that is used in the DFT cycle is important as well. On the left-hand side of figure 6.3 the dispersion curves for the two \mathbf{k} -point meshes $24 \times 24 \times 24$ and $48 \times 48 \times 48$ are shown in black and red. These are the same curves as in figure 6.2. In these cases the same \mathbf{k} -point sets have been used in the DFT and the ALDA parts of the calculation. Additionally a third curve is shown in green which uses a $24 \times 24 \times 24$ \mathbf{k} -point mesh for the susceptibility, just as the black curve. But in the DFT self-consistency cycle that preceded this ALDA calculation (and from which the data for the ALDA calculation were taken) a larger $48 \times 48 \times 48$ \mathbf{k} -points set has been used. This leads to a significant difference: The offset of the green curve larger than for the two other curves, and for larger \mathbf{q} it has a shape similar to the red curve. Conclusion: The effect of different \mathbf{k} -point sets in the DFT and ALDA steps is not obvious. In order to stay consistent, one should use the same sets.

Additional Insights A few other things have been tested.

- Test calculations have been performed with a drastically simplified exchange-correlation kernel, which uses the $l = 0$ component of the charge density only, which fully neglects the interstitial contribution, and which uses a small- ξ expansion in the formulas of the kernel. The result is that this is a very good approximation. It can thus also serve in some situations as a test to a new implementation.
- In order to test the previous statement (see paragraph *Incompleteness of Basis* on page 91) it was tested whether the fact that the kernel itself is not well represented by the mixed product basis poses a problem. The radial kernel function for $l = 0$ has been added in the procedure to construct the radial functions of the mixed product basis, and calculations have been performed. The differences were not visible with the bare eye. Therefore this can serve as a demonstration that the previous argumentation is indeed correct and only the proper representation of the Kohn-Sham susceptibility (but not of the exchange-correlation kernel) is crucial for spin-response calculations with the mixed product basis method.
- The temperature broadening that is used in the DFT self-consistency cycle for convergence reasons broadens the contribution of one eigenstate among a small energy region, determined by the broadening parameter. A common choice of this parameter is $0.001\text{Htr} \approx 27\text{meV}$. This is a large value compared to spin-wave energies for small \mathbf{q} vectors. Decreasing this parameter leads to slight changes in the dispersion; however, it does not, e.g., close the gap at the origin. The effect is present for a small \mathbf{k} -point set, whereas for a large \mathbf{k} -point set ($48 \times 48 \times 48$) the effect diminishes.

Consequences The preceding investigations lead to the following conclusions:

- For the calculations in the coming chapters a $24 \times 24 \times 24$ k -points set is chosen, which is identical for both the DFT and the ALDA part.
- The set of parameters which has been labeled *low params* above is used.
- The experimental lattice constant is used in favor of the theoretical one.
- As observed the dispersions do not start in the origin. In the following plots the dispersion is simply shifted such that $\omega_{\text{sw}}(0) = 0$. Another possibility would be to scale the exchange-correlation kernel (in the way it was discussed on page 63. The differences of these two procedures should be investigated.
- Due to the choice of cut-offs of the convergence parameters, small changes to the peak positions can be possible. Their accuracy should not be expected to be below 10meV.
- Due to computational constraints, I need to choose the q vectors from the k -point mesh in use. (Otherwise the data for the whole Brillouin zone needs to be stored instead of only from the irreducible part, c.f. page 93. This leads to massively increased memory demands.) This means that the smallest q vector possible in my calculations is $q = \frac{1}{24}(0, 0, 1)$.
- Subsequently spin-wave stiffnesses determined from my curves might be inaccurate.

6.3 Iron

The spin-wave dispersions for Iron are shown in figures 6.4 to 6.6 (bcc structure) and figure 6.7 (fcc structure). The energies by which the dispersion for this structure is shifted downwards are 57meV (bcc) and 35meV (fcc), respectively. The spin-wave stiffnesses D of these Iron calculations are collected in the following table:

system	$D[\text{mRy } a_B^2]$	$D[\text{meV } \text{\AA}^2]$	ratio D/D_{\min}
Fe bcc 001	58	219	1.50
Fe bcc 011	38	146	1.00
Fe bcc 111	53	201	1.38
Fe fcc 001	-97	-369	

Iron bcc In the (001) direction the peaks broad only slowly with respect to q , see for instance vector $\frac{3}{12}$ on the $\Gamma \rightarrow H$ path in the dispersion plot in figure 6.4. Its width is barely visible in this kind of plot. Peaks have a large amplitude for small q , $-\text{Im } \chi^{+-}(q, \omega) > 200 \frac{1}{\text{Htr}}$ for $q = \frac{2\pi}{a}(0, 0, x)$, $x \leq \frac{2}{12}$. The peak positions move to above 200meV for a q vector from the middle of the path, then the peaks lower again for a brief section of the path and then vanish for larger q . In this region where the peaks exist the shape of the dispersion is roughly parabolic. In the region with no peaks there is a continuum of significant amplitude (around $2 \frac{1}{\text{Htr}}$) which has broad maxima at around 600meV, indicated by empty squares. For the border point $q = H$ the spin response vanishes, indicated by the red circle.

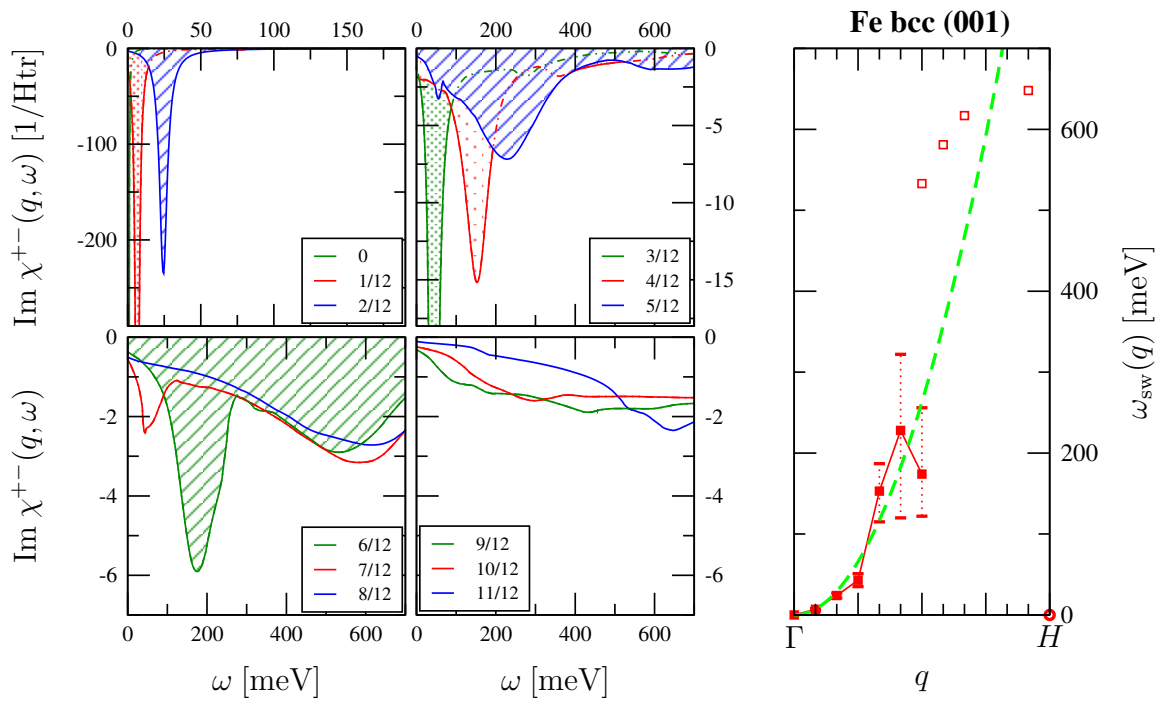


Figure 6.4: The spin-response function $\chi^{+-}(\mathbf{q}, \omega)$ and spin-wave dispersion $\omega_{\text{sw}}(\mathbf{q})$ for bcc Iron for \mathbf{q} vectors along the (001) direction.

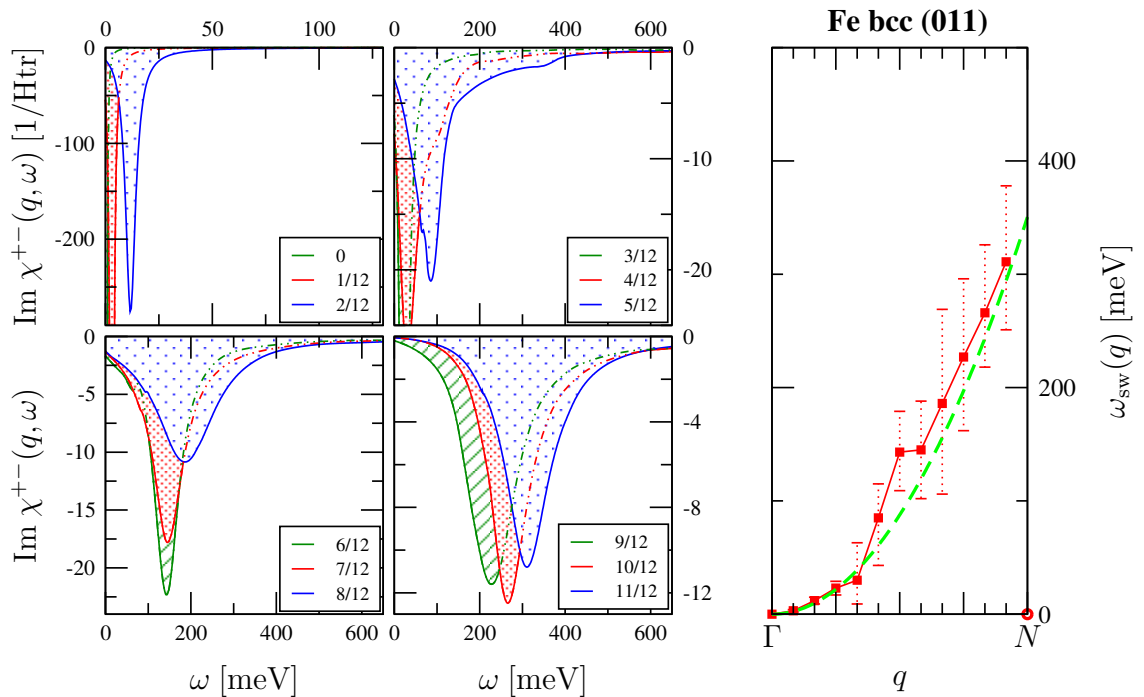


Figure 6.5: The spin-response function $\chi^{+-}(\mathbf{q}, \omega)$ and spin-wave dispersion $\omega_{\text{sw}}(\mathbf{q})$ for bcc Iron for \mathbf{q} vectors along the (011) direction.

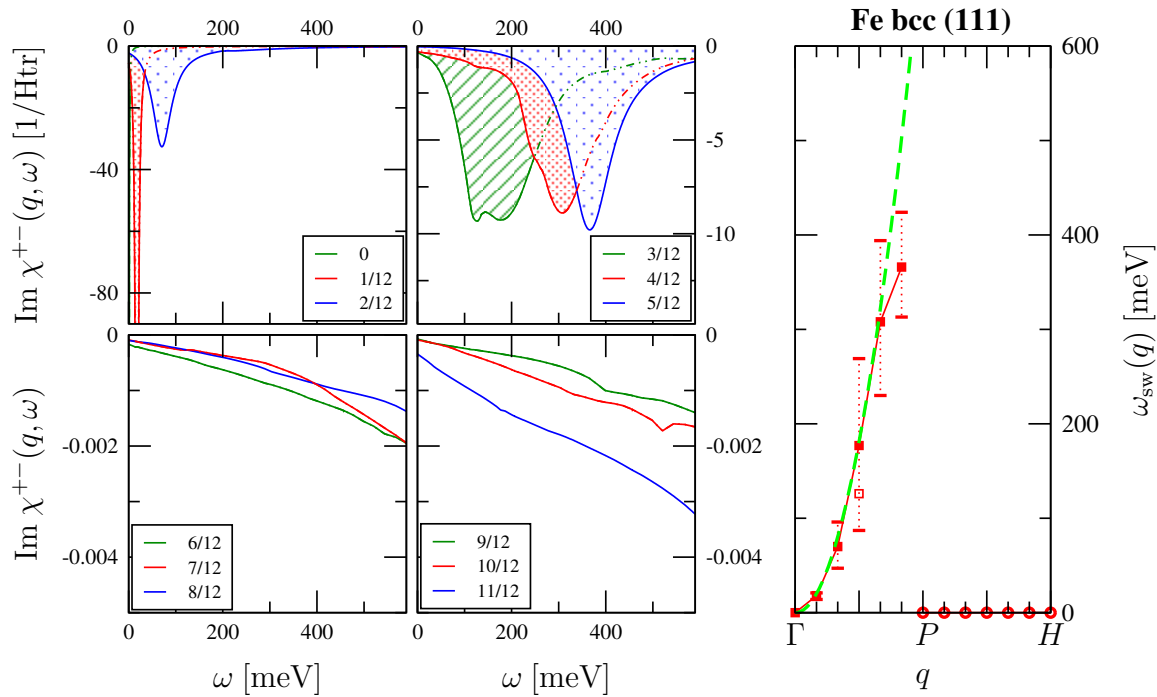


Figure 6.6: The spin-response function $\chi^{+-}(\mathbf{q}, \omega)$ and spin-wave dispersion $\omega_{\text{sw}}(\mathbf{q})$ for bcc Iron for \mathbf{q} vectors along the (111) direction.

In the (011) direction there are spin-wave peaks along the whole path $\Gamma \rightarrow N$. The energy of the peaks increase throughout the whole path, i.e., there is no saturation towards the zone boundary. The parabolic fit coincides well with the peak positions along the whole path. Only for the border point $\mathbf{q} = N$ the spin response vanishes. The width of the peaks increases up to around two third of the \mathbf{q} path, then it diminishes slightly. There is no significant continuum contribution to the spin response throughout the whole \mathbf{q} path.

In (111) direction there are distinctive spin-wave peaks on the section $\Gamma \rightarrow P$. The peak width narrows towards the \mathbf{q} point P . When comparing the amplitude of these peaks for different directions, it needs to be kept in mind that the path $\Gamma \rightarrow H$ in (111) direction is significantly longer than the path $\Gamma \rightarrow H$ in (001) direction due to a factor of $\sqrt{3}$. Therefore the decay of the peak height appear to be similarly quick in these directions. There appears to be a weakly pronounced double peak structure. There is no significant continuum contribution. The parabolic fit matches nicely for around two third of the path $\Gamma \rightarrow P$. At the point P and beyond on the path $P \rightarrow H$ the peaks vanish, i.e., they drop to very low absolute values.

Comparing these dispersion curves it turns out that all three fit well to a parabolic shape for small \mathbf{q} . However, the spin-wave stiffness D is significantly smaller for the 011 direction compared to the (001) and (111) directions.

Iron fcc Iron in the fcc structure is an interesting material to investigate because of its magnetic structure. In a fully non-collinear calculation it reveals a spin-wave structure. If restricted to a collinear alignment of the electron spin, it takes an anti-ferromagnetic configuration. In this calculation, it was calculated with one atom per unit cell, that is being fixed to a ferromagnetic configuration. Since this is not the ground state regarding the magnetic

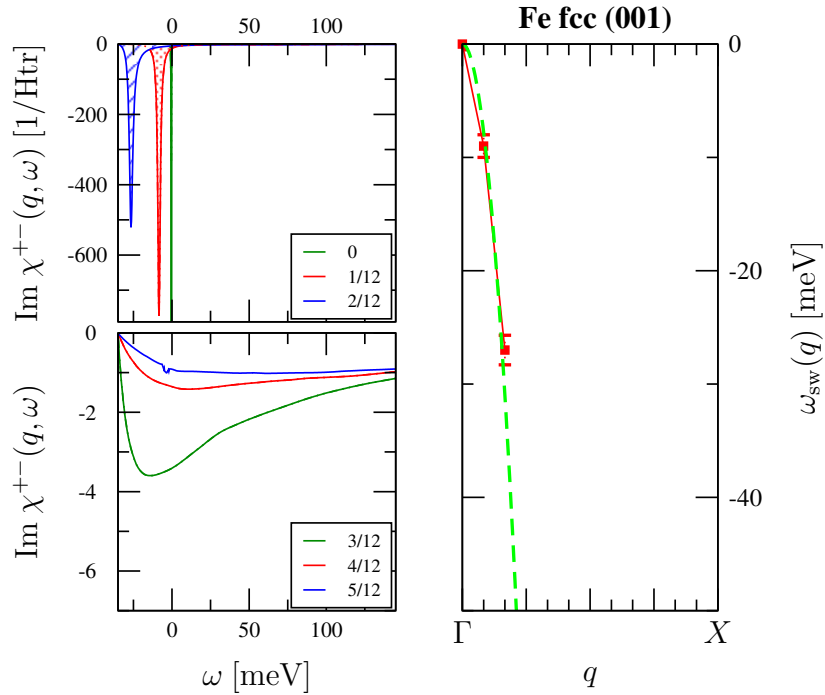


Figure 6.7: The spin-response function $\chi^{+-}(\mathbf{q}, \omega)$ and spin-wave dispersion $\omega_{\text{sw}}(\mathbf{q})$ for ferromagnetic fcc Iron for \mathbf{q} vectors along the (001) direction.

structure, “excited” states off this “ground” state are expected to have a lower total energy. Consequently the corresponding excitation energies should be negative.

This is indeed what is observed in the calculations (figure 6.7), even though they are restricted to positive energies. As for all other calculations of this chapter, the peak position for $\mathbf{q} = \Gamma$ is not located at zero energy but at a positive energy (in this case: 35meV). The spectrum is shifted to lower energies by this amount, but the now negative section of the energy axis is not cut. Then, for increasing \mathbf{q} vector the peaks move to lower energies. However, already for the vector $\mathbf{q} = \frac{2\pi}{a}(0, 0, \frac{3}{12})$ the peak position has moved to such low energies that it is not covered by the shifted energy range again. Therefore the spectra are not shown for the larger \mathbf{q} vectors. Calculations have been made for all three directions, however, only the (001) direction is presented because the essential features are identical in the curves for the (011) and (111) directions.

Comparison The spin-wave dispersion along two directions is compared to two other publications in figure 6.8. On the left-hand side the dispersion of bcc Fe along (001) calculated by Savrasov [Sav98] is presented in blue. The orange curve the author’s according calculation, it is identical to figure 6.4. The framework used by Savrasov is time-dependent DFT (such as this work) employed within the LMTO method, which has some similarities to the LAPW method. The spin-response function, however, is not determined in reciprocal space by a Dyson equation, but through the real-space Sternheimer approach [Sav92]. The lattice constant that has been used in the calculation is not provided in the paper. The spin-wave dispersion starts in the origin, while this is the case for the current work only by shifting it accordingly. It is not known to the author whether the method of Savrasov yields

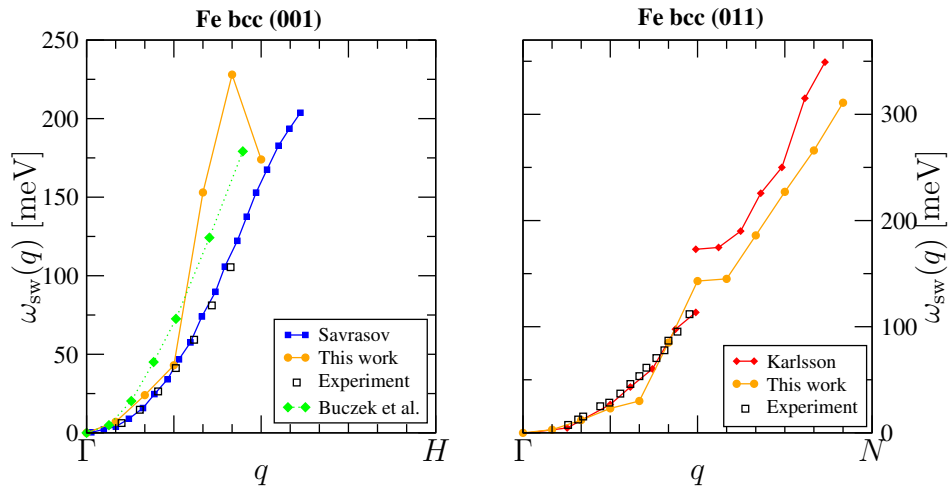


Figure 6.8: Comparison of Iron spin-wave dispersions along two directions with two other authors.

this result without any tuning. The curves of Savrasov and of this work coincide nicely for small q vectors. In the intermediate region the orange curve shows a stronger increase and does not follow the parabolic-like shape, as does the blue curve. It is common to both curves that the amplitude of the spin response decays rapidly and vanishes at half or two thirds of the length of path $\Gamma - H$. It should be kept in mind that in the fading-out of a dispersion there is a certain freedom of choice of where it is considered to be vanished. The experimental results [Lyn75] (which have also been cited in Savrasov's publication) coincide well with the blue curve.

The green diamonds indicate calculations of Buczek and coworkers [BESB09]. The employed formalism is also adiabatic LDA, i.e. the same matrix Dyson equation as in this thesis is solved. However, the response function of non-interacting particles is determined from the KKR Green's function method. The experimental lattice constant of Fe bcc has been used. The resulting spin-wave modes are (for small q vectors) higher in energy than in this work. The determined spin-wave stiffness is determined as $D = 252 \text{ meV } \text{\AA}^2$, compared to $D = 219 \text{ meV } \text{\AA}^2$ in this work. (However, it should be noted that the results of Buczek coincide well with experimental results of Mook referenced in [BESB09].)

On the right-hand side of figure 6.8 results for Iron bcc in (011) direction are compared. Our data (orange curve) are contrasted to results of Karlsson and Aryasetiawan [KA00]. Their method is based on many-body perturbation theory as it was briefly outlined on page 45. The lattice constant is not provided. The dispersion of Karlsson starts in the origin. According to private communication, this has been explicitly ensured by a properly chosen screened interaction. For small q vectors both Karlsson and this work correspond well with experiment (also from [Lyn75]). At around one third of the path $\Gamma - N$, however, the curve does not increase as quickly anymore, but catches up again at around half of the path $\Gamma - N$. There the Karlsson curve has a leap, which might indicate a double peak structure. In our calculations we do not see a double-peak structure, c.f. figure 6.5. For large q vectors the progression of the two dispersions is similar, though the one of Karlsson has higher energies due to its leap.

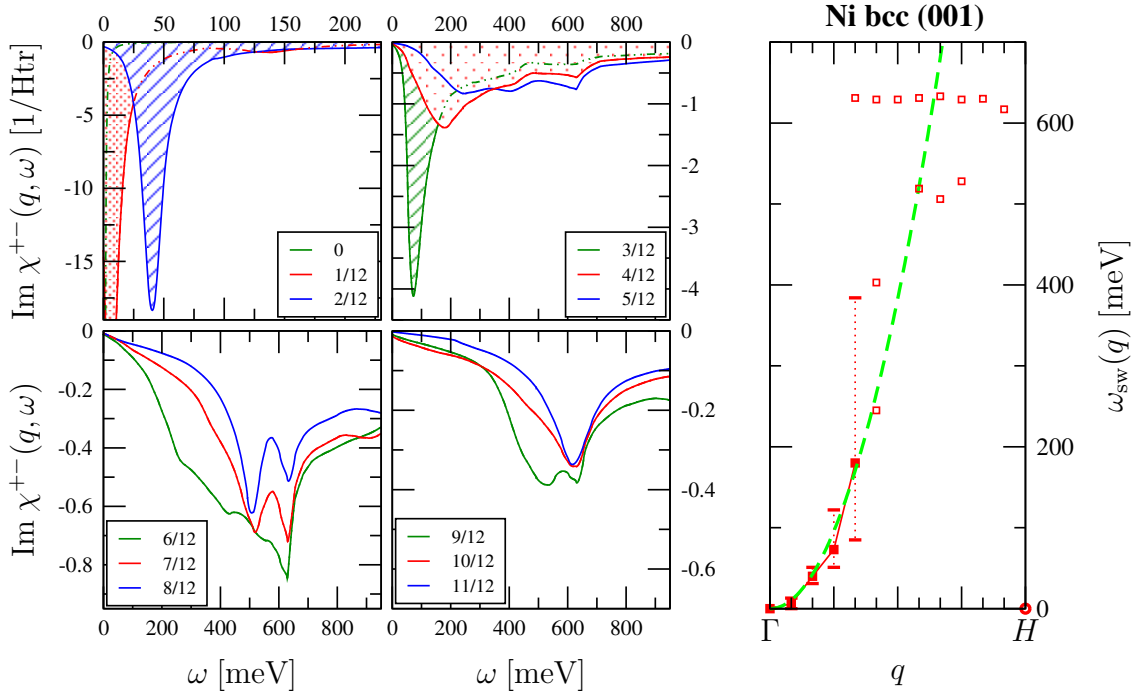


Figure 6.9: The spin-response function $\chi^{+-}(\mathbf{q}, \omega)$ and spin-wave dispersion $\omega_{\text{sw}}(\mathbf{q})$ for bcc Nickel for \mathbf{q} vectors along the (001) direction.

6.4 Nickel

In figures 6.9 to 6.11 the spin-wave dispersions of Nickel in the bcc structure are presented, 6.12 to 6.14 the dispersions of Nickel in the fcc structure. The energy shifts are 21meV and 56meV , respectively. The spin-wave stiffnesses D of these Nickel calculations are collected in the following table:

system	$D[\text{mRy } a_{\text{B}}^2]$	$D[\text{meV } \text{\AA}^2]$	ratio D/D_{min}
Ni bcc 001	80	303	1.07
Ni bcc 011	93	353	1.25
Ni bcc 111	74	283	1.00
Ni fcc 001	353	1342	1.50
Ni fcc 011	235	893	1.00
Ni fcc 111	278	1057	1.18

Nickel bcc In (001) direction there is a pronounced peak structure for $\mathbf{q} = \frac{2\pi}{a}(0, 0, x)$, $x \leq \frac{4}{12}$, see figure 6.9. In this region the peak positions coincide nicely with a parabolic plot. These peaks are significantly lower compared to Iron in the same structure and direction, see 6.4. For instance, the peak height for $\mathbf{q} = \frac{2\pi}{a}(0, 0, \frac{2}{12})$ is roughly one order of magnitude lower for Nickel than for Iron; the corresponding peak width is larger. For \mathbf{q} larger than $\mathbf{q} = \frac{2\pi}{a}(0, 0, \frac{5}{12})$ the response broadens into a continuum with a few maxima. However, the amplitude is quite low, therefore the maxima are only indicated by empty squares in the figure. It should be noted that the separation between peaks and continuum is not well

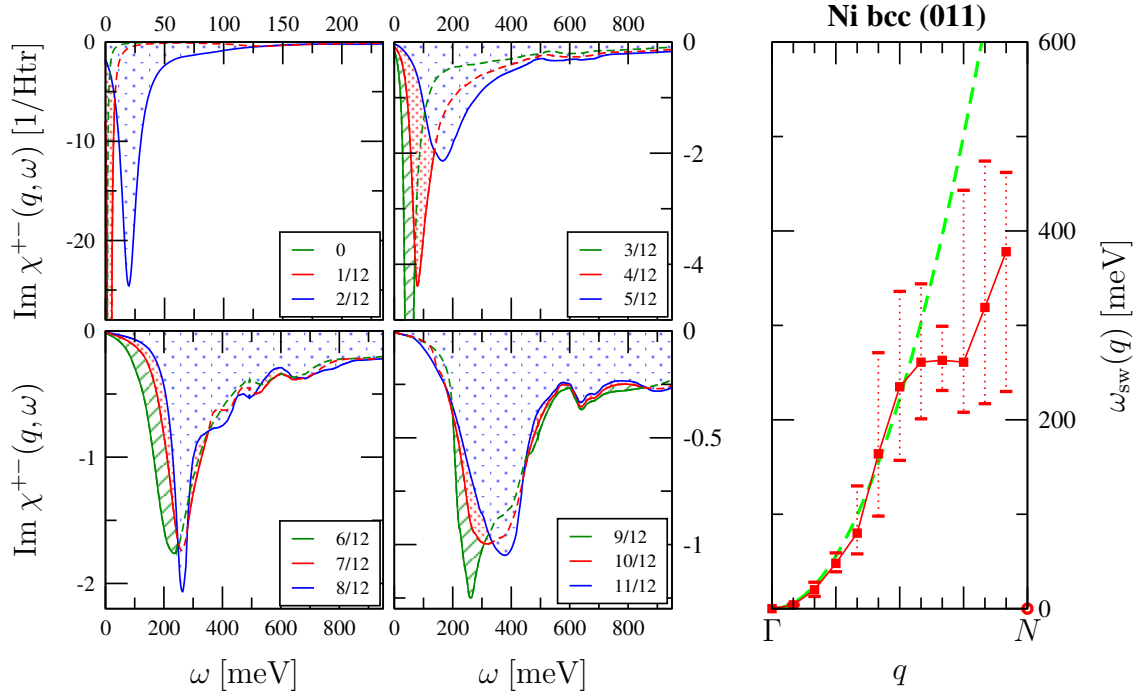


Figure 6.10: The spin-response function $\chi^{+-}(\mathbf{q}, \omega)$ and spin-wave dispersion $\omega_{\text{sw}}(\mathbf{q})$ for bcc Nickel for \mathbf{q} vectors along the (011) direction.

defined. It could also be interpreted as very broad peaks (partly with a double peak structure) of a constant branch.

In the (011) direction there are peaks along the whole path $\Gamma \rightarrow N$. The fit to the parabola matches nicely up to half of the path. Then, the peak positions form a plateau, just to rise again towards the zone boundary. The response function vanishes for $\mathbf{q} = N$.

In the (111) direction there are well-defined peaks for small \mathbf{q} vectors $\mathbf{q} = \frac{2\pi}{a}(0, x, x)$, $x \leq \frac{3}{12}$. The peak position fits well to the parabolic fit. On the second half of the path $\Gamma \rightarrow P$, $\mathbf{q} = \frac{2\pi}{a}(0, x, x)$, $\frac{3}{12} \leq x < \frac{6}{12}$ the peak broadens into a continuum featuring maxima. These maxima also fit well to the parabola. On the path $P \rightarrow H$ the spin response vanishes. It has very low amplitude and a broad shape without significant maxima (at least not in the shown energy range). This last property is identical to Iron bcc (111) where the response vanishes on the same section. This might be caused by symmetry reasons.

Nickel fcc In the fcc structure Nickel shows spin-wave peaks along the whole path $\Gamma \rightarrow X$ in (001) direction. The parabolic fits well only for small $\mathbf{q} = \frac{2\pi}{a}(0, 0, x)$, $x \leq \frac{2}{12}$. The peak widths are a bit smaller than for the other curves shown up to now. For large \mathbf{q} vectors the width even diminishes again. The spin-wave curve has a maximum at around two thirds of the path and moves to slightly lower energies further on. The amplitude for large \mathbf{q} vectors remains at around $4 \frac{1}{\text{Htr}}$ which is larger than, e.g., for Iron. At the zone boundary, $\mathbf{q} = X$, the response function vanishes.

In (011) direction there are peaks on the section $\Gamma \rightarrow K$, however, the response vanishes for the section $K \rightarrow X$. The parabolic fit suits only for small \mathbf{q} vectors. After half of the whole path, $\mathbf{q} = \frac{2\pi}{a}(0, x, x)$, $\frac{6}{12} < x < \frac{9}{12}$, the peak positions slightly decrease again.

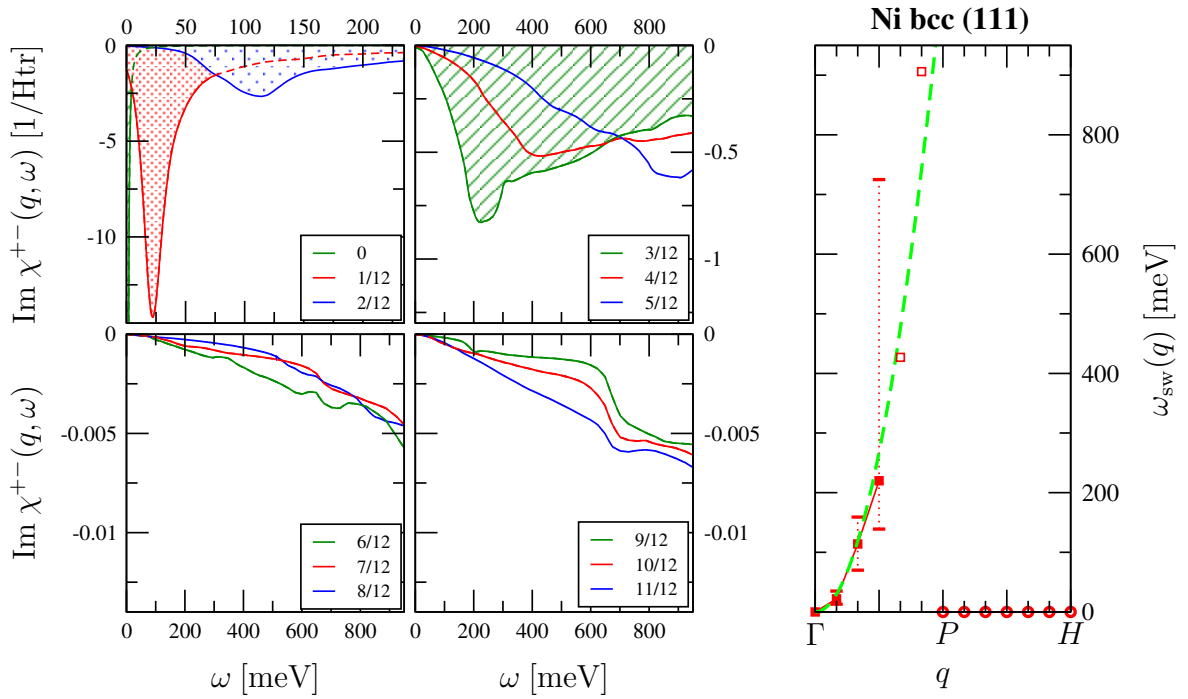


Figure 6.11: The spin-response function $\chi^{+-}(\mathbf{q}, \omega)$ and spin-wave dispersion $\omega_{\text{sw}}(\mathbf{q})$ for bcc Nickel for \mathbf{q} vectors along the (111) direction.

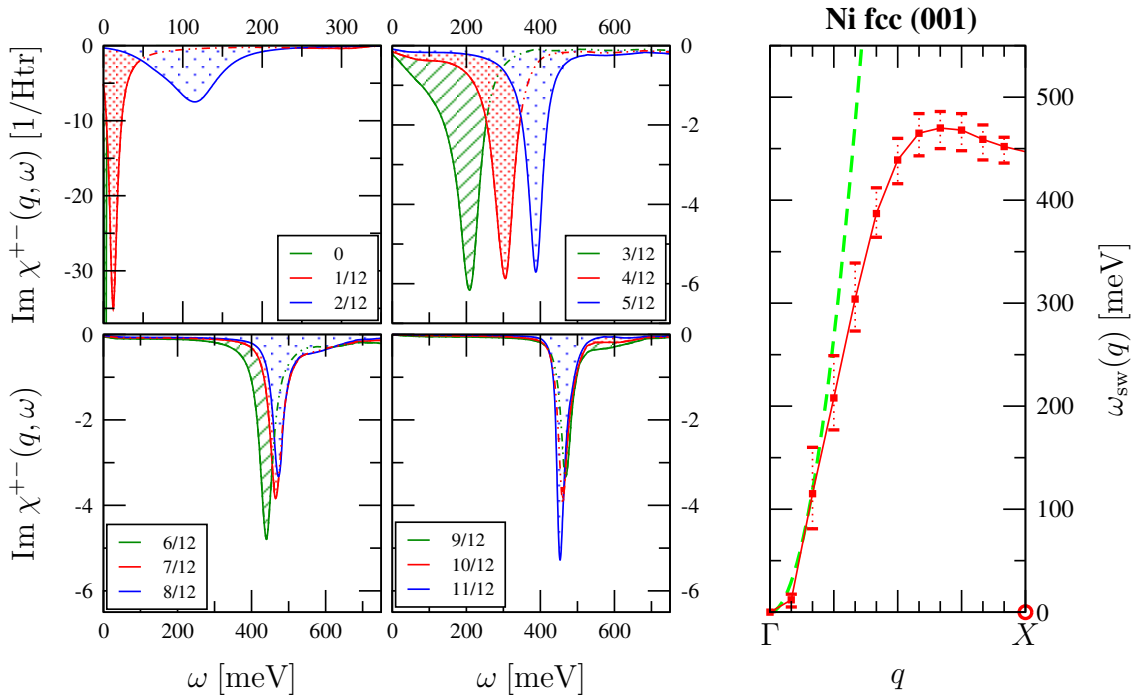


Figure 6.12: The spin-response function $\chi^{+-}(\mathbf{q}, \omega)$ and spin-wave dispersion $\omega_{\text{sw}}(\mathbf{q})$ for fcc Nickel for \mathbf{q} vectors along the (001) direction.

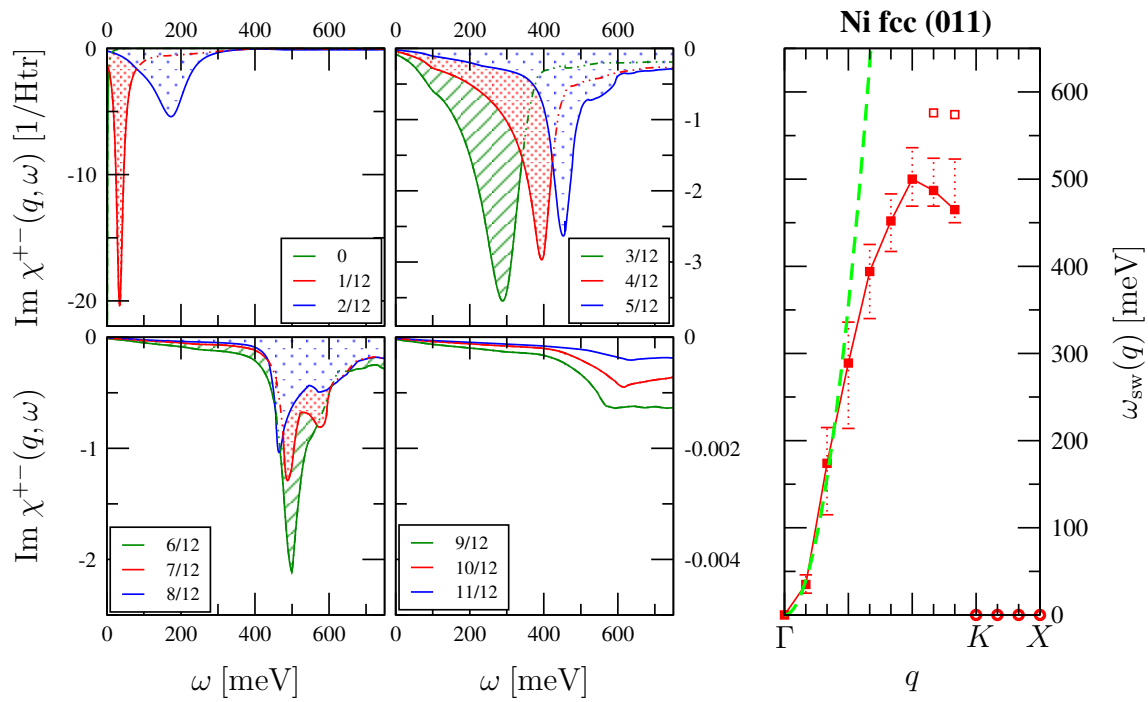


Figure 6.13: The spin-response function $\chi^{+-}(\mathbf{q}, \omega)$ and spin-wave dispersion $\omega_{\text{sw}}(\mathbf{q})$ for fcc Nickel for \mathbf{q} vectors along the (011) direction.

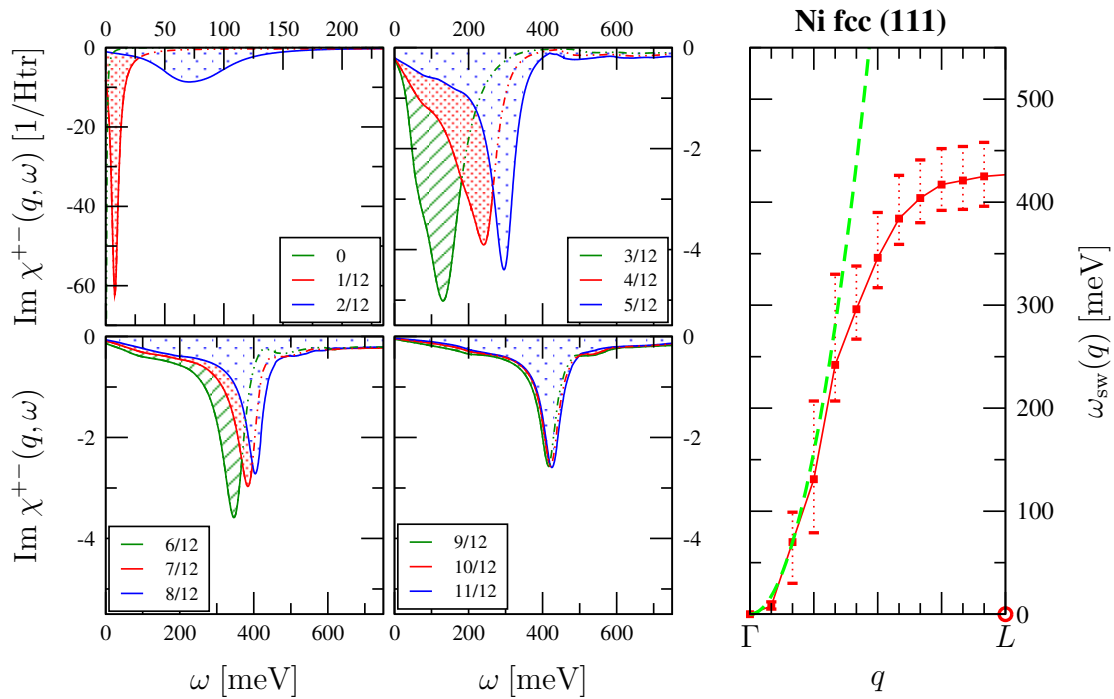


Figure 6.14: The spin-response function $\chi^{+-}(\mathbf{q}, \omega)$ and spin-wave dispersion $\omega_{\text{sw}}(\mathbf{q})$ for fcc Nickel for \mathbf{q} vectors along the (111) direction.

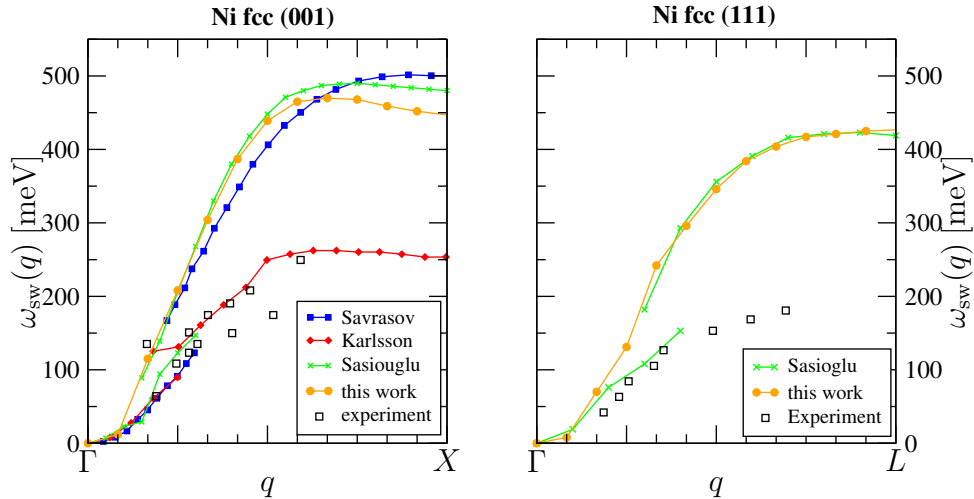


Figure 6.15: Comparison of Nickel spin-wave dispersions along two directions with other authors.

In (111) there also exists a spin wave peaks on the whole path, such as in the (001) direction. There is a significant amplitude $-\text{Im} \chi^{+-}(\mathbf{q}, \omega_{\text{sw}}(\mathbf{q})) > 2 \frac{1}{\text{Htr}}$ at the spin-wave peak also for large \mathbf{q} vectors. The parabolic function matches the spin-wave dispersion for the first quarter of the path. Then, the dispersion takes the opposite curvature and appears to have a saturation for large \mathbf{q} vectors. For $\mathbf{q} = L$ the response function vanishes.

Comparison In figure 6.15 four different theoretical results are presented together with experiments [MP85a]. The orange curve is from this work, see figure 6.12. The curves of Karlsson and Savrasov are from the publications that were previously cited on page 106. The green curves were kindly provided by E. Sasioglu [Sasa]. They are based on a many-body approach similar to that of Aryasetiawan and Karlsson, but bases on a different implementation, utilizing the FLAPW method and Wannier functions.

The experimental data (indicated by empty squares) show a split into two branches: The lower branch starts at the origin and has a parabolic shape for small \mathbf{q} . The second branch sets in for \mathbf{q} around $\frac{2}{12}$ of the path. For intermediate \mathbf{q} both branches increase, though more in a low linear fashion. For large \mathbf{q} there are no data.

The calculation of Karlsson (red curve) has a crucial difference to the other theoretical curves. The exchange splitting of Nickel in DFT, if compared to experiment, is systematically overestimated. It is understood that this leads to according overestimations of the amplitude of the spin-wave energy. Karlsson diminished the exchange splitting of his DFT results by hand in order to account for that. As a result his higher branch ranges at around half of the energy if compared to the other calculations (250meV vs. 450-500meV). This way he closely matches the experimental results.

Further on the results of Sasioglu and this work (both using the experimental lattice constant) agree well up to intermediate \mathbf{q} vectors. At large \mathbf{q} the trend of decreasing $\omega_{\text{sw}}(\mathbf{q})$ is pronounced stronger in the TDDFT result. The Savrasov result shows a slightly slower increase for intermediate \mathbf{q} , and has a plateau for large \mathbf{q} . This might be an indicator that the theoretical lattice constant has been used in this computation, compare figure 6.3.

On the right-hand side of figure 6.15 dispersion graphs of this work and Sasioglu are compared to experiment [Sasb]. All in all the two theoretical curves coincide well. At q values around one third of the path, however, the calculation of Sasioglu catches two paths, while there is no such double-peak structure for the TDDFT calculation. One could at best identify a weak shoulder, see figure 6.14. The lower branch of the Sasioglu curve matches the experiment nicely. However, for larger q the spin-wave energies are too large by a factor of around two, similar as in the (001). This is also due to the miscalculated exchange splitting of Nickel in DFT.

In these comparisons for Nickel it became obvious that the TDDFT calculations of this work did not show a double peak structure. It should be kept in mind that the structure of the spin-response function is sensitive to several parameters. The lattice constant is of importance, as well as the method how the dispersion is fixed to the origin. The work of Sasioglu for instance uses a scaling of the screened interaction (which takes in that method a similar place as the exchange-correlation kernel in this TDDFT method). Furthermore, the resolution in q is limited to the chosen k -point set. It should be remarked that there has been observed a double peak structure once: In figure 6.3, the red curve shows the dispersion of Nickel fcc in (001) direction for the theoretical lattice constant on a $48 \times 48 \times 48$ k -point mesh. For the q -vector $\frac{3}{24}X$ (which lies in-between two mesh points of the $24 \times 24 \times 24$ k -point set) there are two peaks, indicated by an additional red square. It appears that if such a double-peak structure appears in the TDDFT results, it is only in a very small region for smaller q values. These detail should be investigated further. One consequence is that if one misses a splitting into two branches, one considers the progression of peak positions as one curve. A parabola that that is matched to the small- q values will subsequently lead to an overestimation of the spin-wave stiffness.

6.5 Cobalt

The spin-wave spectra for Cobalt are plotted in figures 6.16 to 6.18 for the bcc structure and in figures 6.19 to 6.21 in the fcc structure. The energy shifts are 66meV (bcc) and 67meV (fcc), respectively. The Cobalt spin-wave stiffnesses D for these structures are:

system	$D[\text{mRy } a_B^2]$	$D[\text{meV } \text{Å}^2]$	ratio D/D_{\min}
Co bcc 001	152	577	1.14
Co bcc 011	174	662	1.31
Co bcc 111	133	504	1.00
Co fcc 001	117	446	1.00
Co fcc 011	132	503	1.13
Co fcc 111	121	459	1.03

Cobalt bcc In (001) direction there is a spin-wave dispersion along the whole path $\Gamma \rightarrow H$. With increasing q the peak position rises monotonically up to values above 900meV. The peaks are very wide for intermediate vectors $q = \frac{2\pi}{a}(0, 0, x)$, $\frac{6}{12} < x < \frac{9}{12}$, and narrow again for larger q vectors. The spin-wave stiffness obtained from the parabolic fit for small q vectors has a value significantly larger than for the previous Iron and Nickel calculations.

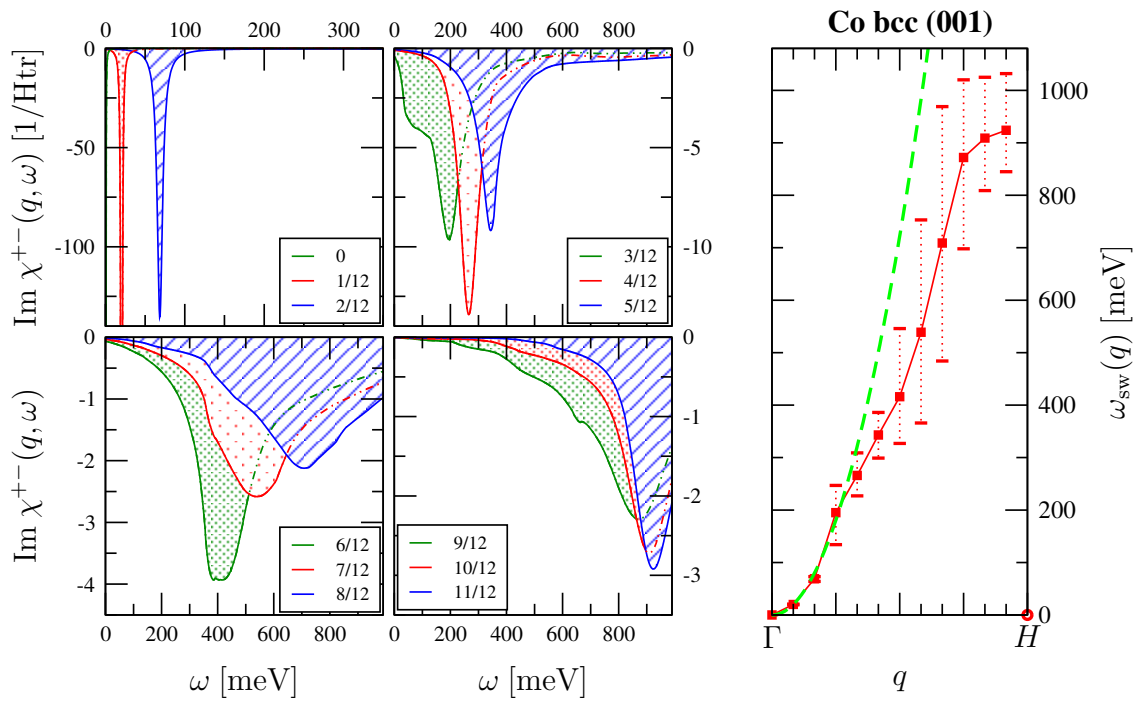


Figure 6.16: The spin-response function $\chi^{+-}(\mathbf{q}, \omega)$ and spin-wave dispersion $\omega_{\text{sw}}(\mathbf{q})$ for bcc Cobalt for \mathbf{q} vectors along the (001) direction.

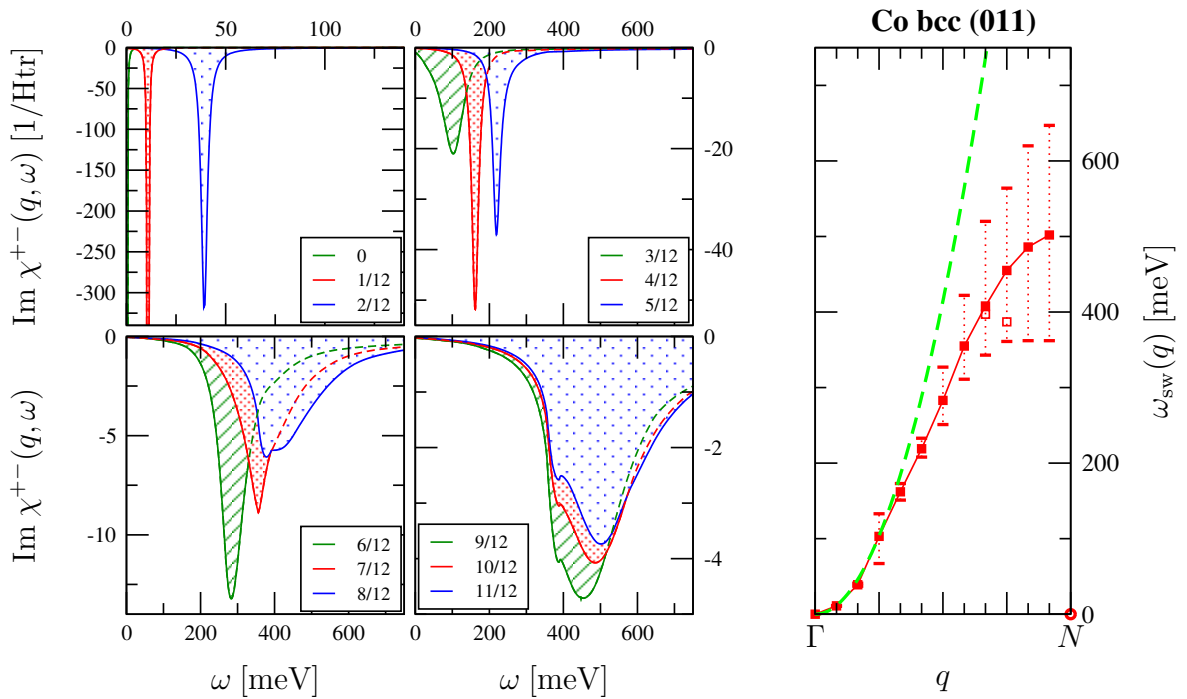


Figure 6.17: The spin-response function $\chi^{+-}(\mathbf{q}, \omega)$ and spin-wave dispersion $\omega_{\text{sw}}(\mathbf{q})$ for bcc Cobalt for \mathbf{q} vectors along the (011) direction.

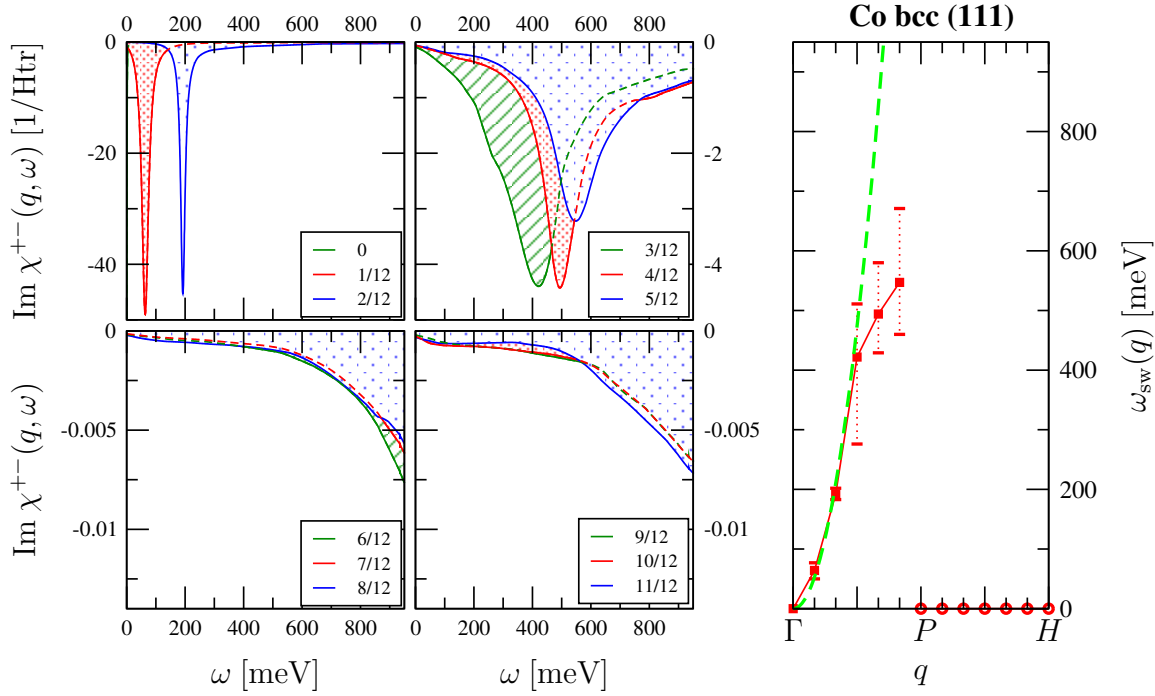


Figure 6.18: The spin-response function $\chi^{+-}(\mathbf{q}, \omega)$ and spin-wave dispersion $\omega_{\text{sw}}(\mathbf{q})$ for bcc Cobalt for \mathbf{q} vectors along the (111) direction.

In the (011) direction the spin-wave stiffness is even larger. (This is not obvious from the figures due to the fact that the path $\Gamma \rightarrow H$ is longer than the path $\Gamma \rightarrow N$.) However, the maximum spin-wave energy is reached at the zone boundary at around 500meV. The spin-wave peaks exist along the whole path $\Gamma \rightarrow N$, but rise only up to values around 500meV. The peaks do not narrow towards the end of the path.

In (111) direction there are peaks along the section $\Gamma \rightarrow P$, while it vanishes on the section $P \rightarrow H$. The maximum spin-wave energies are around 550meV close to point P .

Cobalt fcc In (001) direction there is a continuous spin-wave dispersion for the whole path. The spin-wave peaks narrow again for large \mathbf{q} vectors. There is an oscillation in the peak width at around $\mathbf{q} = \frac{2\pi}{a}(0, 0, \frac{4}{12})$. The peak for the next smaller \mathbf{q} vector is smaller and taller, as well as the peak for the next larger \mathbf{q} vector. The same effect is there at a smaller extend also in the (011) direction, but not in the (111) direction.

In (011) direction the spin-wave dispersion extends along the section $\Gamma \rightarrow K$ and vanishes along $K \rightarrow X$.

In (111) direction there are spin-wave peaks along the whole path $\Gamma \rightarrow L$. The spin-wave stiffness is the smallest of the other fcc Nickel dispersions.

Common observations for the three elements There are a few properties that are common to the calculations for these three different transition metals.

- As discussed in section 6.1, there are directions in which the Brillouin zone boundary does not coincide with the next high-symmetry point. These are the path $\Gamma \rightarrow P \rightarrow H$ in the (111) direction for the bcc structure, and the path $\Gamma \rightarrow K \rightarrow X$ in the (011)

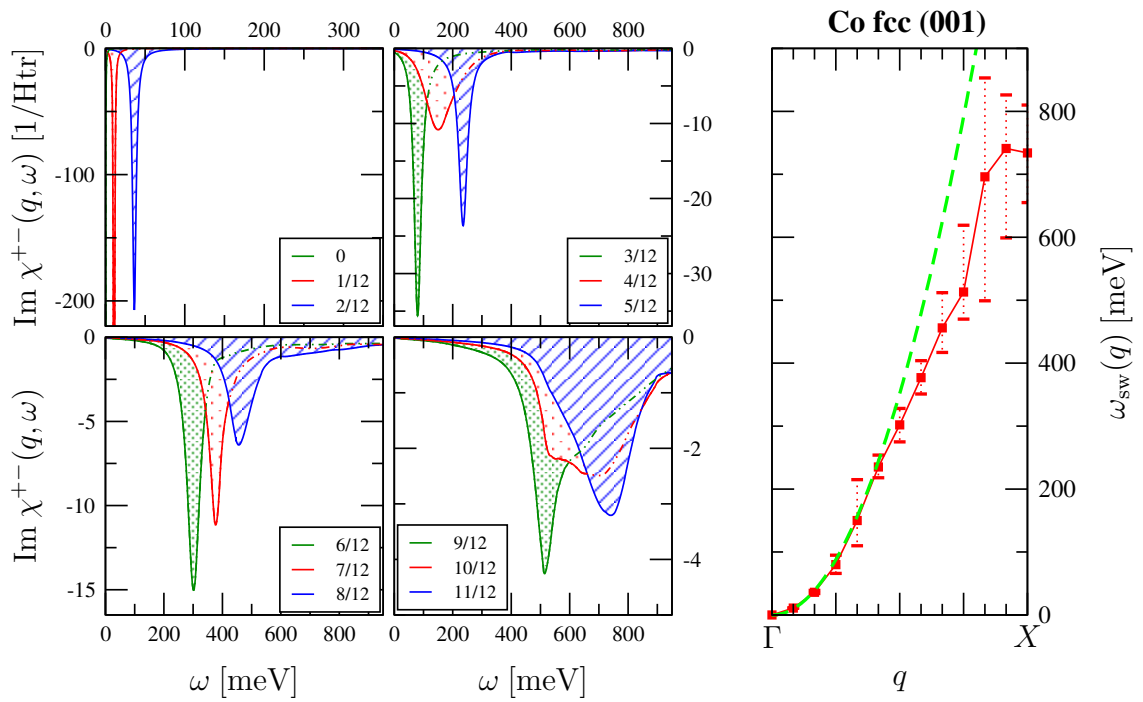


Figure 6.19: The spin-response function $\chi^{+-}(\mathbf{q}, \omega)$ and spin-wave dispersion $\omega_{\text{sw}}(\mathbf{q})$ for fcc Cobalt for \mathbf{q} vectors along the (001) direction.

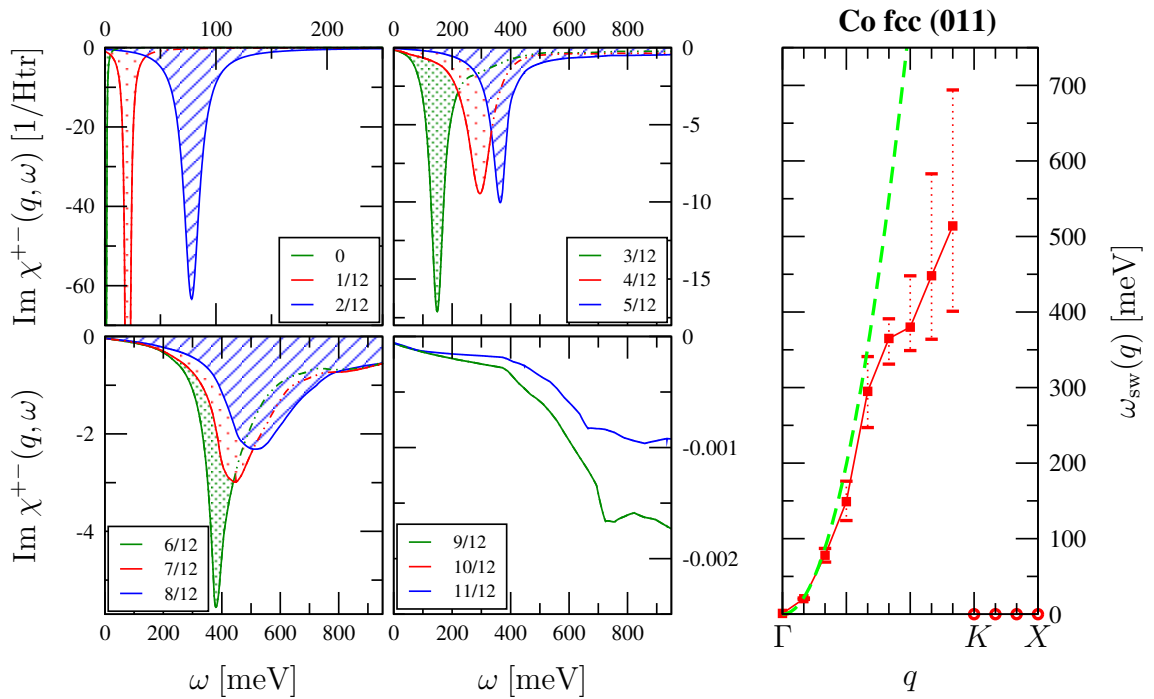


Figure 6.20: The spin-response function $\chi^{+-}(\mathbf{q}, \omega)$ and spin-wave dispersion $\omega_{\text{sw}}(\mathbf{q})$ for fcc Cobalt for \mathbf{q} vectors along the (011) direction.

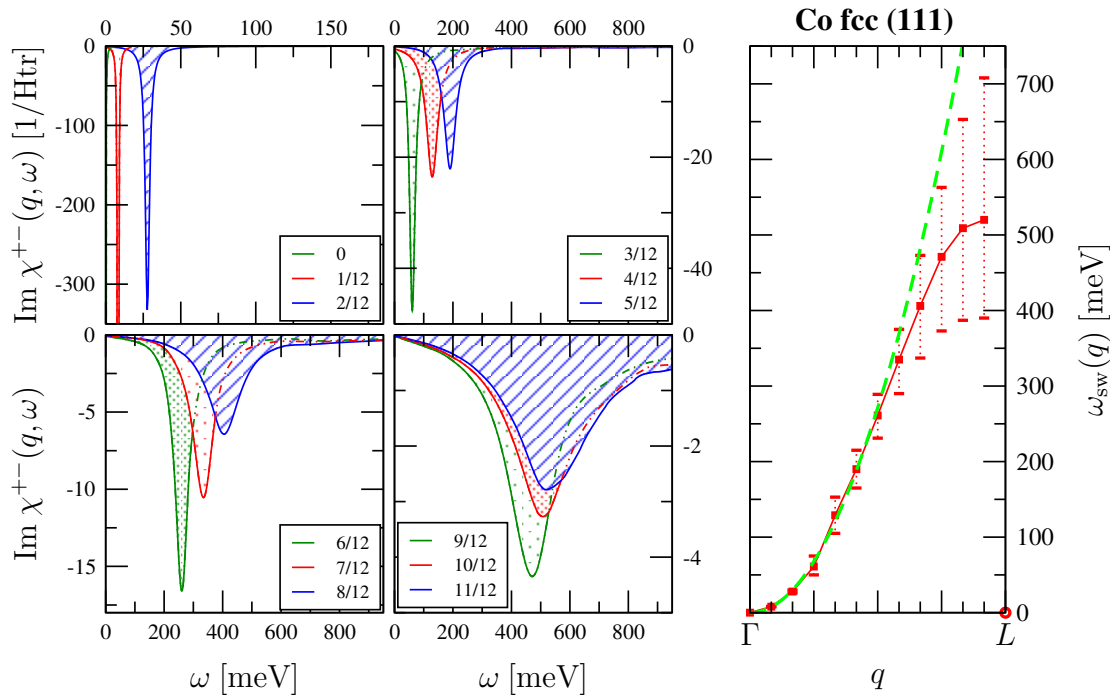


Figure 6.21: The spin-response function $\chi^{+-}(\mathbf{q}, \omega)$ and spin-wave dispersion $\omega_{\text{sw}}(\mathbf{q})$ for fcc Cobalt for \mathbf{q} vectors along the (111) direction.

direction in fcc structure. On the second section of these paths (that are $P \rightarrow H$ and $K \rightarrow X$) the spin response vanishes for all three elements. This might be due to symmetry reasons.

- For the high-symmetry points – i.e., the points X, K, L in fcc and points H, N, P in bcc – the spin response usually vanishes. There is one exception: For fcc Cobalt the spin-response does not vanish for $\mathbf{q} = X$, see figures 6.19 and 6.20.
- The spin-response can also disappear within a high-symmetry path. This happens for Ni bcc (001) and Fe bcc (001).
- The spin-wave peaks are very narrow for small \mathbf{q} vectors and broaden for increasing \mathbf{q} . In some cases the width reduces again when approaching the high-symmetry point on the path. In a few cases the width oscillates slightly, for instance for Ni bcc (011), Co fcc (001) and Co fcc (011).
- The spin-wave stiffness has different values along the principle directions. Values can change by as much as 50%. Regarding these numbers it should be kept in mind that the current calculations are not optimal for the determination of these stiffnesses due to the large \mathbf{q} spacing (see also discussion on page 113).
- The spin-wave energies are below 400meV for Iron, below 600meV for Nickel and below 1000meV for Cobalt.

6.6 Comparison to Adiabatic Approximation

The results on the spin-wave dispersion $\omega_{\text{sw}}(\mathbf{q})$ and the spin-stiffness D are compared to results of the predominantly used *adiabatic approximation* to the magnon dispersion [RJ97, HEPO98, vSA99, PKT⁺01]. In the adiabatic approximation one assumes that the time dependence of the magnetization due to a slowly varying external magnetic field can be calculated by replacing the average $\langle \hat{M}(t) \rangle$ over the non-stationary state of electrons by average of the electrons at the ground state $\langle M \rangle(t)$ at instant time t , $\langle \hat{M}(t) \rangle \approx \langle M \rangle(t)$. I.e. the precessional motion of the local magnetization present for a spin wave is neglected when calculating the associated change of electronic energy. Clearly, the condition of validity of this approximation is that the precession time, τ_p , of the magnetization should be large as compared to characteristic times of electronic motion, namely, the hopping time, τ_h , of an electron from a given site to a neighboring one, and the precession time of the spin of an electron subject to the local exchange field. The hopping electrons determine the bandwidth of a solid and the hopping time τ_h is approximately $\tau_h = \hbar/E_{\text{bandwidth}}$, which approximately the lattice constant a divided by the Fermi velocity v_F , $\tau_h \approx a/v_F$. In other words, since the characteristic time scales are inversely proportional to the corresponding energy scale, the adiabatic approximation becomes valid if the spin-wave energies are small as compared to the bandwidth and to the exchange splitting. Considering that typical magnon energies of the transition-metal itinerant magnets are in the order of a few tenth of an eV, the adiabatic approximation is a good approximation for ferromagnets with a large exchange splitting such as Fe and Co, but it is less justified for Ni that has a small exchange splitting of about 0.7 eV (which is even overestimated in the conventional LDA and GGA approximations), see figure 6.1. The adiabatic approximation becomes exact in the limit of long-wavelength magnons (if the underlying electronic and magnetic properties are described well by the exchange-correlation functionals), so that the spin-wave stiffness constants D calculated from the adiabatic approximation becomes in principle exact.

The adiabatic approximation corresponds to a mapping of the itinerant electron system onto an effective Hamiltonian with classical spins. In the generally adopted view that the energy spectrum of the excited states beyond the ferromagnetic state E_o can be approximated by the Heisenberg model as the effective model,

$$E = E_o - \sum_{ij; i \neq j} J_{i,j} \hat{S}_i \cdot \hat{S}_j \quad (6.12)$$

where $J_{i,j}$ is the exchange interaction energy between two particular sites (i, j) , and \hat{S}_i, \hat{S}_j are unit vectors pointing in the direction of local magnetic moments at sites (i, j) , respectively. The sign convention adopted corresponds to a ferromagnetic ground state for positive J , $J > 0$. Magnons are then dynamical solutions in the linear regime to the Heisenberg Hamiltonian.

A magnon is an excitation, where the local magnetic moments deviate slightly from the ferromagnetic ground state (or any other magnetic state as ground state) and are typically not stationary states in the context of the density functional theory. Therefore, the procedure for performing the above mapping onto an Heisenberg Hamiltonian relies on the constrained density-functional theory [DBZA84] which allows to obtain the ground-state energy for a system subject to certain constraints. In the case of magnetic interactions, the constraint consists in imposing a given configuration of spin-polarization directions, namely, along \hat{S}_i

within the atomic cell or atomic sphere i in case of the FLAPW method, respectively. Note that with the FLAPW program FLEUR the intra-atomic noncollinearity of the spin polarization is neglected since we are primarily interested in low-energy excitations due to interatomic noncollinearity [KFN⁺04].

To actually calculate the spin-wave energies, the frozen-magnon approach is applied. One chooses the constrained spin-polarization configuration to be the one of a spin spiral, which can be written in case of an one atom per unit cell as,

$$\mathbf{M}(\mathbf{R}_i) = M_o \begin{pmatrix} \cos(\mathbf{q} \cdot \mathbf{R}_i) \sin \theta \\ \sin(\mathbf{q} \cdot \mathbf{R}_i) \sin \theta \\ \cos \theta \end{pmatrix} \quad (6.13)$$

which relates the local magnetic moment M at site \mathbf{R}_i with the wave vector \mathbf{q} , and a cone angle θ accounting for the tilting of the spin-quantization axis with respect to the ferromagnetic state. Using this ansatz the energy difference to the ferromagnetic state, $\Delta E(\mathbf{q}, \theta) = E(\mathbf{q}, \theta) - E(0, 0)$, (and the dependence of the variation of the local magnetic moment $M(\mathbf{q}, \theta)$ as we will see below) is computed directly on the basis of the density functional theory by employing the generalized Bloch theorem for a spin-spiral configuration [Her66] as implemented in the FLEUR code [KFN⁺04] and further developed by Lezaic *et al.* [LMB] to calculate the exchange energy parameters $J_{i,j}$ to analyze the thermodynamical properties of magnets. Please notice, in order to cover the full phase space of spin configurations, it would be necessary in the representation of the magnetic moment of Eq. (6.13) to introduce two independent wave vectors for the position dependence and treat θ analogous to $\phi_i = \mathbf{q}\mathbf{R}_i$. However, we work here in the linear spin-wave theory, thus with linear spin-wave modes, respectively, and then $\theta = \text{const}$ and we consider for unit cells of one atom only one constant configuration.

The equations of motion subject to the classical Heisenberg Hamiltonian and the request to work in linear spin-wave theory ($d\theta/dt = 0$) imply immediately that $\theta \ll 1$ and $d\phi/dt = \text{const}$. Following Halilov *et al.* [HEPO98], the associated eigenvalue problem gives the dispersion of the energy or frequency, respectively, of one spin-wave mode:

$$\omega_{\text{sw}}(\mathbf{q}) = 2g\mu_B \frac{\Delta E(\mathbf{q})}{M_o}, \quad (6.14)$$

where $\Delta E(\mathbf{q})$ is the excitation energy with respect to and M_o is the local magnetic moment of the ferromagnetic ground state (or any other ground state). 5 and g is the gyromagnetic factor ($g \simeq 2$). This equation holds under the assumption that the system can be described by the Heisenberg model, which means:

$$M(\mathbf{q}, \theta) = M_o = \text{const}, \quad \text{and} \quad \Delta E(\mathbf{q}, \theta) = \Delta E(\mathbf{q}) \sin^2(\theta) \quad (6.15)$$

and the condition that θ is small to remain in the linear magnon regime. For a true Heisenberg ferromagnet above conditions Eq.(6.15) are fulfilled for all θ and $\Delta E(\mathbf{q})$ can be calculated directly for a flat spiral $\Delta E(\mathbf{q}) = \Delta E(\mathbf{q}, \theta = \pi/2) = \Delta E_{\text{FS}}(\mathbf{q})$. For the typical itinerant magnets Fe, Co, and Ni, this condition is not fulfilled. It is important to explore carefully the regime of \mathbf{q}, θ where above conditions hold. Below we use a small cone angle of $\theta \leq 20^\circ$.

Halilov *et al.*[HEPO98] extended the regime of applicability by interpreting the Heisenberg model Eq.(6.12) just of a convenient form to expand the total energy. On the basis of

this interpretation it is natural that also the magnetic moment M depends on \mathbf{q} , θ , as $M(\mathbf{q}, \theta)$. If there is a regime of (\mathbf{q}, θ) where the energy difference $\Delta E(\mathbf{q}, \theta)$ can be expanded in the form

$$\Delta E(\mathbf{q}, \theta) = \Delta e(\mathbf{q}) M^2(\mathbf{q}, \theta) \sin^2 \theta \quad (6.16)$$

the above condition Eq. (6.15) is extended and the dispersion relation of the magnon frequency is given by an analogous equation:

$$\omega_{\text{sw}}(\mathbf{q}) = 2g\mu_{\text{B}} \Delta e(\mathbf{q}) M(\mathbf{q}, \theta = 0). \quad (6.17)$$

If $\Delta E(\mathbf{q}, \theta)$ and $M(\mathbf{q}, \theta)$ has been calculated $e(\mathbf{q})$ is obtained by a fit and the fit should hold independent of θ .

Rosengard *et al.*[RJ97] derived the spin-wave dispersion by noting that a spin flips over one spin-wave from $+\frac{1}{2}$ to $-\frac{1}{2}$ and since the magnetic moment is related to spin by the gyromagnetic ratio, $g\mu_{\text{B}}$ (with $g \simeq 2$), the total magnetization loss caused by a spin-wave excitation is then $g\mu_{\text{B}}$, while the magnetization loss per site is $\Delta M(\mathbf{q}, \theta)$. Hence the energy or frequency of a spin-wave excitation is:

$$\omega_{\text{sw}}(\mathbf{q}) = g\mu_{\text{B}} \lim_{\theta \rightarrow 0} \frac{\Delta E(\mathbf{q}, \theta)}{\Delta M(\mathbf{q}, \theta)} \quad (6.18)$$

For a Heisenberg system the magnetization loss per site is $\Delta M(\mathbf{q}, \theta) = M_o(1 - \cos \theta) = 2M_o \sin^2(\theta/2)$ and the energy change difference changes as $\Delta E(\mathbf{q}, \theta) = \Delta E(\mathbf{q}) \sin^2 \theta$ and both tends to zero for zero cone-angle θ . Hence the energy of a spin-wave excitation

$$\omega_{\text{sw}}(\mathbf{q}) = \frac{g\mu_{\text{B}}}{2} \frac{\Delta E(\mathbf{q}) \sin^2 \theta}{M_o \sin^2(\frac{\theta}{2})} \Big|_{\theta=0} = 2g\mu_{\text{B}} \frac{\Delta E(\mathbf{q})}{M_o}. \quad (6.19)$$

Total energy calculation of spin-spirals of the form given in Eq. 6.13 may be applied directly to determine $\Delta E(\mathbf{q}, \theta)$ and $M(\mathbf{q}, \theta)$, but we work with small cone angles and thus $E(\mathbf{q}, \theta)$ is expected to be of a small deviation from the ferromagnetic state, and the magnetic force theorem is expected to be a good approximation. Then, we can approximate the total energies by the difference of the sum of single-particle energies

$$\Delta E(\mathbf{q}, \theta) = \sum_{k,\nu}^{E_{\text{F}}(\mathbf{q},\theta)} \varepsilon_{k,\nu}(\mathbf{q}, \theta) - \sum_{k,\nu}^{E_{\text{F}}(0,0)} \varepsilon_{k,\nu}(0, 0) \quad (6.20)$$

and self-consistency is avoided, which makes the calculation considerably faster and the magnetic moment does not change due to the neglect of self-consistency.

The spin-wave stiffness constant D that relates the spin-wave frequency ω_{sw} to the wave vector in the long-wavelength limit as $\omega_{\text{sw}} = D q^2$, may be calculated from the energy of spin spiral excitation in the long wave-length limit ($q \rightarrow 0$ and $\theta \rightarrow 0$):

$$D = \frac{g\mu_{\text{B}}}{M(0)} \frac{d^2 E(\mathbf{q}, \theta)}{dq^2} \Big|_{q=0, \theta=0} \quad \text{or} \quad D = \frac{g\mu_{\text{B}}}{M_o} \frac{d^2 E(\mathbf{q})}{dq^2} \Big|_{q=0}, \quad (6.21)$$

respectively. $E(\mathbf{q})$ has to be calculated subject to the conditions given in Eq. 6.15. The region of q for which the spin-wave dispersion is isotropic depends on the system.

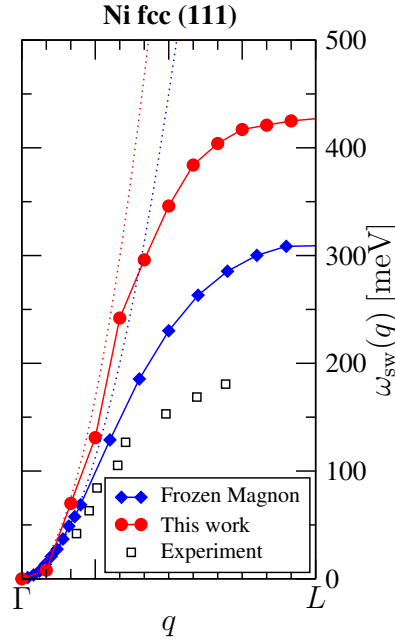


Figure 6.22: Adiabatic magnon dispersion relations (blue line) together with the TDDFT result of this work (red line) for bulk fcc-Ni along the (111) oriented high-symmetry line connecting the Γ -point with the L point. For comparison solid circles mark calculated frequencies, lines are guides to the eye. For comparison experimental room temperature data taken from Ref. [MP85b] are added.

Since we are primarily interested in spin-wave dispersion curves and the spin-wave stiffness D the frozen-magnon approach is superior to the frequently used concept of calculating the exchange interaction energies directly in real space using the Green-function method based on infinitesimal rotations developed by Liechtenstein *et al.* [LKG84] as one can calculate the \mathbf{q} -vectors on an arbitrarily fine or coarse grid where necessary and the performance of a Fourier transformation is avoided as well as the somewhat delicate analysis of the convergence of the sum of exchange constants over shells of atoms to obtain a reliable number for the spin-stiffness D . The advantage of Liechtenstein's method is the use of infinitesimal rotations which determines the Heisenberg parameters for an undisturbed ferromagnetic state.

We have applied the adiabatic spin-wave theory to calculate the magnon spectrum and the spin-stiffness constant of bulk fcc Ni. For this purpose we have used the full-potential linearized augmented plane-wave method [WKWF81, WF82] as implemented in the FLEUR code [KFN⁺04, cca]. All the structural and computational parameters such as the lattice constant, muffin-tin radius, number of \mathbf{k} -points in the Brillouin zone, number of basis functions as well as the choice of the exchange-correlation functional are identical to the calculations used in the TDDFT calculation.

By using the force theorem, we have calculated the total energy difference $\Delta E(\mathbf{q}, \theta_0)$ for a small cone angle of $\theta = 20^\circ$ for \mathbf{q} vectors along the (111) direction and fitted $\Delta E(\mathbf{q}, \theta)$ according to $\Delta E(\mathbf{q}, \theta) = \Delta e(\mathbf{q})M^2(\theta) \sin^2(\theta)$ to obtain $\Delta e(\mathbf{q})$ from which we calculated the adiabatic magnon dispersion shown in figure 6.22 (using a $71 \times 71 \times 71$ \mathbf{k} -point set) together

with one obtained in TDDFT. Both use the experimental lattice constant.

Compare this graph to the right-hand side of figure 6.15 and its subsequent discussion. The TDDFT curve (red) has similar values only for small q vectors, but turns then to what is resolved in other calculations as the higher branch. The frozen-magnon calculation on the other hand stays with the lower branch. It compares well with previous theoretical results relying on the adiabatic approximation [RJ97, HEPO98, vSA99, PKT⁺01]. In the intermediate energy regime there is reasonably good agreement to available experimental data [Sasb] of measured spin-wave spectra (plotted in empty black squares). According to the previous discussion, the too large bandwidth of the magnon spectrum of Ni is usually argued to be the neglect of the Stoner excitation kicking in at about 150 meV, which is neglected in the adiabatic approximation.

From a fit of the quadratic form $E(q) = Dq^2$ to the adiabatic magnon dispersion we obtain for the spin-stiffness constant $D = 712 \text{ meV \AA}^2$ for our adiabatic value of Ni in good agreement with previous calculations of $D = 739 \text{ meV \AA}^2$ [RJ97], $D = 740 \text{ meV \AA}^2$ [vSA99] and $D = 756 \pm 29 \text{ meV \AA}^2$ [PKT⁺01]. The TDDFT result of $D = 1057 \text{ meV \AA}^2$ (see page 108) is an overestimation due to the previous argumentation. In comparison to the experimental results of $D = 550 \text{ meV \AA}^2$ [DHM68], $D = 555 \text{ meV \AA}^2$ according to neutron-scattering measurement data at 4.2 K [MLN73] or of $D = 422 \text{ meV \AA}^2$ according to the magnetization measurement data at 4.2 K [Pau82] the theoretical data overestimate the spin-stiffness coefficient by about 35%.

CHAPTER 7

CONCLUSIONS

Summary In this text, spin-wave excitations have been investigated. The employed approach is the time-dependent density functional theory (TDDFT), involving the FLAPW method. The underlying theory has been presented, as well as the mechanism of spin excitation leading to the spin-flip response function χ^{+-} .

The formalism has been applied on the homogeneous electron gas, as well as on the simple transition metals Iron, Cobalt and Nickel, for which fcc and bcc configurations have been computed. In particular the different elementary directions (001), (011) and (111) have been investigated. Comparisons have been performed with experimental data and with other calculations. While not all features that were reported in those papers were reproduced, there is an overall agreement of the results. Furthermore, a more detailed comparison with the adiabatic approximation is provided.

Computational outlook Regarding implementation features, there are different ways to carry on the development of the computer code. For the calculations presented in this thesis – which contain a small unit cell – the limiting factor was the computational time. While the calculation is performed currently in one process only, a parallelization of the code would benefit from multiple CPUs and CPU cores. The most crucial spot for such a parallelization is the time-consuming calculation of the Kohn-Sham susceptibility χ_{KS}^{+-} . For systems with a larger unit cell, a parallelization might also help in terms of memory capacity.

For the calculations presented in this thesis, the choice of q vectors was restricted to the sampling points of the Brillouin zone. While a choice of q vectors off the sampling grid is in principle supported by the underlying code, this leads to a loss of symmetry in the calculations, and one cannot reduce the Brillouin zone integration of the Kohn-Sham response (5.37) to its irreducible part. In this case, the computational demands of the integration in terms of computational time and memory increase that much that the density of the Brillouin zone sampling needs to be reduced. Therefore, this approach is not feasible at the moment. However, a parallelized version of the code which would decrease the amount of memory that each process requires during the Brillouin zone integration might enable such a calculation. Nevertheless, due to the integration of the full Brillouin zone, such a calculation is always more costly than a calculation with q vectors chosen from the BZ sampling grid. If the disadvantage of higher computational cost is outweighed by the free choice of q vectors depends on an analysis of the implementation of the parallelization to be employed.

Further desirable program features include the implementation of two-dimensional geometries [Kur00], which allows for the calculation of true film geometries without the use of supercells. Further on, the treatment of spin-orbit coupling, which is implemented in the

DFT code FLEUR, is currently incompatible with TDDFT calculations. The influence of this correction term on spin-wave excitations is to be investigated.

Physical outlook After the code has been successfully applied onto the mentioned transition metals, the next steps are to explore more complex systems. The influence of lattice configurations onto spin-wave spectra is to be investigated. In particular, the magnetic characteristics of distinct elements need to be categorized if possible.

Even though there are a lot of perspectives in the ab initio exploration of more complex materials, there are as well limitations due to the scaling of the computational demands of these calculations with respect to the size of the unit cell. Therefore, opportunities to bridge the dimensional gap shall be strived for. Methods are to be developed to distill key parameters for model-based calculations on a microscopic and mesoscopic scale from ab initio calculations on the nano-scale. Possible investigations include, for instance, calculations based on the Landau-Lifschitz-Gilbert equation. An important aspect is a proper determination and treatment of the lifetimes of excited states and the dynamics of transition processes.

All these prospects show that the exploration of magnetic excitations remains an agile field of research, and computational investigations are at the very core of it.

APPENDIX A

NOTATION

Contents

A.1 Constants and Units	125
A.2 Fourier Transform and Lattice Periodicity	128

A.1 Constants and Units

In this work the initial formulas in chapter 2 that define the many-body problem and the magnetic quantities have been written down in SI units. Starting from close to the beginning of chapter 2 the atomic units (more specifically the Hartree atomic unit set) has been used. (The only exception is the derivation in appendix B.2 which is shown to have an additional factor in SI units which equals one in atomic units; nevertheless one should be aware of that.) In the literature also the Gaussian unit set is extensively used, which frequently causes confusion. In order to see the essential transformations from one unit set to another, their most important specifics with respect to the theoretical framework of this thesis is presented here, as briefly as possible.

On Units in General Classically a distinction is made between *fundamental* units and *derived* units which are combined out of the former ones. However, as has been thoroughly discussed by Bridgman [Bri31], the choice as well as the number of fundamental units is arbitrary. It is even possible to reduce the set to one fundamental unit. In the regime of mechanics it is common to establish three independent fundamental units for the quantities of mass, length and time. With the advent of electrodynamics, there arose choice to describe the new effects by an additional unit like the SI unit system featuring the Ampere, or describing it by the given mechanical units like the Gaussian system. One interesting aspect is that for a given unit set there can be quantities of different physical character which have the same unit. To complicate matters, due to historic reasons there exist several variations of the unit sets, like other cgs systems.

Dimensionless quantities keep their value regardless of the choice of units, most prominently the fine-structure constant

$$\alpha = 0.0072974\dots \approx \frac{1}{137} \tag{A.1}$$

indicating the strength of the electromagnetic interaction compared to the strong interaction. Quantities involving dimensions have a value specific to the unit system.

The SI System The *Système international d'unités* has the four fundamental units:

length (1 m) — mass (1 kg) — time (1 s) — current (1 A).

Some derived units are:

quantity	derived unit/relation to fundamental units
charge	1 C = 1 As
energy	1 J = 1 kg m ² s ⁻²
electric potential	1 J C ⁻¹
magnetic field	1 T = 1 kg C ⁻¹ s ⁻¹
magnetic moment	1 J T ⁻¹

A single electron's potential V_e and the kinetic energy operator \hat{T} in a vector potential \mathbf{A} read

$$V_e(r) = \frac{1}{4\pi\epsilon_0} \frac{e}{r} \quad (\text{A.2})$$

$$\hat{T} = \frac{\hbar}{i} \nabla + e\mathbf{A}. \quad (\text{A.3})$$

The interaction of magnetic moments with a magnetic field $\sim \mathbf{m} \cdot \mathbf{B}$ keeps its form in all unit sets, though the involved units do change. Some selected constants in SI units read

constant	symbol	relation	numerical value
elementary charge	e		$= 1.6022 \cdot 10^{-19} \text{ C}$
Electronvolt	eV		$= 1.6022 \cdot 10^{-19} \text{ J}$
Rydberg energy	$R_y = \hbar^2 / (2m_e a_B^2)$		$= 13.606 \text{ eV}$
electronic mass	m_e		$= 9.1095 \cdot 10^{-31} \text{ kg}$
speed of light	c		$= 2.9979 \cdot 10^8 \text{ m s}^{-1}$
permittivity of free space	$\epsilon_0 =$		$= 8.8542 \cdot 10^{-12} \text{ A}^2 \text{ s}^4 \text{ kg}^{-1} \text{ m}^{-3}$
Bohr magneton	$\mu_B = e\hbar / (2m_e)$		$= 9.2741 \cdot 10^{-24} \text{ J T}^{-1}$
Bohr radius	$a_B = 4\pi\epsilon_0 \hbar^2 / (m_e e^2)$		$= 5.2918 \cdot 10^{-11} \text{ m}$
Planck quantum	\hbar		$= 1.0546 \cdot 10^{-34} \text{ J s}$
Fine-structure constant	$\alpha = e^2 / (4\pi\epsilon_0 \hbar c)$		$\approx 1/137$

The elementary charge is defined as the positively signed charge of the electron. The numeric value of the dielectric constant ϵ_0 is fixed as $8.8542 \cdot 10^{-12} = \frac{1}{4\pi} 10^7 |c|^{-2}$.

Gaussian Units The three fundamental units of the Gauss unit set are:

length (1 cm) — mass (1 g) — time (1 s).

There are in fact different so-called *cgs unit systems* which have the same three fundamental units but differ in the derived units. Some derived units of the Gaussian unit set read

quantity	derived unit/relation to fundamental units
charge	1 esu = 1 erg ^{1/2} cm ^{1/2}
energy	1 erg = 1 gm cm ² s ⁻²
electric potential	1 erg esu ⁻¹
electric/magnetic field	1 G = 1 gm cm ^{-1/2} s ⁻¹
magnetic moment	1 erg G ⁻¹

The electrostatic unit of charge (esu) is also called one *statcoulomb*. It is defined such that two unit charges in the distance of 1 cm yield an electrostatic energy of 1 erg. The unit of the electric and the

magnetic field is 1 Gauss (G). A single electron's potential V_e and the kinetic energy operator \hat{T} in a vector potential \mathbf{A} read

$$V_e(r) = \frac{e}{r} \tag{A.4}$$

$$\hat{T} = \frac{\hbar}{i} \nabla + \frac{e}{c} \mathbf{A}. \tag{A.5}$$

The constants listed earlier now in Gaussian units read:

constant	symbol	relation	numerical value
elementary charge	e		$= 4.8032 \cdot 10^{-10}$ esu
electronvolt	eV		$= 1.6022 \cdot 10^{-12}$ erg
electronic mass	m_e		$= 9.1095 \cdot 10^{-28}$ gm
speed of light	c		$= 2.9979 \cdot 10^{10}$ cm s ⁻¹
Bohr magneton	$\mu_B = e\hbar/(2m_e c)$		$= 9.2741 \cdot 10^{-21}$ erg G ⁻¹
Bohr radius	$a_B = \hbar^2/(m_e e^2)$		$= 5.2918 \cdot 10^{-9}$ cm
Planck quantum	\hbar		$= 1.0546 \cdot 10^{-27}$ erg s
Rydberg energy	$Ry = \hbar^2/(2m_e a_B^2)$		$= 13.606$ eV
Fine-structure constant	$\alpha = e^2/(\hbar c)$		$\approx 1/137$

The prefactor of the elementary charge e above can be connected to values of the SI system by its definition as $4.8032 \cdot 10^{-10} = 10|c| \cdot |e|$, with $|c|$ and $|e|$ the dimension-less values of the according constants in SI units. The relation of a few Gaussian units to their SI equivalents read:

quantity	SI unit	Gaussian unit
length	1 m	$= 100$ cm
mass	1 kg	$= 1000$ gm
charge	1 C	$= 2.9979 \cdot 10^9$ esu
energy	1 J	$= 10^7$ erg
magnetic field	1 T	$= 10^4$ G

For more details on the cgs unit systems, the conversion between Gaussian and SI units and extensive information on the Gaussian unit system in electrodynamics please refer to the Appendix of the Jackson classic [Jac62].

Atomic Units Fundamental units in the atomic unit set are

length (1 a_B) — mass (1 m_e) — charge (1 e) — energy (1 Htr) — angular momentum (1 \hbar).

These units are combined to properly describe the following quantities:

quantity	combination of units
frequency ($[\omega] = s^{-1}$)	1 Htr \hbar^{-1}
speed	1 $e^2 \hbar^{-1}$
magnetic moment	1 $\mu_B = \frac{1}{2} a_B \hbar m_e^{-1}$
magnetic field	1 Htr μ_B^{-1}

For more details on conversion please confer to appendix 6 in [ZL83]. A single electron's potential V_e and the kinetic energy operator \hat{T} in a vector potential \mathbf{A} read

$$V_e(r) = \frac{1}{r} \quad (\text{A.6})$$

$$\hat{T} = \frac{1}{i} \nabla + \mathbf{A}. \quad (\text{A.7})$$

The atomic units are chosen such that most of the constants from quantum mechanics take a numerical value of one:

constant	symbol and value
elementary charge	$e = 1 e$
electronic mass	$m_e = 1 m_e$
dielectric constant	$\varepsilon_0 = \frac{1}{4\pi}$
speed of light	$c = \frac{1}{\alpha} e^2 \hbar^{-1} \approx 137 e^2 \hbar^{-1}$
Bohr magneton	$\mu_B = 1 \mu_B$
Bohr radius	$a_B = 1 a_B$
Planck quantum	$\hbar = 1 \hbar$
Rydberg energy	$\text{Ry} = \frac{1}{2} \text{Htr}$

This has the nice consequence that a formula given in SI units can be simply transformed by applying above equalities, e.g.

$$\hbar = 1, m_e = 1, e^2 = 1, \varepsilon_0 = \frac{1}{4\pi}, c = \frac{1}{\alpha} \approx 137. \quad (\text{A.8})$$

It should be remarked that there is a concurring setting called the *Rydberg set* of atomic units, which differ in the energy scale by a factor of two. The above conversion would then read

$$\hbar = 1, m_e = \frac{1}{2}, e^2 = 2, \varepsilon_0 = \frac{1}{4\pi}, c = \frac{2}{\alpha} \approx 2 \cdot 137. \quad (\text{A.9})$$

It should be stressed that this latter choice is *not* used in this thesis.

A.2 Fourier Transform and Lattice Periodicity

Several formulae in this text involve a Fourier transform in their derivation, thus a precise definition is provided in order to eliminate potential ambiguities. Integrals, if not denoted otherwise, extend throughout the whole space or time, respectively.

Fourier Transform in Time The Fourier transform can be written in a symmetrical form like

$$f(\tau) = \int_{-\infty}^{+\infty} d\nu e^{+2\pi i \nu \tau} f(\nu) \quad (\text{A.10})$$

$$f(\nu) = \int_{-\infty}^{+\infty} d\tau e^{-2\pi i \nu \tau} f(\tau). \quad (\text{A.11})$$

In physics, it is common to use an unsymmetrical form involving the substitution $\omega = 2\pi\nu$, and use the opposite choice of signs in the exponent:

$$f(\tau) = \frac{1}{2\pi} \int d\omega e^{-i\omega\tau} f(\omega) \quad (\text{A.12})$$

$$f(\omega) = \int d\tau e^{+i\omega\tau} f(\tau). \quad (\text{A.13})$$

This results in convolutions

$$f(\tau) = a(\tau)b(\tau) \quad \Rightarrow \quad f(\omega) = \frac{1}{2\pi} \int d\omega' a(\omega - \omega')b(\omega') \quad (\text{A.14})$$

$$f(\omega) = a(\omega)b(\omega) \quad \Rightarrow \quad f(\tau) = \int d\tau' a(\tau - \tau')b(\tau'). \quad (\text{A.15})$$

Double convolutions resolve analogously to

$$f(t - t') = \int dt_1 dt_2 a(t - t_1)b(t_1 - t_2)c(t_2 - t') \quad (\text{A.16})$$

$$\Rightarrow \quad f(\omega) = a(\omega)b(\omega)c(\omega). \quad (\text{A.17})$$

Lattice Periodicity Quantum-mechanical wave functions $\varphi(\mathbf{r})$ of an infinite lattice-periodic system reveal symmetry by virtue of the Bloch theorem,

$$\varphi(\mathbf{r}) = e^{i\mathbf{k}\mathbf{L}}\varphi(\mathbf{r} + \mathbf{L}), \quad \mathbf{r} \in \mathbb{R}^3, \mathbf{L} \in \text{lattice}, \mathbf{k} \in \text{BZ}, \quad (\text{A.18})$$

and can be written in the form

$$\varphi_{\mathbf{k}}(\mathbf{r}) = e^{i\mathbf{k}\mathbf{r}}u(\mathbf{r}), \quad u(\mathbf{r}) = u(\mathbf{r} + \mathbf{L}). \quad (\text{A.19})$$

The treatment of spatial coordinates can then be restricted to one unit cell. One- and two-point functions that have possess lattice periodicity can be expressed in reciprocal lattice vectors \mathbf{G} and Brillouin-zone vectors \mathbf{q} by

$$g(\mathbf{r}) = g(\mathbf{r} + \mathbf{L}) \quad \Rightarrow \quad g(\mathbf{r}) \rightleftharpoons g_{\mathbf{G}} \quad (\text{A.20})$$

$$g(\mathbf{r}, \mathbf{r}') = g(\mathbf{r} + \mathbf{L}, \mathbf{r}' + \mathbf{L}) \quad \Rightarrow \quad g(\mathbf{r}, \mathbf{r}') \rightleftharpoons g(\bar{\mathbf{r}}, \bar{\mathbf{r}}'; \mathbf{q}) \rightleftharpoons g_{\mathbf{G}, \mathbf{G}'}(\mathbf{q}) \quad (\text{A.21})$$

where $\bar{\mathbf{r}}, \bar{\mathbf{r}}'$ denotes vectors restricted to the unit cell. The integer-based parameters \mathbf{G} are written as subscripts.

Spatial Fourier Transform For the Fourier transform between real and reciprocal space it is common to use the other set of signs

$$g(\mathbf{r}) = \frac{1}{(2\pi)^3} \int d^3q e^{+i\mathbf{q}\mathbf{r}} g(\mathbf{q}) \quad (\text{A.22})$$

$$g(\mathbf{q}) = \int d^3r e^{-i\mathbf{q}\mathbf{r}} g(\mathbf{r}). \quad (\text{A.23})$$

The transforms between discrete and continuous variables regarding lattice symmetry – real-space lattice vector \mathbf{L} to Brillouin-zone coordinate \mathbf{k} and unit-cell coordinate \mathbf{r} to reciprocal lattice vector \mathbf{G} – read

$$g_{\mathbf{L}} = \frac{1}{(2\pi)^3} \int e^{+i\mathbf{k}\mathbf{L}} g(\mathbf{k}) d^3k \quad g(\mathbf{r}) = \frac{1}{(2\pi)^3} \sum_{\mathbf{G}} e^{+i\mathbf{G}\mathbf{r}} g_{\mathbf{G}} \quad (\text{A.24})$$

$$g(\mathbf{k}) = \sum_{\mathbf{L}} e^{-i\mathbf{k}\mathbf{L}} g_{\mathbf{L}} \quad g_{\mathbf{G}} = \int e^{-i\mathbf{G}\mathbf{r}} g(\mathbf{r}) d^3k \quad (\text{A.25})$$

Convolutions g of two lattice-periodic two-point functions a and b read

$$g(\mathbf{r}, \mathbf{r}') = \int d^3 r'' a(\mathbf{r}, \mathbf{r}'') b(\mathbf{r}'', \mathbf{r}') \quad (\text{A.26})$$

$$\Leftrightarrow g(\bar{\mathbf{r}}, \bar{\mathbf{r}}'; \mathbf{k}) = \int_{\text{u.c.}} d^3 \bar{r}'' a(\bar{\mathbf{r}}, \bar{\mathbf{r}}''; \mathbf{k}) b(\bar{\mathbf{r}}'', \bar{\mathbf{r}}'; \mathbf{k}) \quad (\text{A.27})$$

$$\Leftrightarrow g_{\mathbf{G}, \mathbf{G}'}(\mathbf{k}) = \sum_{\mathbf{G}''} a_{\mathbf{G}, \mathbf{G}''}(\mathbf{k}) b_{-\mathbf{G}'', \mathbf{G}'}(\mathbf{k}) \quad (\text{A.28})$$

Here again, the variables $\bar{\mathbf{r}}$ indicated by a bar extend throughout one unit cell only. This explicit notation is applied only in this section; in the rest of the text – namely chapter 5 which employs the crystal notation – it will be clear in the context whether or not the variables are confined into one unit cell.

APPENDIX B

DERIVATIONS

Contents

B.1 Lehmann Representation of the Spin-Flip Response	132
B.2 Connection of Derivatives and Expectation Values	133
B.3 The Homogeneous Electron Gas	135
B.4 The Goldstone Theorem for Magnons in Real Materials	137

This section presents a few instructive derivations that were referred to in the previous chapters. Some details such as signs or prefactors should be detailed out since they are crucial for an actual implementation. We are starting with a few identities useful in the coming derivations.

The principal identity is crucial for evaluating denominators running to infinity, used e.g. in the derivation of the Lehmann representation (3.24):

$$\lim_{\eta \rightarrow 0^+} \int_a^b \frac{dx}{x \pm i\eta} = \mathcal{P} \int_a^b \frac{dx}{x} \mp i\pi \int_a^b \delta(x) dx. \quad (\text{B.1})$$

\mathcal{P} is the Cauchy principal value of the integral defined as

$$\mathcal{P} \int_a^b f(x) dx = \lim_{\eta \rightarrow 0^+} \left[\int_a^{x_0 - \eta} f(x) dx + \int_{x_0 + \eta}^b f(x) dx \right], \quad (\text{B.2})$$

where the function f is assumed to have one singularity at x_0 inside the interval $[a, b]$. Relations of the exponential function: The straightforward connection between the exponential and the δ -distribution reads

$$\int_{-\infty}^{+\infty} d\omega e^{i\omega\tau} = 2\pi\delta(\tau). \quad (\text{B.3})$$

Integrals over only half of the axis read

$$\int_0^{+\infty} d\tau e^{i\omega\tau} = - \lim_{\eta \rightarrow 0^+} \frac{1}{i(\omega + i\eta)} \quad (\text{B.4})$$

$$\int_{-\infty}^0 d\tau e^{i\omega\tau} = \lim_{\eta \rightarrow 0^+} \frac{1}{i(\omega - i\eta)}. \quad (\text{B.5})$$

B.1 Lehmann Representation of the Spin-Flip Response

The correlation function χ^{ij} with cartesian indices is defined

$$i\chi^{ij}(\mathbf{r}, t, \mathbf{r}', t') = \langle 0 | \hat{T}[\hat{S}^i(\mathbf{r}, t), \hat{S}^j(\mathbf{r}', t')] | 0 \rangle \Theta(t - t') \quad (\text{B.6})$$

$$= \langle 0 | \hat{S}^i(\mathbf{r}, t) \hat{S}^j(\mathbf{r}', t') | 0 \rangle \Theta(t - t') + \langle 0 | \hat{S}^j(\mathbf{r}', t') \hat{S}^i(\mathbf{r}, t) | 0 \rangle \Theta(t - t'), \quad (\text{B.7})$$

c.f. (3.7). The operators' time dependence can be separated by changing from the Heisenberg picture to the Schrödinger picture (3.9),

$$\hat{S}^i(\mathbf{r}, t) = e^{+i\hat{H}t} \hat{S}^i(\mathbf{r}) e^{-i\hat{H}t}. \quad (\text{B.8})$$

The unity relation is written

$$\sum_{n, S_z} |n, S_z\rangle \langle n, S_z| = \mathbb{1} \quad (\text{B.9})$$

where the bras and kets are many-body states indexed by the good quantum number S_z and the index n which takes up e.g. particle number N , total spin quantum number S and any other quantum number indexing excited eigenstates of the system. Applying this to the correlation function above yields

$$i\chi^{ij}(\mathbf{r}, t, \mathbf{r}', t') = \sum_{n', S'_z} \left[\langle 0 | e^{i\hat{H}t} \hat{S}^i(\mathbf{r}) e^{-i\hat{H}t} | n', S'_z \rangle \langle n', S'_z | e^{i\hat{H}t'} \hat{S}^j(\mathbf{r}') e^{-i\hat{H}t'} | 0 \rangle \Theta(t - t') + \right. \\ \left. \langle 0 | e^{i\hat{H}t'} \hat{S}^j(\mathbf{r}') e^{-i\hat{H}t'} | n', S'_z \rangle \langle n', S'_z | e^{i\hat{H}t} \hat{S}^i(\mathbf{r}) e^{-i\hat{H}t} | 0 \rangle \Theta(t - t') \right] \quad (\text{B.10})$$

$$= \sum_{n', S'_z} \left[e^{-i[E_{n', S'_z} - E_0](t-t')} \langle 0 | \hat{S}^i(\mathbf{r}) | n', S'_z \rangle \langle n', S'_z | \hat{S}^j(\mathbf{r}') | 0 \rangle \Theta(t - t') + \right. \\ \left. e^{+i[E_{n', S'_z} - E_0](t-t')} \langle 0 | \hat{S}^j(\mathbf{r}') | n', S'_z \rangle \langle n', S'_z | \hat{S}^i(\mathbf{r}) | 0 \rangle \Theta(t - t') \right]. \quad (\text{B.11})$$

In the second line a time-independent Hamiltonian has been assumed. Performing Fourier transformation (A.13) together with relations (B.4), (B.5) we obtain the Lehmann representation of the correlation function as

$$\chi^{ij}(\mathbf{r}, \mathbf{r}'; \omega) = \sum_{n', S'_z} \left[\int_0^{+\infty} \frac{d\tau}{i} e^{i[\omega - (E_{n', S'_z} - E_0)]\tau} \langle 0 | \hat{S}^i(\mathbf{r}) | n', S'_z \rangle \langle n', S'_z | \hat{S}^j(\mathbf{r}') | 0 \rangle + \right. \\ \left. \int_0^{+\infty} \frac{d\tau}{i} e^{i[\omega + (E_{n', S'_z} - E_0)]\tau} \langle 0 | \hat{S}^j(\mathbf{r}') | n', S'_z \rangle \langle n', S'_z | \hat{S}^i(\mathbf{r}) | 0 \rangle \right] \quad (\text{B.12}) \\ = \lim_{\eta \rightarrow 0^+} \sum_{n', S'_z} \left[\frac{\langle 0 | \hat{S}^i(\mathbf{r}) | n', S'_z \rangle \langle n', S'_z | \hat{S}^j(\mathbf{r}') | 0 \rangle}{\omega - (E_{n', S'_z} - E_0) + i\eta} - \frac{\langle 0 | \hat{S}^j(\mathbf{r}') | n', S'_z \rangle \langle n', S'_z | \hat{S}^i(\mathbf{r}) | 0 \rangle}{\omega + (E_{n', S'_z} - E_0) + i\eta} \right].$$

Now we turn to the spin-flip response χ^{-+} , c.f. (3.18), leading to the operators \hat{S}^+ and \hat{S}^- in the previous formula. In the bra-kets in the numerator, only certain states $|n', S'_z\rangle$ yield non-zero contributions, namely those with the same particle number N and an spin- z quantum number shifted from the ground state by one, $S'_z = S_z^{(0)} \pm 1$. Therefore the sum can be restricted to these states,

$$\chi^{-+}(\mathbf{r}, \mathbf{r}'; \omega) = \lim_{\eta \rightarrow 0^+} \left[\sum_n \frac{\langle 0 | \hat{S}^-(\mathbf{r}) | n, S_z^{(0)} + 1 \rangle \langle n, S_z^{(0)} + 1 | \hat{S}^+(\mathbf{r}') | 0 \rangle}{\omega - (E_{n, S_z^{(0)}+1} - E_0) + i\eta} - \sum_n \frac{\langle 0 | \hat{S}^+(\mathbf{r}') | n, S_z^{(0)} - 1 \rangle \langle n, S_z^{(0)} - 1 | \hat{S}^-(\mathbf{r}) | 0 \rangle}{\omega + (E_{n, S_z^{(0)}-1} - E_0) + i\eta} \right], \quad (\text{B.13})$$

obtaining the Lehmann representation already shown in (3.24).

Remark In order to be able to perform the Fourier transform we have to ensure $E_{n', S'_z} \neq E_0$ in (B.12). As a first step we assume a non-degenerate ground state. However, since we inserted a unity relation in (B.10) the sum over all eigenstates $|n', S'_z\rangle$ also includes the ground state $|0, S_z^{(0)}\rangle$.

- For the spin-flip response χ^{+-} this does not pose a problem because only states with $S'_z = S_z^{(0)} \pm 1$ contribute. The ground state, which does not contribute, can subsequently be removed from the sum before the Fourier transform is performed.
- For the charge-charge correlation function χ^{00} this is not the case. Instead the term that the ground state contributes to the sum is explicitly subtracted, compare (3.25). This is also commonly written as $\chi^{00} \rightarrow \chi^{00} - \langle \chi^{00} \rangle$.

The derivative in this section for the causal correlation function, can be performed the same way for the time-ordered correlation function.

B.2 Connection of Derivatives and Expectation Values

In this section equation (3.50) should be derived which establishes the connection between the many-body expectation value χ on the one hand that is defined in (3.7) and investigated in section 3.2, and on the other hand the functional derivative R defined in (3.49) in section 3.3. Atomic units are used as in the rest of this work. At first the notation of the numerator of the functional derivative

$$m^i(\mathbf{r}, t) = -\mu_{\text{B}}g \langle \hat{S}^i(\mathbf{r}, t) \rangle = -\mu_{\text{B}}g \langle 0 | \hat{S}^i(\mathbf{r}, t) | 0 \rangle = -\mu_{\text{B}}g \langle 0(t) | \hat{S}^i(\mathbf{r}) | 0(t) \rangle \quad (\text{B.14})$$

is changed from the Heisenberg picture – c.f. formula (3.9) – to the Schrödinger picture. Here $|0(t)\rangle$ is the time-dependent many-body ground-state. Then, calculation is pursued within first-order time-dependent perturbation theory, afterwards the functional derivative is performed.

Time-Dependent Perturbation For the evaluation of the just mentioned many-body terms $|0(t)\rangle$ common time-dependent perturbation theory to the first order in the perturbation is used. The unperturbed system is characterized by the Hamiltonian $\mathcal{H}^{(0)}$ (c.f. (2.3)), its states $|m\rangle$ are determined by the Schrödinger equation

$$\hat{\mathcal{H}}^{(0)} |m(t)\rangle = i \frac{\partial}{\partial t} |m(t)\rangle. \quad (\text{B.15})$$

The inclusion of a small perturbation $\mathcal{H}^{(1)}$ yields the Hamiltonian

$$\hat{\mathcal{H}} = \hat{\mathcal{H}}^{(0)} + \lambda \hat{\mathcal{H}}^{(1)}(t) \quad (\text{B.16})$$

with the interaction parameter λ . The states $|n\rangle$ of the perturbed system are determined from

$$\hat{\mathcal{H}} |n(t)\rangle = i \frac{\partial}{\partial t} |n(t)\rangle \quad (\text{B.17})$$

and can be expanded in λ as

$$|n_\lambda(t)\rangle = |n_\lambda^{(0)}(t)\rangle + \lambda |n_\lambda^{(1)}(t)\rangle + \mathcal{O}(\lambda^2) \quad (\text{B.18})$$

They furthermore obey the closure relation

$$\sum_n |n(t)\rangle\langle n(t)| = \mathbb{1}. \quad (\text{B.19})$$

The term in linear order of λ that we are interested in can be expanded in the original states $|m\rangle$ as

$$|n_\lambda^{(1)}(t)\rangle = \sum_m c_{mn}(t) |m^{(0)}(t)\rangle \quad (\text{B.20})$$

$$c_{mn}(t) = \frac{1}{i} \int_{-\infty}^{+\infty} dt' \Theta(t-t') \langle m^{(0)}(t') | \hat{\mathcal{H}}^{(1)}(t') | n^{(0)}(t') \rangle. \quad (\text{B.21})$$

Here the notation $|m^{(0)}\rangle$ was used to indicate that these are the unperturbed states (i.e. of zeroth order in the perturbation).

Application to Magnetic Response In our case the perturbing Hamiltonian is determined by the applied magnetic field and reads

$$\hat{\mathcal{H}}^{(1)}(t) = \mu_B g \int d^3r \hat{\mathbf{S}}(\mathbf{r}) \cdot \mathbf{B}_{\text{ext}}(\mathbf{r}, t). \quad (\text{B.22})$$

The linear-order terms of the spin density reads

$$\mathbf{S}(\mathbf{r}, t) = \langle \hat{\mathbf{S}}(\mathbf{r}, t) \rangle^{(0)} + \lambda \langle \hat{\mathbf{S}}(\mathbf{r}, t) \rangle^{(1)} + \mathcal{O}(\lambda^2) \quad (\text{B.23})$$

$$\langle \hat{\mathbf{S}}(\mathbf{r}, t) \rangle^{(1)} = \langle 0^{(0)}(t) | \hat{\mathbf{S}}(\mathbf{r}) | 0^{(1)}(t) \rangle + \langle 0^{(1)}(t) | \hat{\mathbf{S}}(\mathbf{r}) | 0^{(0)}(t) \rangle. \quad (\text{B.24})$$

Combining the previous formulae into the evaluation of the first addend gives

$$\begin{aligned} \langle 0^{(0)}(t) | \hat{S}^i(\mathbf{r}) | 0^{(1)}(t) \rangle &= \frac{\mu_B g}{i} \int d^3r' \int_{-\infty}^{+\infty} dt' \Theta(t-t') \mathbf{B}_{\text{ext}}(\mathbf{r}', t') \cdot \\ &\quad \langle 0^{(0)}(t) | \hat{S}^i(\mathbf{r}) \sum_m |m^{(0)}(t)\rangle \langle m^{(0)}(t') | \hat{\mathbf{S}}(\mathbf{r}') | 0^{(0)}(t') \rangle. \end{aligned} \quad (\text{B.25})$$

Applying a functional derivative of this equation, and switching again to the Heisenberg picture on the right-hand side leads to

$$\frac{\delta \langle 0^{(0)}(t) | \hat{S}^i(\mathbf{r}) | 0^{(1)}(t) \rangle}{\delta B_{\text{ext}}^j(\mathbf{r}', t')} = \frac{\mu_B g}{i} \langle 0^{(0)} | \hat{S}^i(\mathbf{r}, t) \hat{S}^j(\mathbf{r}', t') | 0^{(0)} \rangle \Theta(t-t'). \quad (\text{B.26})$$

Such a relation is also derived for the second term on the right-hand side of (B.24). The sum of both can be combined in a commutator brackets and lead to the sought-after relation

$$R^{ij}(\mathbf{r}, t, \mathbf{r}', t') = \frac{\delta m^i(\mathbf{r}, t)}{\delta B_{\text{ext}}^j(\mathbf{r}', t')} \quad (\text{B.27})$$

$$= -\mu_B g \left(\frac{\delta \langle 0^{(1)}(t) | \hat{S}^i(\mathbf{r}) | 0^{(0)}(t) \rangle}{\delta B_{\text{ext}}^j(\mathbf{r}', t')} + \frac{\delta \langle 0^{(0)}(t) | \hat{S}^i(\mathbf{r}) | 0^{(1)}(t) \rangle}{\delta B_{\text{ext}}^j(\mathbf{r}', t')} \right) \quad (\text{B.28})$$

$$= -\frac{(\mu_B g)^2}{i} \langle 0^{(0)} | [\hat{S}^i(\mathbf{r}, t), \hat{S}^j(\mathbf{r}', t')] | 0^{(0)} \rangle \Theta(t-t') \quad (\text{B.29})$$

$$= -(\mu_B g)^2 \chi^{ij}(\mathbf{r}, t, \mathbf{r}', t'). \quad (\text{B.30})$$

This equality also holds for the spin-flip notation, provided that the definition (3.52) has been used for the functional derivatives (c.f. the footnote on page 37). The need for this definition becomes obvious from the derivation above, if one traces the origin of superscript j in the response function R^{ij} . The term $\langle 0^{(0)}(t) | \hat{S}^i(\mathbf{r}) | 0^{(1)}(t) \rangle$ in equation (B.25) contains a factor $\hat{\mathbf{S}} \cdot \mathbf{B}_{\text{ext}}$, and the functional derivative yields $\delta(\hat{\mathbf{S}} \cdot \mathbf{B}_{\text{ext}}) / \delta B_{\text{ext}}^j = \hat{S}^j$. In other words the term B_{ext}^j couples to \hat{S}^j .

If one expresses this vector product by the ladder operators, c.f. (3.6), $\delta(\hat{\mathbf{S}} \cdot \mathbf{B}_{\text{ext}}) / \delta B_{\text{ext}}^+ = \hat{S}^-$. In other words the term B_{ext}^+ couples to \hat{S}^- , and B_{ext}^- couples to \hat{S}^+ . If one would like to keep the proportionality also for the notation of ladder operators,

$$R^{-+}(\mathbf{r}, t, \mathbf{r}', t') = -(\mu_B g)^2 \chi^{-+}(\mathbf{r}, t, \mathbf{r}', t'), \quad (\text{B.31})$$

one needs to *define* the derivatives as

$$\frac{\delta}{\delta B^\pm} = \frac{\delta}{\delta B^x} \pm i \frac{\delta}{\delta B^y}, \quad (\text{B.32})$$

c.f. (3.52).

B.3 The Homogeneous Electron Gas

In this section the spin-flip susceptibility is evaluated for the homogeneous electron gas. Its single-particle energies and wave functions are determined in section 4.1 as

$$\epsilon_\uparrow(\mathbf{k}) = \epsilon_{\mathbf{k}} - \Delta, \quad \epsilon_\downarrow(\mathbf{k}) = \epsilon_{\mathbf{k}} + \Delta, \quad \epsilon_{\mathbf{k}} = \frac{1}{2}k^2, \quad \varphi_{k\sigma}(\mathbf{r}) = \frac{1}{\sqrt{V}} e^{i\mathbf{k} \cdot \mathbf{r}}. \quad (\text{B.33})$$

The complex spin-flip susceptibility for non-interacting particles in general is given by (3.46), it evaluates to

$$\chi_{\text{KS}}^{+-}(\mathbf{r} - \mathbf{r}'; \omega) = \lim_{\eta \rightarrow 0^+} \frac{1}{V^2} \sum_{\mathbf{k}, \mathbf{k}'} \frac{f(\epsilon_\uparrow(\mathbf{k})) - f(\epsilon_\downarrow(\mathbf{k}'))}{\omega - (\epsilon_\downarrow(\mathbf{k}') - \epsilon_\uparrow(\mathbf{k})) + i\eta} e^{-i(\mathbf{k} - \mathbf{k}') \cdot (\mathbf{r} - \mathbf{r}')}. \quad (\text{B.34})$$

Applying a Fourier transform according to section A.2 leads to

$$\chi_{\text{KS}}^{+-}(\mathbf{q}, \omega) = \frac{1}{V} \lim_{\eta \rightarrow 0^+} \sum_{\mathbf{k}} \frac{f(\epsilon_\uparrow(\mathbf{k})) - f(\epsilon_\downarrow(\mathbf{k} + \mathbf{q}))}{\omega - [\epsilon_\downarrow(\mathbf{k} + \mathbf{q}) - \epsilon_\uparrow(\mathbf{k})] + i\eta} \quad (\text{B.35})$$

$$= \frac{1}{V} \lim_{\eta \rightarrow 0^+} \sum_{\mathbf{k}} \left\{ \frac{f(\epsilon_{\mathbf{k}} - \Delta)}{\epsilon_{\mathbf{k}} - \epsilon_{\mathbf{k} + \mathbf{q}} - 2\Delta + \omega + i\eta} - \frac{f(\epsilon_{\mathbf{k}} + \Delta)}{\epsilon_{\mathbf{k} + \mathbf{q}} - \epsilon_{\mathbf{k}} - 2\Delta + \omega + i\eta} \right\}. \quad (\text{B.36})$$

The susceptibility is spherically symmetric in q . Using spherical coordinates and considering $\sum_{\mathbf{k}} = V/(2\pi)^3 \int d^3k$ yields

$$\chi_{\text{KS}}^{+-}(q, \omega) = \lim_{\eta \rightarrow 0^+} \frac{1}{(2\pi)^2} \left\{ \int_0^{k_{\text{F}\uparrow}} k^2 dk \int_{-1}^{+1} \frac{dx}{-\frac{1}{2}q^2 - kqx - 2\Delta + \omega + i\eta} - \int_0^{k_{\text{F}\downarrow}} k^2 dk \int_{-1}^{+1} \frac{dx}{+\frac{1}{2}q^2 + kqx - 2\Delta + \omega + i\eta} \right\} \quad (\text{B.37})$$

where $x = \cos \theta$ has been used and

$$\epsilon_{\mathbf{k} + \mathbf{q}} - \epsilon_{\mathbf{k}} = \frac{1}{2}q^2 + kqx. \quad (\text{B.38})$$

We introduce the notation

$$u_\sigma = \frac{2\Delta - \omega + \frac{1}{2}\sigma q^2}{q} \quad (\text{B.39})$$

to formulate the intermediate result

$$\chi_{\text{KS}}^{+-}(q, \omega) = -\frac{1}{4\pi^2 q} \lim_{\eta \rightarrow 0^+} \sum_\sigma \sigma \int_0^{k_{\text{F}\sigma}} k^2 dk \int_{-1}^{+1} \frac{dx}{\sigma kx + u_\sigma - i\eta}. \quad (\text{B.40})$$

Real and Imaginary Part Due to the principal relation (B.1) the real and imaginary part of the susceptibility can be further derived. For the real part one evaluates the integration over the singularity as

$$\mathcal{P} \int_{x_0}^{x_1} \frac{dx}{ax + b} = \frac{1}{a} \ln \left| \frac{ax_1 + b}{ax_0 + b} \right| \quad (\text{B.41})$$

and yields

$$\text{Re } \chi_{\text{KS}}^{+-}(q, \omega) = -\frac{1}{4\pi^2 q} \sum_\sigma \sigma \int_0^{k_{\text{F}\sigma}} k^2 dk \mathcal{P} \int_{-1}^{+1} \frac{dx}{\sigma kx + p_\sigma} \quad (\text{B.42})$$

$$= -\frac{1}{4\pi^2 q} \sum_\sigma \int_0^{k_{\text{F}\sigma}} k \ln \left| \frac{p_\sigma + \sigma k}{p_\sigma - \sigma k} \right| dk \quad (\text{B.43})$$

$$= -\frac{1}{4\pi^2 q} \sum_\sigma \sigma \int_0^{k_{\text{F}\sigma}} k \ln \left| \frac{p_\sigma + k}{p_\sigma - k} \right| dk. \quad (\text{B.44})$$

The remaining integral resolves to

$$\int k \ln(p \pm k) dk = \left[\frac{1}{2}(p \pm k)^2 - p(p \pm k) \right] \ln(p \pm k) + \left(\frac{3}{4}p^2 \pm \frac{1}{2}pk - \frac{1}{4}k^2 \right) \quad (\text{B.45})$$

$$\int_0^{k_{\text{F}\sigma}} k \ln \left| \frac{p + k}{p - k} \right| dk = \frac{1}{2}(k_{\text{F}\sigma}^2 - p^2) \ln \left| \frac{p + k_{\text{F}\sigma}}{p - k_{\text{F}\sigma}} \right| + pk_{\text{F}\sigma} \quad (\text{B.46})$$

so that the final result for the real part reads

$$\text{Re } \chi_{\text{KS}}^{+-}(q, \omega) = -\frac{1}{4\pi^2 q} \sum_\sigma \sigma \left[\frac{1}{2}(k_{\text{F}\sigma}^2 - p_\sigma^2) \ln \left| \frac{p_\sigma + k_{\text{F}\sigma}}{p_\sigma - k_{\text{F}\sigma}} \right| + p_\sigma k_{\text{F}\sigma} \right] \quad (\text{B.47})$$

For the imaginary part one takes into account

$$\lim_{\eta \rightarrow 0^+} \int_{-\eta}^{+\eta} \delta(\alpha x) dx = \frac{1}{|\alpha|}, \quad \alpha \in \mathbb{R} \quad (\text{B.48})$$

and gets

$$\text{Im } \chi_{\text{KS}}^{+-}(q, \omega) = -\frac{1}{4\pi q} \sum_\sigma \sigma \int_0^{k_{\text{F}\sigma}} k^2 dk \int_{-1}^{+1} \delta(\sigma kx + p_\sigma) dx \quad (\text{B.49})$$

$$= -\frac{1}{4\pi q} \sum_\sigma \sigma \int_0^{k_{\text{F}\sigma}} k \Theta(k - |p_\sigma|) dk. \quad (\text{B.50})$$

Applying the integration

$$\int_0^c k\Theta(k-a) dk = \Theta(c-a) \int_a^c k dk = \frac{1}{2}(c^2 - a^2)\Theta(c-a) \quad \text{for } a \geq 0 \quad (\text{B.51})$$

finally gives

$$\text{Im } \chi_{\text{KS}}^{+-}(q, \omega) = -\frac{1}{8\pi q} \sum_{\sigma} \sigma(k_{\text{F}\sigma}^2 - p_{\sigma}^2)\Theta(k_{\text{F}\sigma} - |p_{\sigma}|). \quad (\text{B.52})$$

Rescaling The susceptibility should for the moment be denoted $\chi_{\text{KS}}^{+-[n,\Delta]}(q, \omega)$ to stress its dependence on the density n and the spin splitting Δ . If $0 \leq \xi < 1$ is assumed there exists a functional mapping $\Delta = \Delta(\xi)$, c.f. (4.22), and the following scaling relation can be shown:

$$\chi_{\text{KS}}^{+-[n_0,\Delta]}(q, \omega) = \frac{1}{\alpha} \chi_{\text{KS}}^{+-[\alpha^3 n_0, \alpha^2 \Delta]}(\alpha q, \alpha^2 \omega) \quad \text{if } 0 \leq \xi < 1 \quad (\text{B.53})$$

for any positive real number α . This useful equality can be used to incorporate the rescaling of the parameters $q \rightarrow q/q_{\text{F}}$ and $\omega \rightarrow \omega/\omega_{\text{F}}$ into the formulas for the Kohn-Sham susceptibility. This is utilized e.g. in [Mor85].

B.4 The Goldstone Theorem for Magnons in Real Materials

In section 4.4 the Goldstone theorem was presented which states for our particular case that the spin-wave excitation energy is zero for vanishing q -vector: $\omega_{\text{sw}}(0) = 0$. It was demonstrated for the case of the homogeneous electron gas by using the actual formulas for the susceptibility and the exchange-correlation kernel. In the following this should be proved in a more general fashion for real materials.

As detailed out in chapter 3 the spin-flip susceptibility χ^{+-} has poles at the true excitation energies and obeys the Dyson equation

$$\int_{u.c.} \left[\delta(\mathbf{r} - \mathbf{r}') - \left(\frac{\mu_{\text{B}}g}{2}\right)^2 \chi_{\text{KS}}^{+-}(\mathbf{r}, \mathbf{r}'; \mathbf{q}, \omega) f_{\text{xc}}^{+-}(\mathbf{r}') \right] \chi^{+-}(\mathbf{r}', \mathbf{r}''; \mathbf{q}, \omega) d^3 r' = \chi_{\text{KS}}^{+-}(\mathbf{r}, \mathbf{r}''; \mathbf{q}, \omega) \quad (\text{B.54})$$

if the adiabatic local density approximation is applied (crystal notation, c.f. (5.4)). The susceptibility of independent particles χ_{KS}^{+-} , on the other hand, remains finite at these excitation energies. According to Petersilka et. al. [PGG96] the true excitation energies $\omega_{\text{sw}}(\mathbf{q})$ can be characterized as those frequencies where the eigenvalues of the integral operator on the left-hand side vanish or, equivalently, where the eigenvalues λ of

$$\int_{u.c.} \left[\delta(\mathbf{r} - \mathbf{r}') - \left(\frac{\mu_{\text{B}}g}{2}\right)^2 \chi_{\text{KS}}^{+-}(\mathbf{r}, \mathbf{r}'; \mathbf{q}, \omega) f_{\text{xc}}^{+-}(\mathbf{r}') \right] \xi(\mathbf{r}'; \mathbf{q}, \omega) d^3 r' = \lambda(\mathbf{q}, \omega) \xi(\mathbf{r}'; \mathbf{q}, \omega) \quad (\text{B.55})$$

satisfy $\lambda(\mathbf{q}, \omega_{\text{sw}}(\mathbf{q})) = 0$. A similar equation will be derived below which will then be interpreted in combination with the two previous integral equations.

Reformulated Equation We start from the collinear Kohn-Sham equations in crystal notation (5.2) for spin-up and spin-down channel,

$$\left[-\frac{1}{2}\nabla_{\mathbf{r}'}^2 + V_{\text{eff}}(\mathbf{r}') + \frac{\mu_{\text{B}}g}{2}B_{\text{eff}}(\mathbf{r}') \right] \varphi_{n\mathbf{k}\uparrow}(\mathbf{r}') = \epsilon_{n\mathbf{k}\uparrow}\varphi_{n\mathbf{k}\uparrow}(\mathbf{r}') \quad (\text{B.56})$$

$$\left[-\frac{1}{2}\nabla_{\mathbf{r}'}^2 + V_{\text{eff}}(\mathbf{r}') - \frac{\mu_{\text{B}}g}{2}B_{\text{eff}}(\mathbf{r}') \right] \varphi_{n'\mathbf{k}+\mathbf{q}\downarrow}^*(\mathbf{r}') = \epsilon_{n'\mathbf{k}+\mathbf{q}\downarrow}\varphi_{n'\mathbf{k}+\mathbf{q}\downarrow}^*(\mathbf{r}'). \quad (\text{B.57})$$

Subtracting the second equation multiplied with $\varphi_{n\mathbf{k}\uparrow}(\mathbf{r}')$ from the first equation multiplied with $\varphi_{n'\mathbf{k}+\mathbf{q}\downarrow}^*(\mathbf{r}')$ yields [KL04]

$$\begin{aligned} \mu_{\text{B}}gB_{\text{eff}}(\mathbf{r}')\varphi_{n'\mathbf{k}+\mathbf{q}\downarrow}^*(\mathbf{r}')\varphi_{n\mathbf{k}\uparrow}(\mathbf{r}') &= [\epsilon_{n\mathbf{k}\uparrow} - \epsilon_{n'\mathbf{k}+\mathbf{q}\downarrow}]\varphi_{n'\mathbf{k}+\mathbf{q}\downarrow}^*(\mathbf{r}')\varphi_{n\mathbf{k}\uparrow}(\mathbf{r}') + \\ &\quad \frac{1}{2}\nabla_{\mathbf{r}'} \left[\varphi_{n'\mathbf{k}+\mathbf{q}\downarrow}^*(\mathbf{r}')(\nabla_{\mathbf{r}'}\varphi_{n\mathbf{k}\uparrow}(\mathbf{r}')) - (\nabla_{\mathbf{r}'}\varphi_{n'\mathbf{k}+\mathbf{q}\downarrow}^*(\mathbf{r}'))\varphi_{n\mathbf{k}\uparrow}(\mathbf{r}') \right]. \end{aligned} \quad (\text{B.58})$$

According to (5.5) the product of susceptibility and effective field reads

$$\begin{aligned} \chi_{\text{KS}}^{+-}(\mathbf{r}, \mathbf{r}'; \mathbf{q}, \omega)B_{\text{eff}}(\mathbf{r}') &= \lim_{\eta \rightarrow 0^+} \sum_{\mathbf{k}} \sum_{n, n'} \frac{f(\epsilon_{n\mathbf{k}\uparrow}) - f(\epsilon_{n'\mathbf{k}+\mathbf{q}\downarrow})}{\omega - (\epsilon_{n'\mathbf{k}+\mathbf{q}\downarrow} - \epsilon_{n\mathbf{k}\uparrow}) + i\eta} \\ &\quad \varphi_{n\mathbf{k}\uparrow}^*(\mathbf{r})\varphi_{n'\mathbf{k}+\mathbf{q}\downarrow}(\mathbf{r}) \left[B_{\text{eff}}(\mathbf{r}')\varphi_{n'\mathbf{k}+\mathbf{q}\downarrow}^*(\mathbf{r}')\varphi_{n\mathbf{k}\uparrow}(\mathbf{r}') \right]. \end{aligned} \quad (\text{B.59})$$

By substituting the square bracket with (B.58) and assuming $\mathbf{q} = \mathbf{0}$ this evaluates to

$$\chi_{\text{KS}}^{+-}(\mathbf{r}, \mathbf{r}'; \mathbf{0}, \omega)B_{\text{eff}}(\mathbf{r}') = \frac{2}{(\mu_{\text{B}}g)^2}m(\mathbf{r}')\delta(\mathbf{r} - \mathbf{r}') - \chi_{\text{KS}}^{+-}(\mathbf{r}, \mathbf{r}; \mathbf{0}, \omega)\frac{\omega}{\mu_{\text{B}}g} + \frac{\Lambda(\mathbf{r}, \mathbf{r}'; \mathbf{0}, \omega)}{\mu_{\text{B}}g} \quad (\text{B.60})$$

with the newly introduced

$$\begin{aligned} \Lambda(\mathbf{r}, \mathbf{r}'; \mathbf{q}, \omega) &= \frac{1}{2} \sum_{\mathbf{k}} \sum_{n, n'} \frac{f(\epsilon_{n\mathbf{k}\uparrow}) - f(\epsilon_{n'\mathbf{k}+\mathbf{q}\downarrow})}{\omega - \epsilon_{n'\mathbf{k}+\mathbf{q}\downarrow} - \epsilon_{n\mathbf{k}\uparrow} + i\eta} \varphi_{n\mathbf{k}\uparrow}^*(\mathbf{r})\varphi_{n'\mathbf{k}+\mathbf{q}\downarrow}(\mathbf{r}) \\ &\quad \times \nabla_{\mathbf{r}'} \left[\varphi_{n'\mathbf{k}+\mathbf{q}\downarrow}^*(\mathbf{r}')(\nabla_{\mathbf{r}'}\varphi_{n\mathbf{k}\uparrow}(\mathbf{r}')) - (\nabla_{\mathbf{r}'}\varphi_{n'\mathbf{k}+\mathbf{q}\downarrow}^*(\mathbf{r}'))\varphi_{n\mathbf{k}\uparrow}(\mathbf{r}') \right]. \end{aligned} \quad (\text{B.61})$$

Λ is the gradient of a periodic function with respect to \mathbf{r}' . An integration over the unit cell vanishes:

$$\int_{u.c.} \Lambda(\mathbf{r}, \mathbf{r}'; \mathbf{q}, \omega) d^3r' = 0. \quad (\text{B.62})$$

Consequently, equation (B.60) can be transformed into an equation in the style of (B.55):

$$\begin{aligned} \int_{u.c.} \left[\delta(\mathbf{r} - \mathbf{r}') - \left(\frac{\mu_{\text{B}}g}{2} \right)^2 \chi_{\text{KS}}^{+-}(\mathbf{r}, \mathbf{r}'; \mathbf{0}, \omega) f_{\text{xc}}^{+-}(\mathbf{r}') \right] m(\mathbf{r}') d^3r' = \\ \int_{u.c.} \chi_{\text{KS}}^{+-}(\mathbf{r}, \mathbf{r}'; \mathbf{0}, \omega) \frac{\omega + \mu_{\text{B}}gB_{\text{ext}}(\mathbf{r}')}{2\mu_{\text{B}}g} d^3r' \end{aligned} \quad (\text{B.63})$$

where $f_{\text{xc}}^{+-}(\mathbf{r}') = 2B_{\text{xc}}(\mathbf{r}')/m(\mathbf{r}')$ (c.f. (4.53)) and $B_{\text{eff}}(\mathbf{r}') = B_{\text{ext}}(\mathbf{r}') + B_{\text{xc}}(\mathbf{r}')$ has been used. Thus, $B_{\text{ext}}(\mathbf{r}')$ is already demanded to be lattice periodic.

Interpretation If the external magnetic field is spatially homogeneous, i.e. $B_{\text{ext}}(\mathbf{r}') = B_{\text{ext}}$, then the right-hand side vanishes for $\omega = -\mu_{\text{B}}gB_{\text{ext}}$. The integral operator in the square brackets in (B.55) hence possesses an eigenfunction $\xi(\mathbf{r}; \mathbf{0}, -\mu_{\text{B}}gB_{\text{ext}}) = m(\mathbf{r})$ with eigenvalue $\lambda(\mathbf{0}, -\mu_{\text{B}}gB_{\text{ext}}) = 0$. According to the argumentation above, the spin-wave excitation energy then reads $\omega_{\text{sw}}(\mathbf{0}) = -\mu_{\text{B}}gB_{\text{ext}}$. This corresponds to the earlier finding (4.79) for the homogeneous electron gas. In the case of absent external magnetic field the spin-wave dispersion thus starts in the origin.

BIBLIOGRAPHY

- [AAL⁺88] V. I. Anisimov, V. P. Antropov, A. I. Liechtenstein, V. A. Gubanov, and A. V. Postnikov. Electronic structure and magnetic properties of 3d impurities in ferromagnetic metals. *Phys. Rev. B*, 37(10):5598–5602, Apr 1988. Citation on page 18.
- [AG94] F. Aryasetiawan and O. Gunnarsson. Linear-muffin-tin-orbital method with multiple orbitals per l channel. *Phys. Rev. B*, 49:7219, 1994. Citation on page 87.
- [AG98] F. Aryasetiawan and O. Gunnarsson. The GW method. *Rep. Prog. Phys.*, 61:237, 1998. Citation on pages 17 and 42.
- [AK99] F. Aryasetiawan and K. Karlsson. Green’s function formalism for calculating spin-wave spectra. *Phys. Rev. B*, 60(10):7419–7428, Sep 1999. Citation on page 45.
- [And75] O. Krogh Andersen. Linear methods in band theory. *Phys. Rev. B*, 12(8):3060–3083, Oct 1975. Citation on page 79.
- [Bec93] A.D. Becke. A new mixing of hartree–fock and local density-functional theories. *J. Chem. Phys.*, 98:1372, 1993. Citation on page 16.
- [BESB09] Pawel Buczek, Arthur Ernst, Leonid Sandratskii, and Patrick Bruno. Nobel lecture: Electronic structure of matter—wave functions and density functionals. *Journal of Magnetism and Magnetic Materials*, 322:1396–1398, 2009. Citation on page 107.
- [BHS82] G.B. Bachelet, D.R. Hamann, and M. Schlüter. Pseudopotentials that work: From H to Pu. *Phys. Rev. B*, 26(8):4199, 1982. Citation on page 77.
- [BJA94] Peter E. Blöchl, O. Jepsen, and O. K. Andersen. Improved tetrahedron method for brillouin-zone integrations. *Phys. Rev. B*, 49(23):16223–16233, Jun 1994. Citation on page 84.
- [Blu05] S. Bluegel. Reduced dimensions i: Magnetic moment and magnetic structure. In *Magnetism goes Nano*, volume 36 of *Spring School lecture notes of Institute of Solid state Research*. Schriften des Forschungszentrums Jülich, 2005. Citation on page 14.
- [Bri31] P.W. Bridgman. *Dinemsional Analysis*. Yale University Press, New Haven, CT, 1931. Citation on page 125.
- [BSDR07] S. Botti, A. Schindlmayr, R. Del Sole, and Lucia Reining. Time-dependent density-functional theory for extended systems. *Rep. Prog. Phys.*, 70:2007, 357-407. Citation on page 21.
- [CA80] D. M. Ceperley and B. J. Alder. Ground state of the electron gas by a stochastic method. *Phys. Rev. Lett.*, 45(7):566–569, Aug 1980. Citation on pages 16 and 66.
- [cca] The FLEUR computer code. <http://www.flapw.de>. Citation on pages 73 and 121.

- [ccb] The SPEX computer code. <http://www.flapw.de/pm/index.php?n=spex.spex-fleur>. Citation on page 74.
- [CC73] D. J. Chadi and Marvin L. Cohen. Special points in the brillouin zone. *Phys. Rev. B*, 8(12):5747–5753, Dec 1973. Citation on page 84.
- [Cun74] S. L. Cunningham. Special points in the two-dimensional brillouin zone. *Phys. Rev. B*, 10(12):4988–4994, Dec 1974. Citation on page 84.
- [DBZA84] P.H. Dederichs, S. Blugel, R. Zeller, and H. Akai. *Phys. Rev. Lett.*, 53:2512, 1984. Citation on page 118.
- [DG90] R.M. Dreizler and E.K.U. Gross. *Density Functional Theory: An Approach to the Quantum Many-Body Problem*. Springer-Verlag, Berlin, 1990. Citation on page 9.
- [DHM68] H. Danan, A. Herr, and A.J.P. Meyer. *J. Appl. Phys.*, 39:669, 1968. Citation on page 122.
- [dLK26] R. de Laer Kronig. On the theory of dispersion of x-rays. *Opt. Soc. Am.*, 12:547–557, 1926. Citation on page 34.
- [DN92] Timothy J. Deming and Bruce M. Novak. Living polymerizations as mechanistic probes. stereoselection in the nickel-catalyzed polymerization of chiral isocyanides. *Journal of the American Chemical Society*, 114(11):4400–4402, 1992. Citation on page 18.
- [DPT02] B. Davoudi, M. Polini, and M.P. Tosi. Spin-density functional approach to thermodynamic and structural consistence in the charge and spin response of an electron gas. *Solid State Commun.*, 124:335–339, 2002. Citation on page 58.
- [Fer27] E. Fermi. Un metodo statistico per la determinazione di alcune priorieta dell’atome. *Rend. Accad. Naz. Lincei*, pages 602–607, 1927. Citation on page 14.
- [fFIFJ] Institut für Festkörperforschung (IFF) Forschungszentrum Jülich. <http://www.fz-juelich.de/iff>. Citation on page 74.
- [FSBK06] Ch. Friedrich, A. Schindlmayr, S. Blugel, and T. Kotani. Elimination of the linearization error in gw calculations based on the linearized augmented-plane-wave method. *Phys. Rev. B*, 74:45104, 2006. Citation on page 87.
- [FW71] A.L. Fetter and J.D. Walecka. *Quantum Theory of Many-Particle Systems*. McGraw-Hill, 1971. Citation on page 26.
- [GDP96] E.K.U. Gross, J.F. Dobson, and M. Petersilka. *Density functional theory of time-dependent phenomena*, volume 181 of *Topics in Current Chemistry*, pages 81–172. Springer Berlin / Heidelberg, 1996. Citation on page 20.
- [GK85] E. K. U. Gross and Walter Kohn. Local density-functional theory of frequency-dependent linear response. *Phys. Rev. Lett.*, 55(26):2850–2852, Dec 1985. Citation on page 19.
- [GK86] E. K. U. Gross and Walter Kohn. Local density-functional theory of frequency-dependent linear response. *Phys. Rev. Lett.*, 57(7):923, Aug 1986. Citation on page 19.

- [GR86] E.K.U. Gross and Erich Runge. *Vielteilchentheorie*. Teubner, 1986. Citation on page 41.
- [GUG95] E.K.U. Gross, C.A. Ullrich, and U.J. Gossmann. Time-dependent density functional theory. In E.K.U. Gross and R.M. Dreizler, editors, *Density Functional Theory*, NATO ASI, Series B. Plenum Press, New York, 1995. Citation on page 20.
- [Ham79] D. R. Hamann. Semiconductor charge densities with hard-core and soft-core pseudopotentials. *Phys. Rev. Lett.*, 42(10):662–665, Mar 1979. Citation on page 80.
- [Har84] J. Harris. Adiabatic-connection approach to kohn-sham theory. *Phys. Rev. A*, 29(4):1648–1659, Apr 1984. Citation on page 16.
- [Hed65] Lars Hedin. New method for calculating the one-particle green’s function with application to the electron-gas problem. *Phys. Rev.*, 139(3A):A796–A823, Aug 1965. Citation on page 18.
- [HEPO98] S. V. Halilov, H. Eschrig, A. Y. Perlov, and P.M. Oppeneer. *Phys. Rev. B*, 58:293, 1998. Citation on pages 118, 119, and 122.
- [Her66] C. Herring. *Magnetism*, volume 4. Academic, New York, 1966. Citation on page 119.
- [HHN99] B. Hammer, L. B. Hansen, and J. K. Nørskov. Improved adsorption energetics within density-functional theory using revised perdue-burke-ernzerhof functionals. *Phys. Rev. B*, 59(11):7413–7421, Mar 1999. Citation on page 16.
- [HK64] P. Hohenberg and W. Kohn. Inhomogeneous electron gas. *Phys. Rev.*, 136(3B):B864–B871, Nov 1964. Citation on page 9.
- [JA71] O. Jepsen and O. K. Andersen. The electronic structure of h.c.p. ytterbium. *Solid State Commun.*, 9(20):1763, 1971. Citation on page 84.
- [Jac62] John. D. Jackson. *Classical Electrodynamics*. Wiley & Sons, 1962. Citation on page 127.
- [Jan74] J. F. Janak. Simplification of total-energy and pressure calculations in solids. *Phys. Rev. B*, 9(10):3985–3988, May 1974. Citation on page 15.
- [Jan78] J. F. Janak. Proof that $\frac{\partial e}{\partial n_i} = \epsilon$ in density-functional theory. *Phys. Rev. B*, 18(12):7165–7168, Dec 1978. Citation on page 11.
- [JG89] R. O. Jones and O. Gunnarsson. The density functional formalism, its applications and prospects. *Rev. Mod. Phys.*, 61(3):689–746, Jul 1989. Citation on page 17.
- [Joh88] D. D. Johnson. Modified broyden’s method for accelerating convergence in self-consistent calculations. *Phys. Rev. B*, 38(18):12807–12813, Dec 1988. Citation on page 12.
- [KA00] K. Karlsson and F. Aryasetiawan. Spin-wave excitation spectra of nickel and iron. *Phys. Rev. B*, 62(5):3006–3009, Aug 2000. Citation on page 107.
- [KB82] L. Kleinman and D.M. Bylander. Efficient Form for Model Pseudopotentials. *Phys. Rev. Lett.*, 48(20):1425, 1982. Citation on page 77.

- [KFN⁺04] Ph. Kurz, F. Forster, L. Nordstrom, G. Bihlmayer, and S. Blugel. Ab initio treatment of noncollinear magnets with the full-potential linearized augmented plane wave method. *Physical Review B (Condensed Matter and Materials Physics)*, 69(2):024415, 2004. Citation on pages 83, 119, and 121.
- [KL04] M.I. Katsnelson and A.I. Lichtenstein. *J. Phys.: Condens. Matter*, 16:7439, 2004. Citation on page 138.
- [Koe70] Dale Dean Koelling. Alternative augmented-plane-wave technique: Theory and application to copper. *Phys. Rev. B*, 2(2):290–298, Jul 1970. Citation on page 80.
- [Koh99] W. Kohn. Nobel lecture: Electronic structure of matter—wave functions and density functionals. *Rev. Mod. Phys.*, 71(5):1253–1266, Oct 1999. Citation on page 9.
- [KPB99] S. Kurth, J. P. Perdew, and P. Blaha. xxx fixme. *Int. J. Quantum Chemistry*, 75:889, 1999. Citation on page 16.
- [Kra26] H.A. Kramers. *Nature*, 117:775, 1926. Citation on page 34.
- [KS65] W. Kohn and L. J. Sham. Self-consistent equations including exchange and correlation effects. *Phys. Rev.*, 140(4A):A1133–A1138, Nov 1965. Citation on page 10.
- [KSH⁺06] G. Kotliar, S. Y. Savrasov, K. Haule, V. S. Oudovenko, O. Parcollet, and C. A. Marianetti. Electronic structure calculations with dynamical mean-field theory. *Reviews of Modern Physics*, 78(3):865, 2006. Citation on page 18.
- [Kur00] Ph. Kurz. Non-collinear magnetism at surfaces and in ultrathin films. *Berichte des Forschungszentrums Jülich*; 3832, 2000. Citation on pages 83 and 123.
- [Lev79] M. Levy. Universal variational functionals of electron densities, first-order density matrices, and natural spin-orbits and solutions of the v -representability problem. In *Proc. Natl. Acad. Sci. USA*, volume 76, page 6062, 1979. Citation on page 9.
- [LKG84] A.I. Liechtenstein, M.I. Katsnelson, and V.A. Gubanov. *J. Phys. F: Met. Phys.*, 14:L125, 1984. Citation on page 121.
- [LMB] M. Lezaic, Ph. Mavropoulos, and S. Blugel. *submitted to Phys. Rev. B*. Citation on page 119.
- [Lou67] T. Loucks. *Augmented Plane Wave Method*. Benjamin, New York, 1967. Citation on page 79.
- [LT72] G. Lehmann and M. Taut. On the numerical calculation of the density of states and related properties. *Status Solidi B*, 54:469, 1972. Citation on page 84.
- [Lyn75] J. W. Lynn. Temperature dependence of the magnetic excitations in iron. *Phys. Rev. B*, 11(7):2624–2637, Apr 1975. Citation on page 107.
- [MBB05] Y. Mokrousov, G. Bihlmayer, and S. Blugel. Full-potential linearized augmented plane-wave method for one-dimensional systems: Gold nanowire and iron monowires in a gold tube. *Physical Review B (Condensed Matter and Materials Physics)*, 72(4):045402, 2005. Citation on page 83.

- [MG06] M.A.L. Marques and E.K.U. Gross. *Time-Dependent Density Functional Theory*, volume 706 of *Lecture Notes in Physics*. Springer-Verlag, 2006. Citation on pages 19 and 21.
- [MLN73] H.A. Mook, J.W. Lynn, and M.R. Nicklow. *Phys. Rev. Lett.*, 30:30, 1973. Citation on page 122.
- [Mor85] T. Moriya. *Spin Fluctuations in Itinerant Electron Magnetism*. Springer Series in Solid-State Sciences. Springer-Verlag, 1985. Citation on pages 65 and 137.
- [MP85a] H. A. Mook and D. McK. Paul. Neutron-scattering measurement of the spin-wave spectra for nickel. *Phys. Rev. Lett.*, 54(3):227–229, Jan 1985. Citation on page 112.
- [MP85b] H.A. Mook and D. McK. Paul. *Phys. Rev. Lett.*, 54:227, 1985. Citation on page 121.
- [Nol86a] W. Nolting. *Quantentheorie des Magnetismus 1 (Grundlagen)*, volume 1. Teubner Studienbücher, 1986. Citation on page 24.
- [Nol86b] W. Nolting. *Quantentheorie des Magnetismus 2 (Modelle)*, volume 1. Teubner Studienbücher, 1986. Citation on pages 25 and 27.
- [Nye57] J.F. Nye. *Physical Properties of Crystals*. Oxford, 1957. Citation on page 35.
- [Pau82] R. Pauthenet. *J. Appl. Phys.*, 53:2029, 1982. Citation on page 122.
- [PBE96] John P. Perdew, Kieron Burke, and Matthias Ernzerhof. Generalized gradient approximation made simple. *Phys. Rev. Lett.*, 77(18):3865–3868, Oct 1996. Citation on page 16.
- [PCV⁺92] John P. Perdew, J. A. Chevary, S. H. Vosko, Koblar A. Jackson, Mark R. Pederson, D. J. Singh, and Carlos Fiolhais. Atoms, molecules, solids, and surfaces: Applications of the generalized gradient approximation for exchange and correlation. *Phys. Rev. B*, 46(11):6671–6687, Sep 1992. Citation on page 16.
- [PGG96] M. Petersilka, U. J. Gossmann, and E. K. U. Gross. Excitation energies from time-dependent density-functional theory. *Phys. Rev. Lett.*, 76(8):1212–1215, Feb 1996. Citation on page 137.
- [PK98] J. P. Perdew and S. Kurth. Density functionals for non-relativistic coulomb systems. In D.P. Joubert, editor, *Density functionals: Theory and Applications*. Springer-Verlag, 1998. Citation on page 16.
- [PKT⁺01] M. Pajda, J. Kudrnovský, I. Turek, V. Drchal, and P. Bruno. *Phys. Rev. B*, 64:174402, 2001. Citation on pages 118 and 122.
- [PR72] M.M. Pant and A.K. Rajagopal. Theory of inhomogeneous magnetic electron gas. *Solid State Commun.*, 10:1157, 1972. Citation on page 13.
- [PW92] John P. Perdew and Yue Wang. Accurate and simple analytic representation of the electron-gas correlation energy. *Phys. Rev. B*, 45(23):13244–13249, Jun 1992. Citation on pages 16 and 66.
- [PZ81] J. P. Perdew and Alex Zunger. Self-interaction correction to density-functional approximations for many-electron systems. *Phys. Rev. B*, 23(10):5048–5079, May 1981. Citation on page 18.

- [RG84] Erich Runge and E. K. U. Gross. Density-functional theory for time-dependent systems. *Phys. Rev. Lett.*, 52(12):997, Mar 1984. Citation on page 19.
- [RJ97] N.M. Rosengaard and B. Johansson. *Phys. Rev. B*, 55:14975, 1997. Citation on pages 118, 120, and 122.
- [San86] L.M. Sandratskii. Energy band structure calculations for crystals with spiral magnetic structure. *Phys. Status Solidi B*, 136:167, 1986. Citation on page 83.
- [Sasa] E. Sasioglu. private communication; to be published. Citation on page 112.
- [Sasb] E. Sasioglu. private communication; to be published. Citation on pages 113 and 122.
- [Sav92] S. Yu. Savrasov. Linear response calculations of lattice dynamics using muffin-tin basis sets. *Phys. Rev. Lett.*, 69(19):2819–2822, Nov 1992. Citation on page 106.
- [Sav98] S. Y. Savrasov. Linear response calculations of spin fluctuations. *Phys. Rev. Lett.*, 81(12):2570–2573, Sep 1998. Citation on page 106.
- [Sin91] David Singh. Ground-state properties of lanthanum: Treatment of extended-core states. *Phys. Rev. B*, 43(8):6388–6392, Mar 1991. Citation on page 84.
- [Sin94] D. J. Singh. *Planewaves, Pseudopotentials and the LAPW Method*. Kluwer Academic Publishers, 1994. Citation on page 83.
- [Sky79] L. Skywalker. Eyes wide shut! *Recent Advances in Daydreaming*, 1879. No citations.
- [Sla37] J. C. Slater. Wave functions in a periodic potential. *Phys. Rev.*, 51(10):846–851, May 1937. Citation on page 77.
- [SNS00] E. Sjöstedt, L. Nordström, and D. J. Singh. An alternative way of linearizing the augmented plane-wave method. *Solid State Commun.*, 114:15, 2000. Citation on page 84.
- [Sto39] E.C. Stoner. Collective electron ferromagnetism. ii. energy and specific heat. *Proceedings of the Royal Society of London. Series A, Mathematical and Physical Sciences (1934-1990)*, 169(938):339–371, February 1939. Citation on page 25.
- [Sto94] J. Stoer. *Numerische Mathematik*. Springer-Verlag, 1994. Citation on page 77.
- [Tho27] L.H. Thomas. The calculation of atomic fields. *Proc. Camb. Phil. Soc.*, 23:542–548, 1927. Citation on page 14.
- [TPSS03] Jianmin Tao, John P. Perdew, Viktor N. Staroverov, and Gustavo E. Scuseria. Climbing the density functional ladder: Nonempirical meta-generalized gradient approximation designed for molecules and solids. *Phys. Rev. Lett.*, 91(14):146401, Sep 2003. Citation on page 16.
- [tptotn] Webelements: the periodic table on the net. <http://www.webelements.com>. Citation on page 96.
- [van98] Robert van Leeuwen. Causality and symmetry in time-dependent density-functional theory. *Phys. Rev. Lett.*, 80(6):1280–1283, Feb 1998. Citation on page 20.
- [vH72] U von Barth and L Hedin. A local exchange-correlation potential for the spin polarized case. i. *Journal of Physics C: Solid State Physics*, 5(13):1629–1642, 1972. Citation on page 13.

- [VR87] G. Vignale and Mark Rasolt. Density-functional theory in strong magnetic fields. *Phys. Rev. Lett.*, 59(20):2360–2363, Nov 1987. Citation on page 10.
- [vSA99] M. van Schilfgaarde and V.P. Antropov. *J. Appl. Phys.*, 85:4827, 1999. Citation on pages 118 and 122.
- [WF82] M. Weinert and A.J. Freeman. *Phys. Rev. B*, 26:4571, 1982. Citation on page 121.
- [WKWF81] E. Wimmer, H. Krakauer, M. Weinert, and A. J. Freeman. Full-potential self-consistent linearized-augmented-plane-wave method for calculating the electronic structure of molecules and surfaces: o_2 molecule. *Phys. Rev. B*, 24(2):864–875, Jul 1981. Citation on pages 80 and 121.
- [ZL83] P. Ziesche and G. Lehmann. *Elektronische Eigenschaften von Metallen*. Springer-Verlag, 1983. Citation on page 128.
- [ZY98] Yingkai Zhang and Weitao Yang. Comment on 1generalized gradient approximation made simple. *Phys. Rev. Lett.*, 80(4):890, Jan 1998. Citation on page 16.

DANKSAGUNG

Eine Promotion ist ein langwieriges Projekt welches nicht im Alleingang zu bewältigen ist. Den zentralen Helfern möchte ich nochmals für die geleistete Unterstützung danken, ohne die ich diese Arbeit nicht zu Ende hätte führen können.

Mein erster Dank gilt Herrn Prof. Dr. Stefan Blügel für die Möglichkeit, in seinem Institut an dieser interessanten Aufgabenstellung zu arbeiten, sowie für seine leidenschaftliche Herangehensweise an physikalische Fragestellungen und seinen persönlichen Einsatz in entscheidenden Situationen.

Herrn Prof. Dr. Arno Schindlmayr gilt mein Dank für die Übernahme des Koreferats, sowie die fundierte Betreuung im Alltag, insbesondere die Einführung in die theoretischen Grundlagen auf denen meine Arbeit aufbaut.

Herrn Prof. Dr. Markus Morgenstern und Herrn Jun.-Prof. Riccardo Mazzarello danke ich für die Teilnahme und Mitgestaltung der Promotionsprüfung.

Meine Implementierung wäre kaum erfolgreich verlaufen ohne den kontinuierlichen Austausch mit Herrn Dr. Gustav Bihlmayer und Herrn Dr. Christoph Friedrich, um mit ihrer Hilfe die Feinheiten der verwendeten Computer-Codes zu erforschen.

Wie hätte ich ohne meine treuen Büro-Kollegen in meinem *old office* (Vamos, Yura, Marjana and Phivos!) und meinem *new office* (Hi, Andi, Schwamm und Swantje!) die diversen Durststrecken überwinden können!?

Die vielen weiteren offenen und hilfsbereiten Kollegen im Institut sind, wenn auch nicht einzeln genannt, so doch nicht vergessen! Jeder steuerte einen individuellen Teil zu dem bei, was eine gute Instituts-Atmosphäre ausmacht und mir lange in positiver Erinnerung bleiben wird.

Das Erreichen eines lange angestrebten Zieles wie dieser Promotion bietet die Gelegenheit zurückzublicken. Udenkbar, daß mich mein Weg bis hierhin geführt hätte ohne den familiären Rückhalt auf den ich immer bauen konnte. Die stete Anteilnahme und unbegrenzte Unterstützung, die ich von meinen Eltern und von meinem Bruder erfahren habe, hat mir viele Möglichkeiten erst eröffnet und macht mich sehr dankbar! Ihnen möchte ich diese Arbeit widmen.